INFORMATION TO USERS

This manuscript has been reproduced from the microfilm master. UMI films the text directly from the original or copy submitted. Thus, some thesis and dissertation copies are in typewriter face, while others may be from any type of computer printer.

The quality of this reproduction is dependent upon the quality of the copy submitted. Broken or indistinct print, colored or poor quality illustrations and photographs, print bleedthrough, substandard margins, and improper alignment can adversely affect reproduction.

In the unlikely event that the author did not send UMI a complete manuscript and there are missing pages, these will be noted. Also, if unauthorized copyright material had to be removed, a note will indicate the deletion.

Oversize materials (e.g., maps, drawings, charts) are reproduced by sectioning the original, beginning at the upper left-hand corner and continuing from left to right in equal sections with small overlaps. Each original is also photographed in one exposure and is included in reduced form at the back of the book.

Photographs included in the original manuscript have been reproduced xerographically in this copy. Higher quality 6" x 9" black and white photographic prints are available for any photographs or illustrations appearing in this copy for an additional charge. Contact UMI directly to order.

UMI

A Bell & Howell Information Company
300 North Zeeb Road, Ann Arbor MI 48106-1346 USA
313/761-4700 800/521-0600

UNIVERSITY OF OKLAHOMA

GRADUATE COLLEGE

AN INVESTIGATION OF THE DIURNAL VARIABILITY OF THE CENTRAL COLORADO DOWNSLOPE WINDSTORM

A DISSERTATION

SUBMITTED TO THE GRADUATE FACULTY

in partial fulfillment of the requirements for the degree of

Doctor of Philosophy

By

Daniel Brian Weber

Norman, Oklahoma

1997

AN INVESTIGATION OF THE DIURNAL VARIABILITY OF THE CENTRAL COLORADO DOWNSLOPE WINDSTORM

A DISSERTATION APPROVED FOR

THE SCHOOL OF METEOROLOGY

BY

Brian Fiedler

Frederick H Carr

Dale R Durran

John P. Albert

D C Vaughan

Charles A Doswell III

This work is dedicated to my mother, Nancy Donohue. She was an inspiration to me and is responsible for my return to academia. Though her short yet colorful life she instilled upon me the value of education and the usefulness of a life filled with loyalty and passion. I miss her presence in this physical world and wish she could be here to share the joy.

ACKNOWLEDGEMENTS

I thank my advisor, Doug Lilly for his persistent support during the last five years. I am grateful for his efforts in guiding me down this bumpy path and for putting up with the modeling details and providing fatherly advice. The members of my committee John Albert, Fred Carr, Chuck Doswell, Dale Durran, and Brian Fiedler were helpful in ways they don't realize. Chuck Doswell, in particular, spent a number of afternoons instilling upon me the value of this experience. There are two people not formally on my committee who helped me grow intellectually. Ming Xue and Alan Shapiro deserve honorary committee status since they fielded many questions and spurred on many ideas that are included in this work. In particular, Ming was very helpful in the model development phase. I would like to thank CAPS and Kelvin Droegemeier for giving me the opportunity to work with the ARPS and later forge my own path in the modeling arena.

This research was supported by the National Science Foundation under grant ATM 912-0009. Computations were performed at the Pittsburgh Supercomputer Center and on the University of Oklahoma's ECAS and Hitachi SR2201C computer systems. Last but not least, I thank my family and friends for their support during the last six years. I thank my father and Lynn for providing me with a stable home away from school. One individual stands out from the crowd. Miss Lorien Foote provided me with "fun" and friendship, when I let her, during the majority of my stay here. Lorien was the source of many very funny moments and I thank her and the Foote family for their support.

TABLE OF CONTENTS

LIST OF TABLES

LIST OF FIGURES

ABSTRACT

This study investigates the diurnal variability of the Central Colorado downslope windstorm via linear theory and numerical experiments. A simplified two layer linearized analytical solution is used to characterize the effects of a neutral boundary layer on the mountain wave environment. The theoretical results are compared to simulations from a newly developed mesoscale numerical model and to observations. The results indicate that parameterized surface heating decreases mountain wave intensity, in accordance with observed windstorm tendencies. In terms of the surface wave drag, the numerical solutions of heated flow over idealized mountain profiles conform to the linear analytical findings to within a factor of two. Owing to a parameterized heating cycle, decreases in steady state surface wave drag were observed to be as large as 50%. The decline of wave activity in the simulations and analytical solutions was found to be a function of the mixed layer depth, with thicker mixed layers producing larger reductions.

The two-dimensional simulations of the January 9, 1989 Boulder windstorm event show sensitivities, due to surface heating, that are consistent with observations and linear theory. Tests of similarly configured idealized two and three-dimensional heated mountain wave flows indicate that when the upstream Froude number is less than order unity, the results from the infinite ridge tests can, in general, be applied to a three-dimensional ridge of sufficient cross-flow length. The largest differences between the two and three-dimensional simulations are evident when the flow splits upstream of the mountain. This occurs for Froude numbers greater than unity. In instances where Fr>1,

the pre-heating period steady state flow is substantially different than the infinite ridge case, and upstream blocking far outweighs the effects of parameterized surface heating.

An interesting observation is made regarding the strongly heated experiments. The high drag state associated with the strong mountain wave and downslope windstorm control runs prevail but at a reduced level. The numerical experiments reveal that once a windstorm develops, a well-mixed boundary layer of modest depth (1.5km) is unable to eliminate the high drag state completely. This result suggests that changes in the mean state are necessary for dissipation of the event.

CHAPTER 1

INTRODUCTION

Strong westerly winds in the lee of the Central Colorado Rockies termed "downslope winds" have been observed for many years. Windstorms are characterized by winds greater than 60mph with a duration on the order of several hours. This phenomenon is also observed near other mountain ranges such as the Andes in South America and the Alps in Europe. Until the 1970's, severe wind events were not well understood. With the location of the National Center for Atmospheric Research Mesa Laboratory in Boulder Colorado in the early 1970's, local atmospheric scientists became interested in this phenomenon. Several severe events were investigated and the strong winds attributed to gravity wave-related processes. In the years that followed, numerical and analytical studies addressed different aspects of this phenomenon. However, predicting the onset of strong downslope winds remains a forecasting challenge.

The purpose of this work, using analytical and numerical methods, is to investigate the effects of a developing mixed boundary layer (heating period of the diurnal cycle) on idealized mountain wave flows and to propose an explanation for the observed windstorm tendencies. The desire to investigate this topic developed after reading hundreds of articles on mountain waves and downslope windstorms. There are relatively few papers in the literature addressing the effects of a neutral boundary layer on mountain wave flow. In addition, there was no explanation of the observed diurnal

windstorm bias (presented in the next section). This chapter includes a review of the Central Colorado windstorm observational record, mechanisms for downslope windstorms, studies on heated windstorms, and windstorm prediction. This chapter is closed with a statement of the project's objectives and methods.

1.2 Windstorms Observations

Boulder Colorado is located on the lee slope of the Rocky Mountains and has experienced a significant number of high wind events. Three observational studies using data collected in the Boulder area suggest a diurnal variation in windstorm strength and occurrence. The study by Julian and Julian (1969) includes surface meteorological data, newspaper accounts of wind damage, and emergency calls to the local fire departments over the period 1906-1969. Their analysis reveals both diurnal and seasonal variability to windstorm occurrence. They found frequency minima in the months of June, July, and August and a frequency maximum during January (Figure 1.1). The annual peak in January is associated with a minimum in solar radiation and strong cross-mountain flow.

Brinkmann (1974) found 20 windstorm cases over the 1968-1971 period. Her criterion for windstorm occurrence is sustained winds of 22 m/s or wind gusts to $\geq$33 m/s (hurricane force). Her analysis produces a ratio of approximately 2.5 to 1 for the number of windstorms occurring at night versus during the day. In addition, the most exposed Boulder wind-recording site indicates a tendency for surface wind speed maxima at 3, 7, 15, and 20 LST. She found instances during the nighttime hours where

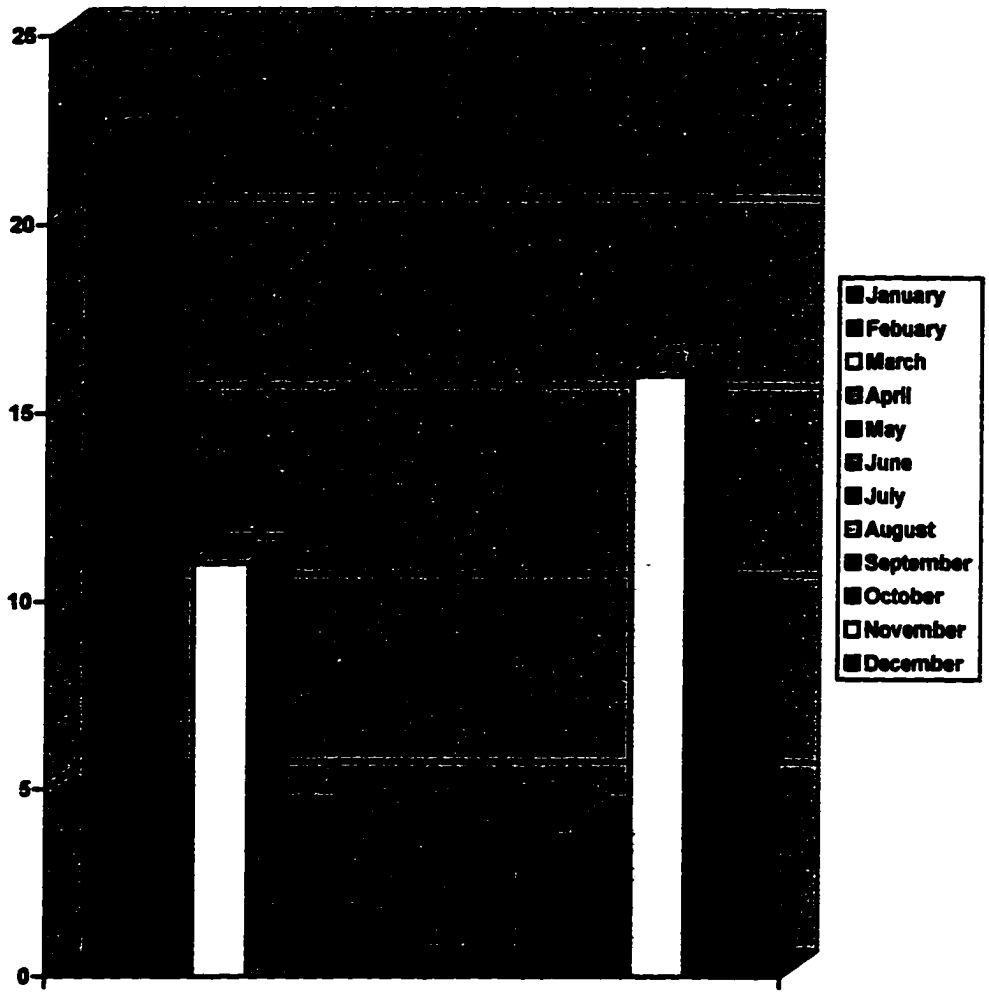

Figure 1.1. Boulder, CO monthly windstorm frequency distribution. The data source is Julian and Julian (1969).

the surface winds subside, only to increase dramatically just before sunrise. Brinkmann notes that the wind maxima propagate eastward down the lee slope. Although damaging winds have been documented during the mid-day hours, this observational study shows that the most severe winds occur during the night.

Whiteman and Whiteman (1974) analyzed data collected from 1869-1972 and obtained results similar to those of Brinkmann. Their study includes an hour by hour frequency distribution and is shown in Figure 1.2. The results show a four-fold difference between the frequency maximum at night and the daytime minimum.

Observations during the January 12, 1972 windstorm in Boulder (Figure 1.3) indicate winds speeds gusting to 100 mph, the instrument limit, with sustained winds of 60 mph for periods greater than an hour. From Figure 1.3, it is clear that winds associated with high wind events are inherently gusty. During the observation period, there are two distinct strong wind periods, from 1230-1330LST and 2030-2200LST (a three hour power failure occurred between 1330-1630LST and is not indicated on the strip chart).

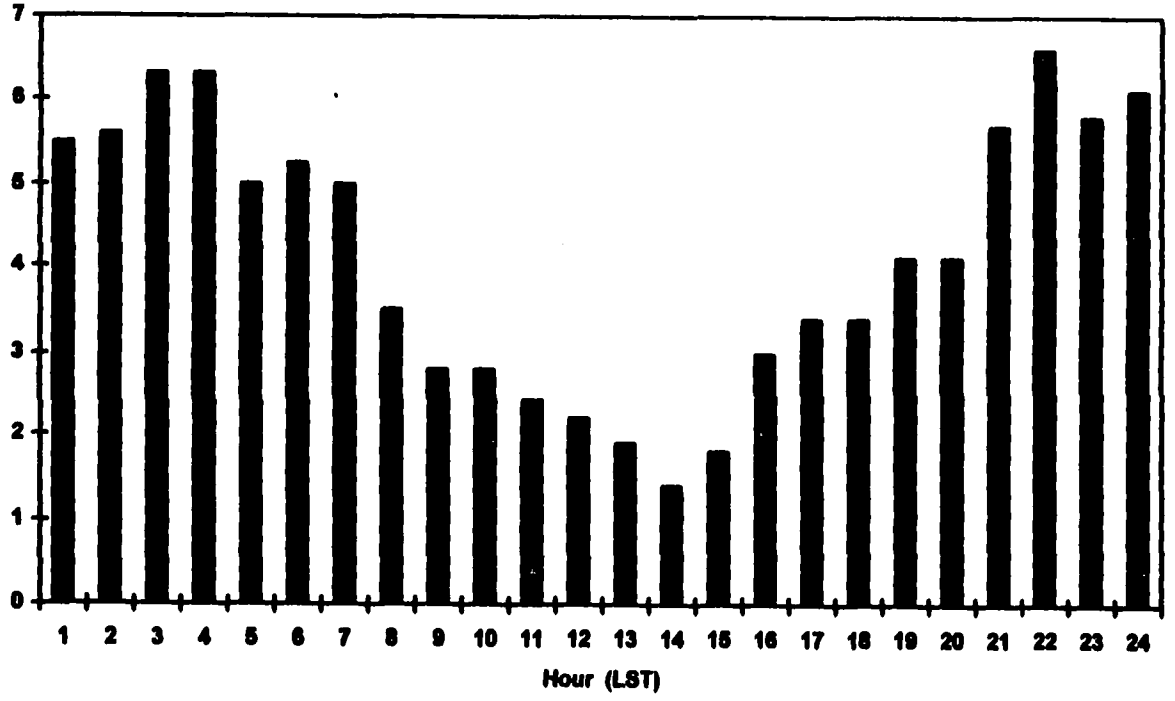

Figure 1.2. Hourly frequency distribution for windstorms observed in Boulder, CO during the period 1869-1972. The data is taken from Whiteman and Whiteman (1974).

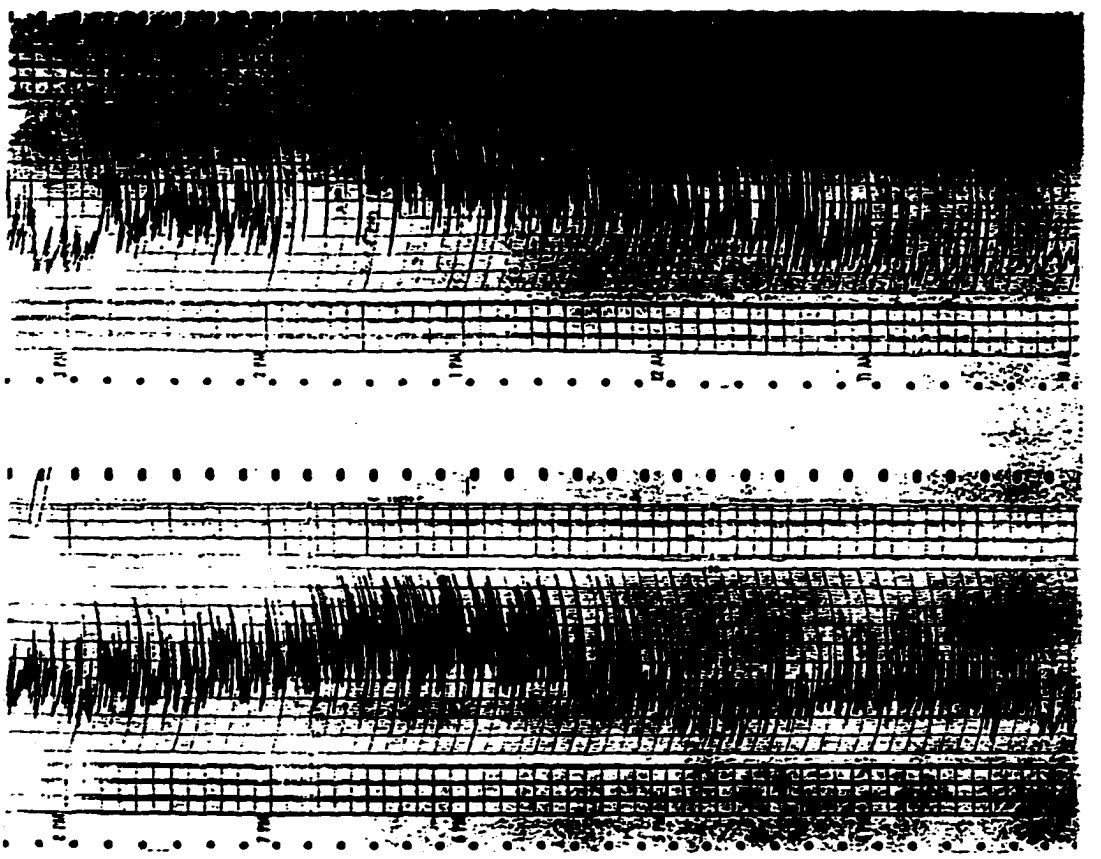

Figure 1.3. Anemometer trace from the Southern Hills Junior high School of Boulder Colorado on January 12, 1972 from 1000-2300LST. A power failure interrupted the chart recording at 1325LST and times after this point should be increased by approximately 3 hours. Vertical scale is in mph and time runs from right to left. (From Lilly and Zipser, 1972)

1.2 Literature Review

This review focuses on the application of analytical methods to downslope windstorm formation and heated mountain flows. The meteorological literature contains hundreds of papers on gravity wave theory and its application to a variety of problems. In this section, gravity wave theory is used in a linear sense to help explain some of the observed mountain wave characteristics. Other theories such as the hydraulic flow analog are introduced to add another perspective for downslope windstorm development. Finally, heated mountain waves and forecasting efforts are discussed from the limited journal entries.

1.2.1 Mechanisms for Downslope Windstorm Generation

Over the past 25 years, a significant effort has been made to unravel the cause of occasional strong winds on the lee side of the Front Range of Colorado, using two and three-dimensional numerical models, analytical theory, and forecasting experience. Three analytical theories explaining the downslope windstorm amplification process are reviewed here.

1.2.1.1 Linear Theory

Several authors (Queney, 1948; Scorer, 1955; Eliassen and Palm, 1960) used linear theory to describe the basic gravity wave response to flow passing over an obstacle in a continuously stratified fluid. Their work addresses wave processes, transfers of momentum and energy with the mean flow, and wave reflection. Klemp

and Lilly (1975) applied linear perturbation theory to estimate the resonant characteristics in multi-layer atmospheres for linear hydrostatic mountain waves. Their analysis considered two, three, and four layer atmospheric configurations. For a three layer atmosphere in which the bottom and top layer stability is greater than that in the middle layer, the maximum surface wind and corresponding wave drag occurs on the lee slope when each of the bottom two layers are ¼ of a vertical wavelength thick. For the two-layer problem in which the lower layer is less stable than the upper layer, the optimum configuration for maximum surface wind response occurs when the lower layer is ½ vertical wavelength deep. The reflection theory has merit since it is easily applied to observed atmospheric temperature profiles. As shown later in this chapter, the three-layer configuration with a less stable middle layer is commonly observed upstream of Boulder severe windstorm events.

1.2.1.1 Finite Amplitude Theory

Large amplitude mountain waves and downslope windstorms are high-energy events and may not be adequately describable by linear analysis. The validity of linear theory for describing downslope windstorms was investigated by Durran (1986, 1990, 1992). Using a non-linear non-hydrostatic numerical model, Durran (1986) found that linear theory is better suited for describing the flow characteristics in single layer atmospheres. For multi-layer atmospheres, the nonlinear effects can be significant and the value of linear analysis is suspect. With the aid of numerical procedures, Durran (1992) applied a two layer Long's equation analysis to investigate

the evolution of finite amplitude forced gravity waves. For atmospheres with a high stability layer superimposed on a low stability layer, the solution showed a significant sensitivity to the height of the interface, with linear theory either over- or underestimating the wave response.

Clark and Peltier (1977, 1984) and Peltier and Clark (1979) conducted a number of non-linear numerical simulations in which significant amplification in the surface wave drag was observed in combination with a wave-induced critical layer. A critical layer occurs when the phase speed of a wave equals the speed of the flow. For waves locked to terrain, this occurs when the wind speed is reduced to zero. In a critical layer, both the horizontal and vertical velocity components vanish. More information concerning critical layers is available in Bretherton (1966) and Gill (1982). Clark and Peltier suggest that strong downslope winds are coupled to the presence of a wave-induced critical layer, with high winds developing shortly after the critical layer appears. A critical layer generally forms after an intensifying wave overturns and breaks. Their numerical model results reveal surface wave drags of order 6 times greater than the linearized counterpart. Clark and Peltier propose, using resonant linear theory, that wave-induced critical layers develop when the distance between the critical layer and the mountain is:

$$H_c = \frac{l}{4} + \frac{n}{2} \quad n = 0,1,2,3\ldots \quad .$$

They contend that the wave-induced critical layer acts as a reflector of the vertically propagating wave energy.

Smith (1985) applies Long's equation to a strongly forced mountain flow. The idealized configuration includes a dividing streamline with an initial upstream height. Above the dividing streamline height the flow is assumed to be undisturbed. Over the mountain, the region above the dividing streamline is assumed to be well-mixed. This method implicitly includes a critical layer and wave-overturning characteristics in the region above the dividing streamline. Smith's theory predicts amplification when the critical layer height is between (¼ + n) and (¾ + n) vertical wavelengths. This amplification is tied to a specific mountain height. If the mountain height is greater than needed, then the upstream conditions may adjust and the theory no longer applies. Durran (1986) and Durran and Klemp (1987) tested this approach to the downslope windstorm problem through the use of a numerical model for a single layer atmosphere. Within the confines of a mean state critical layer required by Smith's theory, the results were verified for a number of critical layer and mountain heights.

1.2.1.3 Hydraulic Theory

The use of hydraulic theory to describe downslope winds was first proposed by Long (1953). Since then, it has been applied by Durran (1986, 1992) to explain the similarity between the hydraulic analog and observed strong downslope winds. The shallow water equations are commonly used to describe hydraulic theory and are reproduced here. Starting with the steady state horizontal momentum and continuity equations for the shallow water system with an overlying free surface,

$$u\frac{\partial u}{\partial x}+g\frac{\partial D}{\partial x}+g\frac{\partial h}{\partial x}=0, \qquad (1.1)$$

$$\frac{\partial (Du)}{\partial x}=0, \qquad (1.2)$$

a relationship for the slope of the free surface can be developed:

$$\frac{\partial h}{\partial x}=\left[1-Fr^{-2}\right]\frac{\partial (D+h)}{\partial x} \quad . \qquad (1.3)$$

The variables in (1.1), (1.2), and (1.3) are u the horizontal velocity, g the acceleration due to gravity, D the thickness of the fluid, and h is the height of the topography. Flow over an obstacle can be divided up into two categories, subcritical and supercritical, according to the Froude number. In shallow water theory, the Froude number is defined by:

$$Fr=\frac{u}{\sqrt{gD}} \quad . \qquad (1.4)$$

The Froude number describes the ratio of the advection and pressure gradient terms. Referring to (1.1), the balance of forces for supercritical flow ($Fr>1$) reveals that the advection term (first term) dominates the pressure gradient term (second term). The resulting acceleration acts to slow the parcel down as it approaches the mountain

crest. The slope of the free surface is positive and the parcel increases its elevation on approach to the crest. In the lee of the obstacle, the free surface has a negative slope and the parcel accelerates down the lee slope. In subcritical flow, the pressure gradient due to the deflection of the free surface dominates the advection term ($Fr < 1$) and the fluid accelerates as it approaches the mountaintop. Following (1.3), the slope of the free surface is negative upstream of the mountain and positive downstream of the mountain. A transition to strong flow on the lee side of the obstacle is possible when subcritical flow becomes supercritical. This occurs when the decrease in the thickness of the fluid and increase in the velocity is sufficient to force the Froude number to greater than unity. A diagram of three types of shallow water flow is presented in Figure 1.4 courtesy of Durran (1990). This figure presents subcritical, supercritical, and hydraulic jump fluid flow patterns over an obstacle. A hydraulic jump is defined as a turbulent energy-dissipative region in which a supercritical flow pattern transforms to subcritical flow, and is commonly compared to severe downslope winds. In this case, potential energy is converted to kinetic energy the entire length of the mountain, creating strong lee side flow. Durran (1986) contends that the processes leading to strong winds in the lee of the mountain are explained most accurately by the hydraulic analog. This theory has its limitations, since the free surface assumption prevents vertical gravity wave propagation.

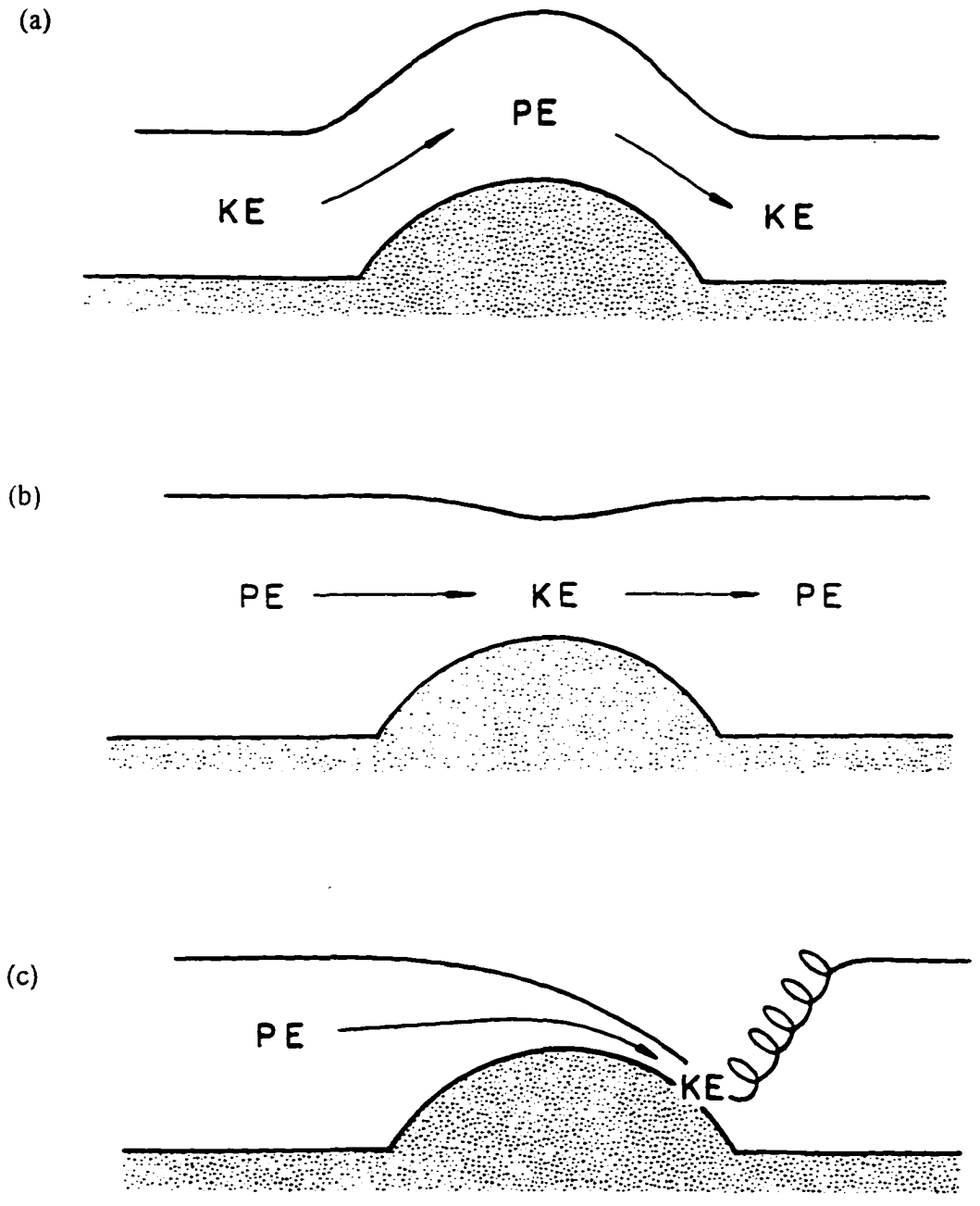

Figure 1.4. Flow regimes for water flowing over an obstacle: (a) supercritical, (b) subcritical, and (c) hydraulic jump. (Taken from Durran, 1990)

1.2.2 Three Dimensional Theory

Studies of three-dimensional flows over mountains are relatively rare in the scientific literature. Only recently have attempts been made to explain the processes associated with flow over isolated mountains using analytical and numerical methods. The numerical approach is discussed later in the forecasting section.

Three-dimensional analytical mountain wave solutions are more difficult to obtain. There are far fewer papers related to three-dimensional analytical gravity wave solutions as compared to the two-dimensional equivalent. The three-dimensional studies include Wurtele (1957) and Crapper (1959, 1962) for non-hydrostatic modes and the recent work of Phillips (1984) and Smith (1980,1988, and 1989) for the hydrostatic modes. Smith's (1980) analytical work discusses a number of issues not previously explored. He uses the Boussinesq linearized hydrostatic set of equations to obtain analytical solutions for flow over a circular mountain. The solution for the streamline deflection is of the form:

$$\eta(\hat{x},\hat{y},\hat{z}) = \frac{h}{2\pi}\int_{-\infty}^{+\infty}\int_{-\infty}^{+\infty} e^{-\hat{\kappa}} e^{\frac{i\hat{z}}{\cos\psi}} e^{i(\hat{k}\hat{x}+\hat{l}\hat{y})} d\hat{k}d\hat{l}, \qquad (1.5)$$

where,

$$\hat{x} = x/a,\ \hat{y} = y/a,\ \hat{z} = z/a,\ \hat{k} = k/a,\ \hat{l} = l/a,\ \hat{\kappa} = \kappa a,$$

$$\kappa = \sqrt{k^2 + l^2},$$

and ψ is the angle of the horizontal wave number vector. Figure 1.5 depicts the analytical vertical streamline deflections at different heights in the vicinity of the mountain. The low-level solution is quite similar in shape to the surface of the mountain. Flow is diverted around the mountain by a horizontal pressure gradient in the cross flow direction. Aloft, the solution magnitude over the mountain is reduced but the disturbance extends a significant distance downstream. The disturbance field widens in both horizontal directions with increasing z in response to the non-zero cross-stream group velocity. From (1.5) it is not clear that the magnitude should decrease with height. This reduction in magnitude is offset in a compressible atmosphere by the decrease in density with height. The wave for a three-dimensional problem would likely break but at a higher altitude than the two-dimensional case. Smith performs an asymptotic analysis far above the mountain to explain the solution results. The largest deflection corresponds to the region near the mountain peak. The decrease in the wave amplitude with height can be attributed to the dispersive properties of three-dimensional gravity waves. The disturbance energy propagates along straight lines with slopes:

$$\frac{dz}{dx} = \frac{c_{gz}}{c_{gx}}, \qquad \frac{dz}{dy} = \frac{c_{gz}}{c_{gy}}, \qquad \frac{dy}{dx} = \frac{c_{gy}}{c_{gx}} .$$

The group velocities with respect to the mountain are:

$$c_{gx} = U\frac{l^2}{k^2+l^2}, \qquad c_{gy} = -U\frac{kl}{k^2+l^2}, \qquad c_{gz} = U\frac{Uk^2}{N(k^2+l^2)^{\frac{1}{2}}} .$$

(a)

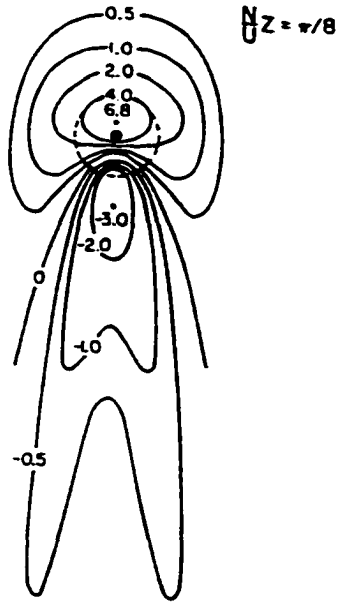

(b)

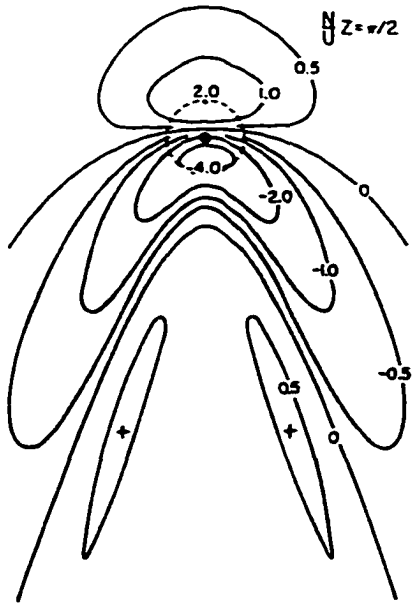

Figure 1.5. Plots of vertical streamline deflection for a three-dimensional linear hydrostatic Boussinesq mountain wave at (a) $Nz/u = \pi/8$ and (b) $Nz/u = \pi/2$. (Taken from Smith, 1980).

For a non-zero y-group velocity the wavelength in the y-direction must be less than infinity ($l > 0$). In the two-dimensional infinite ridge limit, the only non-zero group velocity with respect to the mountain is the vertical component. The slope of the group velocity defines the rate of widening with height. For small c_{gy} and large c_{gz} the slope is large and disturbance energy is transported vertically.

Phillips (1984) obtained an analytical expression for the surface wave drag for a three-dimensional elliptically shaped mountain. His results show that for a cross-stream to downstream mountain width ratio greater that 4:1, 90% of the two-dimensional surface wave drag is retained. Phillips also contends that since the difference of the maximum pressure perturbation between the infinite and finite ridge cases is about 10%, the three-dimensional problem can be reasonably approximated by the simpler two-dimensional solution. For a circular mountain profile, the surface drag is 30% lower than the two dimensional counterpart.

1.2.3 Heated Mountain Waves

Few researchers have addressed the effects of surface heating on mountain waves. Malkus and Stern (1953) performed a linear analysis for a stably stratified atmosphere with a heat source located over an island and the surrounding ocean defined as a heat sink. Their upper boundary condition only allowed lee wave motions in the solution and is not suitable for vertically propagating hydrostatic modes. In addition, their analysis neglected the direct application of diffusion of heat away from the lower boundary.

I have found only one study that includes surface heating or cooling in a non-linear analytical approach. Raymond (1972) uses a modified approach to Long's equation, which forces non-adiabatic near-surface heating and cooling. His analysis includes a single layer atmosphere with a constant upstream wind and stability profile as required by Long's method. The solution procedure involves solving the lower non-linear bottom boundary condition via an iterative numerical method. The source terms are introduced by an arbitrary function in x and z located in close proximity to the surface. This particular source function is defined by a Fourier integral in x and a decaying exponential function in z. Raymond's flux profiles were positioned symmetrically over the mountain with the maximum located at the mountain crest. Results suggest that heated mountains weaken the gravity wave response while cooled mountains enhance the wave activity. These results are limited in scope due to the unrealistic application and spatial arrangement of the source terms in the equation set and from the limited base state conditions. But, more importantly, his analysis did not consider the effects of the airflow on the heat source.

Reisner and Smolarkiewicz (1994) extend Smith's (1980) three-dimensional analysis by including a surface heating term. In their analysis, the magnitude of the heating function is set to follow the mountain height, with the maximum corresponding to the mountain peak. A result is that the heating portion of the solution contributes only positive u'/U perturbations to the solution (Figure 1.6). The heat generated low pressure near the mountain peak creates a horizontal pressure gradient force that accelerates upstream parcels towards the mountain peak. On the

lee side, the heat induced pressure gradient force decelerates the previously accelerated flow. The trajectory related minimum pressure perturbation is located just downstream of the peak and corresponds to the peak in the horizontal perturbation velocity. The placement of this minimum is due to the combination of the low pressure associated on the lee slope from the wave response and the advection of the thermally induced pressure minimum from the mountain peak. They found, by comparing linear theory to the numerical predictions of heated flow over an isolated mountain, that linear theory is in error by as much as a factor of two. The linear three-dimensional analytical solutions are useful as an interpretative guide but are not quantitatively applicable to non-linear problems.

In related works by Durran and Klemp (1983) and Smith and Lin (1982), the sensitivity of mountain wave flow to elevated heat sources was investigated. Their results show that mountain waves are sensitive to latent heat releases, with upstream cloud formation reducing mountain wave activity.

An important issue regarding the work presented in the literature needs to be addressed. In each of the above studies involving surface heating, the heat source is located directly over the mountain (except for Durran and Klemp, 1983) and was not a part of the upstream condition. Therefore, the amount of time the parcel spends over the mountain is small compared to the total trajectory time. In the real atmosphere surface heating occurs far upstream of the mountain as well as near the mountain. On length scales of the mountain width, a nearly horizontally uniform mixed layer develops without the assumed mountaintop bias.

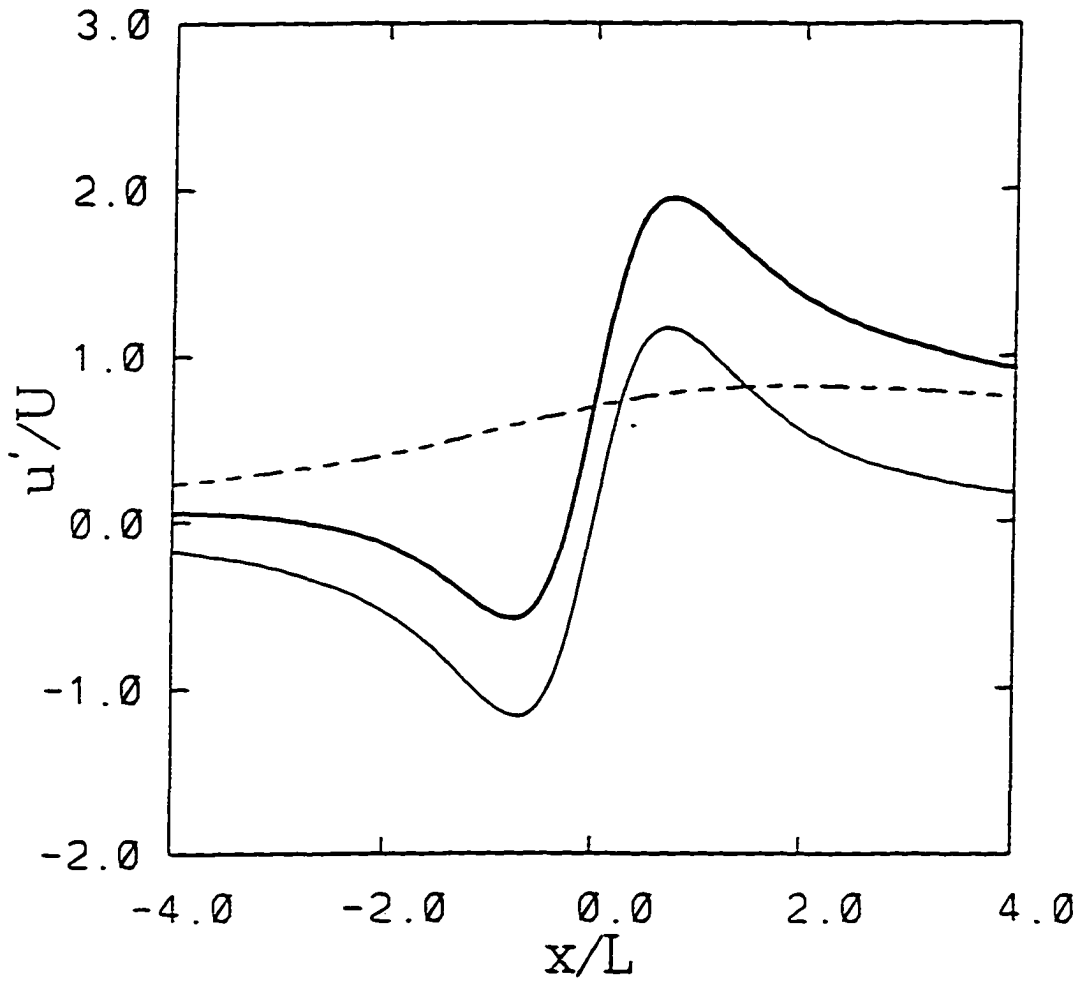

Figure 1.6. Plot of linear three-dimensional analytical u perturbation velocity normalized by the base state value as a function of normalized distance from the mountain peak along the line y=z=0. The bold solid line represents the sum of the gravity wave (thin solid line) and heating (dashed line) contributions to the horizontal velocity perturbation. (Taken from Reisner and Smolarkiewicz, 1994)

1.2.4 Windstorm Prediction

In terms of forecasting the onset, strength, and dissipation of downslope windstorms, there are few non-numerical avenues available to the meteorologist. The analytical methods discussed above are limited in the value added to a specific forecast. Durran (1990) provides a summary of potentially useful suggestions to forecasters for the prediction of downslope windstorms. One of the most relevant issues is an evaluation of the upstream sounding data. The presence of an upstream near-mountaintop inversion and moderate cross-mountain winds (20-40m/s) in the mid-troposphere were found observationally by Brinkmann (1974) and theoretically by Klemp and Lilly (1975) and Durran (1986) to be important to windstorm development. These conditions were shown to favor windstorm development and are commonly observed upstream of the Boulder area during severe windstorm events. Following Clark and Peltier (1977) and Smith (1985), the existence of a critical layer enhances the development of low level high winds. This condition is not very common but is thought to play an important role in the windstorms of the Wasatch Front in Northern Utah and in the Bore of the Yugoslav coast. Along the Wasatch Front, strong easterly winds at the surface are likely when a synoptic scale closed low pressure is situated to the south of Salt Lake City. With this configuration, a critical layer is generally present in the stratosphere.

Another method used to forecast a high wind event is to characterize the synoptic scale weather patterns that favor windstorm development. Five of the most typical synoptic situations were compiled by Scheetz et. al. (1976). The common

theme in each of these categories is the presence of moderate to strong mid-tropospheric westerly flow over the Front Range. Figure 1.7 displays the 500mb chart with the surface low and frontal positions for the configuration most likely to produce the most intense windstorm in terms of wind speed and duration. The stability profile that favors strong windstorms involves a stable layer extending above the mountaintop and a deeper less stable layer in the mid- to upper troposphere. Sounding data collected at Grand Junction, CO on the morning of January 9, 1989 are plotted in Figure 1.8. This figure represents what is thought to be a classic Boulder windstorm sounding. A configuration similar to this was found to be very effective in generating high winds near the surface in the numerical simulations of Durran (1986).

Over the past several years the meteorological community in Boulder, CO have developed an expert forecast system. It is largely an empirical approach put forth by Brown (1986) and Brown et. al. (1992) and is based on a combination of numerical model output and windstorm climatology. The forecast pyramid is built upon upstream atmospheric variables including the geostrophic wind at 1000, 700, and 500mb, the temperature difference between 500 and 300mb, the sign of the vorticity advection at 500mb, and the potential for a surface based stable layer in the lee of the mountains. During the 1990-92 windstorm seasons, it was evaluated and found to predict no greater than a 35% probability of high winds for any 6-hour period in the Boulder area. This system is much better at predicting when high winds would not occur. A similar system was applied to the Fort Collins area with better

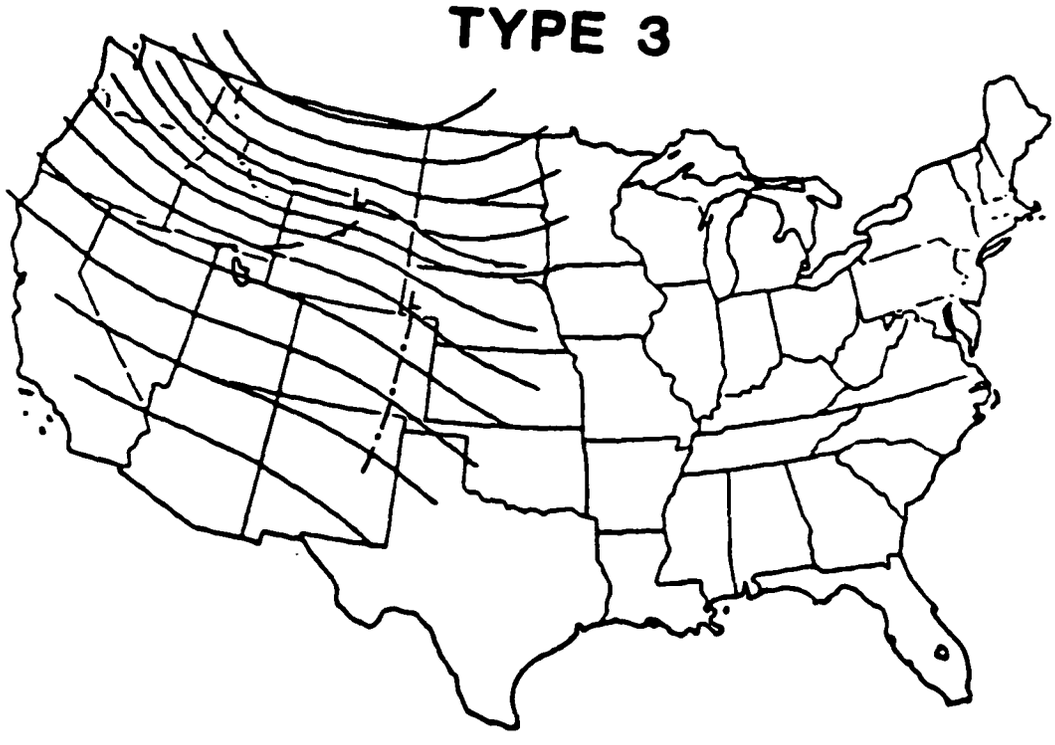

Figure 1.7. Type 3 windstorm composite chart from Scheetz et. al., (1976). Solid lines represent 500 mb height contours and the dashed lines the surface fronts. The dash-dotted line represents the lee side trough.

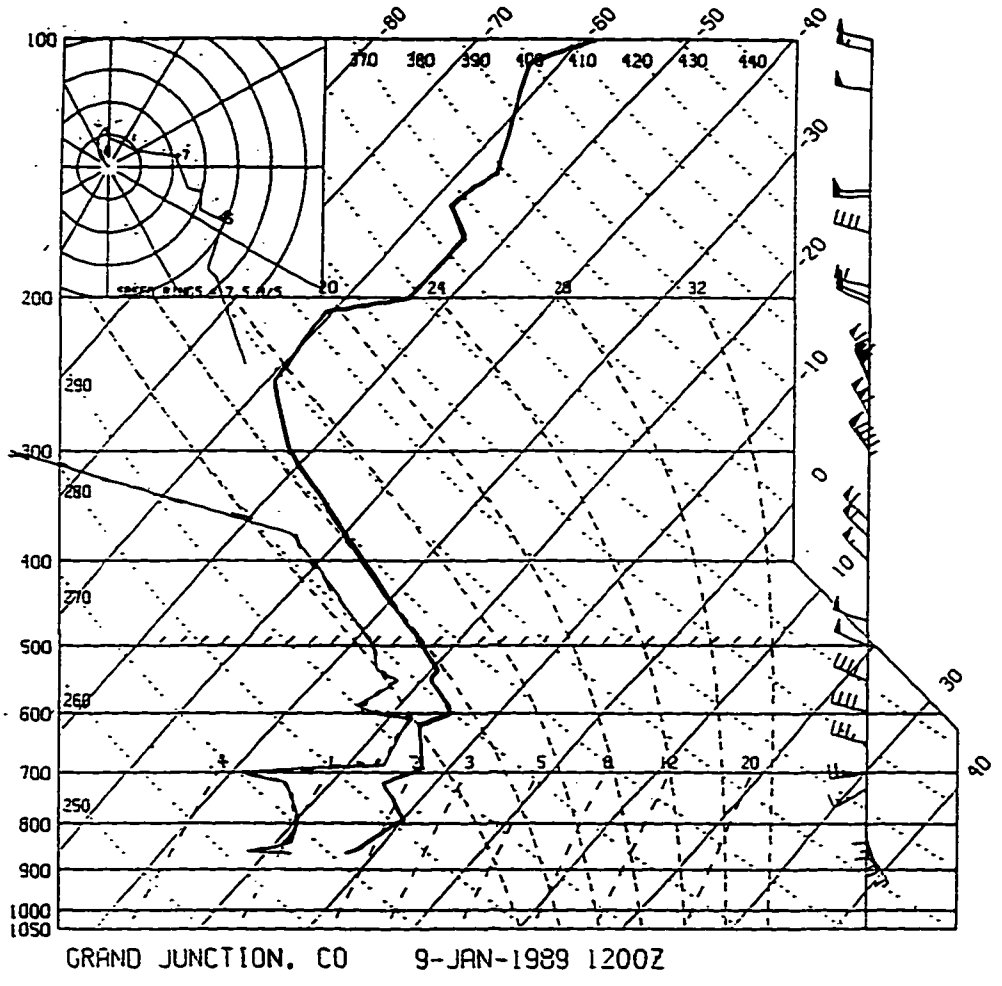

Figure 1.8. Grand Junction, CO sounding data collected 1200UTC January 9, 1989.

results. This expert forecasting system is designed to predict the maximum wind at a specific location, but fails to provide information about the time of onset and dissipation as well as the duration of the event. I contend (with T. Clark and Durran and Klemp, 1987) that these issues are better addressed through the use of numerical prediction methods.

Clark et. al (1994) performed a number of two and three-dimensional simulations of the January 9, 1989 Boulder wind event and compared the results to observations. They noted significant differences between the two and three-dimensional simulations, with the majority of the differences attributed to fine scale structures. In particular for the lee side gust structures, a near equal partitioning of the energy spectrum near the 3-km horizontal length scale is evident in the three-dimensional case. The two-dimensional study displays more energy at larger horizontal scales, with a number of peaks in the wave number spectrum not present in the three-dimensional simulation. Energy spectra for the gust structure in the north-south direction are centered near the 10-km wavelength, following the general observed variability of the terrain and large east-west oriented canyons. Their simulations predicted a windstorm but the location and timing of the event was inaccurate. The forecast location of the jump structures is west of the observed features. They also found that the gust structures were sensitive to model resolution and the surface drag formulation. In support of previous two-dimensional downslope windstorm modeling studies, propagating gusts were predicted by their model in both

the two and three-dimensional simulations. The modeled gusts were found to be similar in structure to those observed with Doppler Lidar.

The general void of detailed three-dimensional numerical simulations of downslope windstorms in the literatures is obviously due to the large domain and resolution requirements. As discussed later in this paper, lateral boundary conditions severely restrict the usefulness of small domain runs. Large computational domains and long time integration are required to fully understand the onset, duration and dissipation of strong windstorms.

1.3 Objectives

As revealed in the literature review, little effort has been focused on the impacts of surface heating on mountain induced gravity waves. Observations (Figure 1.2) indicate that windstorms occur during all hours of the day but are much more frequent at night. Previous work fails to explain the observational record. Raymond's study provides insight to the observed diurnal cycle but is limited in its application due to the constraints associated with Long's finite amplitude theory and the placement of the source terms. Brinkmann, from a relatively small sample size of 20, reported a daytime maximum which is not explained by Raymond's' preliminary results. The purpose of this study is to investigate the Central Colorado observed downslope windstorm diurnal bias via analytical and numerical means. Specifically, I will address the following questions:

1) Is the observed diurnal downslope windstorm frequency distribution attributable to the diurnal heating cycle?

2) To what extent can linear theory be used to predict the non-breaking mountain wave and downslope windstorm response to a well-mixed surface layer?

3) Can the heated gravity wave response in Central Colorado be approximated by two-dimensional simulations or are three dimensions required?

4) Are large eddy motions in the convective boundary layer needed to accurately predict the diurnal response of strong mountain waves and downslope windstorms?

5) Is the surface heat flux budget important in improving the predictability of strong mountain waves?

1.4 Methods

This study applies both analytical and numerical methods to investigate the questions posed in the previous section. The analytical approach involves a simplified linear two-layer solution to assess gravity wave responses to variable horizontal forcing wavelengths and mixed layer depths. The simplified two-layer linear approach is chosen for two reasons. Linear theory captures the basic gravity wave structure and the two-layer configuration allows for the introduction of a neutral surface layer. Other methods used in this study include a scale analysis of the convective boundary layer motions and mountain forced gravity waves. A theoretical limit to downslope windstorm strength is also reviewed.

The majority of the reported results are obtained from application of numerical methods. A numerical model is used to simulate two and three-dimensional mountain wave and downslope windstorm responses to parameterized diurnal heating cycles. The desire to incorporate three-dimensional aspects is brought about by the results of Reisner and Smolarkiewicz (1994) and Clark et. al. (1994). Initially, the model is applied in idealized two and three-dimensional configurations. A more realistic two-dimensional downslope windstorm experiment is included for comparison purposes. The strength of the mountain wave response is measured in terms of first and second order gravity wave properties. Following Eliassen and Palm (1960), computed surface wave drag and vertical profiles of the horizontally integrated vertical flux of horizontal momentum are compared. In most cases, the maxima in horizontal surface wind speeds are used to assess the gravity wave response. All numerical simulations presented in this study adhere to the following protocol:

a) Obtain a steady state non-heated mountain wave solution.

b) Calculate surface heat fluxes and assess the response in terms of wave properties.

An alternative modeling approach that could be performed begins with a characteristic atmospheric profile and applies the cooling portion of the diurnal cycle. A potential problem with this procedure is that the depth of the stable surface layer is small compared to the daytime boundary layer. The anticipated effects would be small since only a shallow stable layer is created overnight. The advantage to the

approach is the generation of near surface stable air upstream of the mountain. It is not clear if the stable air settles in the valleys or is able to pass over the mountain and enhance the wave activity. This problem could be addressed in future work.

In order to keep the analysis simple, the earth's rotation is not included in the experiments. The time scale for the hydrostatic waves ($1/N$) is significantly smaller than for the rotational modes ($1/f$), justifying the non-rotating assumption. For details on the effects of the Coriolis term on the solutions see Lilly (1983) and Clark et. al. (1994). The numerical experiments are categorized in terms of the dimensional arrangement and initial conditions.

1) Two Dimensional Idealized Mountain Profile

   - Non-linear narrow and wide mountain shapes in a single layer atmosphere using two different heat distribution methods (parameterized turbulent diffusion vs. explicit convection).

   - Mean state critical layer simulations for a simple one-layer atmosphere and wide mountain shape.

   - Non-linear parameter range study.

   - Two-layer tuned atmosphere simulations.

2) Two Dimensional Central Colorado January 9, 1989 Windstorm

   - Numerical experiment with a smoothed terrain cross section through Boulder, Colorado (40° N latitude) and Craig, Colorado 12Z sounding.

3) Three Dimensional Idealized Mountain Profile

- Non-linear parameter range experiments for circular and finite ridge mountain shapes (compared to 2-D tests).

This study is organized as follows: Chapter 2 presents a two-layer linear analytical solution and reviews the energetics of mountain waves and the convective boundary layer. Chapter 3 describes the numerical model formulation and Chapter 4 displays model verification test results. Chapter 5 and Chapter 6 focus on the two and three-dimensional numerical simulations and Chapter 7 provides a summary of the results. The appendices give additional information on the model's vertically implicit time marching method, upper $w-\pi$ radiation boundary condition, computational efficiency, streamline and trajectory computations, and atmospheric sounding profiles.

CHAPTER 2

ANALYTICAL METHODS

Strong downslope windstorms have been shown by Durran (1992) and others to be highly non-linear events. Analytical finite amplitude solutions that include a non-linear lower boundary condition are available with the aid of numerical procedures. Given this constraint, a linearized two-layer solution is presented that adds insight to the numerical experiments and observational record. In addition, a scale analysis is provided for mountain waves and boundary layer convection.

2.1 Linear Two-Layer Solution

In the context of this study, linear theory has been applied sparingly in the literature. Diffusion of heat away from the lower boundary complicates the linear analysis considerably by introducing a 4th order governing equation. Not only is it difficult to apply the diffusion term analytically, the results may have little effect on the solution. At the surface, diffusion is useful in transporting heat away from the boundary provided the mixing coefficient is sufficiently large, as is the case in the parameterized methods described later in Chapter 3. But once heat is transferred away from the lower boundary, other effects such as horizontal and vertical advection, with time scales much less than the diffusive time scale, dominate the flow.

A different approach is taken here in regards to the linear analysis. Steady state linear theory is applied from the standpoint that the convective motions, associated with the process of heat redistribution in the mixed layer, are neglected. The objective is to

look at the effects of varying mixed layer depths on wave amplitude. From this perspective, the solutions in the overriding stable layer can be easily solved in terms of the mixed layer depth and the horizontal and vertical scales. This assumption is defended later in this chapter.

During the first part of the diurnal heating cycle, the steady state assumption is not defensible as the mixed layer height is strongly time-dependant. The steady state assumption is most likely to be valid in the late afternoon when the mixed layer height is changing slowly and the heat is distributed over a large vertical extent. A time dependent solution in terms of the mixed layer height is not investigated here but is possible through the application of similarity theory (Garratt, 1994).

As mentioned in the review of Chapter 1, most of the analytical work applies the assumption that the heating source decreases away from the mountain. This restriction is not used here. In the real atmosphere, surface heating is not confined to the mountain and extends far upstream. The result is a boundary layer height that is, on average, nearly uniform upstream of the mountain. Consequently, this analysis investigates the significance of different boundary layer depths on the overlying mountain wave flow.

A linearized two-dimensional Boussinesq equation set in terms of u', w', θ', and π' is used in this analysis. Little generality is lost from the application of the Boussinesq set of equations, as the effects of decreasing density with height are well known (Gutman, 1991). For the analysis given here, the base state wind is constant ($\overline{U}$) with height and equal in both layers. The stratification is defined as $N^2 = \frac{g}{\theta_o}\frac{d\overline{\theta}}{dz}$

and is set to zero in the lower layer (N_1) and to a positive constant (N_2) in the upper layer. The steady state version of the Boussinesq equation set is:

$$\overline{U}\frac{\partial u'}{\partial x} = -C_p\theta_o\frac{\partial \pi'}{\partial x} \quad , \tag{2.1}$$

$$\overline{U}\frac{\partial w'}{\partial x} = -C_p\theta_o\frac{\partial \pi'}{\partial z} + \frac{g\theta'}{\theta_o} \quad , \tag{2.2}$$

$$\overline{U}\frac{\partial \theta'}{\partial x} + w'\frac{\partial \overline{\theta}}{\partial z} = 0 \quad , \tag{2.3}$$

$$\frac{\partial u'}{\partial x} + \frac{\partial w'}{\partial z} = 0 \quad . \tag{2.4}$$

Figure 2.1 sets up the problem graphically. The bottom layer (layer 1) is neutrally stratified ($N_1 = 0$) and represents a well-mixed boundary layer. The upper layer (layer 2) is stratified with N_2 = constant and supports gravity waves. Equations (2.1)-(2.4) combine to give a single equation in perturbation vertical velocity w' :

$$(\frac{\partial^2}{\partial x^2} + \frac{\partial^2}{\partial z^2})w' + \frac{N^2}{\overline{U}^2}w' = 0 \quad . \tag{2.5}$$

Equation (2.5) defines w' in the stratified environment of layer 2. For the neutral stability of layer 1, (2.5) simplifies to:

$$(\frac{\partial^2}{\partial x^2} + \frac{\partial^2}{\partial z^2})w' = 0 \quad . \tag{2.6}$$

and describes potential flow. Equations (2.5) and (2.6) are forced by introducing a base state flow ($\overline{U}$) over a small amplitude mountain. The terrain $h(x)$ is defined by

$$h = h_o e^{ikx} \quad , \tag{2.7}$$

where k is the horizontal wave number and h_o is the mountain height. This expression can be used to represent a single wave or be combined with other wave components in a Fourier series representation of a particular mountain profile. This example is confined to a single wave component without loss of generality.

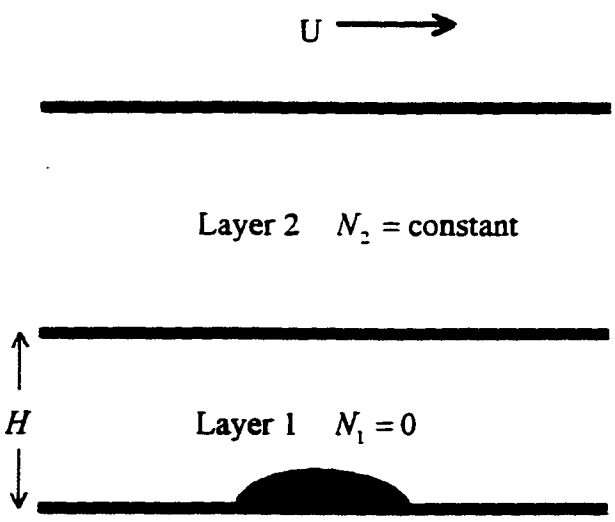

Figure 2.1. Graphical depiction of the two-layer linear problem. In the analysis, the mountain is chosen to be a cosine function.

Solutions to (2.5) and (2.6) are of the form:

$$w'_2(x,z) = \mathrm{Re}(Ce^{i(kx-m_2z)} + De^{i(kx-m_2z)}) \quad , \tag{2.8}$$

$$w'_1(x,z) = \mathrm{Re}(Ae^{-m_1z-ikx} + Be^{m_1z-ikx}) \quad , \tag{2.9}$$

where the wave numbers are:

$$m_2^2 = (\frac{N_2}{U})^2 - k^2 \quad ,$$

$$m_1^2 = k^2 \quad .$$

The wave number in layer 2 is a function of the stability, base state wind, and horizontal wave number. Equation (2.8) is valid for m_2 real. If m_2 becomes imaginary then the solutions no longer admits gravity waves modes and follows the form of (2.9). Assuming hydrostatically forced gravity wave flow in the upper layer (m_2^2 >0), the wavelike solution of (2.8) holds. The wave number in the bottom layer is equivalent to the horizontal wave number. The complex coefficients A, B, C, and D are determined from application of the boundary and matching conditions. The upper boundary condition requires energy to propagate out of the domain. Following Eliassen and Palm (1960) this is true when $\overline{w'p'} > 0$, where the overbar represents the horizontal average. The matching conditions require the displacement and pressure at the layer interface height (z=0) to be equivalent. A number of horizontal wavelengths and mixed layer depths are investigated here. In addition, a discontinuity in density is introduced into the solution. This is intended to represent an inversion placed at the interface between

the two layers. Inversions are commonly observed at the top of the mixed layer. The application of the interface pressure condition follows that of Klemp and Lilly (1975) and can be obtained by integrating the hydrostatic relation. These conditions are presented in terms of the vertical velocity:

$$w'(1) = w'(2) \quad , \qquad \text{at } z = 0$$

$$\frac{\partial w_1'}{\partial z} + \frac{g}{U^2}\frac{\Delta\theta}{\bar{\theta}} w_1' = \frac{\partial w_2'}{\partial z} \quad . \qquad \text{at } z = 0$$

The second matching condition requires continuity of the vertical derivative of the vertical velocity and is equivalent to matching the horizontal pressure gradient term in the two layers. The term $\Delta\theta / \bar{\theta}$ represents the change in potential temperature across the inversion. Physically, the inversion represents external gravity waves along the layer interface. For the non-inversion case this term vanishes. The bottom boundary condition is linearized using:

$$w_1'(0) = \bar{U}\frac{\partial h}{\partial x} = ik\bar{U}h_o e^{ikx} \quad .$$

Enforcing upward energy propagation away from the mountain in the upper layer requires $D = 0$ in (2.8), since the phase $(kx - m_2 z)$ emits only downward propagating energy when sgn(k) = sgn(m_2). The three remaining coefficients are determined from application of the matching and lower boundary conditions:

$$A + B = C \quad ,$$

$$\frac{k}{m_2}(B-A)=C \quad .$$

$$A=e^{-kH}(ik\bar{U}h_o-Be^{-kH}) \quad .$$

where H is the depth of the mixed layer. Solving for the complex coefficients and incorporating them into (2.8) and (2.9) and taking the real parts gives:

$$w_2'(x,z)=\frac{y_3}{y_2^2+y_5^2}\left[(y_2y_4-y_2)\cos(kx+m_2z)-(y_1y_5+y_2^2+y_5)\sin(kx+m_2z)\right] \quad , \tag{2.10}$$

$$w_1'(x,z)=\frac{y_3}{y_2^2+y_5^2}\Big([y_2y_4\cos(kx)-(y_1y_5+y_2^2)\sin(kx)]e^{-kz}$$

$$-[(y_2\cos(kx)+y_5\sin(kx)]e^{kz}\Big) \quad , \tag{2.11}$$

where the constants are given by:

$$y_1=\frac{(k-\frac{g'}{\bar{U}^2})(k+\frac{g'}{\bar{U}^2})-m_2^2}{(k+\frac{g'}{\bar{U}^2})^2+m_2^2} \quad ,$$

$$y_2=\frac{2m_2k}{(k+\frac{g'}{\bar{U}^2})^2+m_2^2} \quad ,$$

$$y_3=k\bar{U}H_oe^{-kH} \quad ,$$

$$y_4=e^{-2kH} \quad ,$$

$$y_5=y_1+y_4 \quad ,$$

with,

$$g' = g\frac{(\theta_2 - \theta_1)}{\bar{\theta}} \quad .$$

Results from the two-layer solution are presented in terms of normalized surface wave drag. For a linear hydrostatic Boussinesq system, the steady state surface wave drag is equivalent to the vertical flux of horizontal momentum (Eliassen and Palm, 1960):

$$\tau_{ss} = -\bar{U}\rho_o \int u'w'dx = \int p'w'dx \quad , \qquad (2.12)$$

$$\overline{pw} = \frac{1}{2}\rho_o(0)\frac{\bar{U}}{k}\,\mathrm{Im}\,Part\{w(z)^* w_2(z)\} \quad ,$$

where $w(z)^*$ denotes the complex conjugate and $\overline{pw}$ is the average over one wavelength. The vertical flux of horizontal momentum can be shown to be:

$$\overline{pw} = \rho_o(0)\bar{U}\frac{y_2 y_3^2}{(y_2^2 + y_5^2)} \quad ,$$

or,

$$\overline{pw} = \rho_o(o)\bar{U}(k\bar{U}H_o)^2 e^{-2kH}\frac{\dfrac{2m_2 k}{(k+\frac{g'}{\bar{U}^2})^2 + m_2^2}}{[\dfrac{2m_2 k}{(k+\frac{g'}{\bar{U}^2})^2 + m_2^2}]^2 + [\dfrac{(k+\frac{g'}{\bar{U}^2})(k-\frac{g'}{\bar{U}^2})}{(k+\frac{g'}{\bar{U}^2})^2 + m_2^2} + e^{-2kH}]^2} \quad .$$

The sensitivity of the surface wave drag to the mixed layer depth, horizontal wavelength, and for the hydrostatic case the inversion strength, is illustrated by the

colored curves in Figure 2.2. For this analysis, the base state wind is $U = 20$m/s and the static stability in the upper layer is $N = 0.01$. The flux is normalized by the $H = 0$ case. As indicated in the figure, the steady state momentum flux in the upper layer is significantly affected by changes in the thickness of the mixed layer and to a lesser extent by the horizontal wave number. The results reveal a nearly 80% reduction of the wave activity in layer 2 for a mixed layer depth of 3km. The wave number dependence is small, with only a 6% decrease in the remaining wave activity for the non-hydrostatic case versus the hydrostatically forced flows for a 3km deep neutral layer. Interestingly, the plot also shows that an inversion acts to offset the reduction of mountain wave activity due to the development of a neutral layer. For a 1.5 ° K inversion, a mixed layer of 0.5km depth is required to remove the inversion layer mountain wave enhancement. A 10 ° K inversion, although not likely to be observed during windstorms, greatly enhances the mountain wave activity. The enhancement is likely due to surface wave effects, but a detailed study has not been performed to confirm this. This analysis can be extended to systems with more than two layers.

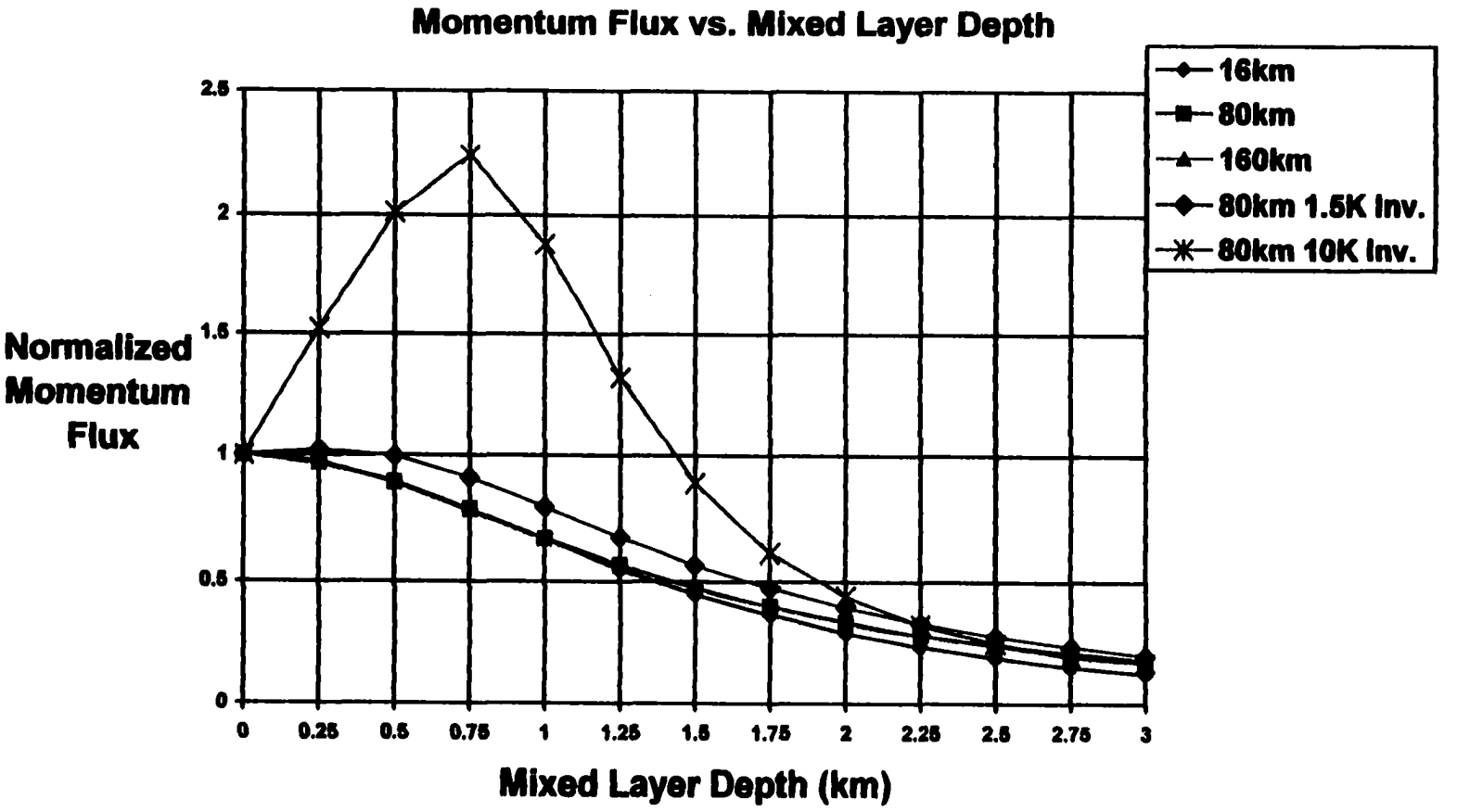

Figure 2.2. Plot of the analytical steady state vertical flux of horizontal momentum curves as a function of mixed layer depth, horizontal wave number (16, 80, and 160 km) and inversion strength. The values are normalized by the H =0 steady state values.

2.2 Energy and Scaling Considerations

2.2.1 Downslope Windstorm Horizontal Velocity Limit

A simplified system can be used to estimate the maximum winds generated by flow over an obstacle. One such method involves the Bernoulli equation (Fiedler, 1992). Consider the case in which the terrain elevations upstream and downstream of the mountain are equal and the entire upstream flow is reduced to a thin layer in the lee of the mountain. For irrotational flow upstream of the mountain, the Bernoulli relation can be applied along the surface streamline:

$$\frac{1}{2}q_1^2 + \int \frac{dp_1}{\rho} + gz_1 = \frac{1}{2}q_2^2 + \int \frac{dp_2}{\rho} + gz_2 = \text{constant} \ . \qquad (2.13)$$

The subscripts 1 and 2 represent the upstream and downstream values, respectively. Since the height of the streamline is approximately the same upstream and downstream, (2.13) reduces to:

$$\frac{1}{2}q_1^2 + \int \frac{dp_1}{\rho_o} = \frac{1}{2}q_2^2 + \int \frac{dp_2}{\rho_o} \ , \qquad (2.14)$$

where $q = u$ and the density is assumed to be constant for a Boussinesq atmosphere. Solving for the downstream wind (u_2), we obtain:

$$\frac{1}{2}u_2^2 = \frac{1}{2}u_2^2 + \int \frac{dp_1}{\rho_o} - \int \frac{dp_2}{\rho_o} \ .$$

Assuming a hydrostatic atmospheric profile and confining the entire upstream flow to a small depth downstream of the mountain, the difference in pressure between the upstream and downstream points is approximated by:

$$\int \frac{dp_1}{\rho_o} - \int \frac{dp_2}{\rho_o} = \int_z^H \frac{g}{\rho_o} \frac{d\overline{\rho}}{dz}(H - z)dz \quad .$$

If z =0, and the static stability is assumed constant and defined as $N^2 = \frac{g}{\rho_o}\frac{d\overline{\rho}}{dz}$, the resulting relation for the downstream wind is:

$$u_2^2 = u_1^2 + N^2 H^2 \quad . \qquad (2.15)$$

Equation (2.15) relates the downstream wind speed to the static stability and the change in height of the fluid from its upstream value. For a fluid depth on the order of H =10km and static stability $N = 0.01$, the downstream wind speed is on the order of 100m/s. All known observations of windstorms in the lee of the Colorado Rockies lie within the above limit, with wind gusts from 30-60 m/s commonly observed, but no observations of wind speeds approaching 100m/s.

2.2.2 Mountain Wave Scale Analysis

The scaling of such events can be estimated using the vertical and horizontal time and length scales. The length of the forcing mechanism, the mountain wave number k, gives the horizontal scale in this case. For a linearized Boussinesq

atmosphere with a constant base state wind, the vertical scale (wave number) is a simple function of the base state wind, static stability, and the horizontal wave number. The Scorer (1955) parameter is:

$$l^2 = \frac{N^2}{\overline{U}^2} - k^2 \quad .$$

One time scale can be determined from the velocity and the length scales ($a / \overline{U}$) and represents the time a parcel takes to move through the standing wave. For hydrostatically forced mountain flow with a standard atmospheric temperature and wind profile, the vertical length scale is on the order of 10km. The corresponding time scale is approximately 1-2 hours. In numerical predictions, a steady state value is often obtained after the non-dimensional time of $\overline{U}t / a = 60$, where a is the horizontal length scale. This measure refers to the time it takes for a parcel to pass through the wave. A second time scale can be defined which involves the Brunt-Vaisala frequency N. Taking the reciprocal gives dimensions of time on the order of $1/N$. Typical values of N in the troposphere are on the order of 0.01 s^{-1} and equate to an approximate oscillation period of 10 minutes. The velocity scale can be defined by the vertical displacement times the stability. This equates to the maximum vertical distance an upstream parcel could be displaced before all the kinetic energy of the parcel has been converted to potential energy. For a 1km tall mountain and stability of 0.01 1/s, the velocity scale is on the order of 10 m/s. From this perspective, a 1km tall mountain can force significant perturbations on the base state to the point in which non-linear effects

become important. From the above scaling arguments, it is apparent that the key variables include the static stability, base state wind, mountain height, and horizontal wavelength. These quantities form a basis that will be used in the numerical experiments of Chapters 5 and 6.

2.2.3 Convective Boundary Layer Scaling

Motions in the convective boundary layer can often be estimated using similarity theory. This theory is based on the characteristic length and time scales associated with the development of the heated boundary layer. Following a standard text on atmospheric convection, such as Emanuel (1994), it is shown that the velocity scale in a convective boundary layer can be estimated by:

$$w^* \approx (z_i \overline{w'B'})^{\frac{1}{3}} \quad . \tag{2.16}$$

For a mixed layer depth of 1km and a buoyancy flux $\overline{w'B'} = 0.10$ (equivalent to a heating rate of $100 W/m^2$), the convective scale velocity is on the order of 1m/s. A number of modeling and observation studies support this scaling result. The horizontal scale of the most unstable convective motion (L_c) in a three-dimensional Rayleigh convection problem with free slip boundaries can be formulated in terms of the fluid depth H.

$$L_c = 2\sqrt{2}H$$

Thus, for a three-dimensional heated surface problem, the horizontal scale is approximately six times the vertical scale. The time scale for convection can be estimated from the velocity and length scales.

$$t_{conv} \approx \frac{L_c}{w^*} \approx 5-10 \text{minutes}$$

2.2.4 Discussion

For linear waves, the mountain height is small and the resulting contribution in the boundary layer from the convective motions is on the same order of magnitude as the gravity wave perturbations. For large amplitude mountain waves and downslope windstorms, the convective motions are an order of magnitude smaller than those generated by the gravity wave. The convective time, length, and velocity scales are significantly smaller than those associated with a strong gravity wave. From this perspective, the convective motions should play a minor role in the gravity wave solution. From a gravity wave perspective, as illustrated in Figure 2.2, the impact of the boundary layer convective motions is most important in terms of the development of the mixed layer height with time.

To test these scaling arguments, a simplified two-dimensional mountain wave simulation is presented in Chapter 5 for an explicitly resolved convective boundary layer solution and a less resolved diffusive approach.

CHAPTER 3

NUMERICAL MODEL

A new three dimensional model (with a two dimensional option) is used to simulate dry heated mountain wave flows. The model, ARPI3D, was constructed initially in a simple two-dimensional framework to test horizontal boundary condition applications for use in the ARPS. The code is extensively documented and the initialization of the horizontally homogeneous base state variables follows that of the ARPS.

Since its inception, ARPI3D was modified to include a simple coordinate transformation, a vertically-implicit solving technique, and a linearized upper radiation condition between pressure and vertical velocity. In addition, this model solves for the non-dimensional Exner function π instead of pressure. Initially, ARPI3D included a "p" (pressure) or "pi" (Exner function) option but the p-option was later dropped for the more efficient pi-system. The inclusion of the non-linear pressure gradient and divergence term coefficients closes the model energy budget. The decision to include the total potential temperature in the pressure gradient term is not solely based on the goal of energy conservation. It was due in part from tests comparing the linearized and total term versions. Perturbations on the order of 30% of the base state potential temperature were observed in the breaking wave regions in the stratosphere.

3.1 Equation Set

The ARPI3D equation set is:

$$\frac{\partial u}{\partial t} + u\frac{\partial u}{\partial x} + v\frac{\partial u}{\partial y} + w\frac{\partial u}{\partial z} = -c_p\theta\frac{\partial \pi}{\partial x} + fv - fw + D_u + turb_u \quad , \qquad (3.1)$$

$$\frac{\partial v}{\partial t} + u\frac{\partial v}{\partial x} + v\frac{\partial v}{\partial y} + w\frac{\partial v}{\partial z} = -c_p\theta\frac{\partial \pi}{\partial y} - fu + D_v + turb_v \quad , \qquad (3.2)$$

$$\frac{\partial w}{\partial t} + u\frac{\partial w}{\partial x} + v\frac{\partial w}{\partial y} + w\frac{\partial w}{\partial z} = -c_p\theta\frac{\partial \pi'}{\partial z} + g\frac{\theta'}{\bar{\theta}} + fu + D_w + turb_w \quad , \qquad (3.3)$$

$$\frac{\partial \theta}{\partial t} + u\frac{\partial \theta}{\partial x} + v\frac{\partial \theta}{\partial y} + w\frac{\partial \theta}{\partial z} = D_\theta + turb_\theta + S_\theta \quad , \qquad (3.4)$$

$$\frac{\partial \pi}{\partial t} + u\frac{\partial \pi}{\partial x} + v\frac{\partial \pi}{\partial y} + w\frac{\partial \pi}{\partial z} = -\frac{R_d}{c_v}\pi\left(\frac{\partial u}{\partial x} + \frac{\partial v}{\partial y} + \frac{\partial w}{\partial z}\right) + \frac{R_d}{c_v}\frac{\pi}{\theta}\frac{d\theta}{dt} \quad . \qquad (3.5)$$

The total Cartesian velocities u, v, and w are defined as:

$u = \bar{U} + u'$, $\bar{U}$ is the base state wind in the x direction.

$v = \bar{V} + v'$, $\bar{V}$ is the base state wind in the y direction.

$w = w'$, is the velocity in the z direction.

The thermodynamic variables, non-dimensional pressure, potential temperature, and their base state equivalents are computed according to:

$$\pi = \bar{\Pi} + \pi' \quad \text{and} \quad \pi = \left(\frac{p}{p_o}\right)^{\frac{R_d}{c_p}}, \qquad \text{with} \quad \bar{\Pi} = \left(\frac{\bar{p}}{p_o}\right)^{\frac{R_d}{c_p}} \quad ,$$

$$\theta = \bar{\theta} + \theta' \quad .$$

The coriolis terms f and f' are:

$$f = 2\Omega \sin(\phi) \quad ,$$

$$f' = 2\Omega \cos(\phi) \quad ,$$

where Ω is the angular velocity of the Earth and ϕ the latitude. Equations (3.1)-(3.5) describe the Euler equations with the addition of a heat source S_θ in the potential temperature and pressure equations and turbulent and computational mixing terms in (3.1)-(3.4). Normally, mesoscale models make a number of approximations that are focused primarily on the linearization of the meteorologically insignificant acoustic modes. In this application, the non-linear pressure gradient terms were found to contribute significantly in strongly forced mountain wave flows and are incorporated in the current model configuration. The non-linear divergence terms is included to close the model energetics. The non-linear pressure gradient term reduces the time step slightly but improves the numerical solution. Little improvement is noted when the coefficient of the divergence term is at full strength. Equations (3.1)-(3.5) conserve energy in the absence of friction, mixing, and heat.

The above equation set can be transformed to a terrain following coordinate system by:

$$\zeta = \frac{z_t(z - z_s)}{z_t - z_s} \quad ,$$

where z_t is the top of the model domain, z_s is the height of the surface, and z is the physical height of the computational surface. Using the chain rule, the coordinate transformation is given by:

$$J_1 = \frac{\partial \zeta}{\partial x}, \qquad J_2 = \frac{\partial \zeta}{\partial y}, \qquad J_3 = \frac{\partial \zeta}{\partial z}.$$

The spatial derivatives in the transformed system become:

$$\left.\frac{\partial \phi}{\partial x}\right|_z = \left.\frac{\partial \phi}{\partial x}\right|_\zeta + J_1 \frac{\partial \phi}{\partial \zeta}, \tag{3.6}$$

$$\left.\frac{\partial \phi}{\partial y}\right|_z = \left.\frac{\partial \phi}{\partial y}\right|_\zeta + J_2 \frac{\partial \phi}{\partial \zeta}, \tag{3.7}$$

$$\frac{\partial \phi}{\partial z} = J_3 \frac{\partial \phi}{\partial \zeta}, \tag{3.8}$$

for any variable ϕ. Applying equations (3.6) - (3.8) to equations (3.1)-(3.5) the transformed system of equations become:

$$\frac{\partial u}{\partial t}+u\frac{\partial u}{\partial x}+v\frac{\partial u}{\partial y}+W^c\frac{\partial u}{\partial \zeta}=-c_p\theta(\frac{\partial \pi'}{\partial x}+J_1\frac{\partial \pi'}{\partial \zeta})+fv-f'w+turb_u+D_u \quad , \quad (3.9)$$

$$\frac{\partial v}{\partial t}+u\frac{\partial v}{\partial x}+v\frac{\partial v}{\partial y}+W^c\frac{\partial v}{\partial \zeta}=-c_p\theta(\frac{\partial \pi'}{\partial y}+J_2\frac{\partial \pi'}{\partial \zeta})-fu+turb_v+D_v \quad , \quad (3.10)$$

$$\frac{\partial w}{\partial t}+u\frac{\partial w}{\partial x}+v\frac{\partial w}{\partial y}+W^c\frac{\partial w}{\partial \zeta}=-c_p\theta J_3\frac{\partial \pi'}{\partial \zeta}+g\frac{\theta'}{\bar{\theta}}+f'u+turb_w+D_w \quad , \quad (3.11)$$

$$\frac{\partial \theta'}{\partial t}+u\frac{\partial \theta'}{\partial x}+v\frac{\partial \theta'}{\partial y}+W^c\frac{\partial \theta'}{\partial z}+wJ_3\frac{\partial \bar{\theta}}{\partial z}=turb_\theta+D_\theta+S_\theta \quad , \quad (3.12)$$

$$\begin{aligned}&\frac{\partial \pi'}{\partial t}+u\frac{\partial \pi'}{\partial x}+v\frac{\partial \pi'}{\partial y}+W^c\frac{\partial \pi'}{\partial z}+wJ_3\frac{\partial \bar{\Pi}}{\partial z}\\&=-\frac{R_d}{c_v}\pi(\frac{\partial u}{\partial x}+\frac{\partial v}{\partial y}+\frac{\partial W^c}{\partial \zeta})+\frac{R_d}{c_v}\frac{\pi}{\theta}\frac{d\theta}{dt}\end{aligned} \quad . \quad (3.13)$$

The contravariant vertical velocity is defined by,

$$W^c=\frac{d\zeta}{dt}=\frac{\partial \zeta}{\partial x}\frac{dx}{dt}+\frac{\partial \zeta}{\partial y}\frac{dy}{dt}+\frac{\partial \zeta}{\partial z}\frac{dz}{dt} \quad ,$$

or following (3.6)-(3.8), $W^c=J_1u+J_2v+J_3w$.

The base state variables $\bar{U},\bar{V},\bar{\theta},\bar{\Pi}$ are horizontally homogeneous and hydrostatically balanced.

$$\frac{\partial \bar{\Pi}}{\partial \zeta}=-\frac{g}{c_p\bar{\theta}} \quad .$$

The turbulent mixing terms are described in detail in Section 3.2. The numerical smoothing terms D_u, D_v, D_w, D_θ are composed of computational mixing and Rayleigh damping:

$$D_u = C_u + R_u \quad ,$$

$$D_v = C_v + R_v \quad ,$$

$$D_w = C_w + R_w \quad ,$$

$$D_\theta = C_\theta + R_\theta \quad .$$

Sections 3.4.1 and 3.4.2 give a detailed description of the computational mixing and Rayleigh damping terms.

3.2 Sub-Grid Scale Closure

The sub-grid scale processes are those that cannot be predicted explicitly by the model. In the planetary boundary layer (PBL), the sub-grid scale mixing can contribute significantly to the evolving flow field. Thus, considerable work has focused on estimating the unresolved flow patterns. When the surface is heated and the atmosphere becomes unstable, convection occurs initially on scales proportional to the mixed layer height. There are a number of ways in which to represent convective processes in the boundary layer by the model. Two types of mixing mechanisms are presented and encoded in the model.

The first method applies strong diffusion in areas of neutral or unstable lapse rates. This sub-grid closure scheme requires large eddy viscosities capable of mixing

the unstable boundary layer and developing the height of the mixed layer in a timely manner. Since the convective elements are not explicitly resolved. this type of scheme allows for large horizontal and vertical grid spacings on the order of 5000m and 200m, respectively. This method is preferred if the convective motions in the boundary layer are small when compared to the surrounding flow.

A second method of addressing the unstable boundary layer is the Large Eddy Simulation (or LES). The purpose of the LES is to explicitly resolve the majority of the convection in the heated boundary layer. As shown by Deardorff (1980) and many others, this requires resolutions on the order of 100 meters in each spatial direction. This approach makes use of the sub-grid closure scheme, but the amount of energy in the unresolved scales is significantly reduced. Most researchers are satisfied when 90-95% of the fluxes, energy, and variances are explicitly resolved.

For large three-dimensional mountain wave flows, the LES resolution requirements place a severe constraint on the size of the domain that can be studied with current computing power. Horizontal resolution on the order of 400-1000 m is suitable for simulating mountain waves but is not sufficient to resolve properly the convective elements in the mixed layer. Thus, simulations of broad mountain ranges are better served by the eddy viscosity method than the LES approach. The scale analysis of Chapter 2 indicates that strong mountain wave flows are more energetic than boundary layer circulations. But in the interest of evaluating the sub-grid closures, both methods are tested and the results are compared in Chapter 5.

The turbulent parameterization scheme used in this study follows the base model of Sullivan et. al. (1994). It was first developed by Deardorff (1980) and later applied by Moeng (1984). This scheme is chosen because of its simplicity and ability to match the simulated planetary boundary layer solution to Monin-Obukov similarity theory in a LES. The method utilizes a 1.5 order closure scheme that predicts turbulent kinetic energy (e) for use in the determination of the eddy viscosity. For simulations with horizontal resolutions greater than 200m, the convective motions in the early development stage of the boundary layer cannot be adequately resolved. The mixing length in the convective boundary layer is enhanced following Sun and Chang (1986). This modification was incorporated after tests the using the Wangara Day 33 data set and the baseline Deardorff eddy viscosity model predicted an untimely development of the mixed layer height. The unmodified Deardorff and Sun and Chang schemes are presented later in this section. The sub-grid closure terms are given in Cartesian coordinates and equated to their coordinate transformed counterparts via:

$$\begin{aligned} turb_u &= \frac{\partial(-\tau_{11})}{\partial x} + \frac{\partial(-\tau_{12})}{\partial y} + \frac{\partial(-\tau_{13})}{\partial z} \\ &= \frac{\partial(-\tau_{11})}{\partial x} + J_1 \frac{\partial(-\tau_{11})}{\partial \zeta} + \frac{\partial(-\tau_{12})}{\partial y} + J_2 \frac{\partial(-\tau_{12})}{\partial \zeta} + J_3 \frac{\partial(-\tau_{13})}{\partial \zeta} \end{aligned} ,$$

$$\begin{aligned} turb_v &= \frac{\partial(-\tau_{21})}{\partial x} + \frac{\partial(-\tau_{22})}{\partial y} + \frac{\partial(-\tau_{23})}{\partial z} \\ &= \frac{\partial(-\tau_{21})}{\partial x} + J_1 \frac{\partial(-\tau_{21})}{\partial \zeta} + \frac{\partial(-\tau_{22})}{\partial y} + J_2 \frac{\partial(-\tau_{22})}{\partial \zeta} + J_3 \frac{\partial(-\tau_{23})}{\partial \zeta} \end{aligned} ,$$

$$turb_w = \frac{\partial(-\tau_{31})}{\partial x} + \frac{\partial(-\tau_{32})}{\partial y} + \frac{\partial(-\tau_{33})}{\partial z}$$
$$= \frac{\partial(-\tau_{31})}{\partial x} + J_1 \frac{\partial(-\tau_{31})}{\partial \zeta} + \frac{\partial(-\tau_{32})}{\partial y} + J_2 \frac{\partial(-\tau_{32})}{\partial \zeta} + J_3 \frac{\partial(-\tau_{33})}{\partial \zeta}$$

$$turb_\theta = \frac{\partial(-\tau_{\theta 1})}{\partial x} + \frac{\partial(-\tau_{\theta 2})}{\partial y} + \frac{\partial(-\tau_{\theta 3})}{\partial z}$$
$$= \frac{\partial(-\tau_{\theta 1})}{\partial x} + J_1 \frac{\partial(-\tau_{\theta 1})}{\partial \zeta} + \frac{\partial(-\tau_{\theta 2})}{\partial y} + J_2 \frac{\partial(-\tau_{\theta 2})}{\partial \zeta} + J_3 \frac{\partial(-\tau_{\theta 3})}{\partial \zeta}$$

The strain tensors are defined by:

$$\tau_{11} = -2\nu_t S_{11} \ ,$$

$$\tau_{12} = -2\nu_t S_{12} \ ,$$

$$\tau_{13} = -2\nu_t S_{13} \ ,$$

$$\tau_{22} = -2\nu_t S_{22} \ ,$$

$$\tau_{23} = -2\nu_t S_{23} \ ,$$

$$\tau_{33} = -2\nu_t S_{33} \ .$$

By definition $\tau_{21} = \tau_{12}$, $\tau_{32} = \tau_{23}$, $\tau_{31} = \tau_{13}$. Following Deardorff (1980) the eddy viscosity is:

$$\nu_t = C_k l e^{\frac{1}{2}} \ ,$$

where $C_k = 0.1$. The velocity stresses ($S_{ij's}$) in Cartesian and transformed coordinates are given by:

$$S_{11} = \frac{1}{2}\left(\frac{\partial u}{\partial x} + \frac{\partial u}{\partial x}\right) = \frac{\partial u}{\partial x} + J_1 \frac{\partial u}{\partial \zeta} \quad ,$$

$$S_{12} = \frac{1}{2}\left(\frac{\partial v}{\partial x} + \frac{\partial u}{\partial y}\right) = \frac{1}{2}\left(\frac{\partial u}{\partial y} + J_2 \frac{\partial u}{\partial \zeta} + \frac{\partial v}{\partial x} + J_1 \frac{\partial v}{\partial \zeta}\right) \quad ,$$

$$S_{13} = \frac{1}{2}\left(\frac{\partial w}{\partial x} + \frac{\partial u}{\partial z}\right) = \frac{1}{2}\left(\frac{\partial w}{\partial x} + J_1 \frac{\partial w}{\partial \zeta} + J_3 \frac{\partial u}{\partial \zeta}\right) \quad ,$$

$$S_{22} = \frac{1}{2}\left(\frac{\partial v}{\partial y} + \frac{\partial v}{\partial y}\right) = \frac{\partial v}{\partial y} + J_2 \frac{\partial v}{\partial \zeta} \quad ,$$

$$S_{23} = \frac{1}{2}\left(\frac{\partial w}{\partial y} + \frac{\partial v}{\partial z}\right) = \frac{1}{2}\left(\frac{\partial w}{\partial y} + J_2 \frac{\partial w}{\partial \zeta} + J_3 \frac{\partial v}{\partial \zeta}\right) \quad ,$$

$$S_{33} = \frac{1}{2}\left(\frac{\partial w}{\partial z} + \frac{\partial w}{\partial z}\right) = J_3 \frac{\partial w}{\partial \zeta} \quad .$$

The scalar fluxes are defined by:

$$\tau_{\theta 1} = -\nu_\theta \frac{\partial \theta}{\partial x} = -\nu_\theta [\frac{\partial \theta}{\partial x} + J_1 \frac{\partial \theta}{\partial \zeta}] \quad ,$$

$$\tau_{\theta 2} = -\nu_\theta \frac{\partial \theta}{\partial y} = -\nu_\theta [\frac{\partial \theta}{\partial y} + J_2 \frac{\partial \theta}{\partial \zeta}] \quad ,$$

$$\tau_{\theta 3} = -\nu_\theta \frac{\partial \theta}{\partial z} = -\nu_\theta [J_3 \frac{\partial \theta}{\partial \zeta}] \quad .$$

The eddy diffusion is defined in terms of the mixing length, average grid spacing, and the eddy viscosity using:

$$v_\theta = (1 + \frac{2l}{\Delta})v_t \quad .$$

The average grid spacing is defined by the relation $\Delta = (\Delta x \Delta y \Delta \zeta)^{\frac{1}{3}}$. The sub-grid scale kinetic energy (e), used in defining the mixing length l and the eddy viscosities v_t and v_θ, is predicted following:

$$\frac{\partial e}{\partial t} + u\frac{\partial e}{\partial x} + v\frac{\partial e}{\partial y} + W^c\frac{\partial e}{\partial \zeta} = P + B + D - E \quad ,$$

where P is the shear production term, B the buoyant production term, D the diffusion of e , and E the dissipation of e. The sub-grid scale energy source or sinks terms are defined as:

$$P = -\tau_{ij}S_{ij} \quad ,$$

$$B = \frac{g}{\bar{\theta}}\tau_{\theta 3} \quad ,$$

$$E = C_l\frac{e^{\frac{3}{2}}}{l} \quad ,$$

$$D = \frac{\partial}{\partial x_i}(2v_t\frac{\partial e}{\partial x_i}) \quad ,$$

where $C_l = 0.93$ and each index i, j are summed from 1 to 3. The mixing length above the boundary layer is computed following Deardorff (1980):

$$l = \Delta, \text{ for neutral and unstable stratification} \quad ,$$

$$l = \frac{0.76e^{\frac{1}{2}}}{N}, \text{ for stable stratification} ,$$

where N is the grid computed static stability.

$$N = (\frac{g}{\theta} J_3 \frac{\partial \theta}{\partial \zeta})^{\frac{1}{2}}$$

In the Sun and Chang application, Deardorff's length scale in the unstable boundary layer is replaced by a fraction of the observed peak wavelength for the vertical velocity component (λ_m). Caughey and Palmer (1979) obtained an expression for the peak λ_m for experimental data collected in the Kansas, Minnesota, and Ashchurch field studies. The following expression provides a good fit to the observed data:

$$\lambda_m = 1.8 Z_i [1 - \exp(-4\frac{z}{z_i}) - 0.0003 \exp(8\frac{z}{z_i})] ,$$

$$l = 0.25 \lambda_m ,$$

where z_i is the depth of the mixed layer and z the height above the ground surface. The last term inside the square bracket is small and is here omitted. The inversion height is diagnosed by comparing the surface potential temperature to the potential temperature in and above the mixed layer.

3.3 Surface Flux Parameterization

A simple surface drag formulation is used to represent the surface stress. The method presented here follows that implemented by Miller and Durran (1991) and can

be found in Haltiner and Williams (1980). The surface stress for the u and v velocity components is computed by:

$$\tau_{13} = c_d |V| u \quad . \tag{3.14}$$

$$\tau_{23} = c_d |V| v \quad . \tag{3.15}$$

V is the magnitude of the surface wind computed at the first point above the surface. Equation (3.14) and (3.15) describe the flux for an unbalanced base state. Subtracting the base state strain from (3.14) and (3.15) allows the base state wind to be in friction balance:

$$\tau_{13}(surf) = \max[0, c_d(|V|u - |\bar{V}|\bar{u})] \quad ,$$

$$\tau_{23}(surf) = \max[0, c_d(|V|v - |\bar{V}|\bar{v})] \quad ,$$

where $\bar{u}$ and $\bar{v}$ are the base state surface wind components. This formulation reduces the stress for only positive perturbations. The negative perturbations remain unchanged. The drag coefficient is computed from the relation:

$$c_d(z) = c_d(z_{surf}) \left[\frac{\ln(\frac{z_{surf}}{z_o})}{\ln(\frac{z}{z_o})} \right]^2 \quad ,$$

where z_{surf} is the height at which the drag coefficient is valid. The above is either substituted in for the flux in the explicit method or is a source term in the implicit

method. The surface heat flux is introduced as a flux or a volume source term. The source term has the form:

$$\tau_{\theta 3}(k) = \frac{H_o}{c_p \bar{\rho}} \max(heat_{\min}, \sin \omega t) \quad , \tag{3.16}$$

where H_o is the maximum heating rate in watts per unit area, c_p the specific heat, $\bar{\rho}$ the base state density at the level of heating, $heat_{\min}$ the minimum heating magnitude, and k is the level at which the heat is applied (the surface in this study). The period ω is specified in the input file. If the flux option is chosen, the magnitude is specified and replaces the coefficient in (3.16).

3.4 Numerical Smoothing

3.4.1 Computational Mixing

Two types of numerical smoothing are used in this study. The first type, computational, acts to remove small-scale structures created by non-linear aliasing and dispersive effects created by the advection scheme. This smoother is of fourth order and is applied to u', v', w', θ' in the horizontal and vertical directions. The form follows that used in the ARPS and is computed in computational space using:

$$C_u = -C_H \left[\frac{\partial^4 u'}{\partial x^4} + \frac{\partial^4 u'}{\partial y^4} \right] - C_V \left[\frac{\partial^4 u'}{\partial \zeta^4} \right] \quad ,$$

$$C_v = -C_H \left[\frac{\partial^4 v'}{\partial x^4} + \frac{\partial^4 v'}{\partial y^4} \right] - C_V \left[\frac{\partial^4 v'}{\partial \zeta^4} \right] \quad ,$$

$$C_w = -C_H\left[\frac{\partial^4 w'}{\partial x^4} + \frac{\partial^4 w'}{\partial y^4}\right] - C_V\left[\frac{\partial^4 w'}{\partial \zeta^4}\right] .$$

$$C_\theta = -C_H\left[\frac{\partial^4 \theta'}{\partial x^4} + \frac{\partial^4 \theta'}{\partial y^4}\right] - C_V\left[\frac{\partial^4 \theta'}{\partial \zeta^4}\right] .$$

The specified mixing coefficients are C_H and C_V, and are generally chosen to be on the order of 10^{-4} times the grid spacing to the fourth power.

3.4.2 Rayleigh Damping

Additional smoothing is used to damp gravity waves in the upper part of the modeling domain when the top boundary is set to the rigid lid condition. This type of numerical damping is designed to simulate a radiation condition by preventing reflection of gravity wave energy off of the top boundary (rigid lid). For this type of damping to be effective, the damping layer needs to be greater that one vertical wavelength in depth and a minimum of 30 grid points (Klemp and Lilly, 1978 and Durran and Klemp, 1983). Commonly referred to as Rayleigh damping, it is applied to u', v', w', θ' and is defined here by:

$$r(z) = -\frac{\alpha}{2}(1 - \cos(\pi \frac{z - z_D}{z_T - z_D})), \qquad \text{for } z > z_D .$$

The damping terms are:

$$R_u = r(z)u' ,$$

$$R_v = r(z)v' ,$$

$$R_w = r(z)w \quad ,$$

$$R_\theta = r(z)\theta' \quad ,$$

where z_D is the height at which the damping begins and z_T is the height of the top of the model. The coefficient α represents the maximum damping coefficient (s^{-1}) at the top of the damping layer, generally selected so that the dominant horizontal wave number is damped after about 25 time steps.

3.5 Boundary Conditions

Boundary conditions can pose a formidable challenge to long term mesoscale numerical predictions and to simulations that interact significantly with flow adjacent to the boundaries. The only true physical boundary in this numerical model is the bottom boundary. Much effort has been spent developing lateral and vertical boundary conditions for models whose domains are not periodic. To my knowledge, a fully robust open lateral boundary condition, which properly handles a combination of acoustic, gravity, and inertial waves, does not exist. As a result, this model includes a variety of schemes for predicting the time dependent variables at the lateral and vertical boundaries.

3.5.1 Lateral Formulation

There is a need to specify the normal advection and velocity terms at the first grid point outside the physical boundary. The normal velocity boundary condition is presented first. ARPI3D includes 5 choices for computing the boundary values of the

normal velocity at the lateral boundaries. The reason for such a variety is simple: each specific modeling application could require a different type of boundary condition.

The five lateral boundary condition options for the normal velocity components are:

a) the zero gradient condition

b) the Orlanski (1976) condition

c) the vertically averaged Orlanski phase speed scheme of Klemp and Lilly (1979), later modified by Durran and Klemp (1983)

d) the Klemp-Wilhelmson (1978) constant phase speed method

e) a newly developed hydrostatically (or environmentally) estimated phase speed

Schemes (b)-(e) are designed to allow waves in the interior of the model domain to pass freely out through the horizontal boundary with minimal reflection. With the exception of the zero gradient condition (which is self-explanatory), all of the above methods estimate the gravity wave phase speed and replace the normal velocity component equation of motion with outflow advection:

$$\frac{\partial u^{\tau}}{\partial t}+(u+\hat{c}_u)^{\tau}\left(\frac{\partial u}{\partial x}+J_1\frac{\partial u}{\partial \zeta}\right)^{\tau}=0 \quad , \tag{3.17}$$

$$\frac{\partial v^{\tau}}{\partial t}+(v+\hat{c}_v)^{\tau}\left(\frac{\partial v}{\partial y}+J_2\frac{\partial v}{\partial \zeta}\right)^{\tau}=0 \quad . \tag{3.18}$$

The spatial derivatives in (3.17) and (3.18) are computed on the small time step (τ), whereas the advective and gravity wave phase speeds are determined using big time step (t) data. The small and large time steps are described in more detail in Section 3.6. The above selection for computing the phase velocity on the big time step and the gradient on the small time step stems from linear mountain waves test results.

For method (d), the gravity wave phase speeds $\hat{c}_u$ and $\hat{c}_v$ are specified by estimating the fastest gravity wave phase speed. For method (e), the phase speed is estimated by the linear hydrostatic value. It can be found from the relation:

$$\hat{c}_u = \frac{\omega}{k} = \frac{Nk}{k(k^2 + m^2)^{\frac{1}{2}}}$$

For hydrostatic modes $k \Rightarrow 0$ and we have:

$$\hat{c}_u = \frac{N}{m} = \overline{U},$$

where the vertical wave number $m = N / \overline{U}$ is the hydrostatic limit corresponding to the fastest wave. The method is also applied to the v velocity component. For moist convection, Klemp and Lilly (1979) found it was advantageous to over-estimate the phase speed rather than underestimate it.

A review of (c), from the Durran and Klemp (1983) implementation, is given here. The vertically averaged phase speeds are formulated by solving (3.17) and (3.18) for the local gravity wave phase speed and averaging only the outgoing components. The inward directed components are set to zero prior to averaging. The vertically

averaged phase speeds $(u+\hat{c})^t$ for u and v are computed using the following relationships:

$$(u+\hat{c}_u)^t(1) = \sum_{k=2}^{nz-2} \min\left[-u_{\max}, \min[0, \frac{\Delta x}{\Delta t}\frac{(u_{2jk}^{t-\Delta t} - u_{2jk}^{t})}{(u_{3jk}^{t-\Delta t} - u_{2jk}^{t-\Delta t})}]\right] ,$$

$$(u+\hat{c}_u)^t(nx) = \sum_{k=2}^{nz-2} \min\left[u_{\max}, \max[0, \frac{\Delta x}{\Delta t}\frac{(u_{nx-1jk}^{t-\Delta t} - u_{nx-1jk}^{t})}{(u_{nx-1jk}^{t-\Delta t} - u_{nx-2jk}^{t-\Delta t})}]\right] ,$$

$$(v+\hat{c}_v)^t(1) = \sum_{k=2}^{nz-2} \min\left[-v_{\max}, \min[0, \frac{\Delta y}{\Delta t}\frac{(v_{i2k}^{t-\Delta t} - v_{i2k}^{t})}{(v_{i3k}^{t-\Delta t} - v_{i2k}^{t-\Delta t})}]\right] ,$$

$$(v+\hat{c}_v)^t(ny) = \sum_{k=2}^{nz-2} \min\left[v_{\max}, \max[0, \frac{\Delta y}{\Delta t}\frac{(v_{iny-1k}^{t-\Delta t} - v_{iny-1k}^{t})}{(v_{iny-1k}^{t-\Delta t} - v_{iny-2k}^{t-\Delta t})}]\right] ,$$

where $u_{\max}$ and $v_{\max}$ are magnitudes of the fastest phase speed allowed by the time step and the grid spacing. The above equation is discretized using the leapfrog centered in time and upstream in space scheme. If the phase velocity is directed outward, then the velocities are updated using (3.17) and (3.18). If the flow $(u+\hat{c})$ is directed inward, the velocity is unchanged or relaxed back to the base state according to a specified relaxation coefficient.

For methods (b) and (c) the phase speed is computed following Orlanski (1976). Note that the original Orlanski form is obtained by removing the vertical averaging step in the Durran and Klemp procedure.

For the horizontal advection terms at the lateral boundary, the higher order advection schemes cannot be directly applied. At an outflow boundary, the stable first

order one-sided upstream differencing scheme is used for the normal horizontal advection term. On inflow boundaries, the normal advective term is set to zero since there is no information on the gradient of the advected variable outside the boundary.

The lateral boundary conditions for the fourth order computational mixing terms follows those used in the ARPS. The intermediate computational mixing value (second order derivative) at the point just inside the boundaries is used to set the value of the point outside the boundary. All other quantities that require definition of intermediate quantities at the boundary computations, such as the stress and strain terms in the sub-grid scale closure model, invoke the zero gradient condition.

3.5.1 Vertical Formulation

The commonly used Rayleigh sponge-rigid upper boundary and fixed bottom boundary conditions are employed in this model. In addition, following Klemp and Durran (1983), a radiation condition between w and π is available at the top boundary. The radiation condition forces the numerical solution at k=nz-1 for w and k=nz-2 for π with a linear analytical Boussinesq relation. The analytical solution allows upward propagating gravity wave energy to pass vertically out of the top boundary and removes the need for a sponge in the top part of the model domain. This method can reduce significantly the vertical extent of the computational domain without a degradation of the solution in a wide variety of gravity wave problems. The radiation condition is given later in this section.

When the rigid boundary condition is applied to the top and bottom boundaries. the perturbation scalar quantities in the vertical, with the exception of π at the surface. are set to zero gradient following:

$$u(i,j,1) = u(i,j,2), \text{ and } u(i,j,nz-1) = u(i,j,nz-2) \ ,$$

$$v(i,j,1) = v(i,j,2), \text{ and } v(i,j,nz-1) = v(i,j,nz-2) \ ,$$

$$\theta'(i,j,1) = \theta'(i,j,2), \text{ and } \theta'(i,j,nz-1) = \theta'(i,j,nz-2) \ ,$$

$$\pi'(i,j,1) = \pi'(i,j,2), \text{ and } \pi'(i,j,nz-1) = \pi'(i,j,nz-2) \ .$$

The non-dimensional pressure π' at k=1 is computed using an extrapolation condition:

$$\pi'(i,j,1) = 2*\pi'(i,j,2) - \pi'(i,j,3) \ .$$

The vertical velocity and the contravariant vertical velocity at the lower boundary are defined by the relationship between the slope and the horizontal wind speed and the impermeability condition, respectively. The vertical velocity at the lower boundary is

$$w(i,j,2) = u(\frac{\partial h}{\partial x} + J_1 \frac{\partial h}{\partial \zeta}) + v(\frac{\partial h}{\partial y} + J_2 \frac{\partial h}{\partial \zeta}) \ .$$

The contravariant vertical velocity is

$$W^c(i,j,2) = 0 \ .$$

For the rigid upper boundary condition, both vertical velocities are set to zero

$$w(i,j,nz-1) = W^c(i,j,nz-1) = 0 \ .$$

Quantities involved in intermediate steps at the boundary for the turbulent and computational mixing terms make use of the zero gradient condition, regardless of the top boundary condition type.

The upper radiation condition makes use of the linear Boussinesq hydrostatic system of equations. This formulation follows that developed by Klemp and Durran (1983):

$$\hat{\pi}' = \frac{N}{c_p \bar{\theta} (k_x + k_y)^{\frac{1}{2}}} \hat{w} \quad ,$$

where $\hat{\pi}'$ and $\hat{w}$ are Fourier transformed non-dimensional pressure and vertical velocity, N is the local static stability, k_x and k_y are the horizontal wave numbers, $\bar{\theta}$ is the local base state potential temperature, and c_p is the specific heat. A comparison of the upper radiation and Rayleigh sponge-rigid lid upper boundary conditions for a simulated linear hydrostatic mountain wave is given in Chapter 4.

3.6 Discretized Equations

The model equations are computed using spatially centered finite differences on the Arakawa (1966) staggered C-grid. The grid box is illustrated in Figure 3.1. The velocity variables are located on the sides of a grid box and define the physical model boundaries. The scalar quantities are defined at the center of each grid box. The model scalar variables are computed on scalar points from 1 to nx-1 and 1 to ny-1 in the horizontal plane and from 2 to nz-2 in the vertical direction (Figure 3.2). The u velocity is computed from 1 to nx , 1 to ny-1, and 2 to nz-2 . The v velocity component

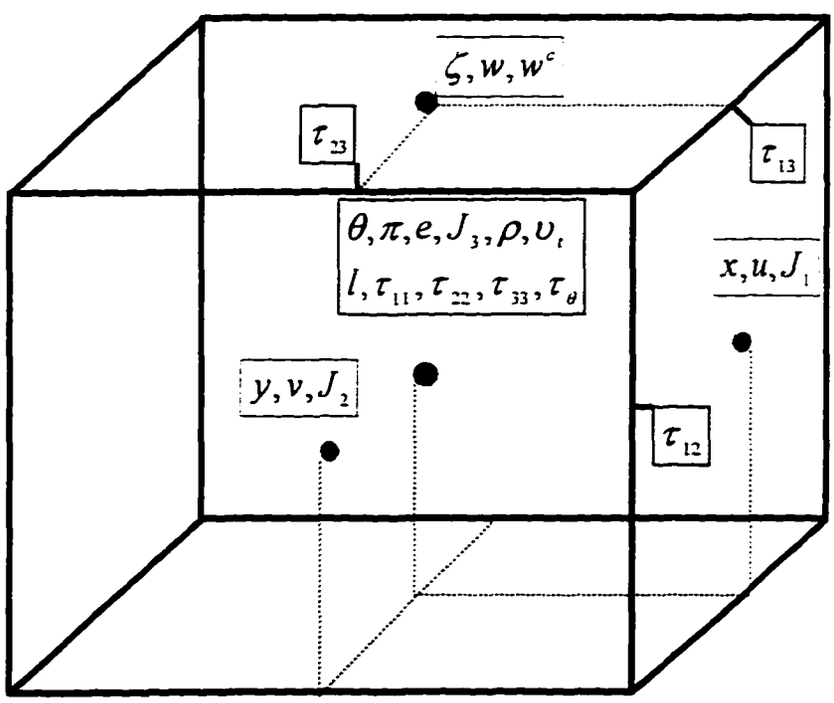

Figure 3.1. ARPI3D grid box displaying the spatial arrangement of the scalar and vector quantities.

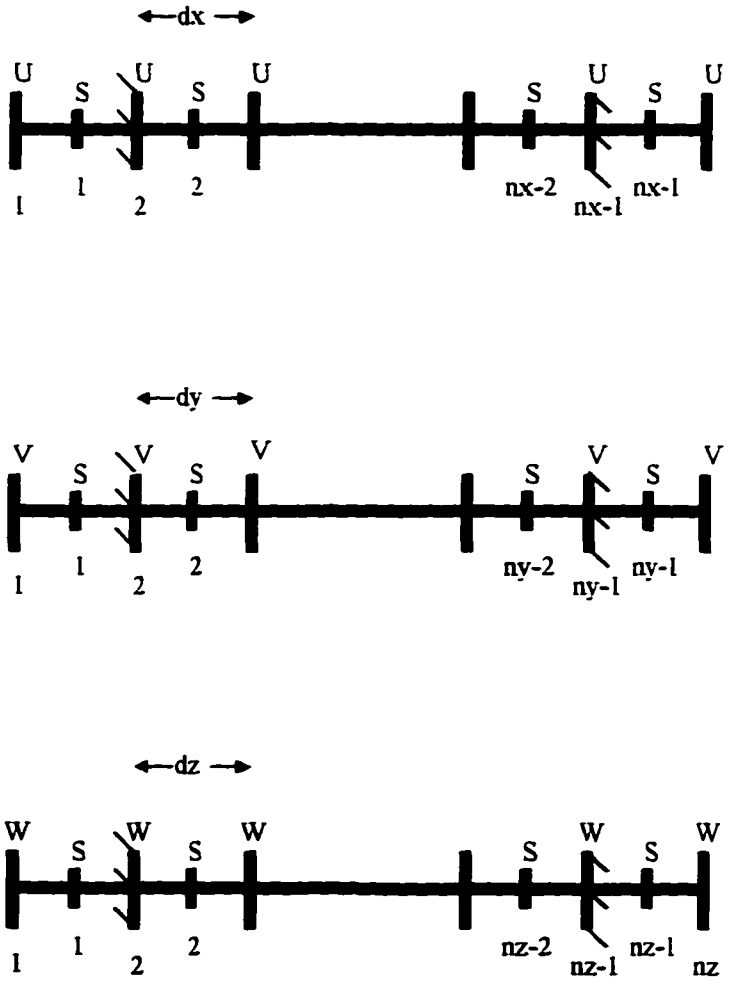

Figure 3.2. Location of the scalar and velocity points in terms of each of the model axes. Hatching indicates the physical model domain.

is computed from 1 to nx-1, 1 to ny, and 2 to nz-2. The vertical velocity is computed from 1 to nx-1, 1 to ny-1, and 2 to nz-1.

The spatial derivatives for the gravity, inertial, and acoustic wave terms are differenced using centered second order accurate finite differences. The time integration follows the split time step approach of Klemp and Wilhelmson (1978). The time integration is broken up into two parts: terms evaluated using big time step information, denoted by the superscript t corresponding to advective, gravity, and inertial wave modes as well as all mixing terms and sub-grid scale processes. The terms evaluated on the small time step, denoted by the superscript τ, represent the acoustic modes and include the pressure gradient and divergence terms. The forcing terms computed on the big time step are used in the small time step to advance the dependent variables forward in time. This approach has been implemented and tested by a number of modeling efforts including Durran and Klemp (1983) and the ARPS (1995). The full discretized equation set is:

$$\frac{u^{\tau-\Delta\tau}-u^{\tau}}{\Delta\tau} = -c_p\overline{\theta}^{x^t}\left[\delta_x\pi' + \overline{\overline{J_1\delta_\zeta\pi'}^{x}}^{\zeta}\right]^{\tau} - advu^t + f\overline{v}^{xy^t} - f\overline{w}^{x\zeta^t} + turb_u^t + D_u^t \quad ,$$

$$\frac{v^{\tau-\Delta\tau}-v^{\tau}}{\Delta\tau} = -c_p\overline{\theta}^{y^t}\left[\delta_y\pi' + \overline{\overline{J_2\delta_\zeta\pi'}^{y}}^{\zeta}\right]^{\tau} - advv^t - f\overline{u}^{xy^t} + turb_v^t + D_v^t \quad ,$$

$$\frac{w^{\tau-\Delta\tau}-w^{\tau}}{\Delta\tau} = -c_p\overline{\theta}^{\zeta^t}\left[(1-\beta)(\overline{J_3}^{\zeta}\delta_\zeta\pi')^{\tau} + \beta(\overline{J_3}^{\zeta}\delta_\zeta\pi')^{\tau-\Delta\tau}\right] + g\overline{\left(\frac{\theta'}{\overline{\theta}}\right)}^{\zeta^t}$$

$$- advw^t + f\overline{u}^{x\zeta^t} + turb_w^t + D_w^t \quad ,$$

$$\frac{\theta^{t+\Delta t}-\theta^{t-\Delta t}}{2\Delta t}=-adv\theta^{t}+turb_{\theta}^{t}+D_{\theta}^{t}+S_{\theta}^{t}\quad .$$

$$\frac{\pi^{\tau+\Delta\tau}-\pi^{\tau}}{\Delta\tau}=-adv\pi^{\tau}-\frac{R_d}{c_v}\pi^{\tau}[(\delta_x u^{\tau+\Delta\tau}++\delta_y v^{\tau+\Delta\tau}+\beta\delta_z w^{\tau})-(1-\beta)\delta_z w^{\tau+\Delta\tau}]$$

$$+\beta\frac{\overline{w}^{z}g}{c_p\bar{\theta}}+(1-\beta)\frac{\overline{w}^{z}g}{c_p\bar{\theta}}+\frac{R_d}{c_v}\frac{\pi^{\tau}}{\theta}\delta_t\theta^{t}\quad .$$

Note that all the variables except for θ' are advanced on the small time step using the forward time scheme. The forcing terms for $u, v, w,$ and π are applied in the small time step. The small time step is advanced using the forward scheme in n steps where

$$n=2\frac{dt}{d\tau}\quad .$$

In the non-dimensional pressure equation, the scheme is referred to as forward-backward differencing since the updated velocities are used in the divergence term. The potential temperature is evaluated and integrated on the big time step using leapfrog time differencing. The non-dimensional pressure and w are advanced using the fully explicit forward scheme or the vertically implicit forward scheme. The implicit scheme removes the vertical grid spacing time step restriction for acoustic wave propagation. The vertically implicit scheme follows the Crank-Nicholson method and is absolutely stable with respect to vertical sound wave propagation. The Crank-Nicholson scheme requires more computations due to the need to solve a tridiagonal matrix, but is beneficial for horizontal to vertical grid spacing ratios greater than 2.5. Use of the 2 time step mode splitting method reviewed above allows for certain unstable acoustic

modes to exist. Durran and Klemp (1983) suggest that values of β between 0.5 and 1.0 successfully damps the unstable modes. These unstable modes are due to interactions between the sound waves and the advective and gravity waves as shown by Skamarock and Klemp (1992). A description of the vertically implicit $w-\pi$ solving technique is given in Appendix A. Appendix B reviews $w-\pi$ upper boundary condition used in the vertically implicit time marching scheme.

The spatial averaging and differencing operators are defined by:

$$\bar{\phi}^{ns} = \frac{\phi(s+\frac{n\Delta s}{2}) + \phi(s-\frac{n\Delta s}{2})}{2} ,$$

$$\delta_{ns}\phi = \frac{\phi(s+\frac{n\Delta s}{2}) - \phi(s-\frac{n\Delta s}{2})}{n\Delta s} .$$

The horizontal and vertical advection terms are differenced using an energy conserving scheme first proposed by Arakawa (1966) and later modified to the fourth order equivalent advective form by Xue and Lin (1991). This form conserves the first and second order moments.

$$advu^t = \frac{4}{3}[\overline{\bar{u}^x\delta_x u}^x + \overline{\bar{v}^x\delta_y u}^y + \overline{\bar{W}^{c^x}\delta_\zeta u}^\zeta] - \frac{1}{3}[\overline{\bar{u}^{2x}\delta_{2x}u}^{2x} + \overline{\bar{v}^{xy}\delta_{2y}u}^{2y} + \overline{\bar{W}^{c^{x\zeta}}\delta_{2\zeta}u}^{2\zeta}] ,$$

(3.19)

$$advv^t = \frac{4}{3}[\overline{\bar{u}^y\delta_x v}^x + \overline{\bar{v}^y\delta_y v}^y + \overline{\bar{W}^{c^y}\delta_\zeta v}^\zeta] - \frac{1}{3}[\overline{\bar{u}^{xy}\delta_{2x}v}^{2x} + \overline{\bar{v}^{2y}\delta_{2y}v}^{2y} + \overline{\bar{W}^{c^{y\zeta}}\delta_{2\zeta}v}^{2\zeta}] ,$$

(3.20)

$$advw^t = \frac{4}{3}[\overline{\overline{u}^{\zeta}\delta_x w}^{x} + \overline{\overline{v}^{\zeta}\delta_y w}^{y} + \overline{\overline{W}^{c\zeta}\delta_{\zeta} w}^{\zeta}] - \frac{1}{3}[\overline{\overline{u}^{x\zeta}\delta_{2x} w}^{2x} + \overline{\overline{v}^{y\zeta}\delta_{2y} w}^{2y} + \overline{\overline{W}^{c\zeta}\delta_{2\zeta} w}^{2\zeta}].$$

(3.21)

$$adv\theta^t = \frac{4}{3}[\overline{\overline{u\delta_x\theta'}^{x}} + \overline{\overline{v\delta_y\theta'}^{y}} + \overline{\overline{W^c\delta_{\zeta}\theta'}^{\zeta}}] - \frac{1}{3}[\overline{\overline{u^x\delta_{2x}\theta'}^{2x}} + \overline{\overline{v^y\delta_{2y}\theta'}^{2y}} + \overline{\overline{W^{c\zeta}\delta_{2\zeta}\theta'}^{2\zeta}}] +$$

$$\frac{4}{3}[\overline{\overline{w\delta_{\zeta}\bar{\theta}}^{\zeta}}] - \frac{1}{3}[\overline{\overline{w^{\zeta}\delta_{2\zeta}\bar{\theta}}^{2\zeta}}] \quad , \qquad (3.22)$$

$$adv\pi'^t = \frac{4}{3}[\overline{\overline{u\delta_x\pi'}^{x}} + \overline{\overline{v\delta_y\pi'}^{y}} + \overline{\overline{W^c\delta_{\zeta}\pi'}^{\zeta}}] - \frac{1}{3}[\overline{\overline{u^x\delta_{2x}\pi'}^{2x}} + \overline{\overline{v^y\delta_{2y}\pi'}^{2y}} + \overline{\overline{W^{c\zeta}\delta_{2\zeta}\pi'}^{2\zeta}}]$$

(3.23)

The contravariant vertical velocity is computed using

$$W^c = \overline{\overline{u^{\zeta}J_1}^{x}} + \overline{\overline{v^{\zeta}J_2}^{y}} + w\overline{J_3}^{\zeta} \quad .$$

The sub-grid scale contributions are discretized according to:

$$turb_u^t = \delta_x(-\tau_{11}) + \overline{\overline{J_1\delta_{\zeta}(-\tau_{11})}^{x}}^{\zeta} + \delta_y(-\tau_{12}) + \overline{\overline{J_2}^{x}\delta_{\zeta}(-\tau_{12})}^{y\zeta} + \overline{J_3}^{x}\delta_{\zeta}(-\tau_{13}) \quad ,$$

$$turb_v^t = \delta_x(-\tau_{21}) + \overline{\overline{J_1}^{y}\delta_{\zeta}(-\tau_{21})}^{x\zeta} + \delta_y(-\tau_{22}) + \overline{\overline{J_2\delta_{\zeta}(-\tau_{22})}^{y}}^{\zeta} + \overline{J_3}^{y}\delta_{\zeta}(-\tau_{23}) \quad ,$$

$$turb_w^t = \delta_x(-\tau_{31}) + \overline{\overline{J_1\delta_{\zeta}(-\tau_{31})}^{\zeta}}^{x} + \delta_y(-\tau_{32}) + \overline{\overline{J_2\delta_{\zeta}(-\tau_{32})}^{\zeta}}^{y} + \overline{J_3}^{\zeta}\delta_{\zeta}(-\tau_{33}) \quad ,$$

$$turb_{\theta}^t = \delta_x(-\tau_{\theta 1}) + \overline{\overline{J_1\delta_{\zeta}(-\tau_{\theta 1})}^{x\zeta}} + \delta_y(-\tau_{\theta 2}) + \overline{\overline{J_2\delta_{\zeta}(-\tau_{\theta 2})}^{y\zeta}} + J_3\delta_{\zeta}(-\tau_{\theta 3}) \quad .$$

The stresses are computed using:

$$\tau_{11} = -2\nu_t\left[\delta_x u + \overline{J_1\delta_\zeta u}^{x\zeta}\right] ,$$

$$\tau_{12} = -2\overline{\nu_t}^{xy}\left[\frac{1}{2}(\delta_x v + \overline{\overline{J_1}^{y}\delta_\zeta \overline{v}^{x}}^{\zeta} + \delta_y u + \overline{\overline{J_2}^{x}\delta_\zeta \overline{u}^{y}}^{\zeta})\right] ,$$

$$\tau_{13} = -2\overline{\nu_t}^{x\zeta}\left[\frac{1}{2}(\delta_x w + J_1\delta_\zeta \overline{w}^{x\zeta} + \overline{J_3}^{x\zeta}\delta_\zeta u)\right] ,$$

$$\tau_{22} = -2\nu_t\left[\delta_y v + \overline{J_2\delta_\zeta v}^{y\zeta}\right] ,$$

$$\tau_{23} = -2\overline{\nu_t}^{y\zeta}\left[\frac{1}{2}(\delta_y w + J_2\delta_\zeta \overline{w}^{y\zeta} + \overline{J_3}^{y\zeta}\delta_\zeta v)\right] ,$$

$$\tau_{33} = -2\nu_t\left[J_3\delta_\zeta w\right] .$$

The sub-grid scale kinetic energy is integrated on the big time step using the leapfrog scheme.

$$\frac{e^{t+\Delta t} - e^{t-\Delta t}}{2\Delta t} = -adve^t + P + \frac{g}{\overline{\theta}}\overline{\tau_{\theta 3}}^{\zeta} + \delta_x(2\overline{\nu_t}^{x}\delta_x e) + \delta_y(2\overline{\nu_t}^{y}\delta_y e) + \delta_\zeta(2\overline{\nu_t}^{\zeta}\delta_\zeta e) - C_l\frac{e^{\frac{3}{2}}}{l}$$

The advection and shear production terms are:

$$adve^t = \frac{4}{3}[\overline{u\delta_x e}^{x} + \overline{v\delta_y e}^{y} + \overline{W^c\delta_\zeta e}^{\zeta}] - \frac{1}{3}[\overline{\overline{u}^{x}\delta_{2x}e}^{2x} + \overline{\overline{v}^{y}\delta_{2y}e}^{2y} + \overline{\overline{W}^{c\zeta}\delta_{2\zeta}e}^{2\zeta}] ,$$

$$P = 2\nu_t S_{11}S_{11} + 2\nu_t\overline{S_{12}S_{12}}^{xy} + 2\nu_t\overline{S_{13}S_{13}}^{x\zeta} + 2\nu_t S_{22}S_{22} + 2\nu_t\overline{S_{23}S_{23}}^{y\zeta} + 2\nu_t S_{33}S_{33} .$$

The strains are:

$$S_{11} = \delta_x u + \overline{J_1 \delta_\zeta u}^{x\zeta} \quad ,$$

$$S_{12} = \frac{1}{2}\left[\delta_x v + \overline{\overline{J_1}^{y} \delta_\zeta \overline{v}^{x}}^{\zeta} + \delta_y u + \overline{\overline{J_2}^{x} \delta_\zeta \overline{u}^{y}}^{\zeta} \right] \quad ,$$

$$S_{13} = \frac{1}{2}\left[\delta_x w + J_1 \delta_\zeta \overline{w}^{x\zeta} + \overline{J_3}^{x\zeta} \delta_\zeta u \right] \quad .$$

$$S_{22} = \delta_y v + \overline{J_2 \delta_\zeta v}^{y\zeta} \quad ,$$

$$S_{23} = \frac{1}{2}\left[\delta_y w + J_2 \delta_\zeta \overline{w}^{y\zeta} + \overline{J_3}^{y\zeta} \delta_\zeta v \right] \quad ,$$

$$S_{33} = J_3 \delta_\zeta w \quad .$$

The mixing terms $D_u^t, D_v^t, D_w^t, D_\theta^t$ are represented by:

$$D_u^t = C_u^t + R_u^t = -\left[C_H[\delta_x^2(\delta_x^2 u') + \delta_y^2(\delta_y^2 u')]\right] - \left[C_V[\delta_\zeta^2(\delta_\zeta^2 u')]\right] - \overline{r(\zeta)}^{x} u' \quad ,$$

$$D_v^t = C_v^t + R_v^t = -\left[C_H[\delta_x^2(\delta_x^2 v') + \delta_y^2(\delta_y^2 v')]\right] - \left[C_V[\delta_\zeta^2(\delta_\zeta^2 v')]\right] - \overline{r(\zeta)}^{y} v' \quad ,$$

$$D_w^t = C_w^t + R_w^t = -\left[C_H[\delta_x^2(\delta_x^2 w) + \delta_y^2(\delta_y^2 w)]\right] - \left[C_V[\delta_\zeta^2(\delta_\zeta^2 w)]\right] - \overline{r(\zeta)}^{\zeta} w \quad ,$$

$$D_\theta^t = C_\theta^t + R_\theta^t = -\left[C_H[\delta_x^2(\delta_x^2 \theta') + \delta_y^2(\delta_y^2 \theta')]\right] - \left[C_V[\delta_\zeta^2(\delta_\zeta^2 \theta')]\right] - r(\zeta)\theta' \quad .$$

The computational mixing coefficients C_H and C_V are held constant and generally chosen to be on the order of 0.0005. Finally, an Asselin (1972) is applied to all the predicted variables on the big time step to prevent the divergence of the odd-even time step solutions:

$$\phi^t = \phi^t + \upsilon(\phi^{t-\Delta t} - 2\phi^t + \phi^{t-\Delta t})$$

A smoothing coefficient υ of 0.2 strongly damps the computational modes without affecting the physical modes significantly.

CHAPTER 4

MODEL VERIFICATION

Since this is a new model, several tests were conducted to validate the numerical formulations, with five of the most important test groups presented here. The validation suite includes: two two-dimensional analytical mountain wave solutions, a simplified one-dimensional surface flux test using the Wangara data set, a three-dimensional density current simulation, and a two-dimensional simulation of the January 11, 1972 Boulder Colorado windstorm. With regard to the Boulder January 11, 1972 windstorm test, the current model is compared to established models. New results that are related to the proper numerical simulation of strong mountain waves are presented. Table 4.1 summarizes key model parameters used in each test.

Table 4.1 Summary of Model Test Parameters

Parameter	Linear	Linear Rad.	Long's	Wangara	Bubble	Boulder
nx	98	98	386	7	50	130
ny	4	4	4	7	50	4
nz	83	43	83	70	53	86
Δx (m)	2000	2000	400	80000	800	1000
Δy (m)	---	---	---	80000	800	---
Δz (m)	200	200	250	30	100	341
Δt (s)	20	20	10	20	4	5.0
$\Delta \tau$ (s)	5	5	1	20	1	2.5
$\overline{U}$ (m/s)	20	20	10	0	0	Sounding
N (s^{-1})	0.01956	0.01956	0.0108	Sounding	0	Sounding
$\overline{T}$ ($^{\circ}K$)	250	250	---	Sounding	---	Sounding
$\Delta\theta$ ($^{\circ}K$)	--	---	---	---	-4.0	---
λ_z (m)	---	---	---	---	2000	---
λ_x (m)	---	---	---	---	14000	---
h_m (m)	1	1	500*	0	500	2000
a_x (m)	10000	10000	2000*	0	2000	10000
a_y (m)	---	---	---	0	2000	---
$C_h / \Delta x^4$	0.00001	0.00001	1.0e-5	0	5.0e-5	0.0004
$C_v / \Delta z^4$	0.0	0.0	0.0	0	5.0e-5	0.00001
α (s^{-1})	0.0025	---	---	---	---	0.0015
z_D (m)	8000	---	---	---	---	18000
υ	0.2	0.2	0.2	0.2	0.2	0.2

*Terrain profile was numerically iterated using the non-linear lower boundary condition, starting with an initial height of h = 570 m and width a_x = 2000 m. Sounding data are listed in Appendix E.

4.1 Two Dimensional Linear Hydrostatic Mountain Wave

Two tests were performed using a linear hydrostatically forced mountain profile in an isothermal atmosphere. The goal here is to verify the model's ability to reproduce basic mountain wave characteristics. In the first test, a Rayleigh sponge is applied to the top half of the domain (from 8-16 km) in combination with the rigid upper boundary condition ($w = 0$). The second test incorporates the upper linear hydrostatic $w - \pi$ radiation condition at the 8km level. All other parameters remain unchanged and are given in Table 4.1.

The numerical solutions are compared to their analytical counterparts. Following Smith (1979), analytical solutions to a linear compressible hydrostatic mountain flow are developed in terms of streamline displacement from the undisturbed upstream value. For linearized compressible hydrostatic flow, the differential equation for streamline deflection is:

$$\frac{\partial^2 \delta}{\partial z^2} + l^2 \delta = 0 \quad , \tag{4.1}$$

where δ is the streamline displacement and l^2 is the Scorer parameter describing the vertical structure of the disturbance. The Scorer parameter is defined by:

$$l^2 = g^2 \left[\frac{1}{C_p \overline{T} \overline{U}^2} - \frac{1}{4R^2 \overline{T}^2} \right] .$$

The mountain profile is bell shaped:

$$h(x) = \frac{h_m a^2}{x^2 + a^2} \quad . \tag{4.2}$$

The distance from the center of the mountain is x, a is the mountain quarter-width, and h_m is the mountain height. Applying the mountain profile to the lower boundary condition $\delta(x,0) = h(x)$, and assuming the disturbance vanishes at large distances up and downstream of the mountain, the solution for streamline displacement is:

$$\delta(x,z) = \left(\frac{\bar{\rho}}{\rho_o}\right)^{-\frac{1}{2}} h_m a \frac{a\cos(lz) - x\sin(lz)}{x^2 + a^2} \quad ,$$

where ρ_o is the air density at the surface ($z = 0$) and $\bar{\rho}$ is the base state density. The analytical velocity fields are functions of the streamline deflection:

$$u_{aH}(x,z) = -\frac{\bar{U}}{\bar{\rho}} \frac{\partial(\bar{\rho}\delta(x,z))}{\partial z} \quad , \tag{4.3}$$

$$w_{aH}(x,z) = \bar{U} \frac{\partial \delta(x,z)}{\partial x} \quad . \tag{4.4}$$

In (4.3) and (4.4), w is obtained and then u is computed using the anelastic continuity equation.

Results from the Rayleigh sponge rigid lid test are presented in Figures 4.1 and 4.2. Figure 4.1 displays the model, analytical, and difference perturbation horizontal velocities at a non-dimensional time $Ut/a = 60$ (30000 seconds). Figure 4.2 follows the convention of Figure 4.1 for the vertical velocity field. The present model reproduces the analytical fields with acceptable accuracy. The difference fields indicate a slight

upstream tilt with height of the wave structure and accounts for most of the observed error. The maximum and minimum perturbations are within 10% of the analytical values at a height of one vertical wavelength (approximately 6.4 km). The upper radiation condition test requires only half the grid points in the vertical when compared to the sponge case. Figures 4.3 and 4.4 reveal similar characteristics found in the Rayleigh damping-rigid lid test. This suggests that for weakly forced hydrostatic flows the radiation condition can be used without appreciable loss in numerical accuracy. Both tests compare favorably with results presented by Nance and Durran (1994). They conducted a number of linear hydrostatic mountain wave experiments with similar initial and boundary conditions and computed difference fields to measure model accuracy. Their error characteristics are quite similar to the present models in terms of magnitude and location.

Another measure of the accuracy of a numerical model is the transport of wave energy with height. One type of wave activity, as discussed by Eliassen and Palm (1960), is the vertical flux of horizontal momentum. The momentum flux at the surface can be expressed by:

$$M_f = -\int_{-\infty}^{+\infty} \bar{\rho} u' w' dx = \int_{-\infty}^{+\infty} p \frac{\partial h}{\partial x} dx \quad . \tag{4.5}$$

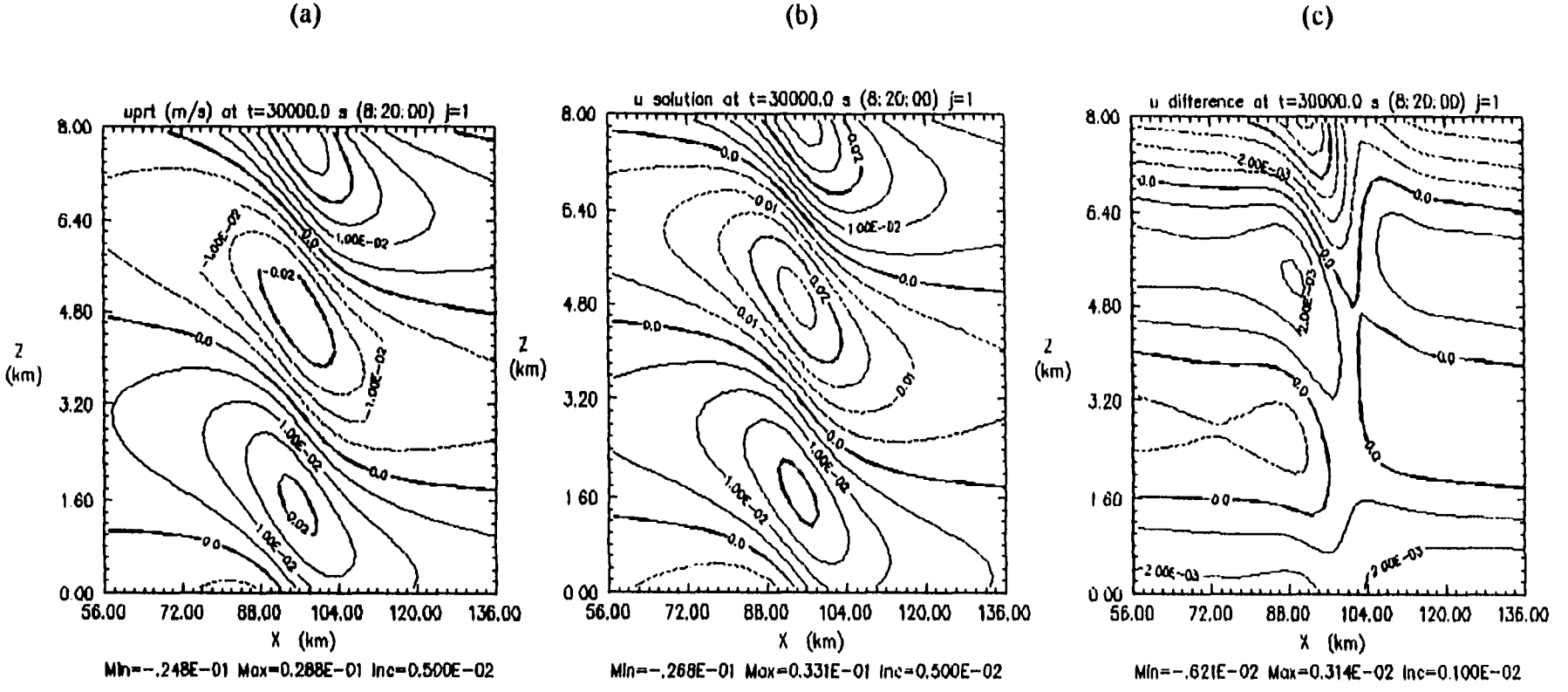

Figure 4.1. Numerical model results for a linear hydrostatic mountain wave test using the Rayleigh damping rigid lid combination at time $Ut/a = 60$ (30000 seconds) for (a) u', (b) u_{all}, (c) $u' - u_{all}$. The contour interval is (a), (b) 0.005 m/s and (c) 0.001 m/s. The area depicted is centered over the mountain and is 80 km x 8 km.

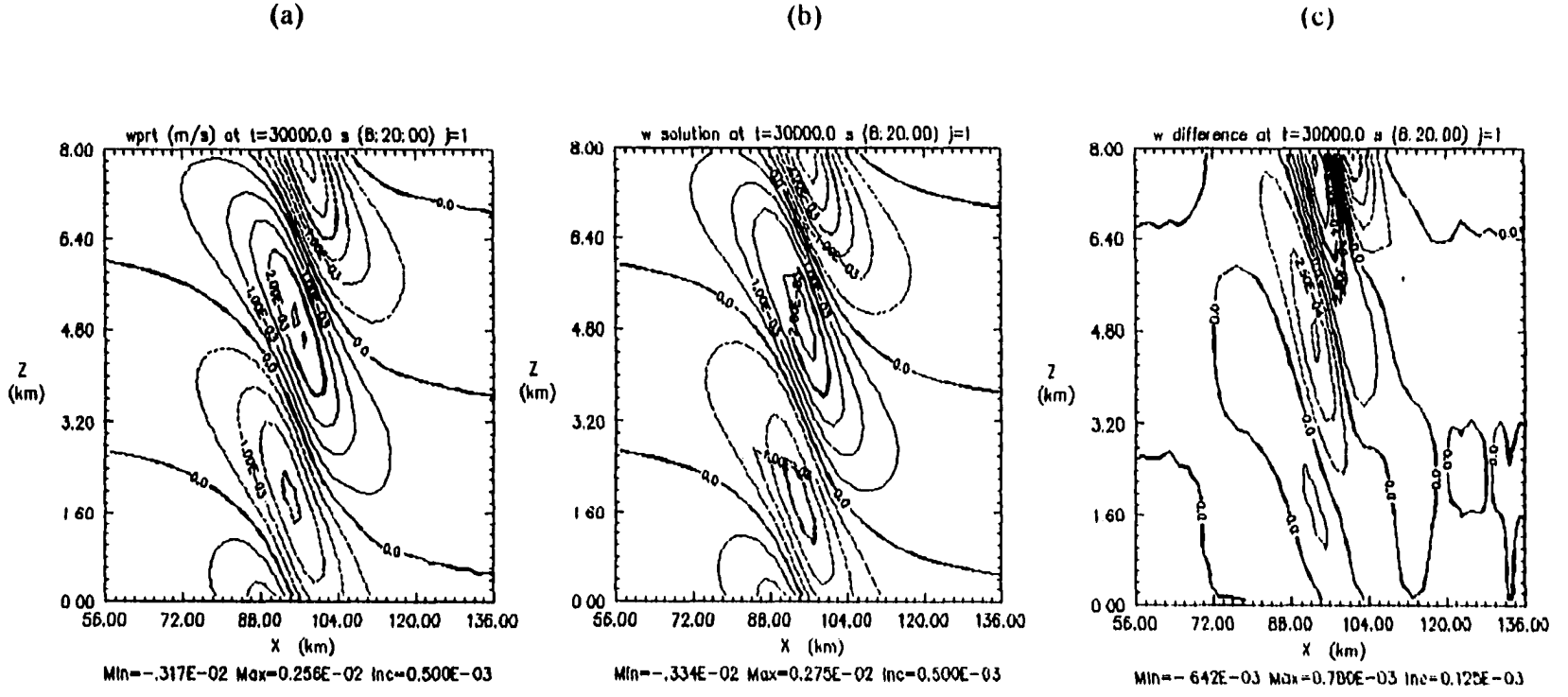

Figure 4.2. Numerical model results for a linear hydrostatic mountain wave test using the Rayleigh damping rigid lid combination at time $Ut/a = 60$ (30000 seconds) for (a) w', (b) w_{all}, and (c) $w' - w_{all}$. The contour interval for (a) and (b) is 0.0005 m/s, and (c) 0.000125 m/s. The area depicted follows that of Figure 4.1.

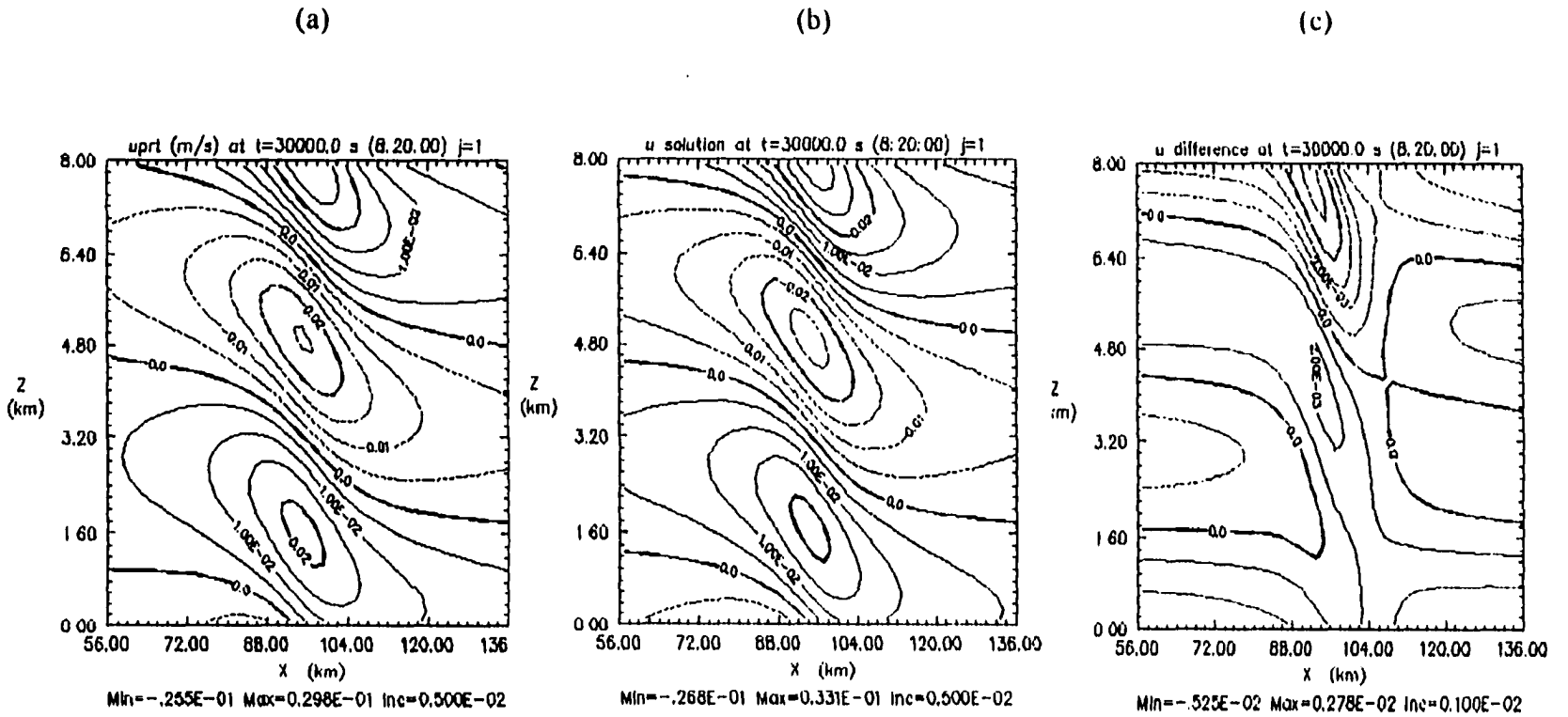

Figure 4.3. Numerical model results for a linear hydrostatic mountain wave test using the upper radiation condition at time lt/a = 60 (30000 seconds) for (a) u', (b) u_{all}, (c) $u' - u_{all}$. The contour interval is (a), (b) 0.005 m/s and (c) 0.001 m/s. The area depicted follows that given in Figure 4.1.

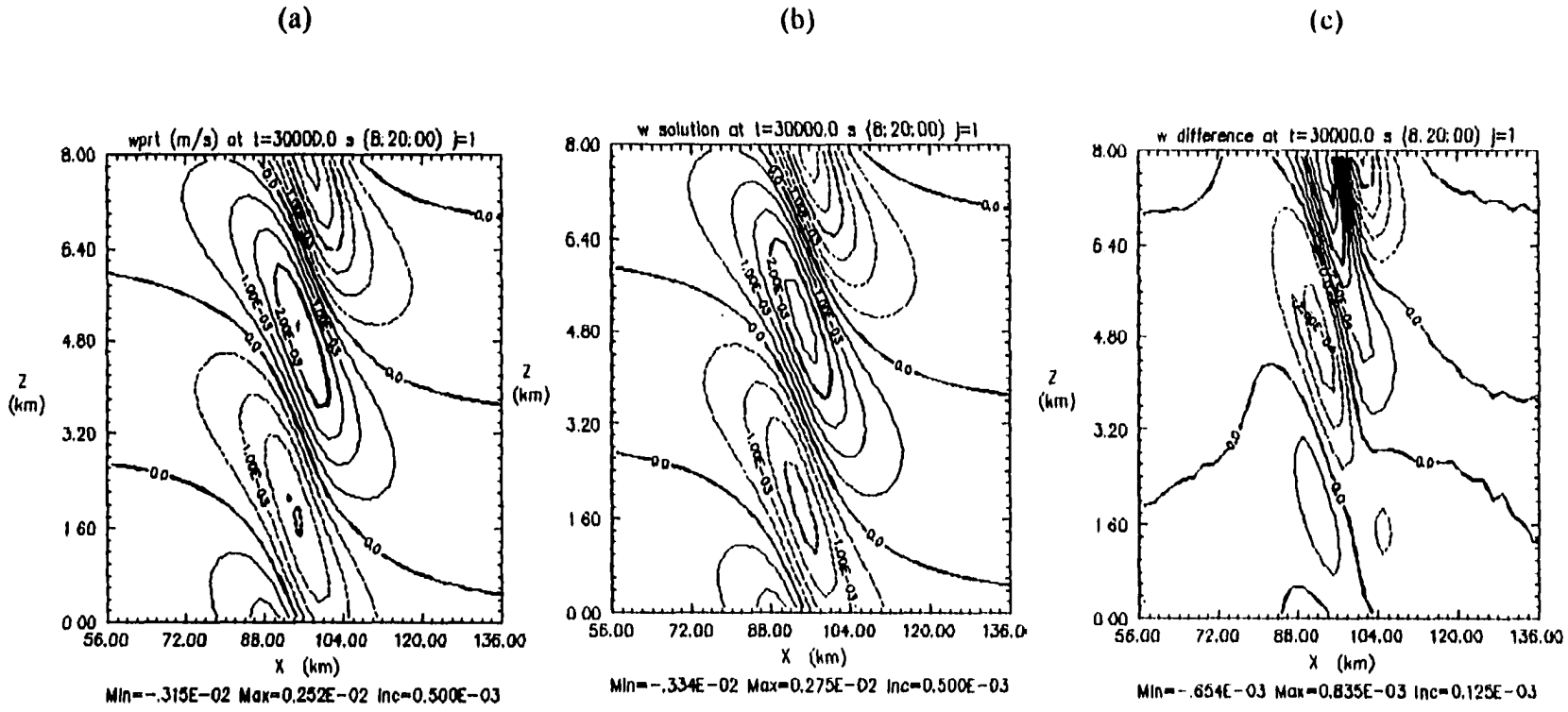

Figure 4.4. Numerical model results for a linear hydrostatic mountain wave test using the upper radiation condition at time Ut/a = 60 (30000 seconds) for (a) w', (b) w_{all}, and (c) $w' - w_{all}$. The contour interval in (a), (b) is 0.0005 m/s and (c) 0.000125 m/s. The area depicted follows that given in Figure 4.1.

The momentum flux at the surface is equal to but opposite in sign to the vertical flux of wave energy or surface wave drag, where u' and w' represent the perturbation velocities and $\overline{\rho}$ the base state density. The momentum flux is often normalized by the linear hydrostatic value.

$$M_H = -\frac{\pi}{4}\rho_o N \overline{U} h_m^2 \quad .$$

where ρ_o is the surface reference density and N is the static stability for an isothermal atmosphere:

$$N^2 = \frac{g^2}{C_p \overline{T}} \quad .$$

Figure 4.5 reveals a difference of only a few percent between the rigid lid/sponge and linear radiation condition tests. Both cases support momentum fluxes of 90% or better at one vertical wavelength and 95% of the normalized value at the surface. For steady state mountain waves, Eliassen and Palm (1960) show that the vertical flux of horizontal momentum remains constant with height when $U \neq 0$. The present model produces a nearly vertical profile and is consistent with other compressible models (Durran and Klemp, 1983 and ARPS, 1995). Normalized flux profiles approach unity for horizontal model domains twice that used above (not shown).

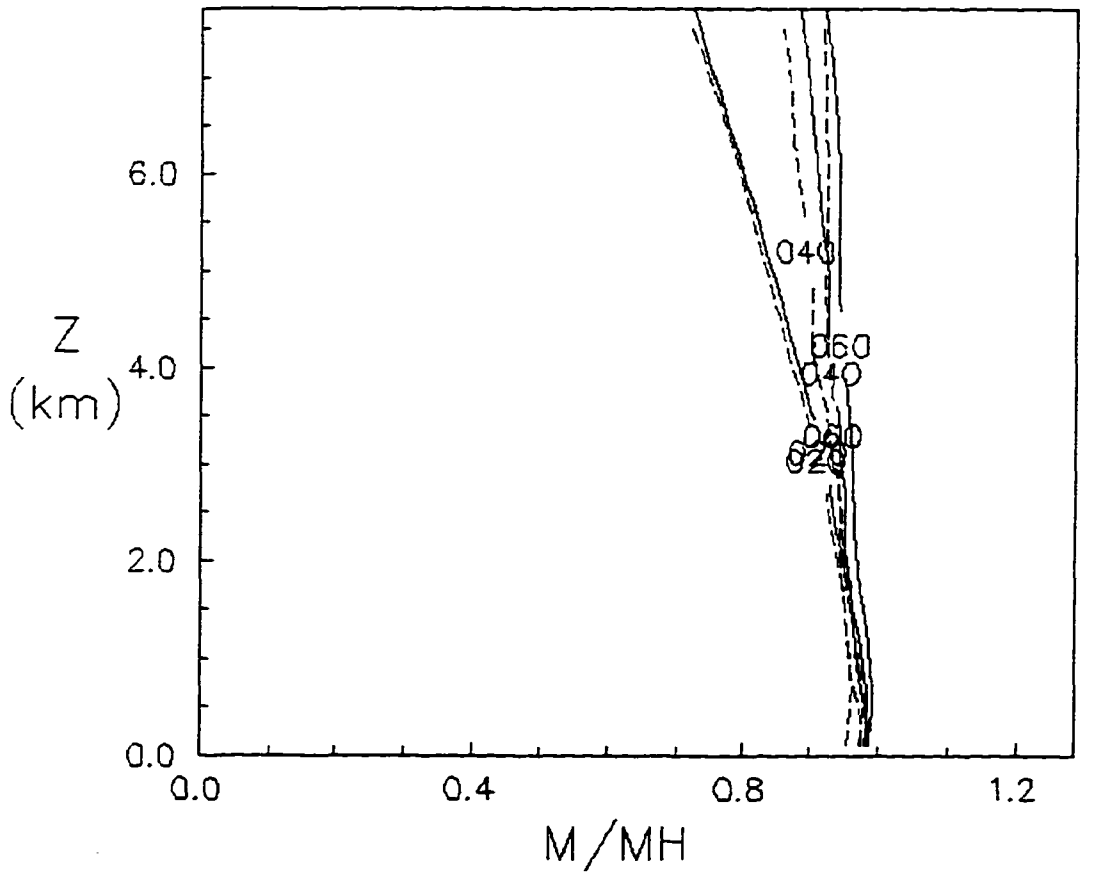

Figure 4.5. Vertical flux of horizontal momentum at Ut/a = 20, 40 ,60 normalized by the linear hydrostatic value. Solid lines represent the Rayleigh damping solution and the dashed lines represent the upper radiation condition results. One vertical wavelength is approximately 6.4 km.

4.2 Two-Dimensional Finite Amplitude Boussinesq Flow

The model is tested using a two-dimensional non-linear Boussinesq flow and compared to Long's (1953) solution. Following Durran and Klemp's (1983) implementation of Long's solution, the differential equation for the streamline deflection from the undisturbed upstream height is similar to the linear case presented in Section 4.1. The equation for streamline deflection is:

$$\frac{\partial^2 \delta}{\partial x^2} + \frac{\partial^2 \delta}{\partial z^2} + l^2 \delta = 0 \quad . \tag{4.6}$$

The non-hydrostatic component is represented by the x derivative. With the Brunt-Vaisala frequency defined by:

$$N^2 = \frac{g}{\theta_o} \frac{\partial \bar{\theta}}{\partial z} \quad .$$

The Scorer parameter is $l = \frac{N}{\bar{U}}$. For a constant base state flow and static stability, Equation (4.6) describes non-linear flow using a linear differential equation. The lower boundary condition $\delta(x, z_s) = z_s$ is non-linear and cannot be directly applied. After implementation of the linearized upper radiation condition, the solution to (4.6) is

$$\delta(x,z) = h_m a \,\mathrm{Re}\left[\int_0^l \exp[i(kx + (l^2 - k^2)^{\frac{1}{2}} z) - kb]dk + \int_l^\infty \exp[ikx - kb - (k^2 - l^2)^{\frac{1}{2}} z)]dk \right] \quad .$$

A numerical approximation for the non-linear lower boundary streamline deflection is made using the initial terrain profile from (4.2). The procedure involves solving (4.6) for the surface streamline deflection using the initial terrain profile. The resulting streamline is substituted back into the non-linear lower boundary condition and iterated until the change in streamline deflection is within acceptable limits. Steffensen's Algorithm found in Burden and Faires (1989) is used to obtain the iterated non-linear lower boundary condition for use in the numerical model. For an initial mountain height of 570 meters and mountain quarter-width of 2 km, the final mountain peak is 500 meters with the crest shifted upstream a few hundred meters. The analytically determined velocity perturbations have the same form as (4.3) and (4.4) without the base state density term:

$$u_{aNH}(x,z) = -\bar{U}\frac{\partial \delta(x,z)}{\partial z} \quad , \tag{4.7}$$

$$w_{aNH}(x,z) = \bar{U}\frac{\partial \delta(x,z)}{\partial x} \quad . \tag{4.8}$$

The analytical velocities were calculated using the same horizontal spacing used by the model but with an enhanced vertical grid spacing of 50 m.

The numerical model is prepared by applying the Boussinesq approximation to the buoyancy term in (3.3) and substituting a reference potential temperature into the total potential temperature for the pressure gradient terms of (3.1)-(3.3). The advection terms were removed from the pressure equation (3.5). In this form, the pressure is allowed to change according to the linearized divergence term. The input parameters for this test are provided in Table 4.1 under Long's test group. The numerical solutions for

θ', π' are reproduced in Figure 4.6 at a non-dimensional time of $Ut/a = 60$ (12000 seconds). Only the center portion of the domain (measuring 40 km across and 8 km deep) is shown. A comparison of the approximately steady state model predicted u', w', analytical u_{aNH}, w_{aNH}, and associated difference fields ($u' - u_{aNH}$ and $w' - w_{aNH}$) is presented in Figure 4.7 and 4.8. Overall, the model reproduces the analytical solution reasonably well. The maxima and minima are within 7% for u and to within a few percent for w at a height of one vertical wavelength (approximately 5.8 km). The combined phase and amplitude errors for the velocities at the height of one vertical wavelength are on the order of 10-20%. Most of the difference is related to phase errors. Additional tests (not presented here) indicate that both the radiation and Rayleigh sponge/rigid lid applications produce similar errors in magnitude and phase. Note that these phase errors are consistent with those from the linear hydrostatic tests in Section 4.1.

For this test, the vertical flux of momentum is nearly constant with height and within a few percent of the normalized non-linear value at Ut/a = 60 (Figure 4.9). Analytical streamlines (trajectories involving a single time level of data) were computed and compared to the model equivalents with the results illustrated in Figure 4.10. The streamlines are computed by advancing a parcel through the respective velocity fields using a predictor-corrector method. The trajectory method and test solutions are presented in Appendix C. In general, the numerical model provides a good representation of the analytical streamline pattern over the mountain and displays errors characteristic similar to those shown in Figure 4.7 and 4.8.

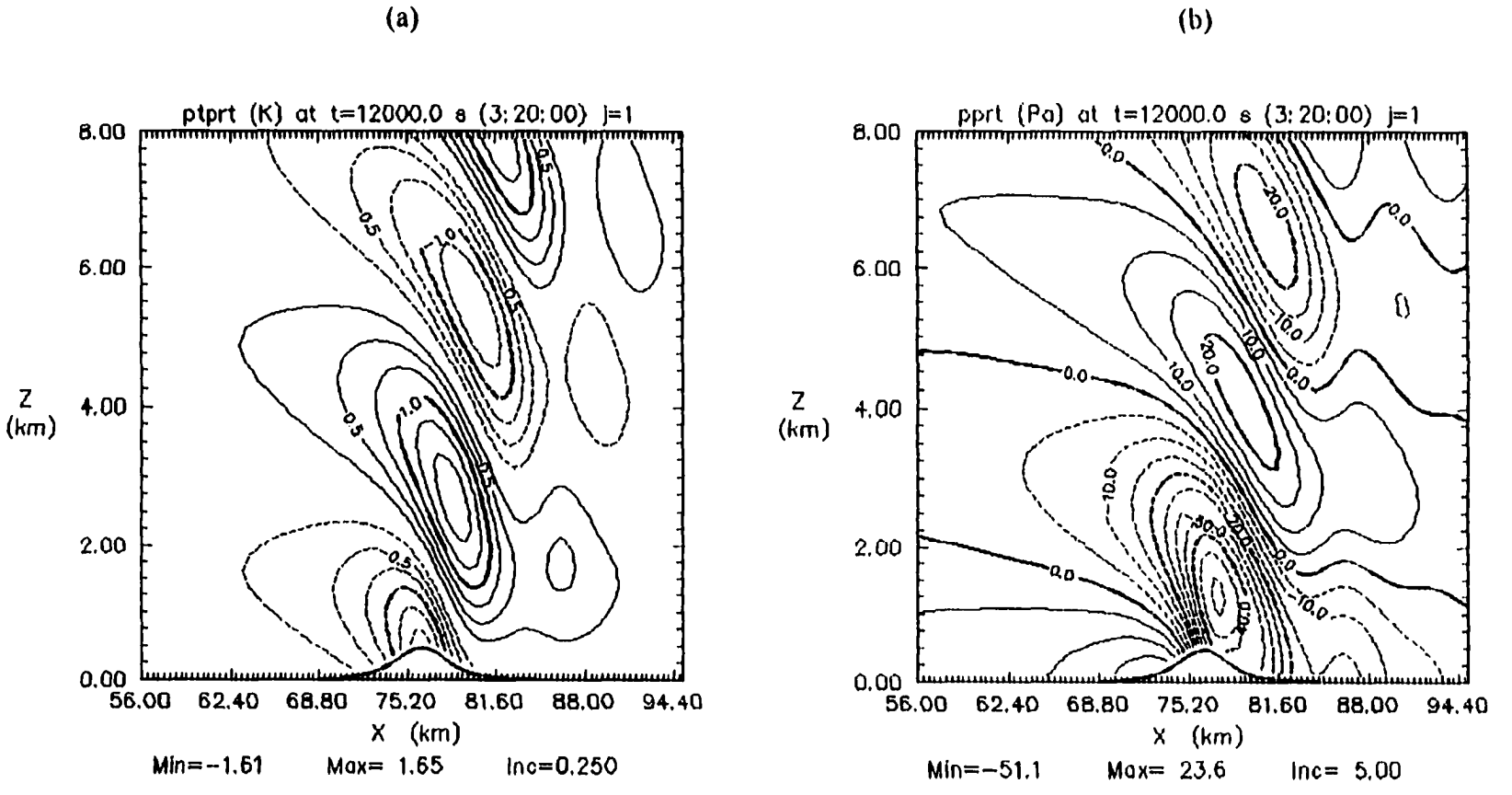

Figure 4.6. Numerical solution for a non-linear Boussinesq forced mountain wave using the linear hydrostatic upper radiation condition for (a) θ' and (b) π' at time $Ut/a = 60$ (12000 seconds). The contour intervals are (a) 0.25 °K, and (b) 5.0 Pa. The plot is centered over the mountain with dimensions 40 km x 8 km.

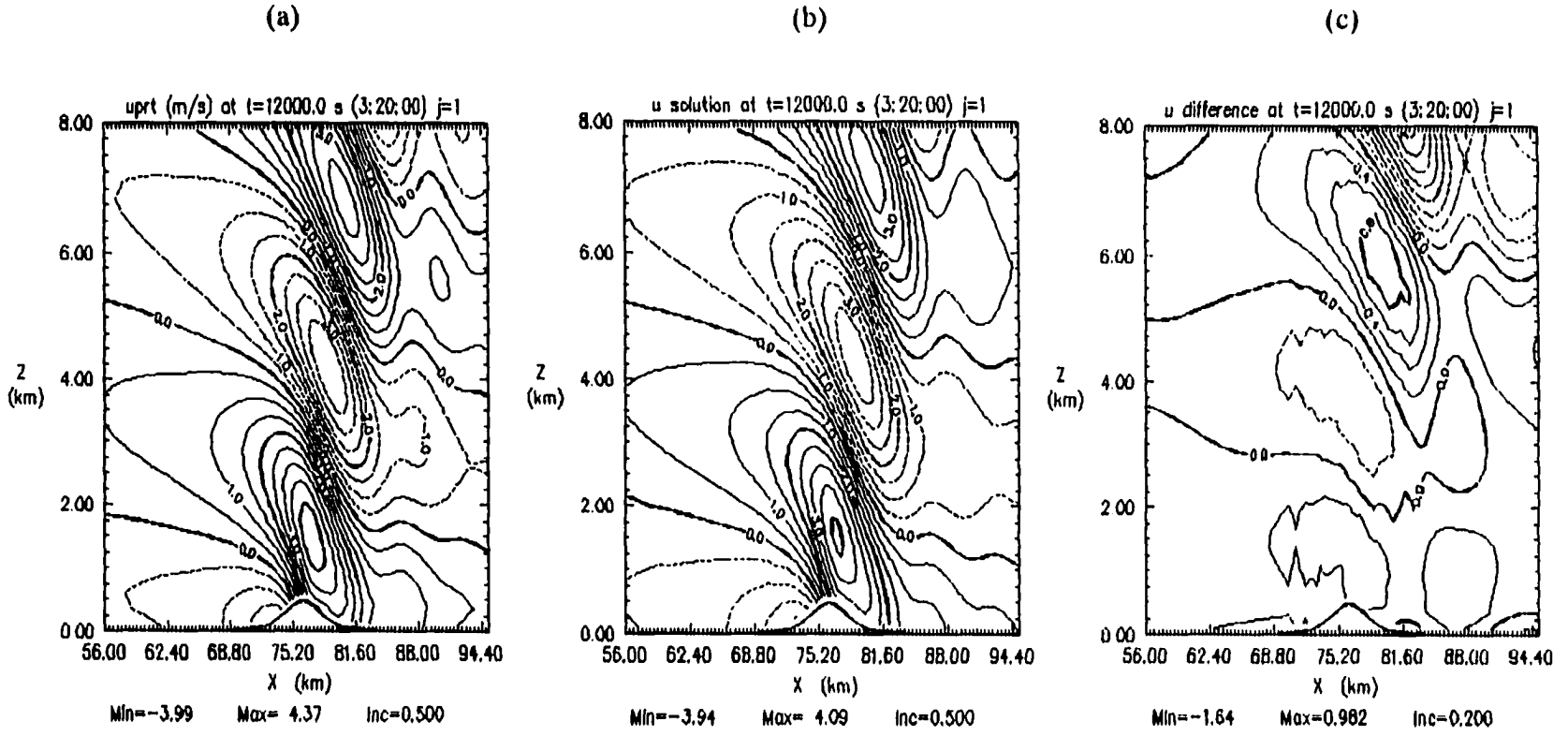

Figure 4.7. Numerical and analytical solutions and difference fields for the non-linear Boussinesq mountain wave using the linear hydrostatic upper radiation condition at time $Ut/a = 60$ (12000 seconds) for (a) u', (b) u_{aNH}, (c) $u' - u_{aNH}$. The contour interval for (a) and (b) is 0.5 m/s and (c) 0.2 m/s. The plot is centered over the mountain with dimensions 40 km x 8 km.

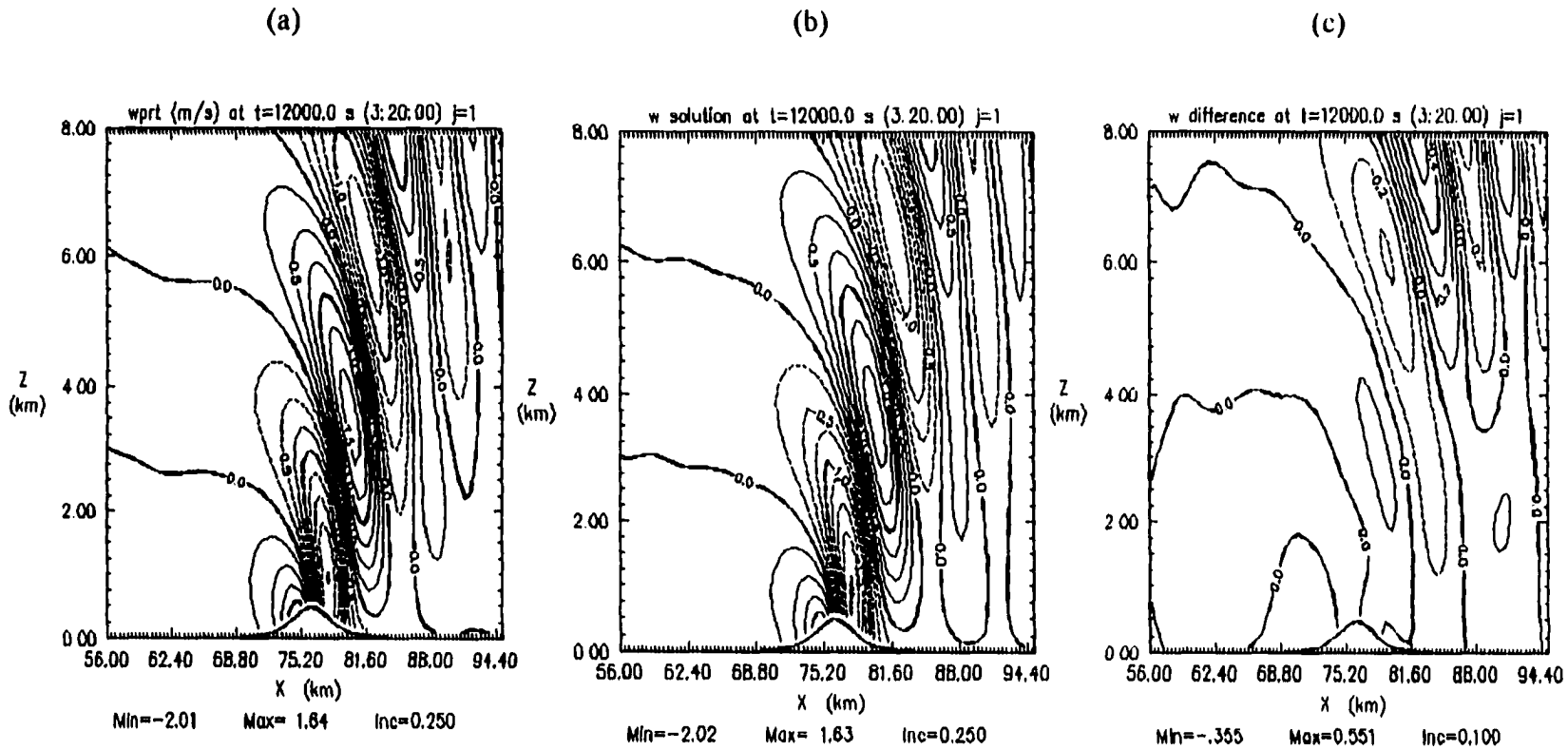

Figure 4.8. Numerical and analytical solutions and difference fields for the non-linear Boussinesq mountain wave using the linear hydrostatic upper radiation condition at time $Ut/a = 60$ (12000 seconds) for (a) w', (b) w_{aNH}, and (c) $w' - w_{aNH}$. The contour interval for (a) and (b) is 0.25 m/s and (c) 0.1 m/s. The area shown follows that shown in Figure 4.7.

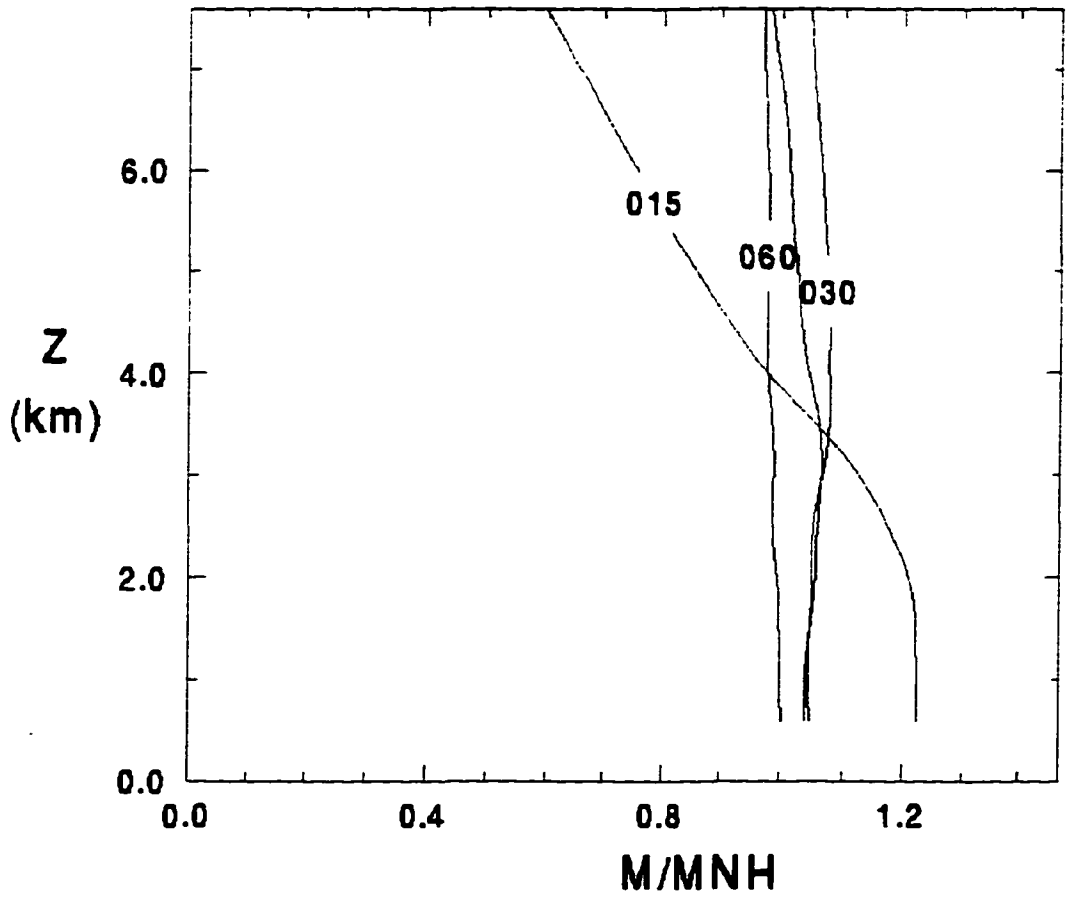

Figure 4.9. Vertical profile of the vertical flux of horizontal momentum for Ut / a = 15, 30, 45, and 60 normalized by the non-linear Boussinesq value. One vertical wavelength is approximately 5.8 km.

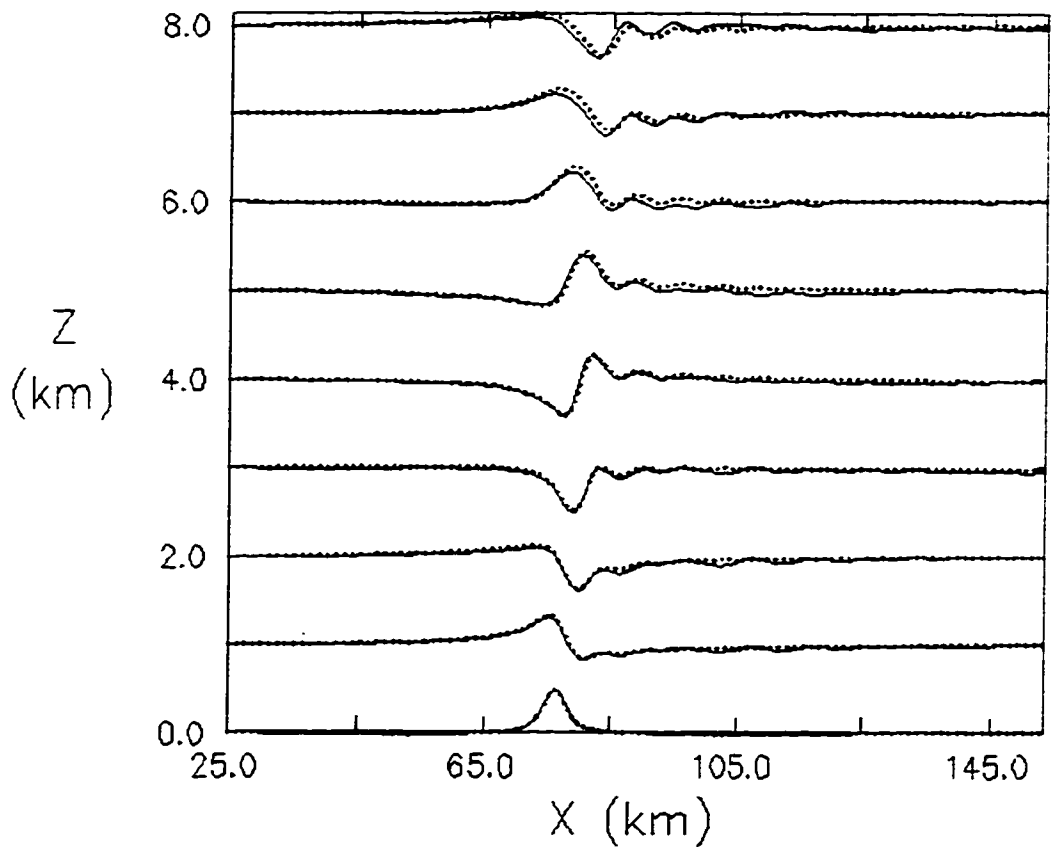

Figure 4.10. Comparison of numerically computed streamlines for the numerical model solution (solid line) and the analytical solution (dotted line) for the non-linear Boussinesq test ($Na/U \approx 2$) at a non-dimensional time $Ut/a = 60$.

4.2 Wangara Day 33

A simple test of the surface parameterization scheme is performed in conjunction with the Wangara Day 33 data set. The simulation is initialized with the observed 9 am vertical profiles of θ, u, and v. The primary focus of this test is to validate the sub-grid scale mixing of the potential temperature field when heat is applied to the surface. No horizontal gradients are present in the initial data set and therefore no gradients develop during the coarse of the simulation. Yamada and Mellor (1975) updated the horizontal wind fields with estimated geostrophic values computed from surface pressure data. Their results indicate that even with the estimated change in the geostrophic winds with time, the predicted profiles deviated from the observed data. Therefore, mixing of the horizontal wind components is not evaluated here. Since this is a one-dimensional test, it is an opportunity to tune the mixing length parameter for simulations not capable of resolving boundary layer convective cells. The relevant input parameters are listed in Table 4.1 under the Wangara test group. Following Sun and Chang (1986), heat flux was applied at the surface with a magnitude of 0.216 and half-period of 11 hours. Figure 4.11 compares the observed and model predicted potential temperature profiles as a function of time. The simulation compares favorably to the observed data. The turbulent mixing scheme captures both the average temperature and mixed layer depth.

(a)

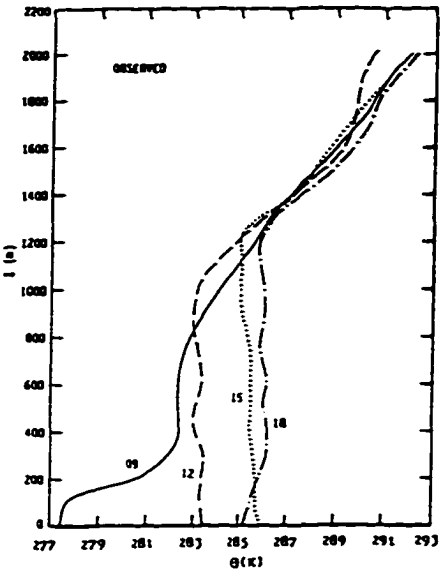

(b)

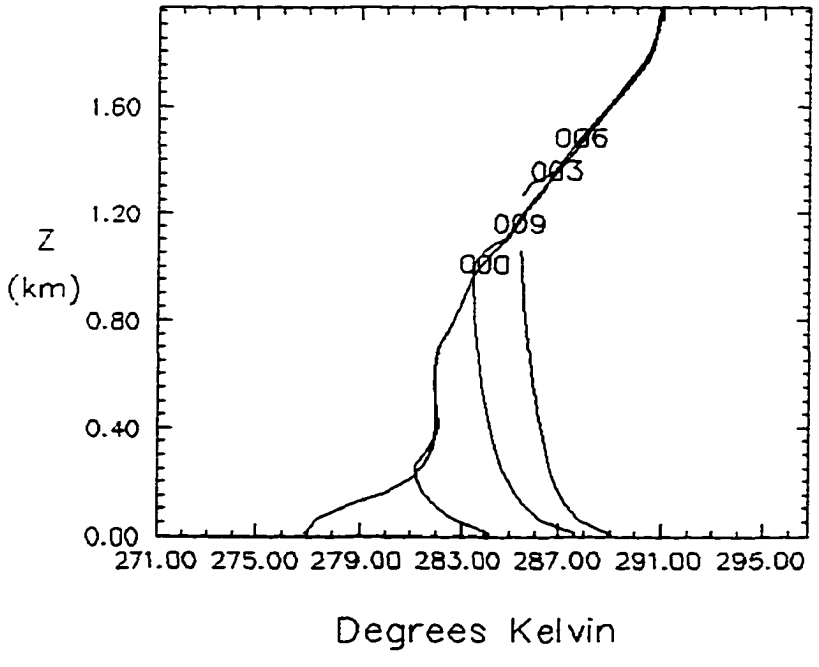

Figure 4.11. Vertical θ profiles from the (a) observed Wangara Test Day 33 from Sun and Chang, (1986), and (b) model at 9 am, 12 noon, 3 p.m., and 6 p.m. local time.

4.4 Three Dimensional Symmetry Test

ARPI3D is tested for symmetry errors by dropping a cold bubble over a symmetric mountain in a neutral environment. The initial bubble perturbation was -4 K with the mountain defined by (4.2). The model parameters used in this test are listed in Table 4.1 under the Bubble test group. This test is designed to show errors in the numerical implementation, which are asymmetric in nature. The horizontal velocities u and v, are symmetric out to 11 decimal places at t=3000 seconds on a CRAY J90 computer. As the bubble moved out of the domain, slight asymmetries were noted (at the 10th place) in the horizontal velocity fields. This test was rerun using zero gradient lateral boundary conditions. The horizontal velocity fields remained symmetric out to the 14th place at t=3000 seconds. It appears that slight asymmetries are introduced by the lateral boundary condition scheme.

4.5 Idealized January 11, 1972 Boulder Colorado Windstorm Simulations

A number of researchers have numerically simulated the Boulder CO, January 11, 1972 windstorm event. The numerical results are often compared to the observed storm structures reported by Lilly and Zipser (1972) and Lilly (1978). Many of the observed windstorm characteristics, such as strong lee side surface winds and wave breaking regions in the upper troposphere and lower stratosphere, are well-represented by the numerical models. This is quite remarkable given the application of an idealized terrain profile (see equation 4.2), the estimated thermodynamic upstream profile, and the two-dimensionality of the numerical experiments.

This test group is broken up into three sections. The first section compares the present model's numerical prediction to the historical numerical studies. The second part exposes the sensitivity of the numerical solution to the vertical resolution and advection scheme accuracy, and the third section addresses the lateral boundary condition issue.

4.5.1 Comparison with Previous Numerical Studies

Two well known two-dimensional numerical simulations of the Boulder January 11, 1972 windstorm were conducted by Peltier and Clark (1979) (denoted as PC) and Durran and Klemp (1983) (denoted as DK). Despite significant differences in terms of the system of equations, initial and boundary conditions, and solution techniques, results from the two models compare favorably. Both display amplification of the mountain wave and subsequent wave breaking structure in the lower stratosphere and upper troposphere with strong surface winds in the lee of the mountain crest. Numerical results from PC and DK and the present model, in terms of total potential temperature, are displayed in Figure 4.12 and 4.13. The present model's results using a mountain shape defined by (4.2) and upstream conditions closely matches those reported by DK. Model parameters for this test are listed in Table 4.1 under the Boulder test group. The thermodynamic profile is evaluated from a sounding supplied by DK with the lowest pressure set to 820 mb and an isentropic layer between 820 mb and 685 mb. Data for levels above 110 mb were obtained from PC's initial Grand Junction 1200Z sounding. For comparison with DK, the horizontal advection terms are approximated by a centered fourth order scheme. The vertical advection terms are computed using a centered second order scheme. The second order equivalent to that presented in (3.19)-(3.23) is

obtained by setting the coefficients in the first terms to unity and omitting the second term. The observed cross section obtained from observations as reported by Lilly and Zipser (1972) is given in Figure 4.14. This model compares favorably with results from DK and PC. All three models generate similar transient gravity waves and wave breaking turbulent regions over the mountain crest.

As with previously reported aspects of the numerical storm, the wave response grows continuously and becomes unstable for the selected time step after approximately t=10,000 seconds. A comparison of the surface wave drag as a function of time from DK, PC, and the current model are given in Figure 4.15 (a) and (b), respectively. The DK and PC models project an initial peak at approximately t=1000 seconds (due to the startup procedure) and then level off until about 6000 seconds, when the wave response and corresponding surface wave drag increases significantly. DK noted that the solution was unsteady and amplified with time, contrary to the observed storm, and suggests the unbounded growth may be due to the absence of surface friction. The solid line in Figure 4.15 (b) traces the surface wave drag computed from the present model. The surface drag time series from this model follows that given by DK and PC.

During the process of comparing the results from ARPI3D to previously reported numerical predictions, significant sensitivities were uncovered that were related to vertical grid resolution (or advection scheme accuracy), and lateral boundary conditions. These factors separate or combined, produce dramatic changes in the outcome of the experiments. The next two sections focus on these issues.

(a) (b) (c)

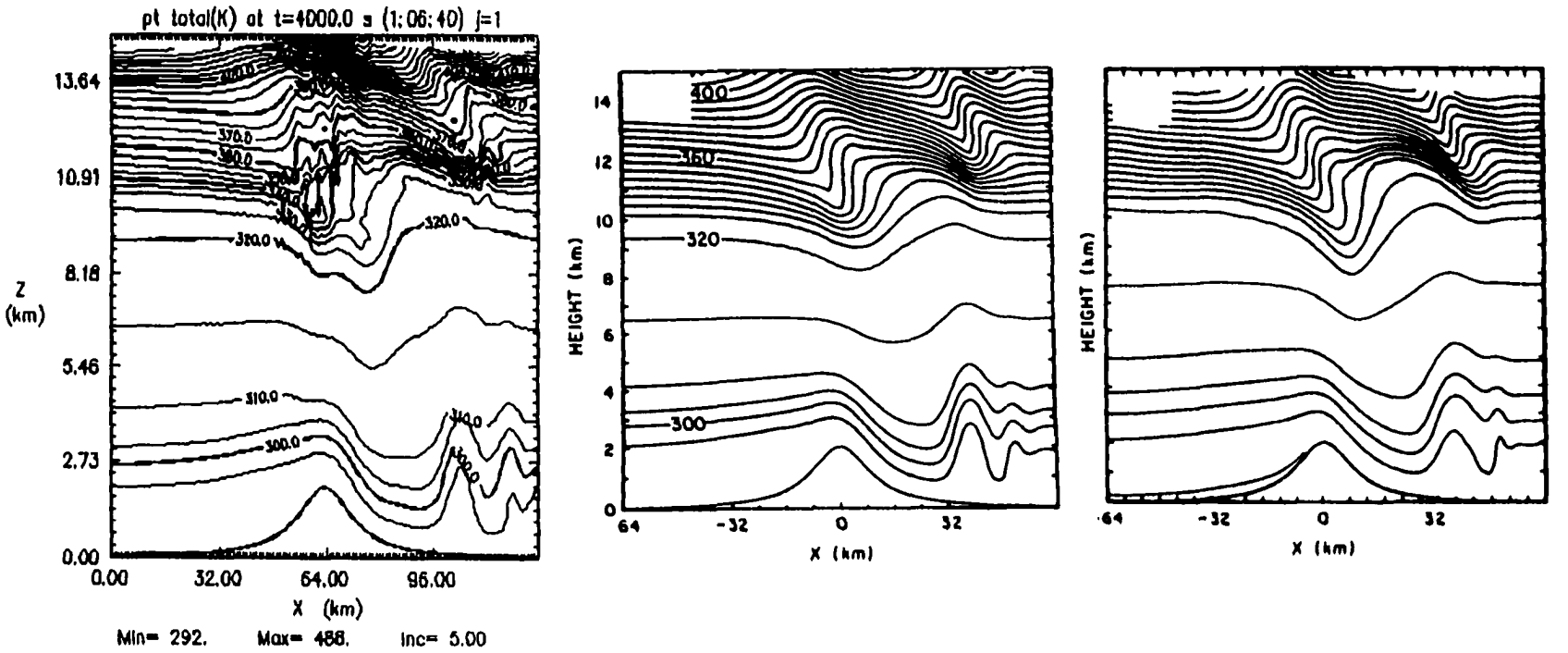

Figure 4.12. Isentropes for the January 11, 1972 Boulder, CO windstorm at t=4000s from (a) the present model, (b) DK, and (c) PC (at 4160s). The contour interval for (a) and (b) is 5 ° K and unknown in (c).

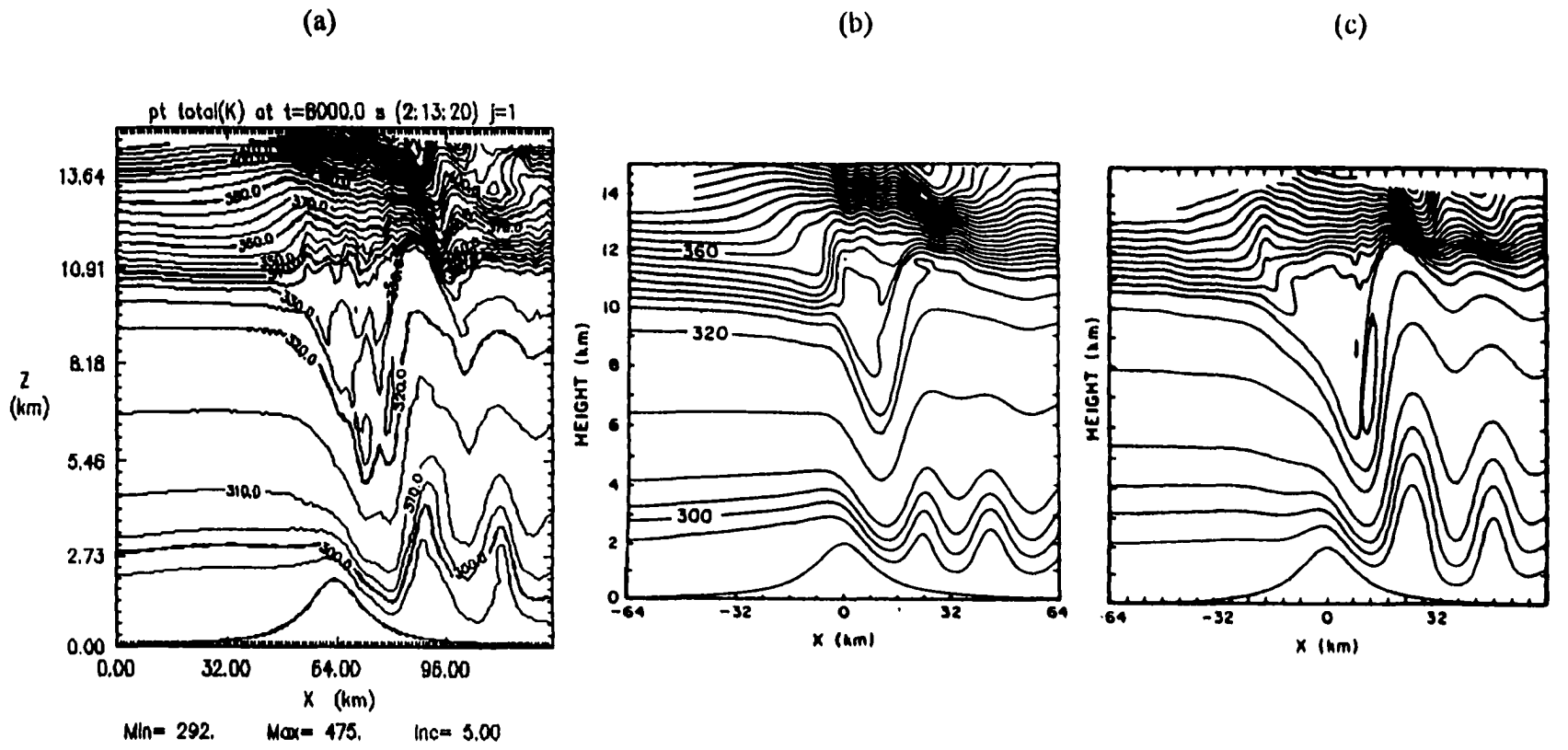

Figure 4.13. Isentropes for the January 11, 1972 Boulder, CO windstorm at t=8000s for (a) the present model, (b) DK and (c) PC. The contour interval for (a) and (b) is 5 ° K and is unknown in (c).

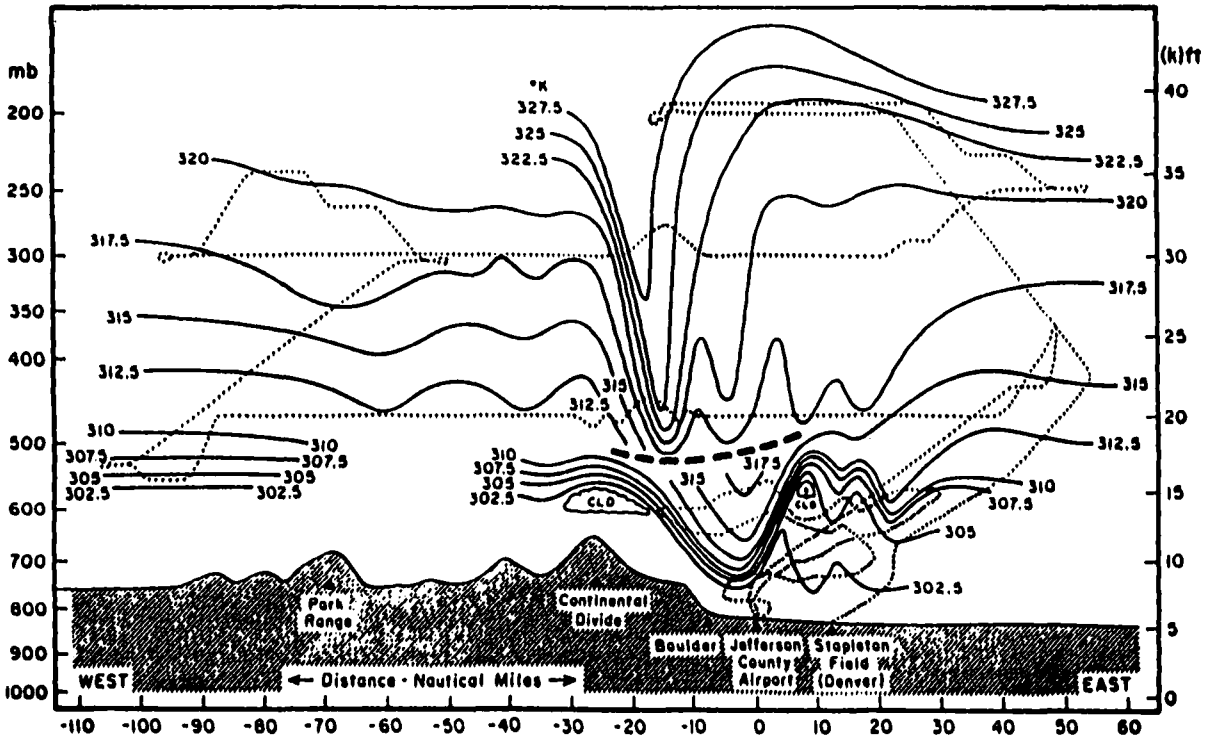

Figure 4.14. Observed potential temperature cross section from Lilly and Zipser (1972) for the January 11, 1972 Boulder Colorado windstorm.

(a)

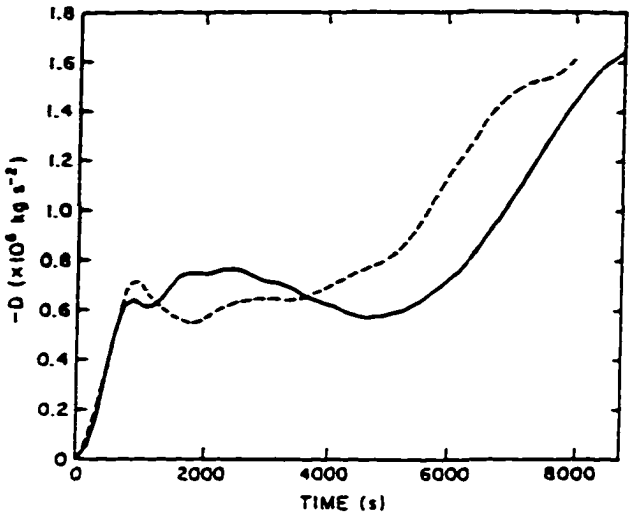

(b)

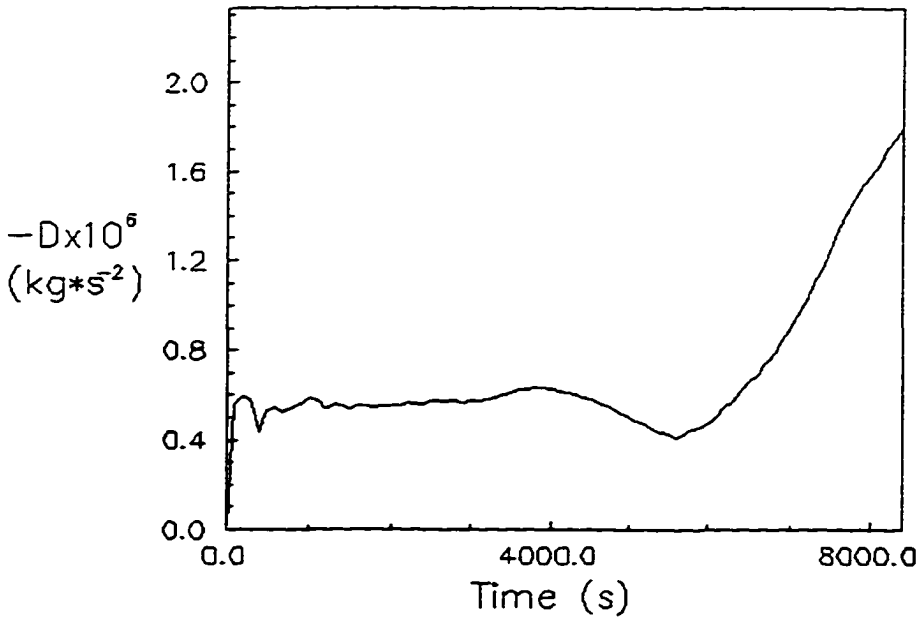

Figure 4.15. Plots of surface wave drag as a function of time for (a) Durran and Klemp (solid line) and Peltier and Clark (dashed line), and (b) for ARPI3D.

4.5.2 Sensitivity to Vertical Resolution

In order to remove any potential lateral boundary effects and investigate the above noted sensitivities, two experiments were conducted in which the mountain is located at the 200-km mark of a 430-km wide domain. The experiments are distinguished by different vertical grid resolutions: dz=150m and dz=341m. All other model options and parameters remained unchanged except for a decrease in the time step to allow the simulation to continue during the amplification period without violating the CFL time step criteria. Both simulations, using second order vertical advection, place the wave breaking and turbulent zones at the base of the stratosphere, with the coarsely resolved case (dz=341m) exhibiting a stronger wave response in this region. A comparison of the total potential temperature fields is given in Figure 4.16. The wave activity in the stratosphere above the main breaking level is more coherent in the dz=150m case than in its coarser resolved counterpart. The vertical wavelength in the stratosphere is approximately 6km and resolved by 17 grid points in the coarse resolution and by nearly 40 grid points in the fine resolution case. A surface drag comparison for the vertical resolution tests is plotted in Figure 4.17. The coarsely resolved simulation displays a similar wave amplification pattern as the original simulation (Figure 4.15b), while the dz=150m case indicates an initial delay in the amplification process by approximately 5000s. The pseudo-steady state wave drag is noticeably lower for the dz=150m case. The amplification of the stratospheric momentum flux in the coarse resolution run is reduced (delayed), suggesting that the vertical transfer of wave energy and wave dissipation is sensitive to vertical grid resolution (Figure 4.18).

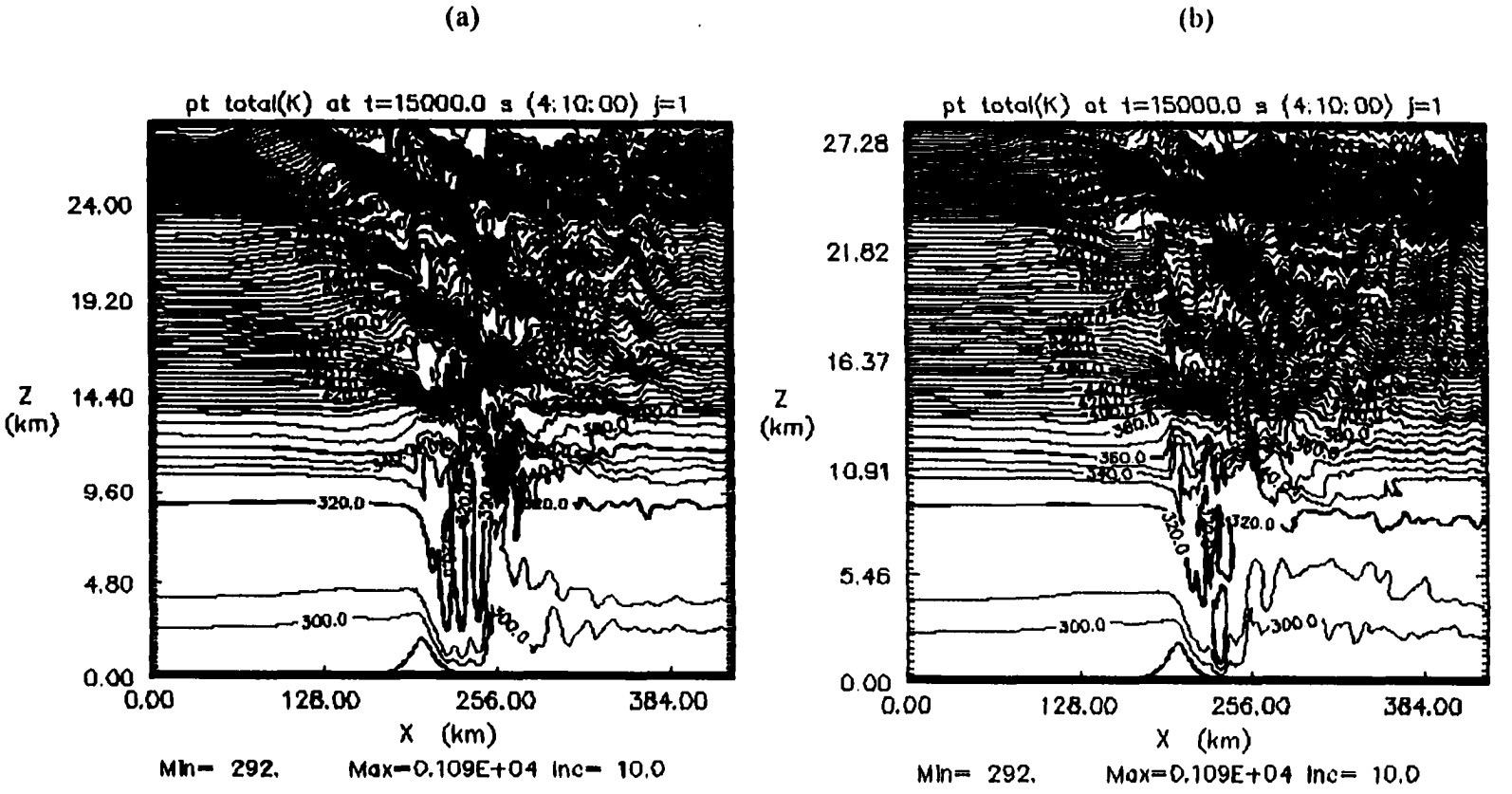

Figure 4.16. Large domain (430x28km) model simulated isentropes for the January 11, 1972 Boulder, CO windstorm at t=15,000 seconds for (a) dz=150m, and (b) dz=341m, after both cases achieved high drag states. Second order vertical advection is used in both runs. The contour interval is 10 °K and the entire model domain is plotted.

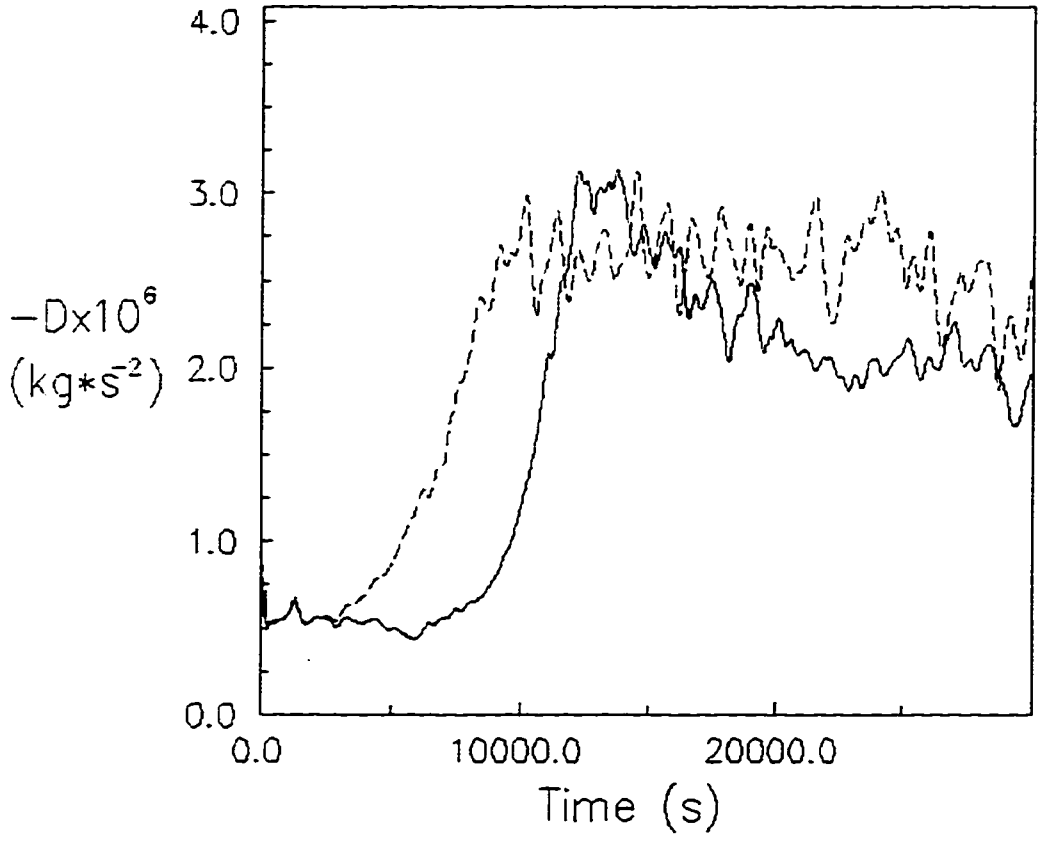

Figure 4.17. Surface wave drag for dz=150m (solid line) and dz=341m (dashed line) simulations. Note the dashed line follows the small domain results from Figure 4.15(b).

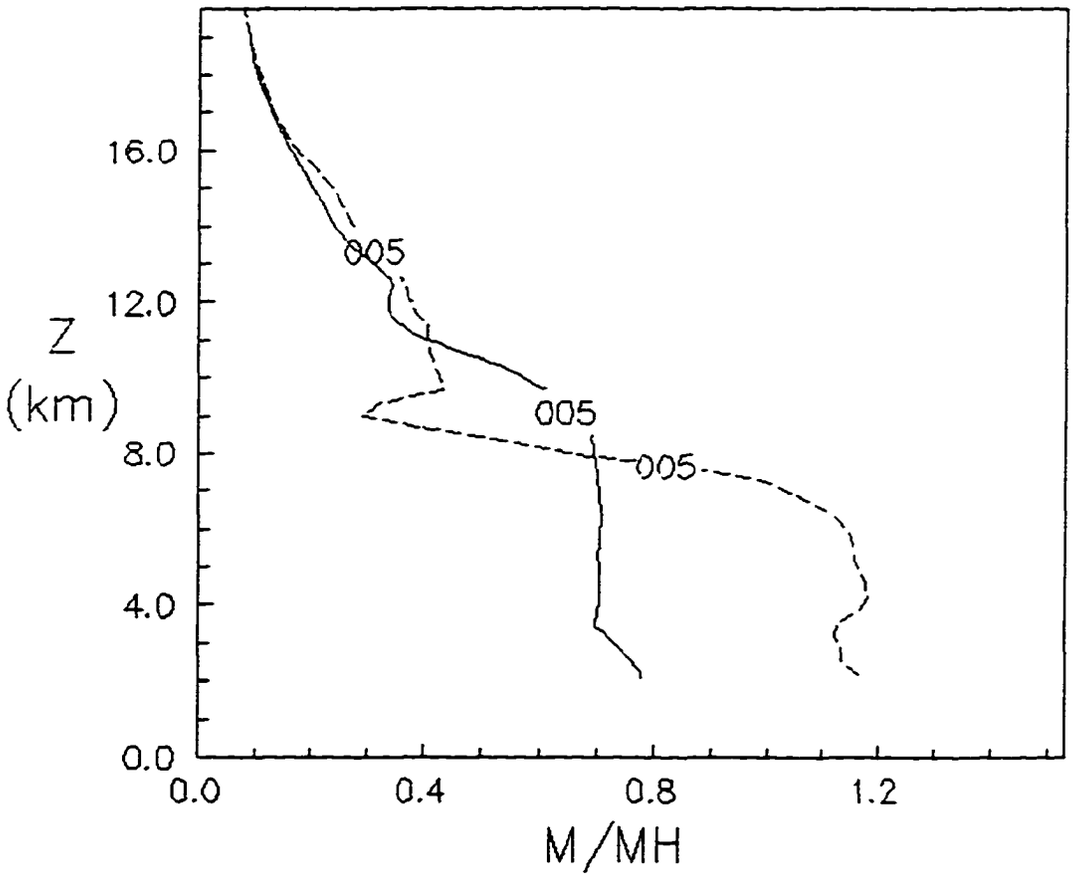

Figure 4.18. Vertical profile of the normalized vertical flux of horizontal momentum for the dz=150m case (solid line) and the dz=341m case (dashed line) at t=5000 seconds. The flux was normalized by an estimated mid-tropospheric value. Note the increased wave activity near the tropopause for the dz=150m run.

4.5.3 Lateral Boundary Influence

As alluded to in the previous section, the lateral boundaries can pose a formidable threat to mountain wave prediction. In this section, two of the five boundary conditions discussed in Chapter 3 are tested for the dz=150m case. One method of testing lateral boundary conditions is first to perform a large domain control run in which boundary influences are minimal in a desired location. Then, conduct boundary condition sensitivity experiments for a smaller upstream domain, with the boundary in close proximity to the forcing mechanism. The control run for these tests is the high-resolution large domain run of the previous section. The two experiments involve the vertically averaged phase scheme of Durran and Klemp (1983) and the environmental phase speed. The environmental gravity wave phase speed was set to $2*\overline{U}$. The choice of phase speed is somewhat arbitrary but it ensures that any gradient in the normal velocity component that reaches the boundary is passed on to the outside point. The inflow boundary (west boundary) is located 63.5km upstream of the mountain crest. This location corresponds to the 136.5km mark in the large domain control run. The simulations were advanced to t=5,000 seconds and the perturbation u fields in the first 50km of the domain are compared in Figure 4.19 to the same area of the control run. In the control run, the perturbation fields are smooth, with significant wave energy present upstream of the mountain. Note that the velocity perturbations are nearly zero at the inflow boundary in the vertically averaged Orlanski case (Figure 4.19b). The environmentally determined phase speed compares rather well to the control run

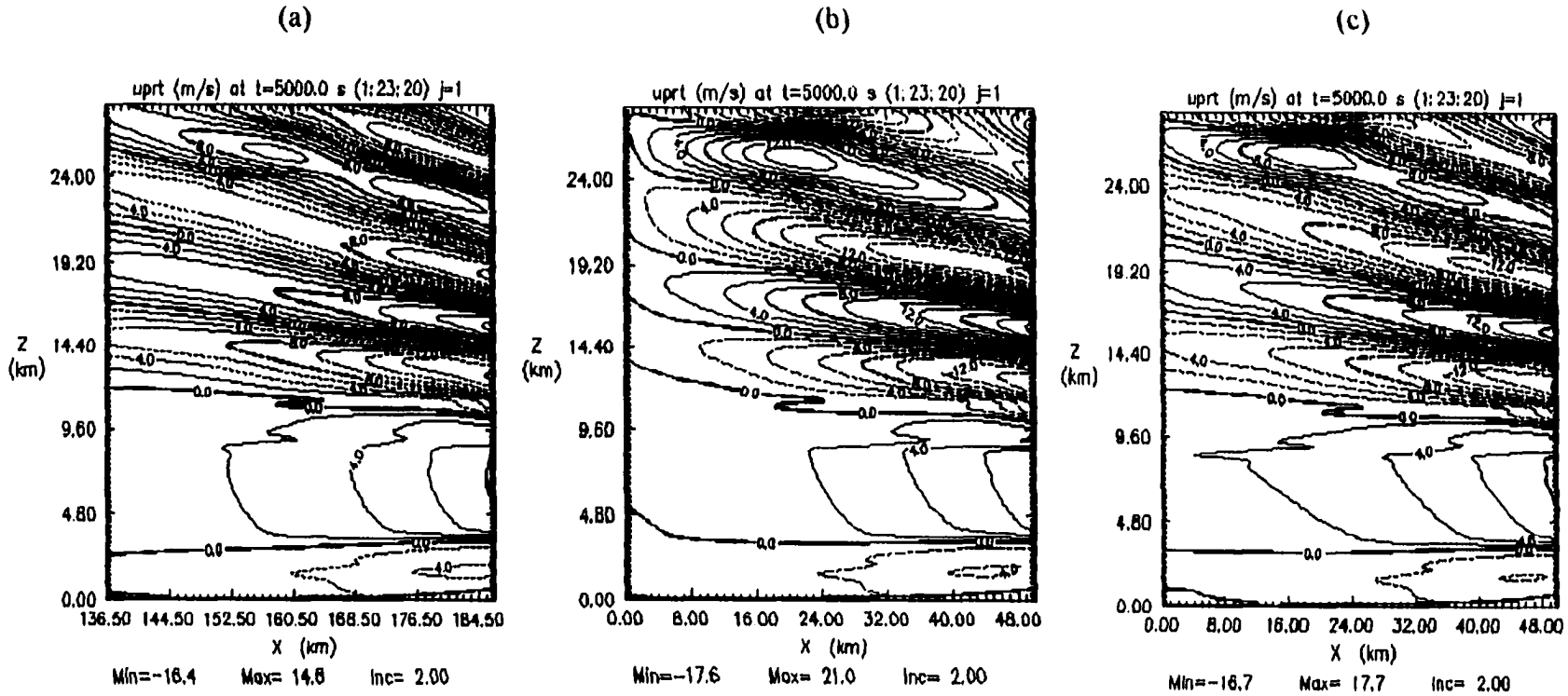

Figure 4.19. Comparison of the perturbation horizontal velocity (u') at t=5000 seconds for (a) large domain control run, (b) vertically averaged Orlanski phase speed, and (c) constant phase speed ($c'_{in} = -2\overline{U}$). The contour interval is 2.0 m/s. The domain displayed is 50x28km and represents the same area with respect to the mountain peak in the control run (a). For (b) and (c) the left edge of the plot is the inflow boundary.

perturbation u field, although there are still noticeable errors. The errors in the Orlanski case are of sufficient magnitude to hamper wave development over the mountain crest severely. In fact, the amplification stage present in the control run is delayed in the vertically averaged Orlanski run until approximately t=20,000 seconds. The reason for this is tied to the development of the flow reversal region above the mountain. The inflow boundary reduces the negative u' field in the vicinity of the tropopause to almost zero. The interior velocity field is unable to develop a wave-induced critical layer in a timely fashion. The amplification for the environmentally determined phase speed case occurs at approximately t=9000 seconds, nearly 1 hour prior to the control run. The reason for this behavior is unclear, but may be due to the smaller domain size.

The formulation of the lateral boundary condition for the normal velocity component, following Orlanski, is inherently flawed. The advection equation approach in (3.17) and (3.18) requires the quantity $(u + c)$ to be directed outward to modify the normal velocity at the outermost grid point. The computed phase speed is a function of the normal velocity field. As the solution approaches a steady state, the time tendency approaches zero, reducing the magnitude of the velocity used in the advection equation. For the vertically averaged Orlanski case, the phase speed and corresponding solutions for t<2,000 seconds at the boundary is very similar to the control run. But as the solution advances, errors in the first order determination of the quantity $(u + c)$ and spatial derivatives generate inward pointing phase velocities. The time dependent structure of the horizontal wind field at the boundary for the vertically averaged Orlanski case supports the findings of Durran et. al. (1993). Their study compares various phase

speed estimation methods, including the Orlanski method, at the lateral boundaries in a single layer shallow water system. They reported that early in the simulation the Orlanski method reproduces the true phase speed reasonably well. But as partial reflections due to numerical errors occur at the boundary, the computed phase speed deteriorates significantly and becomes a poor representation of the true phase speed.

4.6 Model Test Summary

This newly developed numerical model compares favorably with a number of steady state analytical solutions and currently existing models in similar flow regimes. In regards to the well-known Boulder windstorm of January 11, 1972, the model performs admirably when measured against current models and observations. The windstorm tests reveal sensitivities not previously reported in terms of vertical resolution and lateral boundary condition type. Results from Sections 4.5.2 and 4.5.3 suggest that tighter constraints on the vertical grid resolution and lateral boundary conditions are needed in future windstorm prediction studies. Given the strong gradients of base state variables and the frequent development of a wave breaking region, the commonly used method of dividing the vertical wavelength by the grid spacing produces less than adequate results. Improved forecasts are possible by either increasing the vertical resolution or improving the accuracy of the advection scheme.

CHAPTER 5

TWO DIMENSIONAL HEATED MOUNTAIN WAVE SIMULATIONS

This chapter investigates idealized and observed two-dimensional surface heated mountain wave flows through the use of a mesoscale numerical model. Researchers have frequently applied two-dimensional numerical models to the observed downslope wind events in Central Colorado. The success of the two-dimensional studies is largely due to the fact that the Front Range of the Rocky Mountains are oriented in the north-south direction. Their north-south wavelength is substantial and acts as a two dimensional barrier to the predominantly westerly flow.

Six two-dimensional test groups are used to evaluate the heating and cooling aspects of the diurnal cycle. They include finite amplitude narrow and wide mountain profiles, mean state critical layer tests, non-dimensional parameter (Froude number) range experiments, and the observed January 9, 1989 Boulder Colorado windstorm. Each group approaches the windstorm problem from a different perspective, ranging from analytical comparisons to the January 9, 1989 highly variable recorded event. The tests are designed to isolate the impacts of the parameterized surface heating on the numerically generated mountain wave flows. In each test group, a comparison is made between the non-heated or control run and their heated counterparts. Direct evaluations are possible since the control runs are advanced the same length in time as the heated runs. In the heated cases, an approximate steady state is attained before the diurnal

cycle is activated. One idealized cooling simulation is performed at the completion of the heating period.

As mentioned in Chapter 3, the redistribution of surface heating in this model is accomplished in one of two ways. In one method, a strong diffusion coefficient is applied to distribute the heating in the vertical. Due to its strong dependence on the turbulent kinetic energy budget and mixing length, this method is referred to as the parameterized approach. It is best suited for horizontal grid spacing equal to or greater than 1000m. The parameterized method works well for flow over long wavelength mountains. In the second technique, I attempt to explicitly resolve the convection in the developing boundary layer. The mixing length is an order of magnitude smaller than that used in the parameterized approach and allows for the development of a superadiabatic layer near the surface. A random number generator is applied to the heating term at the beginning of the diurnal cycle. These small spatial variations in the potential temperature field near the surface grow with time into efficient convection, responsible for nearly all of the heat redistribution in the boundary layer. The explicit technique requires resolution on the order of 100m in each dimension to resolve accurately the developing mixed layer eddies. This approach is better suited for short wavelength mountains that force non-hydrostatic gravity waves or lee waves. Lee waves require horizontal grid spacing of order 400m. Note that in all heated simulations, the upstream lower boundary is heated, allowing for a more realistic boundary layer evolution. Recent and relevant surface flux observations are presented in the next section.

5.1 Surface Heat Flux Measurements

The choice of a maximum heat flux for use in the numerical simulations is guided in part by a recent field study conducted in the Boreal forest of Saskatchewan and Manitoba, Canada. The Boreal Ecosystems Atmosphere Study (BOREAS) is designed to improve the understanding of energy exchanges between the boreal forest and the lower atmosphere. A description of the project can be found in Sellers et. al. (1995).

Data collection began in August 1993 and continued through 1996. The majority of the measurements were taken in contiguous periods spanning several days and included data from eddy correlation equipment on a surface tower network. Flux measurements were enhanced with observations from four instrumented aircraft. At the end of 1995, two years into the study, a detailed wintertime boundary layer study was conducted. This period represents the first in-depth study of the Boreal forest ecosystem during the winter months. Tree-top sensible heat fluxes as high as 400 W/m^2 were measured near the end of March 1996. Figure 5.1, courtesy of Black (1996), displays a plot of sensible heat flux as a function of time at a site in the Boreal forest and is typical for data collected during March 1996. These observations provide evidence that significant heating can take place in the tree canopy above the snow-covered tundra.

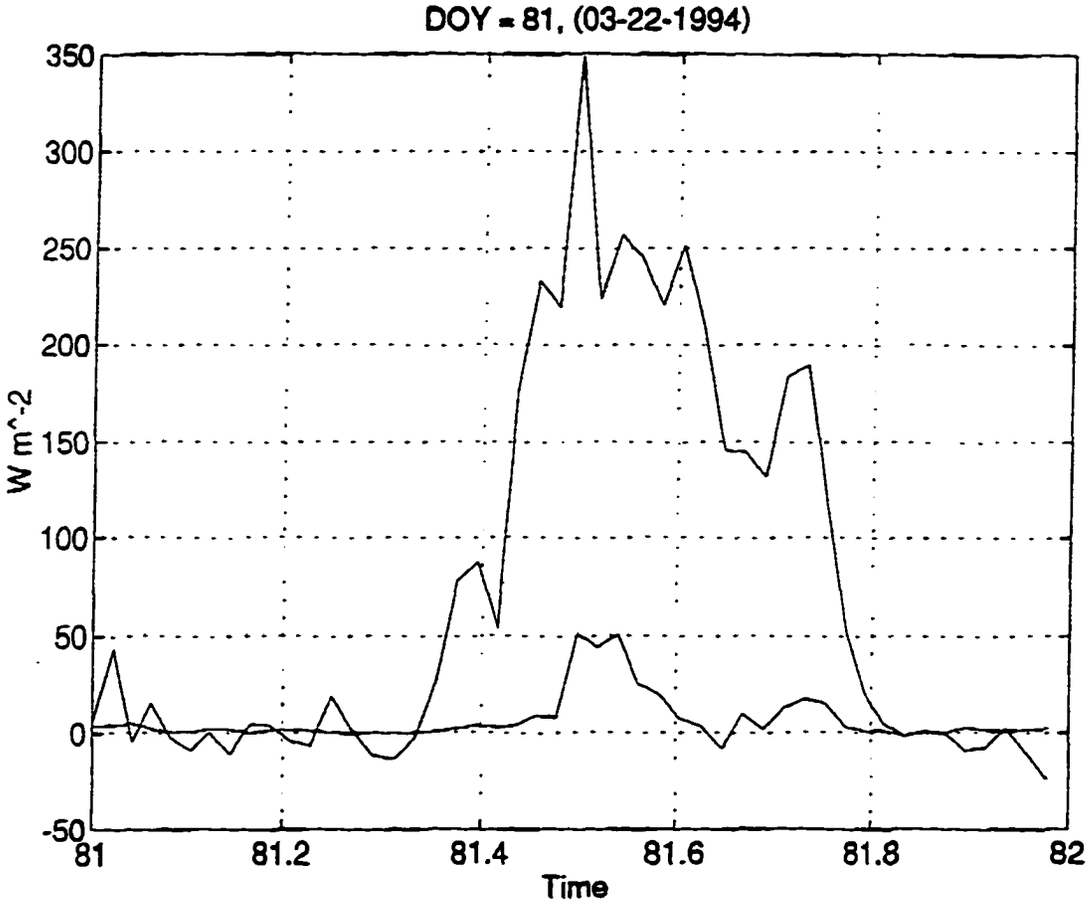

Figure 5.1. Plot of sensible heat flux (top curve) and latent heat flux (bottom curve) for the period March 22, 1996 inclusive. The data were collected at the Old Aspen Site PANP in Saskatchewan, Canada.

5.2 Idealized Finite Amplitude Mountain Wave Flow

Three tests are conducted for finite amplitude wide and narrow mountain forced flows. Referring to (4.2), the mountain quarter wavelength a is 10km and 2km for the wide and narrow mountain tests, respectively. Two narrow mountain simulations are offered to measure the sensitivity of the gravity wave response aloft to the developing boundary layer circulation. One prediction of a wide mountain flow is made and the resulting wave activity contrasted with that predicted by linear theory. The results obtained in this section will be used in all of the remaining numerical experiments.

5.2.1 Heated Narrow Mountain Tests

Two methods of heat distribution are investigated here using a narrow mountain profile. The non-hydrostatic effects can be measured by the ratio of the horizontal to vertical wavelengths, where values approaching unity indicate scale equivalence and signify substantial non-hydrostatic forcing. For this test the ratio is:

$$\frac{Na}{U} \approx 2.16 \ ,$$

where N =0.0108 s^{-1} is the static stability, a=2 km the quarter wavelength parameter, and U =20 m/s is the base state wind. The mountain profile is estimated by (4.2). The non-linear effects are measured by the gravity wave strength (Nh) normalized by the base state wind. For the narrow mountain case with h = 300m, the non-linear effects are classified as moderate with:

$$\frac{Nh}{U} \approx 0.324 \ .$$

Table 5.1 provides a summary of the model parameters used in the two-dimensional simulations presented in this Chapter. For this particular test, the model parameters are listed under the narrow mountain test group.

The approach to steady state of a mountain wave simulation can be evaluated using a time series of the computed surface wave drag. This test indicates a steady state at approximately Ut/a=60 or 12,000 seconds. Therefore, in both the parameterized and explicit heated runs the heating cycle begins at 12,000 seconds. Recalling (3.16), the diurnal heating cycle is:

$$\tau_{\theta 3}(k) = \frac{H_o}{c_p \overline{\rho}} \max(heat\ \min, \sin \omega t) \quad ,$$

with a maximum value of $100 W/m^2$ and a heating period of 12 hours. The heating cycle begins with zero amplitude and grows to a maximum at 6 hours. The sine wave time representation produces a shape similar to the observed diurnal cycle. As introduced in Chapter 1, the majority of windstorms occur during the winter months when the days are shorter than 12 hours. The length of day chosen here is arbitrary and is likely longer than would be experienced during the peak downslope windstorm period.

5.2.2 Parameterized vs. Explicit: Results and Discussion

Each simulation is advanced to t=55,000 seconds, or a non-dimensional time Ut/a = 275. The comparison includes a time series of surface wave drag, vertical profiles of vertical fluxes of horizontal momentum, and x-z cross-sections of selected

Table 5.1 Two-Dimensional Heated Mountain Wave Parameter Summary

Parameter	Narrow	Wide	7km Critical	17km Critical	2-Layer	NLP030,010,002	Boulder
nx,ny,nz	434,4,83	434,4,83	434,4,113	434,4,213	245,4,83	163/237,4,75/103	650,4,115
Δx (m)	200	1000	1000	1000	1500	2000	1000
Δy (m)	---	---	---	---	---	---	---
Δz (m)	50	100	100	100	200	100,200,250	250
t (s)	5.0	10.0	5.0	5.0	10	10,20,20	5.0
τ (s)	0.5	2.0	2.5	2.5	2.5	2.5,2.5,4.0	2.5
$\overline{U}$ (m/s)	10	20	20	20	20	10	Sounding+
$NH/\overline{U}$	0.324	0.293	0.31,0.39,0.47	0.10,0.31,0.52	0.6,0.3	3.0,1.0,0.2	---
N (1/s)	0.0108	0.01956	0.01047	0.01047	0.02,0.01	0.03,0.01,0.002	Sounding+
$\overline{T}$ (°K)	---	250	---	---	---	---	---
h (m)	300	300	600,750,900	200,600,1000	600	1000	Profile*
a (m)	2000	10000	10000	10000	10000	15000	Profile*
H_o (W/m^2)	100	100	200,-40	200	300	360,300,60	200
ω (hrs)	24	24	24	24	27.7	72,27.7,16.6	24
$C_h/\Delta x^4$	0.00001	0.00001	0.0005	0.0005	0.0005	0.0005	0.0004
$C_v/\Delta z^4$	0.0	0.0	0.0001	0.0001	0.0005	0.0005	0.00001
υ	0.2	0.2	0.2	0.2	0.2	0.2	0.2

*Terrain profile is created from the ARPS terrain pre-processor. ** Sounding data is listed in Appendix E.

perturbation fields. Figure 5.2 limns a comparison of the normalized vertical profiles of momentum flux at $Ut/a = 75$, 150, and 225 for the parameterized run (solid line) and the explicit run (dashed line). The curves are normalized by the two-dimensional linear hydrostatic values. For the parameterized experiment, the profiles are relatively smooth, with nearly vertical orientation and exhibit decreasing wave activity with increasing time and mixed layer depth. Overall, the mountain flux profiles for the explicit case compares favorably with the parameterized pattern. At $Ut/a = 75$ and 150, the profiles are nearly identical. At $Ut/a = 225$, the explicit case generates flux near the top of the mixed layer (approximately 1.0 km) that is 35% greater than its parameterized counterpart. This is likely due to the inclusion of the convective elements in the flux computation. But as the distance above the inversion increases the difference between the explicit and parameterized experiments is reduced to less than 10% at the height of 2/3 vertical wavelength (approximately 4 km). Plots of the perturbation horizontal velocity in Figure 5.3 and potential temperature in Figure 5.4 contrast the results between the two classes of heat redistribution. Figure 5.3 presents the horizontal velocity perturbation at $Ut/a = 225$ near the mountain peak. The location of the maximum surface wind moves upslope and approaches the mountaintop as the mixed layer deepens. In the potential flow limit, the maximum wind is located at the mountain peak upstream of the maximum associated with a mountain wave. Figure 5.4 contrasts the simulated isentropes of each test for the entire model domain. As evident in Figure 5.3, both simulations predict a nearly identical upstream boundary layer height, to within 50 meters (see the 294 ° K isentrope). The disturbances in the

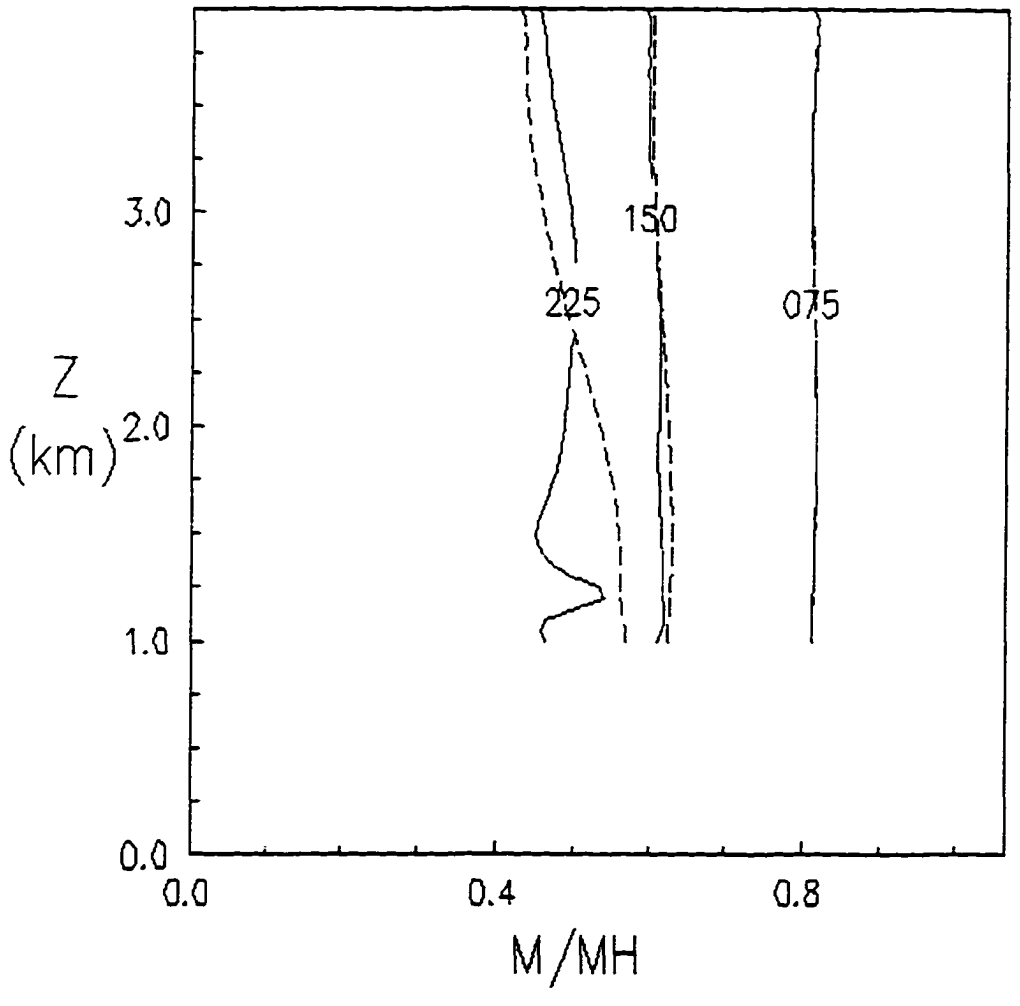

Figure 5.2. Vertical profile of the vertical flux of horizontal momentum for heated narrow mountain flow for the parameterized case (solid lines) and explicit method (dashed lines) at non-dimensional times of Ut/a = 75, 150, and 225.

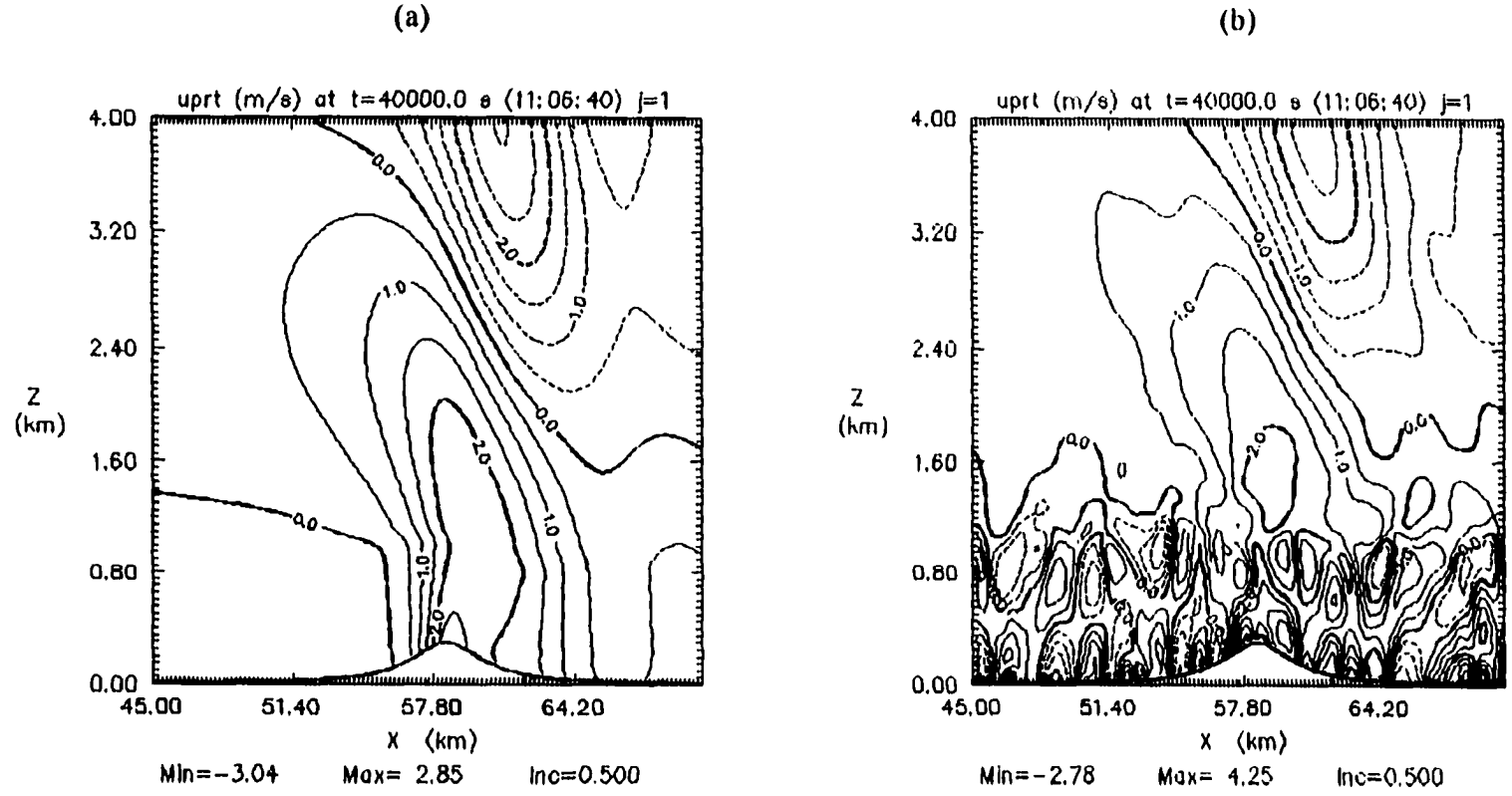

Figure 5.3. Perturbation horizontal velocity for a finite amplitude heated short wavelength mountain flow for (a) the parameterized case and (b) the explicit simulation at $Ut/a = 225$ (40,000 seconds). Area depicted is in the vicinity of the mountain peak extending to the model top. The contour interval is 0.5 m/s.

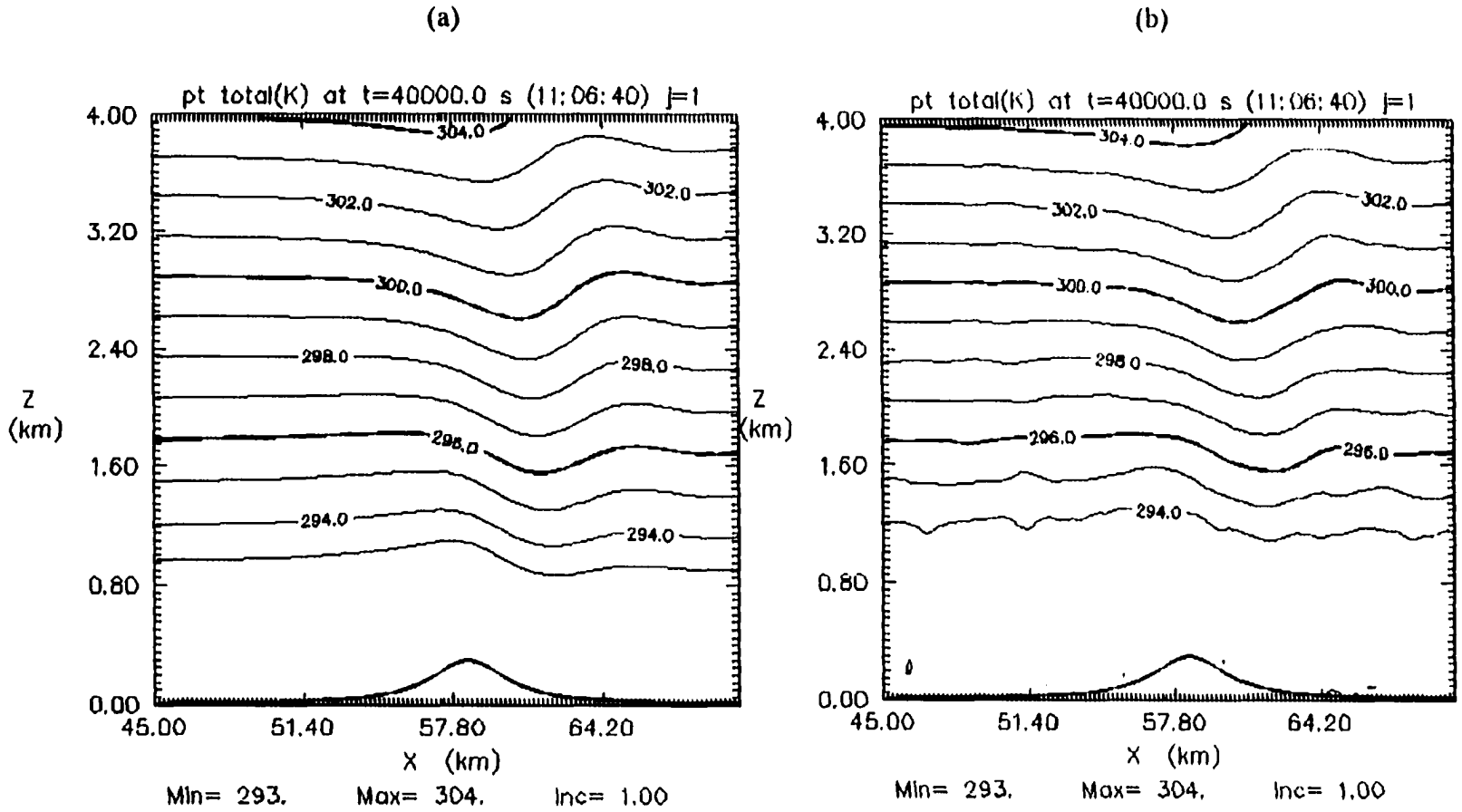

Figure 5.4. Isentropes for a finite amplitude heated narrow mountain flow for (a) parameterized and (b) explicit runs at $Ut/a = 225$ (40,000 seconds). The area shown follows that of Figure 5.3. The contour interval is 1.0° K.

potential temperature field near the top of the mixed layer in the explicit case exhibit a dominant wavelength on the order of 5 km or less. In these experiments, the perturbations at the top of the mixed layer become lee wave sources. The minimum vertical wavelength that could propagate vertically ($2\pi N/U$) in this example is nearly 6 km. Thus, gravity waves with horizontal wavelengths less than 6km are classified as evanescent waves and do not propagate vertically. The majority of the disturbances measure less than 6 km in length and do not contribute significantly to the momentum flux at higher elevations.

The ratio of the horizontal wavelength of the convection to the depth of the mixed layer in Figure 5.3 (b) is approximately 4:5 to 1. The grid spacing is 200 x 50 meters corresponding to approximately 20 grid points per convective cell in each spatial direction. Note that the gravity wave activity aloft is clearly visible in both cases although slightly modified in the explicit experiment. Inspecting the predicted turbulent kinetic energy field e best illuminates individual convective plumes in the explicit mixed layer. Figure 5.5 illustrates the total e cross-section at $Ut/a = 225$ for each test. The structures of the e field in these plots are markedly different. The convective plumes in (b) extend to nearly 1.3 km above the surface. This is due primarily to the method in which the mixing length l is computed and the randomness of the initial temperature perturbation. The vertically oriented e fields in (b) correspond to resolved updrafts in the simulated two-dimensional dry convection. In these tests the primary source of e is the buoyant production (see page 56):

$$B = \frac{g}{\bar{\theta}}(1+\frac{l}{\Delta})\nu_t \frac{\partial \theta}{\partial z} \quad .$$

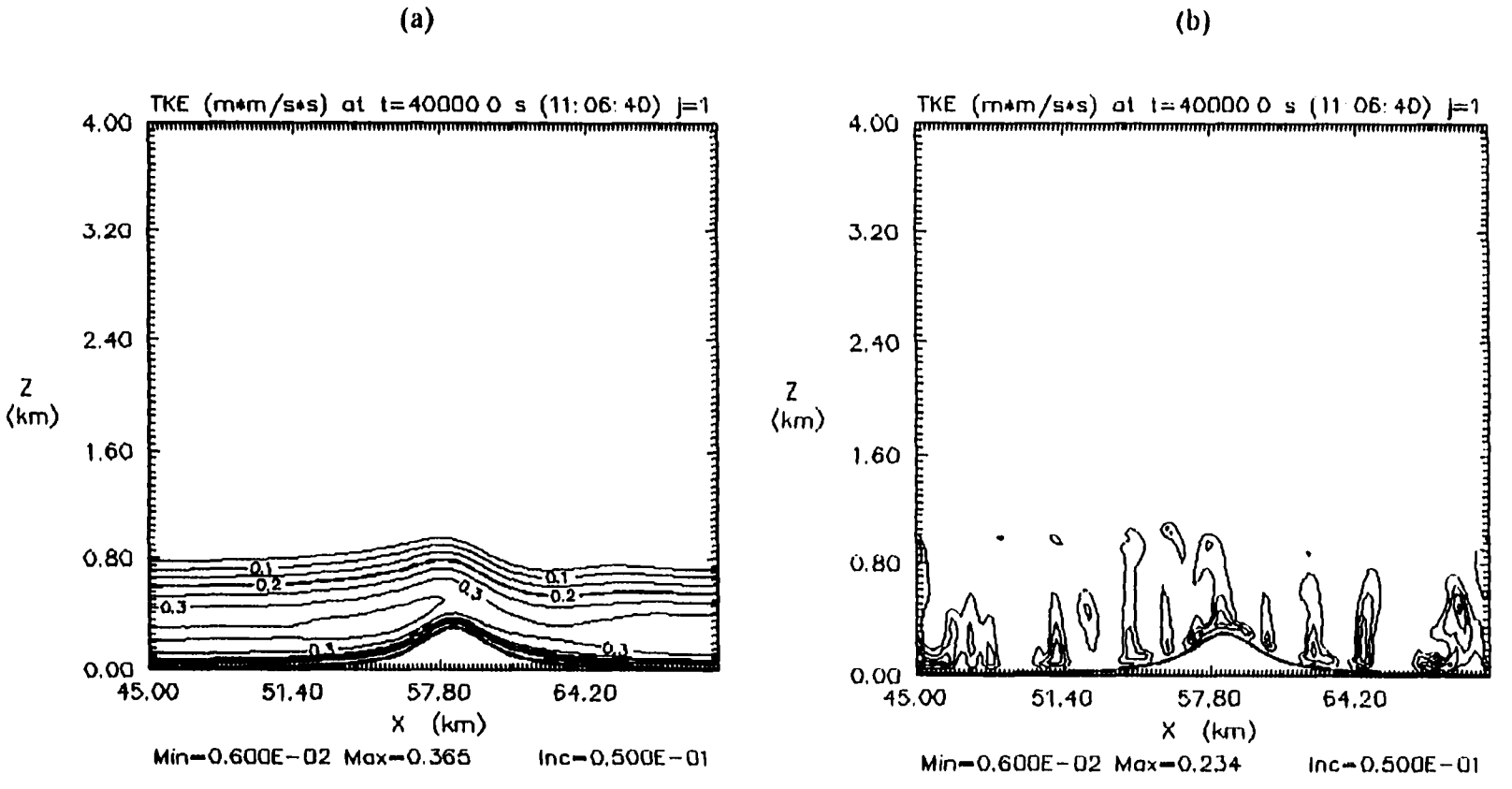

Figure 5.5. Model predicted turbulent kinetic energy for a finite amplitude heated narrow mountain flow for the (a) parameterized and (b) explicit tests at $Ut/a = 225$ (40,000 seconds). Area depicted follows that in Figure 5.4. The contour interval is $0.05 m^2/s^2$.

The mixing length in the parameterized method can be an order of magnitude larger than the explicit case. As a result, resolved convection can be produced in the parameterized case but the depth and magnitude will be hampered since the vertical mixing will reduce any developing vertical potential temperature gradients.

As portrayed in the explicit and parameterized simulations, the convective motions modify the surface winds significantly but the flow aloft remains largely unchanged. The kinetic energy from this moderately non-linear case is comparable to that found in boundary layer convective motions. Yet, both tests reveal a nearly 50% reduction in wave energy aloft at the conclusion of the diurnal heating cycle. The majority of wave degradation stems from the results of convection and not the convection itself. From a mountain wave perspective, the differences in the parameterized and explicit experiments are small. This result favors the use of the computationally efficient parameterized approach for the redistribution of heat in the convective boundary layer. Choosing the parameterized technique allows the simulation of large two and three-dimensional downslope windstorms with today's computer resources. In support of the coarser grid spacing selection, Clark et. al. (1994) show that horizontal grid spacings on the order of 500-1000 meters are sufficient for resolving the hydrostatic modes and the majority of the shorter wavelength lee waves.

5.2.3 Heated Wide Mountain Flow Test

The impacts of a parameterized diurnal cycle on a longer wavelength mountain profile of moderate height are presented here. The mountain quarter wavelength is five times that given in Section 5.2.1 and therefore forces mainly hydrostatic gravity wave

modes. The stability and base state wind are nearly twice those of the previous case. The resulting hydrostatic measure is:

$$\frac{Na}{U} \approx 9.7 \quad ,$$

where $N = 0.0195$ (isothermal), $a = 10$ km, and $U = 20$m/s. For $h = 300$ m, the non-linear measure or inverse Froude number is:

$$\frac{Nh}{U} \approx 0.293 \quad ,$$

approximately the same as given in the narrow mountain simulations. A summary of the model parameters used in this test is provided in Table 5.1 under the wide mountain test group. A steady state solution for the wide mountain case is obtained at $Ut/a = 60$ or $t = 30{,}000$ seconds, after which the diurnal heating is activated via the parameterized method, and the simulation advanced to 80,000 seconds ($Ut/a = 160$). The horizontal velocity (Figure 5.6) and potential temperature (Figure 5.7) are well mixed in the neutral layer and the maximum and minimum perturbations aloft are approximately 5-10% lower than the steady state values.

Both the narrow and wide heated mountain wave simulations exhibit reduced surface wave drag as the heating cycle increases the depth of the mixed layer (Figure 5.8). The largest deviations in the momentum flux from the wide mountain control run steady state values are observed at the end of the experiment, in conjunction with the maximum depth of the mixed layer (Figure 5.9). The decrease in momentum flux for the parameterized run is approximately 18%, nearly one third of the reduction

experienced by the heated narrow mountain test (49%). Most of the discrepancy can be explained by the fact that for the narrow mountain run, the static stability is approximately one-half that used in the wide mountain simulation. This point is illustrated in Figure 5.10. The resulting mixed layer depth for the wide mountain case is about half that of the narrow ridge simulation. As illustrated in Chapter 2, the reduction of wave activity in the stable layer aloft is a function of the mixed layer depth (H). Referring to Figure 2.2, linear theory predicts for a horizontal wavelength of 80 km (the main contributor of the a = 10 km mountain shape) and mixed layer depth of 0.6 km, a reduction of integrated wave activity ($u'w'$) on the order of 16%. The corresponding linear theory estimate for reduction in wave activity for the narrow ridge is 43%. Linear theory captures nearly all the simulated reductions in wave activity associated with heated mountain wave flows of this variety. These results lend support for linear theory in estimating the wave behavior for moderately non-linear mountain flows under the influence of surface heating.

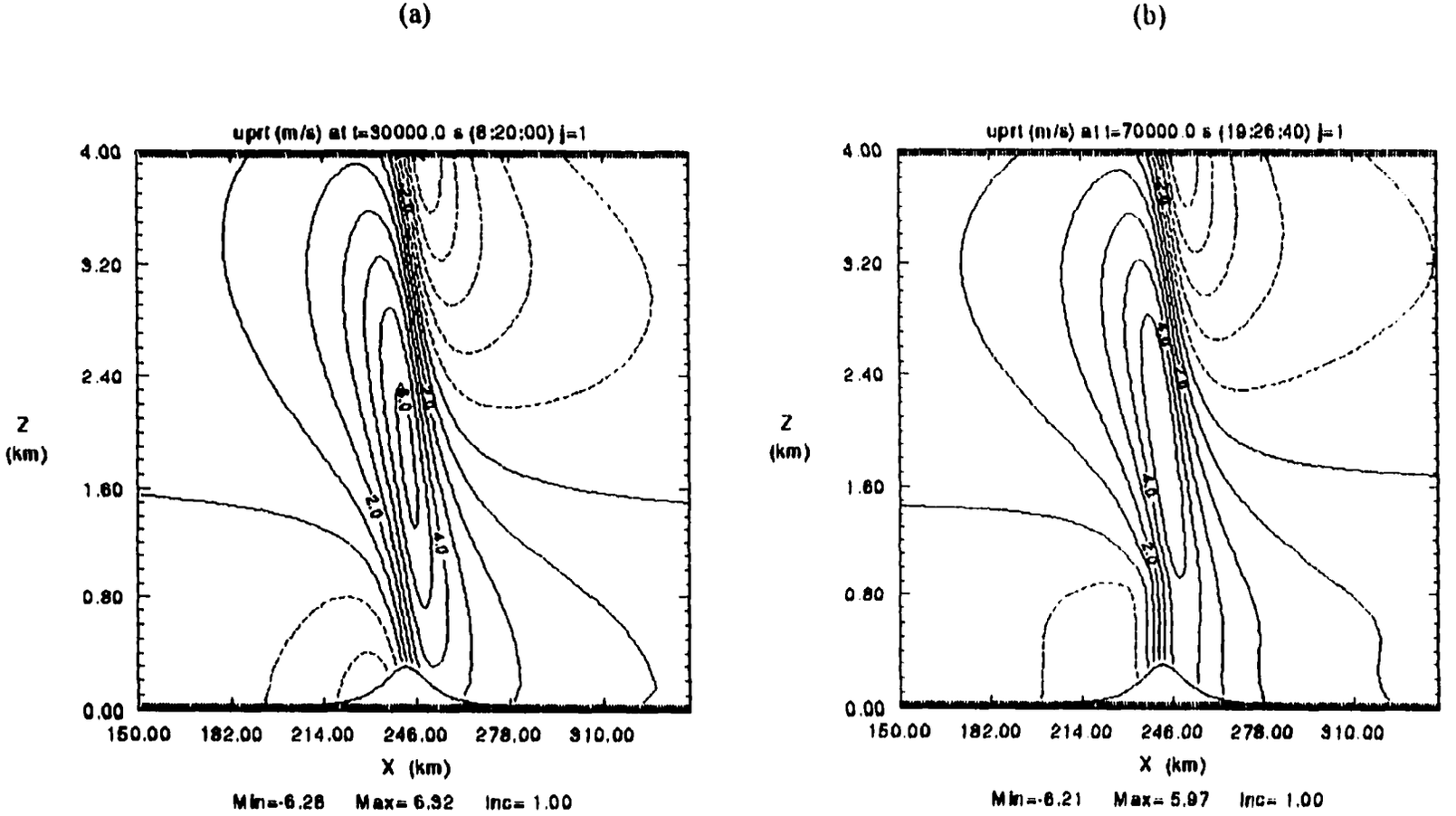

Figure 5.6. Perturbation horizontal velocity for a finite amplitude heated wide mountain flow at (a) t=30,000 and (b) t=70,000 seconds. Area depicted is in the vicinity of the mountain peak upward to the model top. The contour interval is 1.0 m/s.

(a)

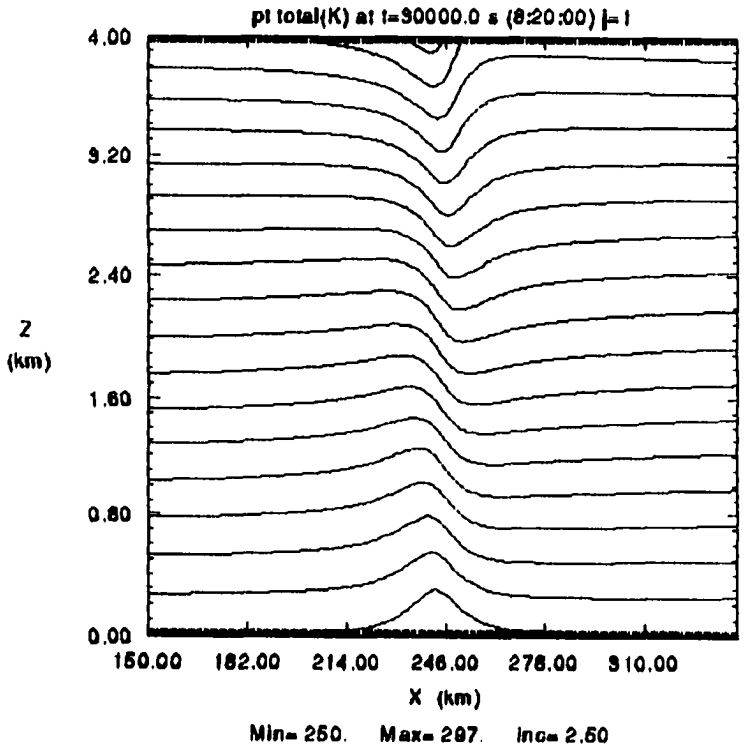

(b)

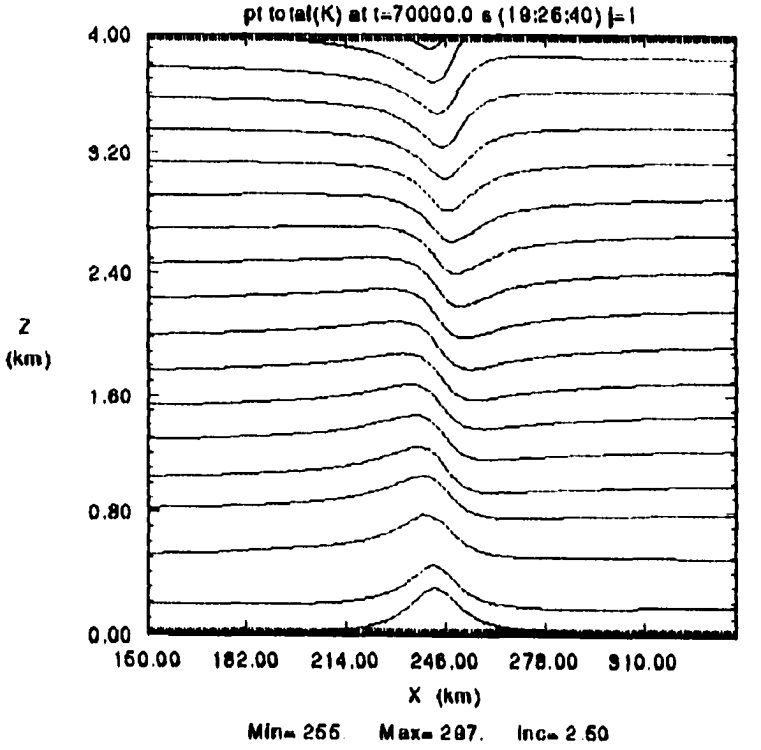

Figure 5.7. Model generated isentropes for a finite amplitude heated wide mountain flow for (a) t=30,000 and (b) t=70,000 seconds. Area depicted follows that of Figure 5.6. The contour interval is 2.5 ° K.

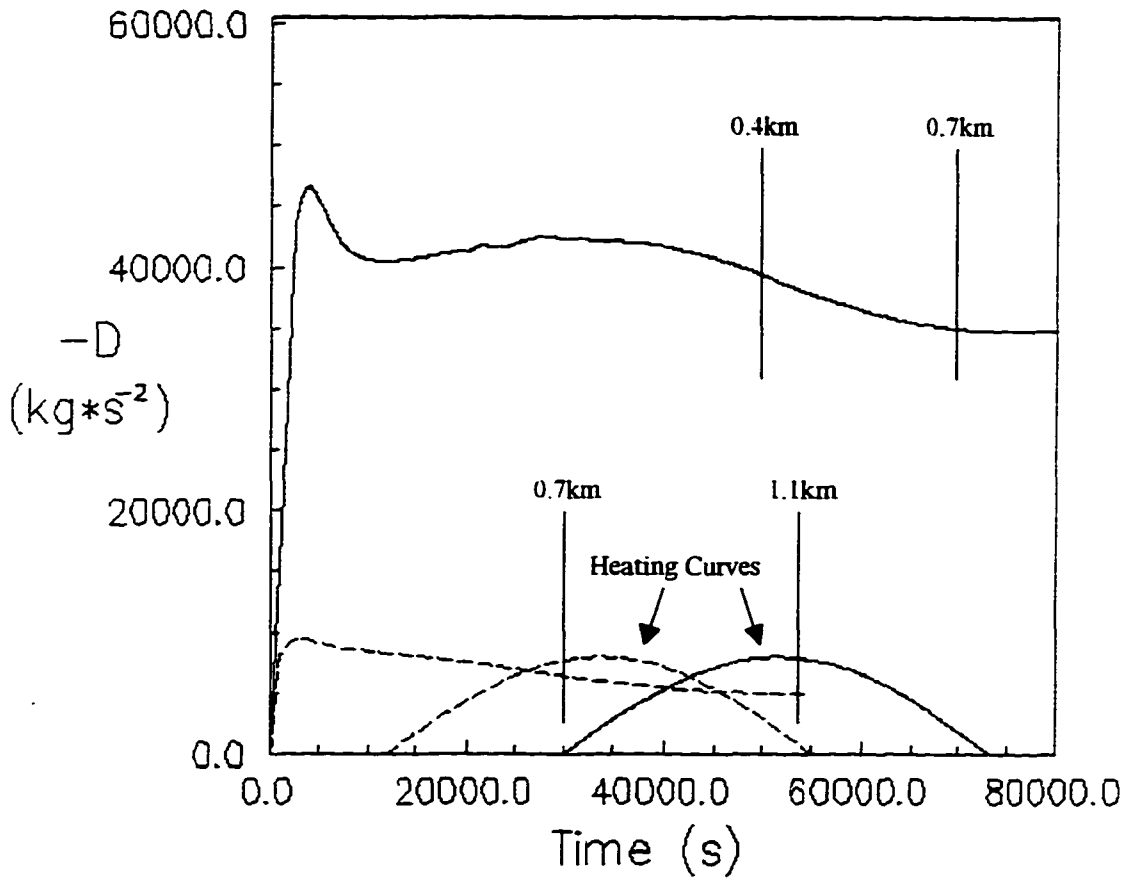

Figure 5.8. Plot of surface wave drag as a function of time for the parameterized heated wide (solid) and narrow (dashed) ridge flow tests. Heating curves are provided at the bottom of the plot for the wide (solid) and narrow (dashed) mountain tests. The maximum heating rate for both tests is $100\,w/m^2$. The vertical lines represent the approximate mixed layer depth.

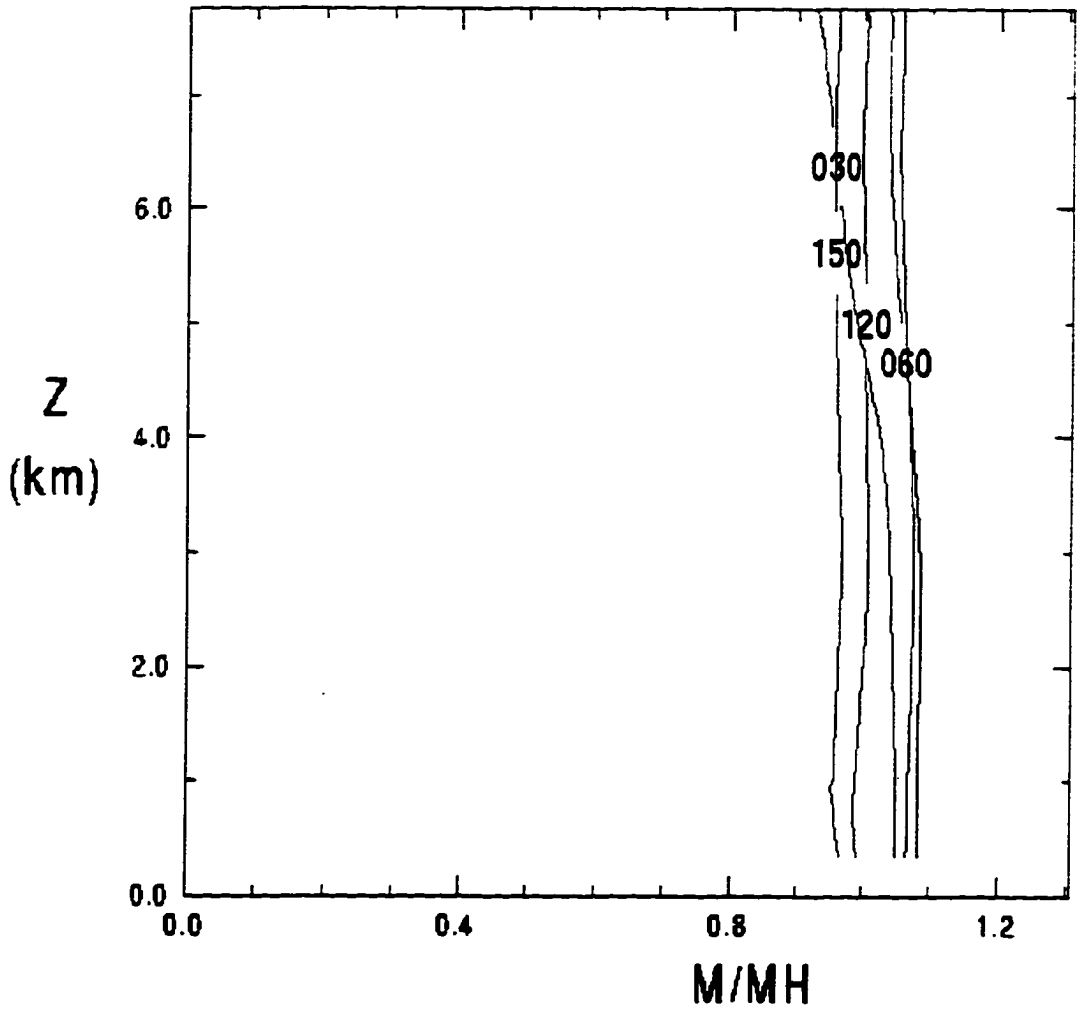

Figure 5.9. Vertical profile of the vertical flux of horizontal momentum at $Ut/a = 60$, 80, 100, 120, and 140 for the heated wide ridge flow test. Profiles are normalized by the linear hydrostatic Boussinesq value. One vertical wavelength is approximately 6.4 km.

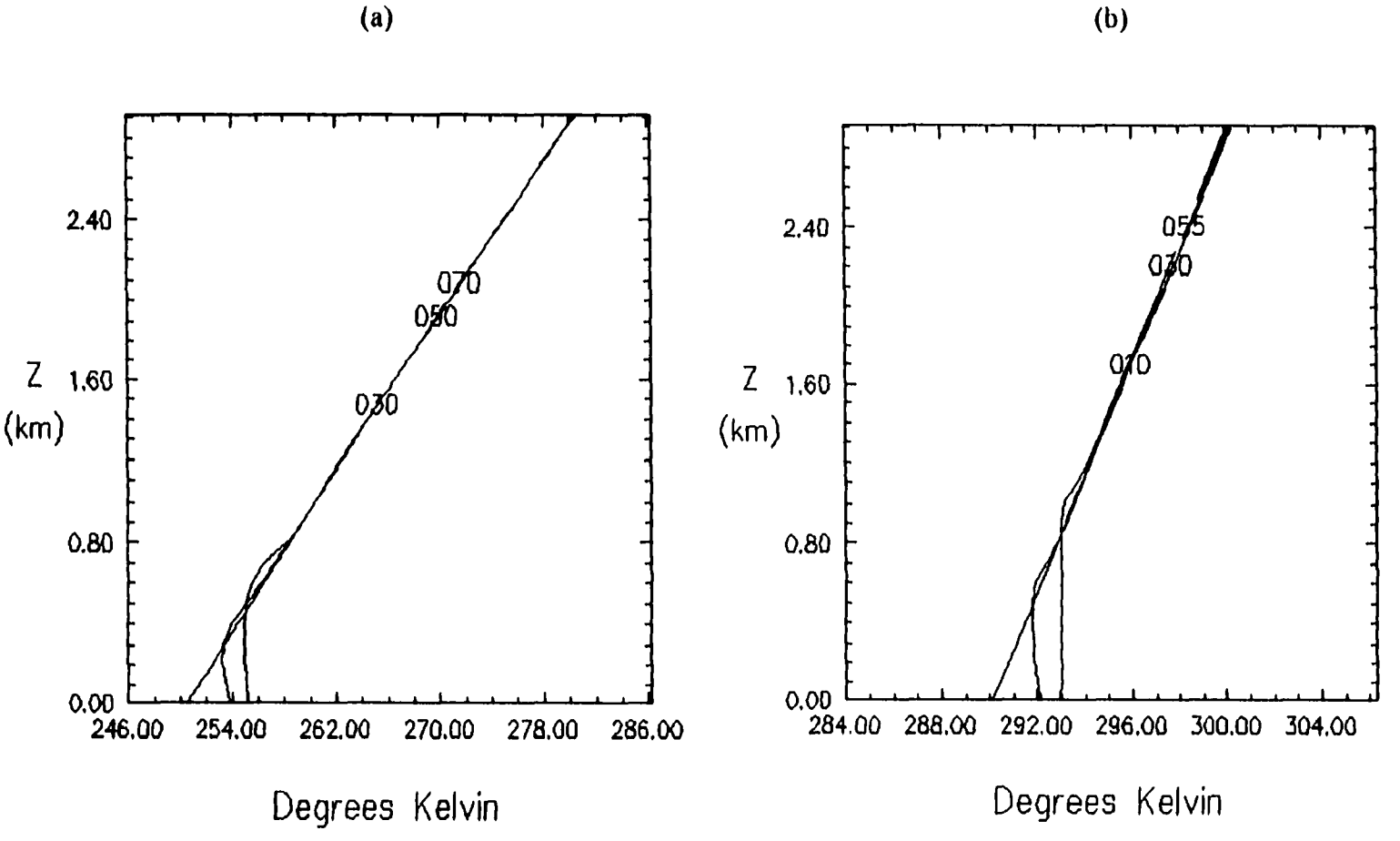

Figure 5.10. Vertical profiles of potential temperature upstream of the mountain at the beginning, middle and end of the heating cycle for (a) wide and (b) narrow ridge parameterized tests. Line labels are in kilo-seconds.

5.3 Mean State Critical Layer Experiments

Downslope windstorms frequently display elevated regions of flow reversals and enhanced turbulence with weak or neutral stability. These regions are commonly referred to as critical layers. Current numerical models are quite capable of producing such features as evident in the January 11, 1972 Boulder windstorm simulation illustrated in Chapter 4. A critical layer exists when the phase velocity of the wave equals that of the transport medium. For the case of airflow over mountains, as alluded to earlier, this occurs when the cross-mountain wind speed is reduced to zero. These experiments are designed to classify the sensitivity of mountain wave flow to surface heating in the presence of varying mean-state critical layer heights. One experiment is extended to include the response due to a parameterized nocturnal cooling period. Simulations with a mean state critical layer are similar to those found in downslope windstorms: they both involve a critical layer, above which reduced wave activity is observed.

Studies of mean state critical layers in mountain wave simulations are presented by Durran (1986) and Durran and Klemp (1987). Durran investigates the amplification mechanisms of strong downslope windstorms. He compared numerical predictions of flow over a mountain with varying critical layer heights to the linear amplification model of Peltier and Clark (1979, 1983), to Smith's (1985) hydrostatic non-linear analytical theory, and to the hydraulic analog. He found, for a Boussinesq atmosphere, the numerically predicted low and high drag states followed Smith's non-linear theory and to a lesser, yet significant, degree the hydraulic analog. He concluded that the

height of the wave-breaking region is sensitive to subtleties in the flow, including upstream inversion heights and that the prediction of the onset and placement of the wave-overturning layer can only be addressed through the use of numerical models. Two of Durran's critical layer test groups are investigated here. The two groups are defined by the height of the mean state critical layer, 7 km and 17 km. Following Durran's work has at least two benefits. The first is the evaluation of the model in another non-linear environment by comparing the numerical solutions with Smith's predictions and Durran's numerical results. The second allows for a direct assessment of the mature windstorm's sensitivity to changes in the low-level stability given a simplified mountain shape and base state wind profile.

Motivated by the results of Chapter 4, the resolution in the present study is enhanced over what Durran used. Grid spacings were dx =1000 m and dz =100 m as compared to Durran's dx =1500 m and dz =333 m. The Boussinesq option was invoked in the model for all of the critical layer tests. The details of the Boussinesq modification are summarized in the finite amplitude test description in Chapter 4.

5.3.1 7 km Mean State Critical Layer Results

The experimental set-up follows Durran (1986). The base state wind is reduced in a shear layer from 20m/s at 5 km to zero at 7 km. From 7 km to the top of the model domain (11 km) the base state wind is set to zero. All simulations are performed without surface friction parameterization. Table 5.1 presents a listing of the pertinent model parameters under the 7 km Critical test category. This experimental group is composed of three separate simulations in which only the mountain height

varies. The mountain heights used in these tests are 600m, 750m, and 900m, which corresponds to a non-linear factor or inverse Froude number Nh/U = 0.314, 0.392, and 0.471, respectively. These tests are similar to those given in the second line of Durran's Table 1. The mountain profiles are defined by the "Witch of Agnesi" profile in (4.2). The mountain quarter wavelength is a = 10 km. The heating cycle for each test began at t = 35,000 seconds (Ut/a = 70) and the prediction advanced to t = 80,000 seconds or a non-dimensional time of Ut/a = 160. The h = 750 m case is extended to Ut/a = 240 using an estimated minimum surface cooling rate of -40 W/m^2. The time dependant cooling function is given in Section 3.3. The present model's control runs reproduced the results of Durran's Table 1 reasonably well, although the computed surface wave drags are lower. Figure 5.11 compares the normalized surface wave drag detemined from the present model with those from Durran (1986). Figure 5.12 displays the computed surface drag time series for all the 7 km critical layer tests. Both the h=750 m and h=900 m tests achieve high drag states approximately 3.5 times that predicted by linear hydrostatic theory, while the h=600 test produces significantly sub-linear theory surface wave drag. These results agree with those illuminated by Smith's theory. The surface wave drag, measured at the end of the heating period, for the heated h=900 m and h=750 m simulations were reduced by 28% and 22%, respectively. In both cases, the mixed layer achieved a depth of approximately 2.0 km. During the h=750 m cooling period (between 80,000 and 120,000 seconds) the surface drag increases but remains considerably lower than the control run. An experiment initialized with a neutral surface layer depth equal to the maximum mixed layer depth obtained for the h = 750 m heated case was performed with the results presented in Figure 5.12 for

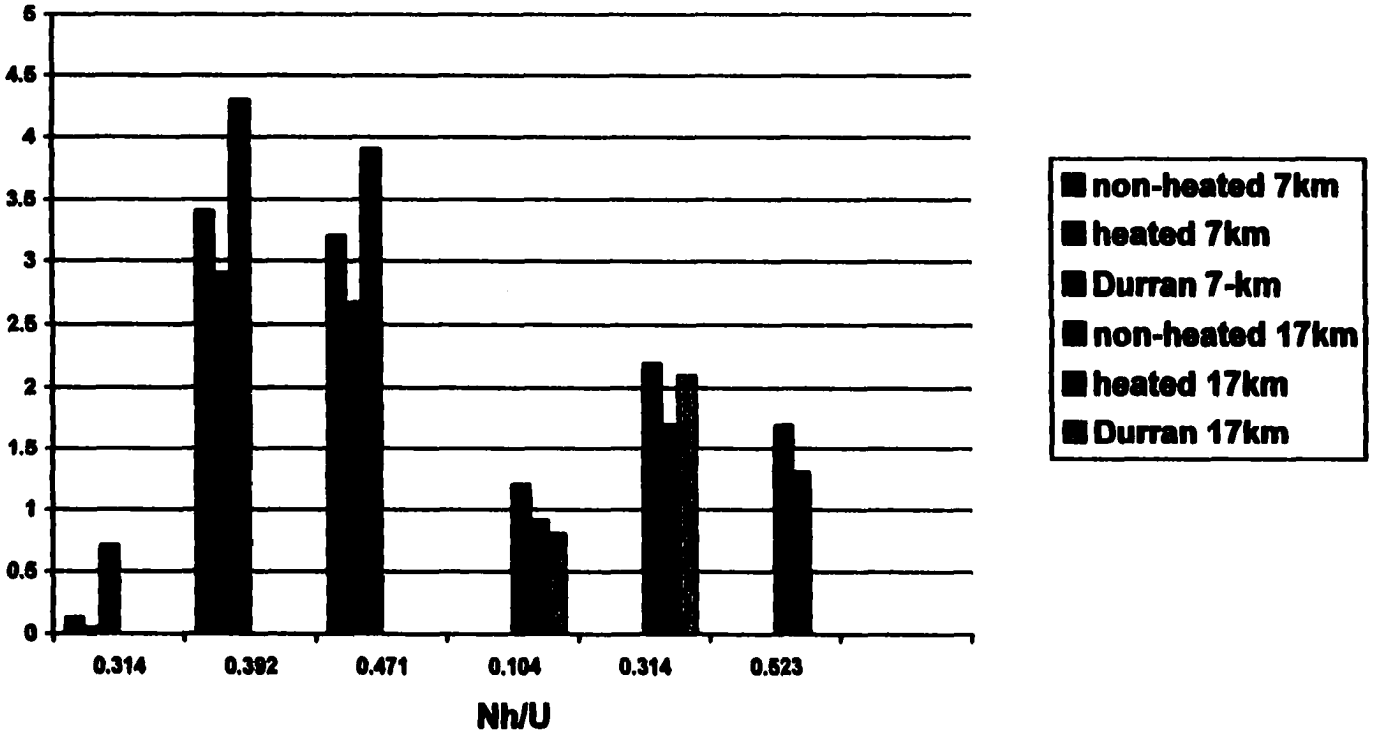

Figure 5.11. Normalized surface wave drag as a function of mountain height and critical layer height. Results from Durran's (1986) results are indicated by the far right bar in all but the far right group. The far left bar in each group represents the non-heated present model results and the center bar depicts the heated results.

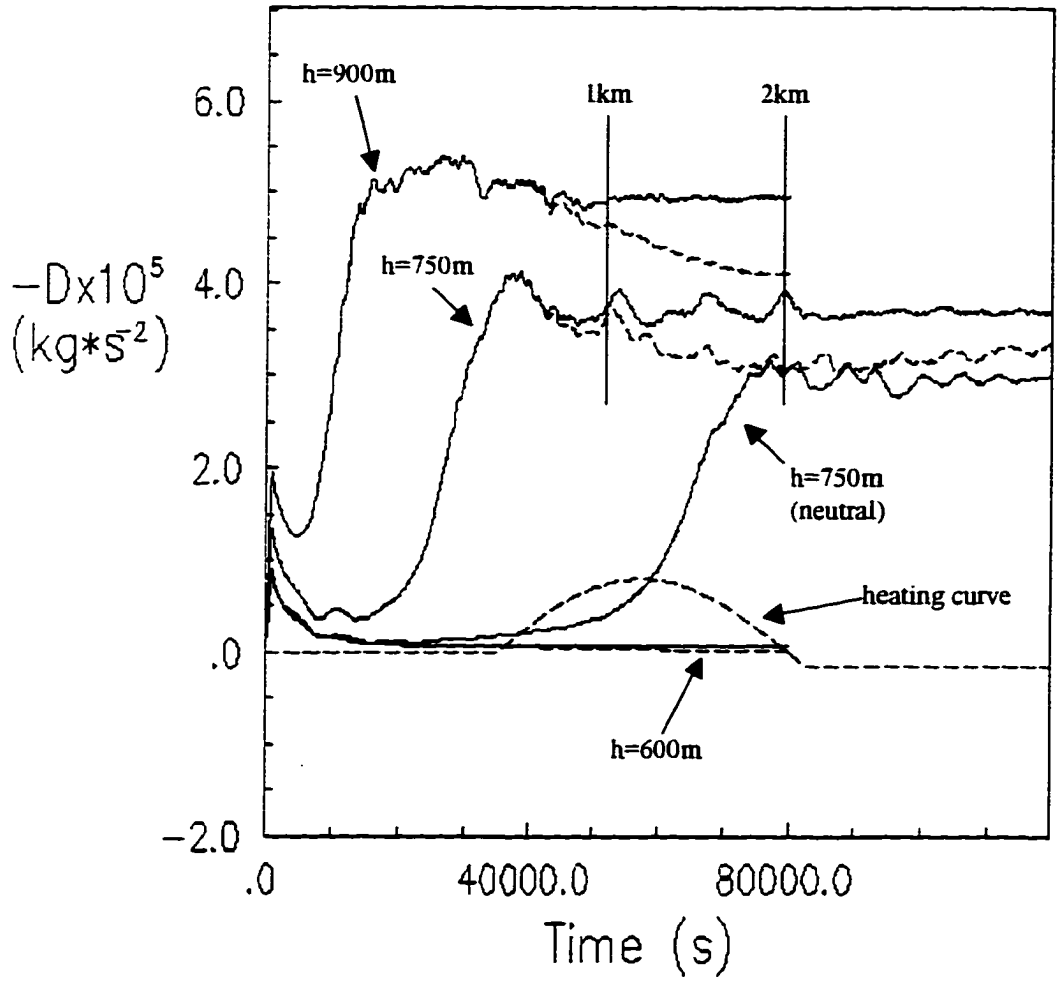

Figure 5.12. Time series plot of computed surface wave drag for all tests with a mean state critical layer at 7 km. The solid lines represent the control runs and the dashed lines the heated simulations. The heating curve is provided at the bottom of the plot with a maximum heating rate of $200\,w/m^2$ and a minimum rate of $-40\,w/m^2$. The vertical lines represent the approximate mixed layer depth.

comparison. No heat is applied and the simulation is advanced to $t = 80{,}000$ seconds. The graph shows that for nearly 14 hours the wave drag remains nearly an order of magnitude lower than the control and heated runs. At $t = 80{,}000$ seconds the heated and neutral layer simulations exhibit nearly identical surface wave drags and peak surface winds. Two different paths are used to achieve the same result. Since the growth rate was small, a low drag state could have been mistakenly estimated prior to $t = 40{,}000$ seconds. In this test, no gravity waves are present in the neutral surface layer. The distance from the top of the neutral layer to the base of the critical layer is 5 km, of which 2 km involves a linear decrease in the base state wind. The vertical wave number increases and the vertical wavelength decreases in the shear layer. Reports by Blumen (1965) and Klemp and Lilly (1975) present a case for linear resonance. The $h = 600$ m heated simulation exhibits a low steady state drag and undergoes a near 50% reduction at the completion of the diurnal heating cycle.

Figure 5.13 displays the normalized surface wave drag curve for the analytical two layer 80 km wavelength solution from Chapter 2 (line) and the final surface wave drag for the three heated 7 km critical layer tests (circular points). Note that all three critical layer runs points rest above the curve, indicating that for a 80 km wavelength mountain profile, linear theory overestimates the wave suppression due to a well mixed surface layer. The best estimate by linear theory is made for the $h = 600$ m low drag state condition in which the error is approximately 10%. For the high drag states of the $h = 900$ m and $h = 750$ m tests, linear theory under estimates the wave amplitude by factor of two. The $h = 900$ and $h = 750$ m cases exhibit a 10% reduction in the maximum predicted surface wind at the conclusion of the heating cycle (Figure 5.14).

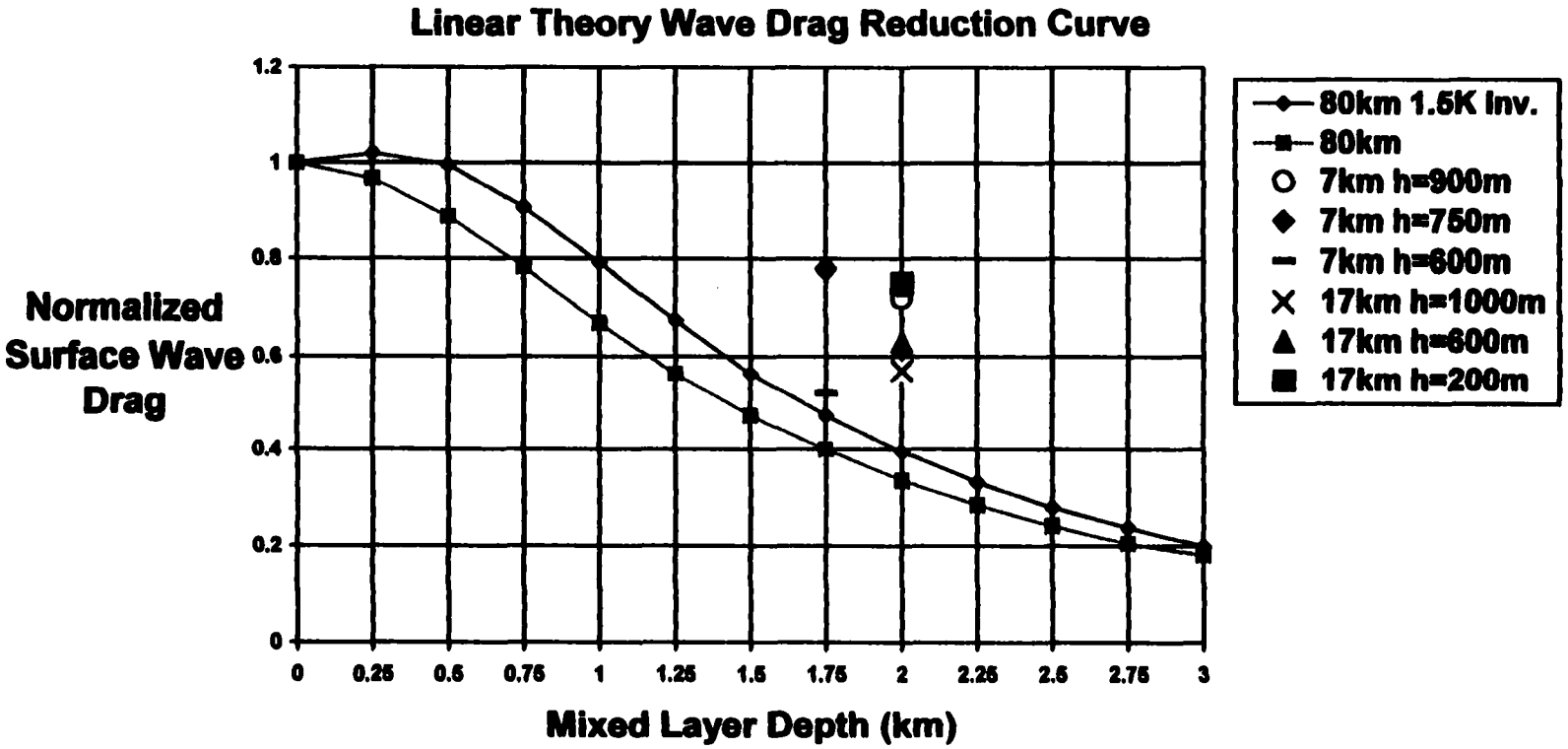

Figure 5.13. Plot of the linear analytical steady state surface wave drag curve as a function of mixed layer depth and horizontal wave length (80 km) and 7 km heated critical layer tests. The values are normalized by the H=0 steady state values. Plotted points represent the normalized surface drag at the conclusion of the heating cycle for the simulations indicated in the box above.

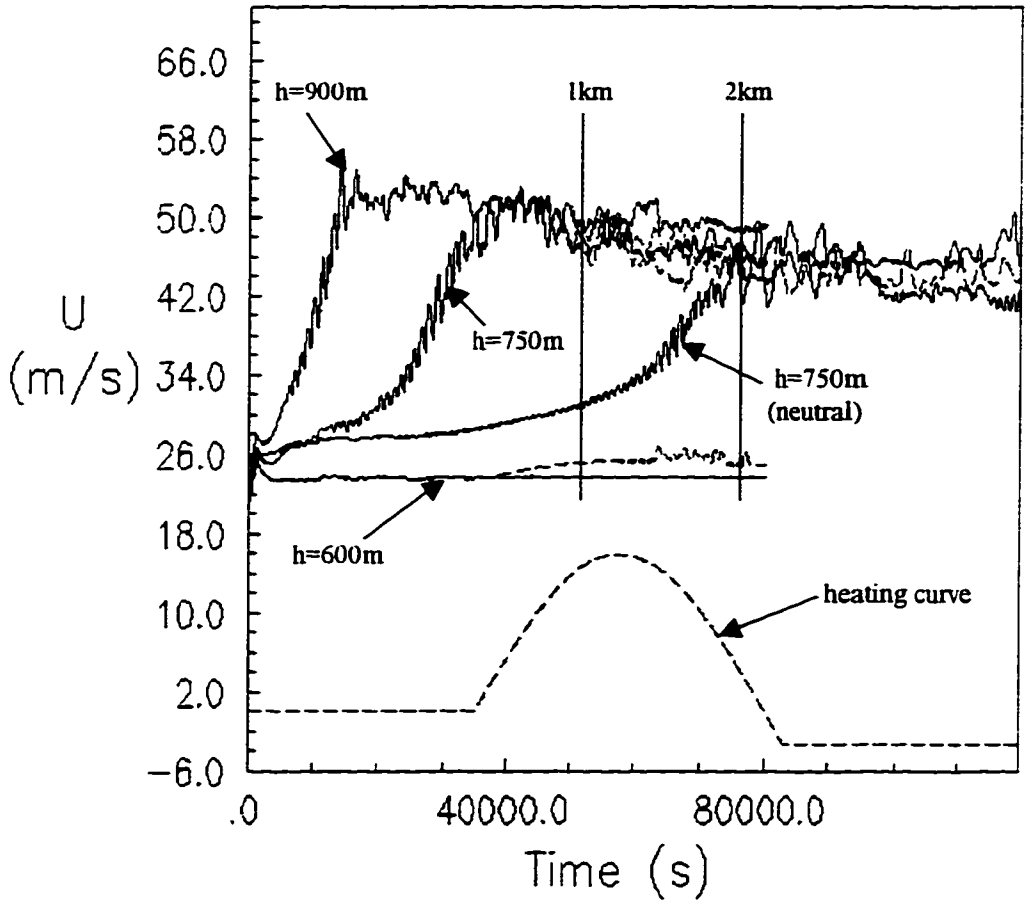

Figure 5.14. Time series plot of the maximum surface wind speed with a mean state critical layer at 7 km for all control and heated tests. The solid line represents the control runs and the dashed line the heated tests. The heating curve is provided at the bottom of the plot with a maximum heating rate of $200\,w/m^2$ and a minimum rate of $-40\,w/m^2$. The vertical lines represent the approximate mixed layer depth.

Most of the reduction in surface u' take place late in the heating cycle, corresponding to the maximum mixed layer depth. Note the hydraulic jump-like structure downstream of the mountain peak at x= 320 km and wave induced critical layer at approximately z= 4.8 km (Figures 5.15 and 5.16). As anticipated, very little wave activity is present above the critical layer (z=7 km).

The h = 750 m test was extended 40,000 seconds past the end of the heating cycle. The purpose of this experiment is to gain insight on the effects of nocturnal cooling on a heated mountain wave. Although the main goal of this study is to investigate the diurnal trends from the heating perspective, the cooling period is also a likely contributor to the observed trends, since gravity wave magnitude is a direct function of stability (N). A stable near-surface layer develops as a result of the parameterized cooling function (Figure 5.17). The stability in the surface layer is similar to the original base state profile and is approximately one-third the depth of the mixed layer height (not shown). In response to the increase in static stability at the surface, the wave drag and maximum wind speed increase during the simulated nocturnal period, recovering nearly one-third of the reduction attributed to the heating period. But, the remnants of the heating cycle are clearly visible, with the presence of an elevated mixed layer of appreciable depth (Figure 5.18). It is clear from this experiment that the mixed layer continues to restrain the mountain wave response, albeit from an elevated location. The overall character of the simulation remains unchanged from that at t = 80,000 seconds. Additional cooling period simulations were not conducted in order to focus on heating portion of the daily trend.

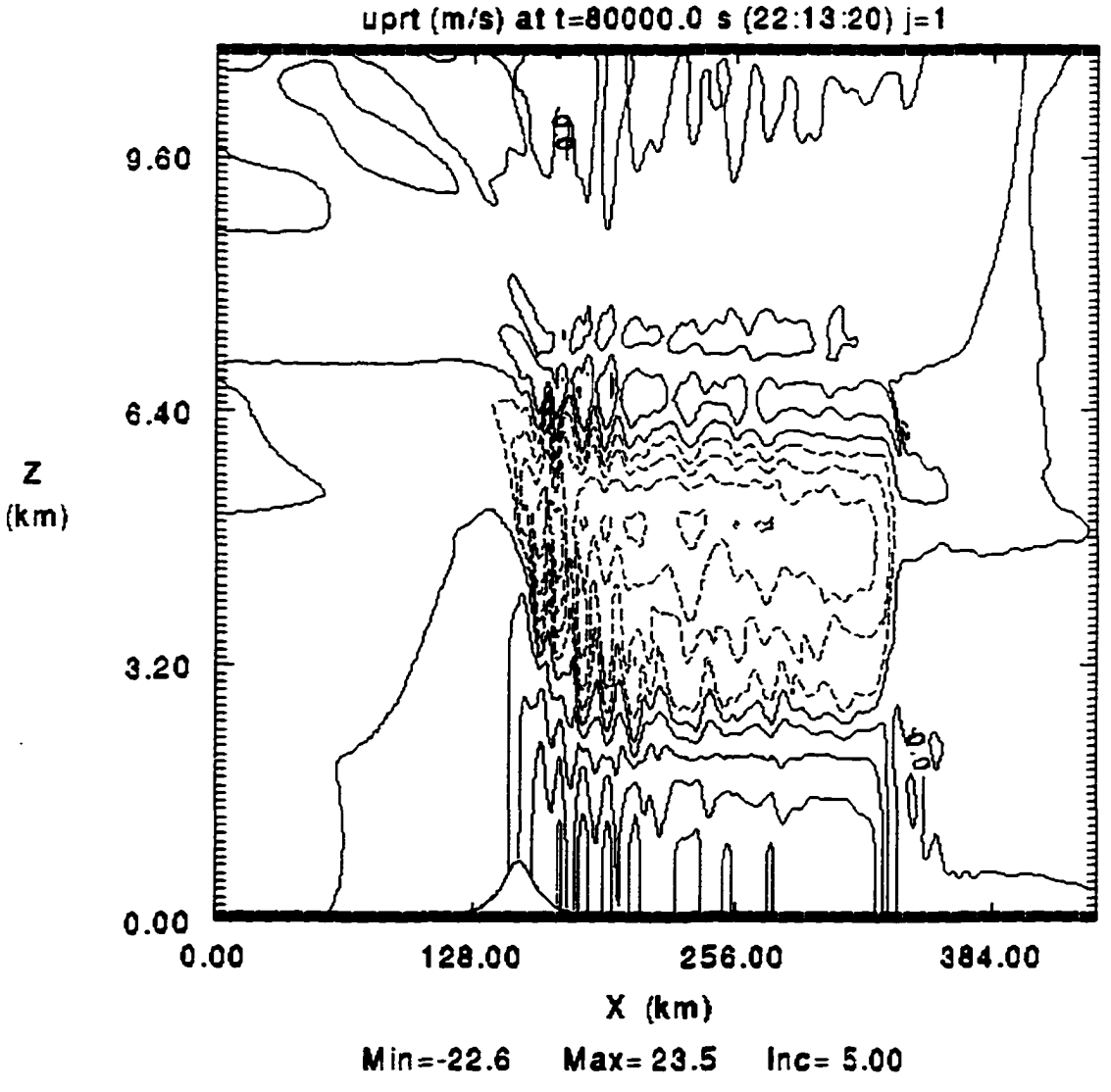

Figure 5.15. Numerical model perturbation horizontal velocity for a mean state critical layer at 7 km for the $h = 750$ m heated case at $t = 80{,}000$ seconds. Area depicted is the entire model domain. The contour interval is 5.0 m/s.

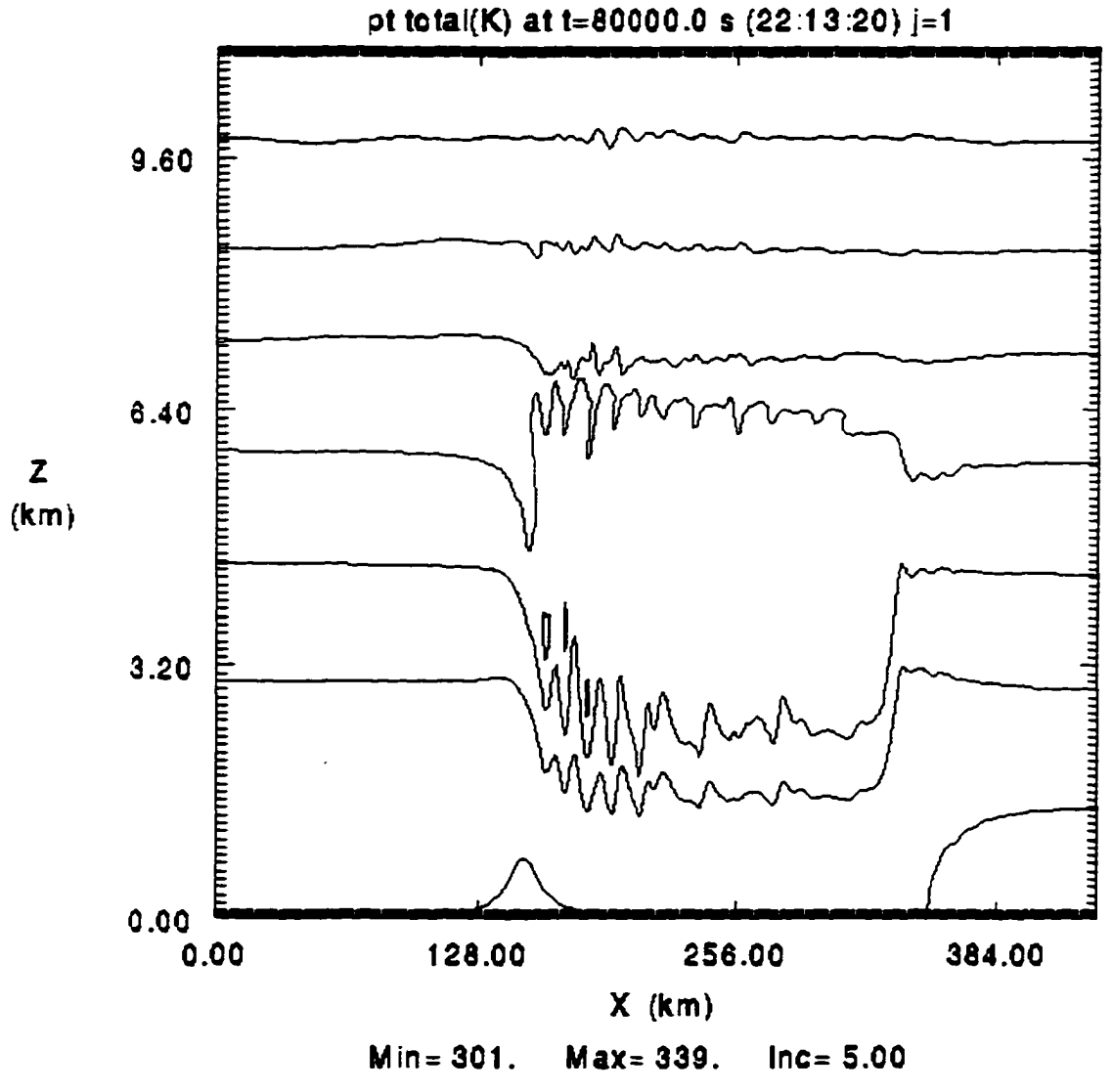

Figure 5.16. Total potential temperature for a mean state critical layer at 7 km for the $h = 750$ m heated case at $t = 80{,}000$ seconds. Area depicted is the entire model domain. The contour interval is 5 ° K.

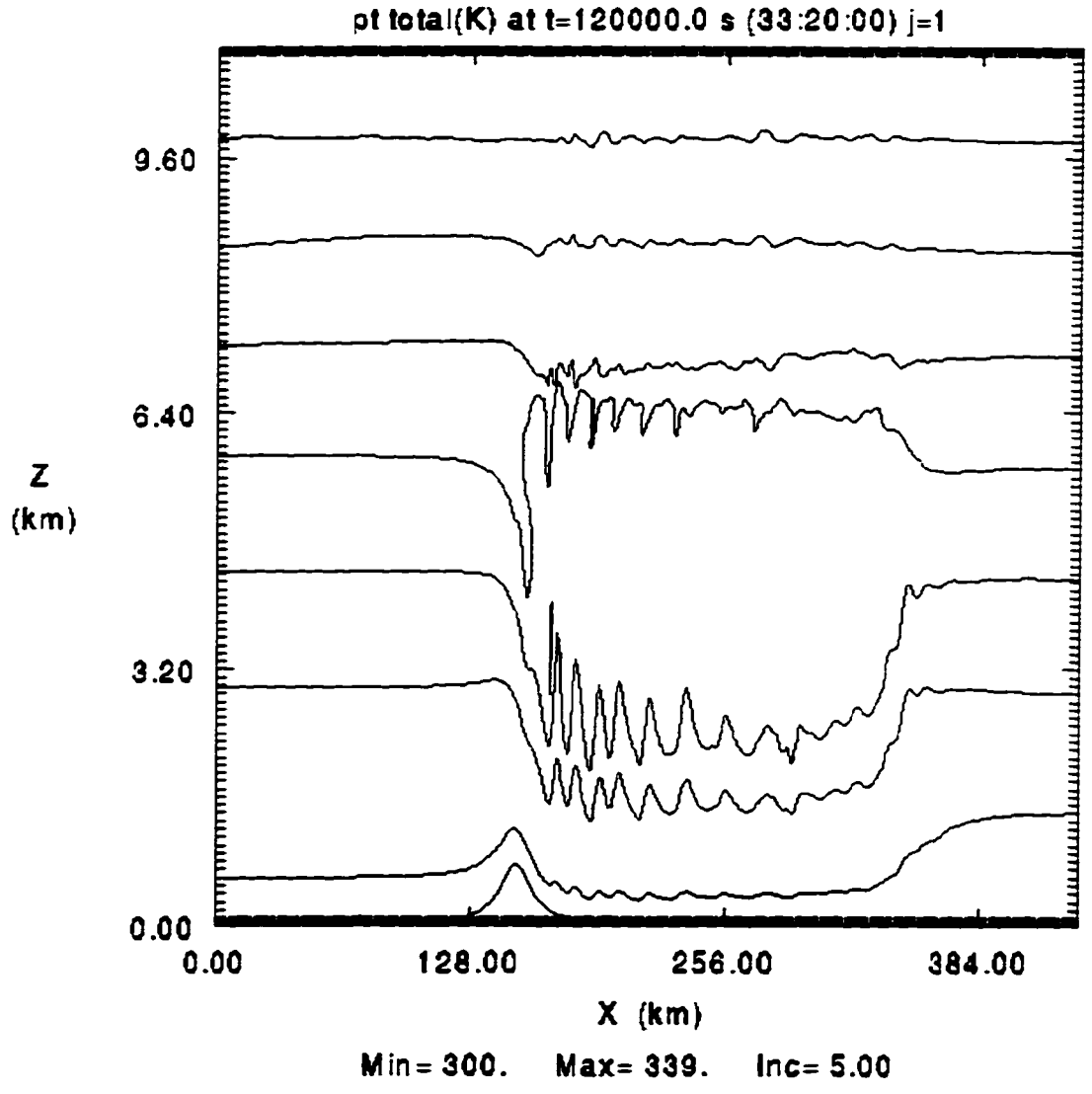

Figure 5.17. Total potential temperature for a mean state critical layer at 7 km for the $h = 750$ m cooling portion at $t = 120{,}000$ seconds ($Ut/a = 240$). Area depicted is the entire model domain. The contour interval is 5 ° K.

5.3.2 17 km Mean State Critical Layer Results

This section presents experiments with a mean state critical layer at 17 km and mountain heights of $h = 200$, 600, and 1000 m. These tests differ from the previous work since multiple waves in the vertical are possible. The non-linear effects are estimated by $Nh/U = 0.104$, 0.314, and 0.523 for the $h = 200$, 600, and 1000m tests, respectively. As before, each case is brought to a steady state and the diurnal heating cycle enabled. The steady state was estimated at approximately $t = 35000$ seconds or $Ut/a = 70$ for each test (Figure 5.18), even though there was a slight increase with time of the surface wave drag to the end of the simulation. For the $h = 1000$, and 600 m tests a significant reduction of 43% and 37% from the non-heated run is noted at the end of the heating cycle. For each heated run the mixed layer developed to a height of 2 km by the end of the heating period. For the $h = 200$ m case, a high drag state was not attained and the drag reduction due to heating is approximately 26%. Reductions for each case are plotted on Figure 5.13. The graph indicates linear theory overpredicted the reduction by about a factor of two. The weakly forced case ($h = 200$ m) exhibited the largest deviation from linear theory. This is contrary to earlier results in which moderately non-linear hydrostatic and non-hydrostatic heated simulations followed linear theory reasonably well. The peculiar behavior for the $h = 200$ m case may be due to enhanced resonance, as the effective gravity wave guide depth changes with the height of the mixed layer. The vertical wavelength in each test is 12 km. The shear layer below the critical layer is a likely candidate for reflecting part of the wave

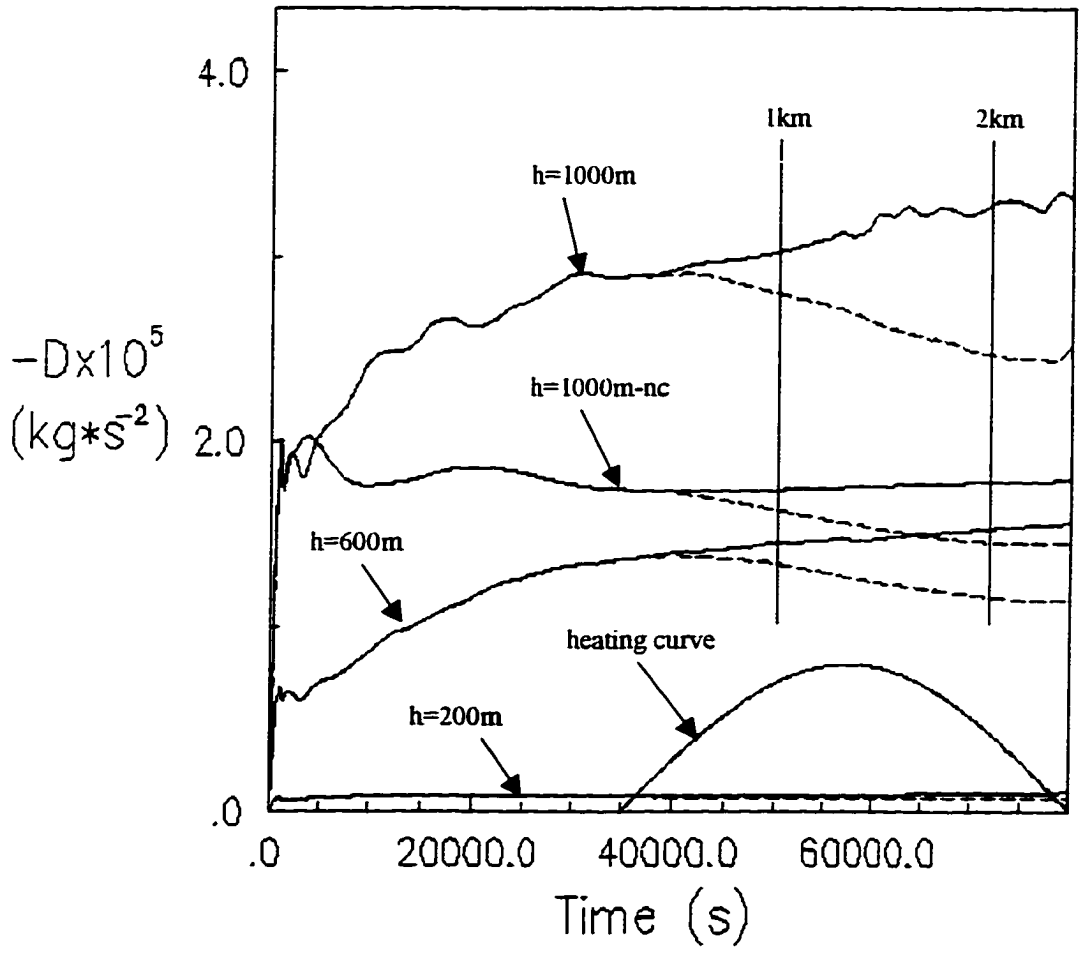

Figure 5.18. Time series plot of the surface wave drag for the control (solid lines) and heated (dashed lines) runs with a mean state critical layer at 17 km for h = 1000, 600, 200m, and h = 1000m constant base state wind with height (1000m-nc). The heating curve is provided at the bottom of the plot with a maximum heating rate of $200\, w/m^2$. Vertical lines indicate the approximate depth of the mixed layer.

energy back toward the surface. The reduction in maximum wind speed for the h=1000 m and 600m tests are on the order 10 % (Figure 5.19). There is actually an increase in the maximum surface wind speed in the $h = 200$ m case. This is due to the generation of poorly resolved convective cells in the boundary layer. In each of the heated tests, small-scale features are present when the heating is strongest and are an artifact of poorly resolved convection. The turbulent parameterization scheme is unable to properly mix the near surface super adiabatic layer and the horizontal grid spacing is too coarse to properly resolve the convective motions. Location of the maximum u perturbation field (not shown) for the $h = 1000$ m and 600 m simulations move down the lee slope of the mountain and onto the downwind plain during the heating period. The magnitude of the surface wind maximum is about 10-15% lower in the heated tests as compared to the control case. In the $h = 200$ m test maximum surface winds were observed to increased and can be attributed to the convective boundary layer motions. The perturbation horizontal velocity and total potential temperature fields at $t = 75{,}000$ seconds for the $h = 1000$ case are illustrated in Figures 5.20 and 5.21. As alluded to earlier, both fields show signs of poorly resolved convection far downstream of the mountain crest.

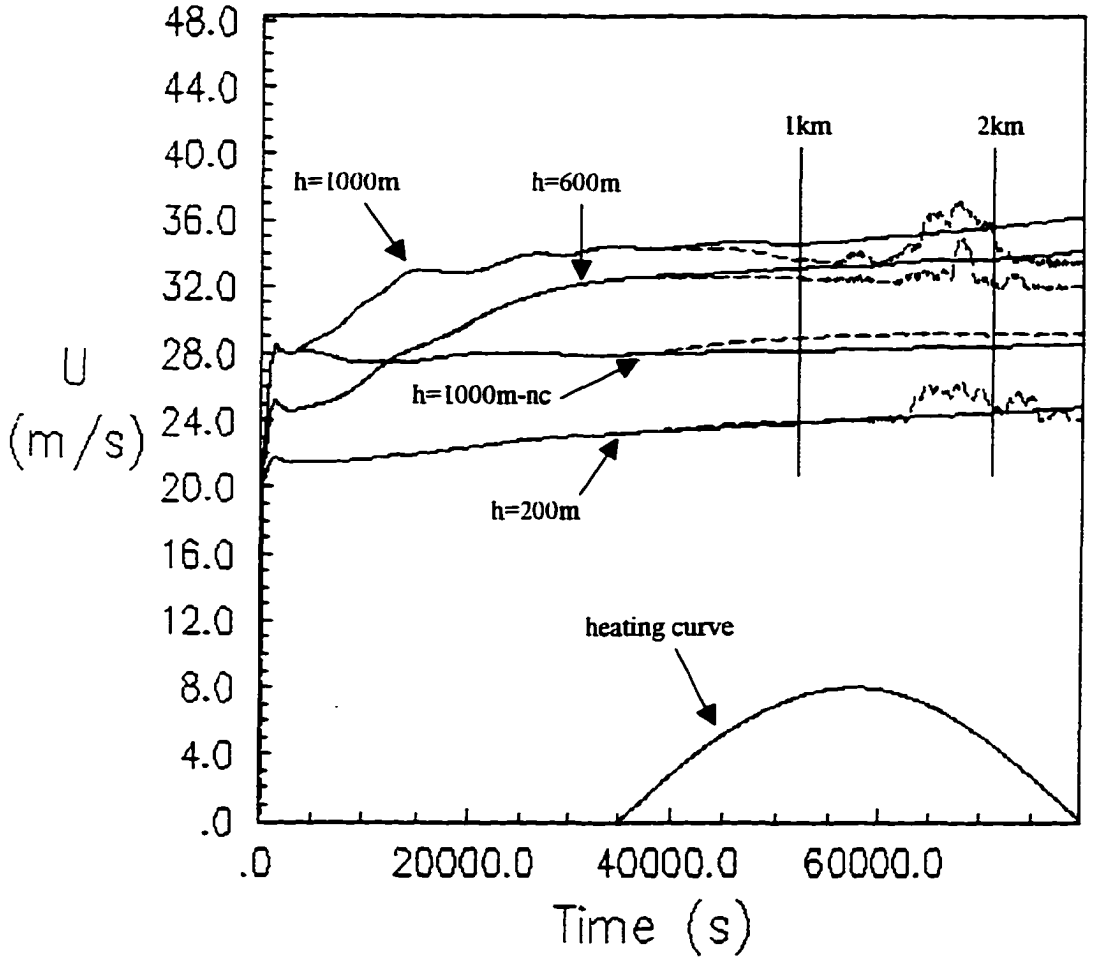

Figure 5.19. Time series of the maximum surface wind speed for all tests with a mean state critical layer at 17 km. The solid and dashed lines represent control and heated solutions, respectively. The heating curve is provided at the bottom of the plot with a maximum heating rate of $200\, w/m^2$. Vertical lines indicate the approximate depth of the mixed layer.

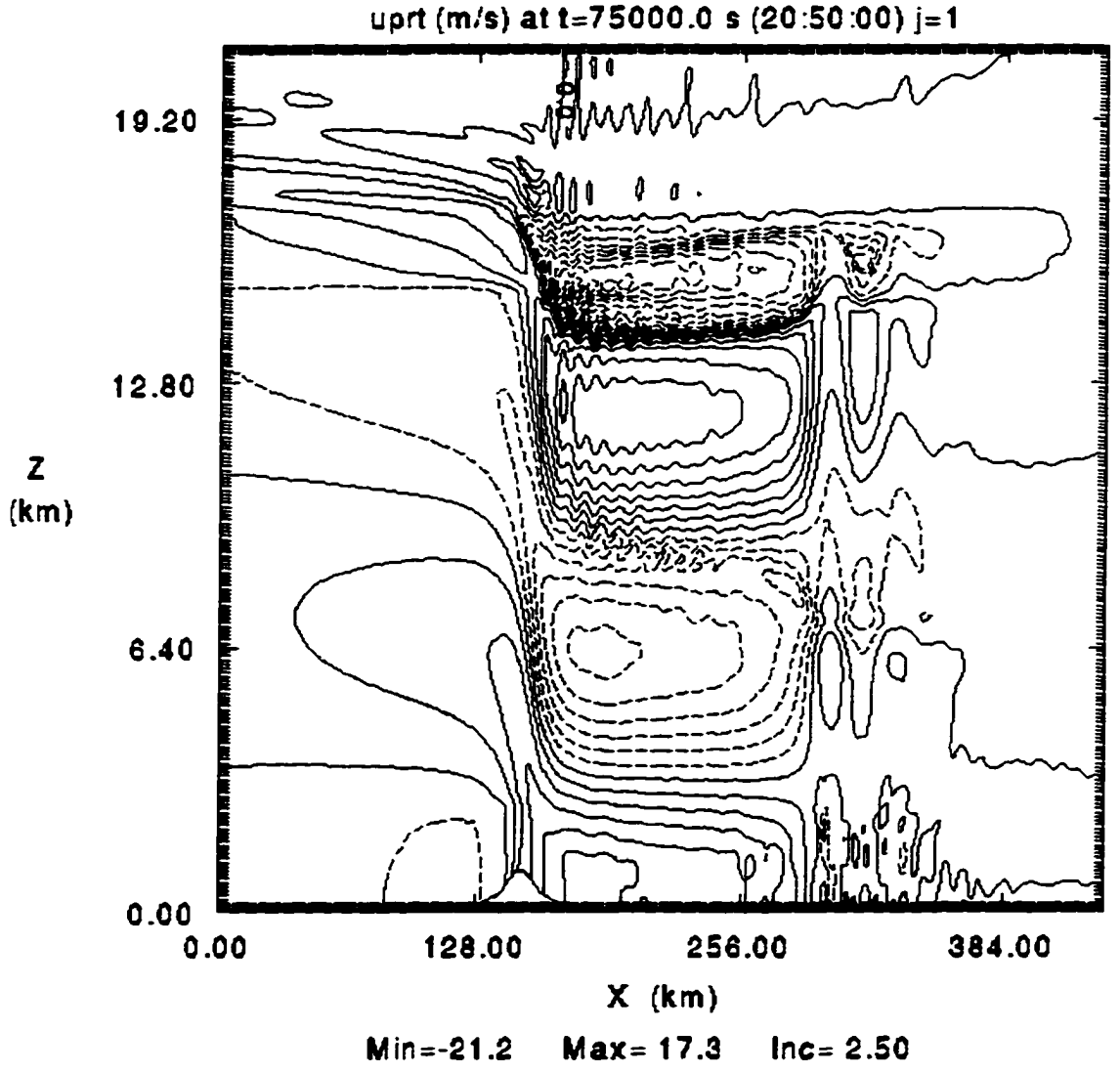

Figure 5.20. Perturbation horizontal velocity for the heated mean state critical layer test at 17 km for the $h = 1000$ m case at $t = 75{,}000$ seconds for the entire model domain. The contour interval is 2.5 m/s.

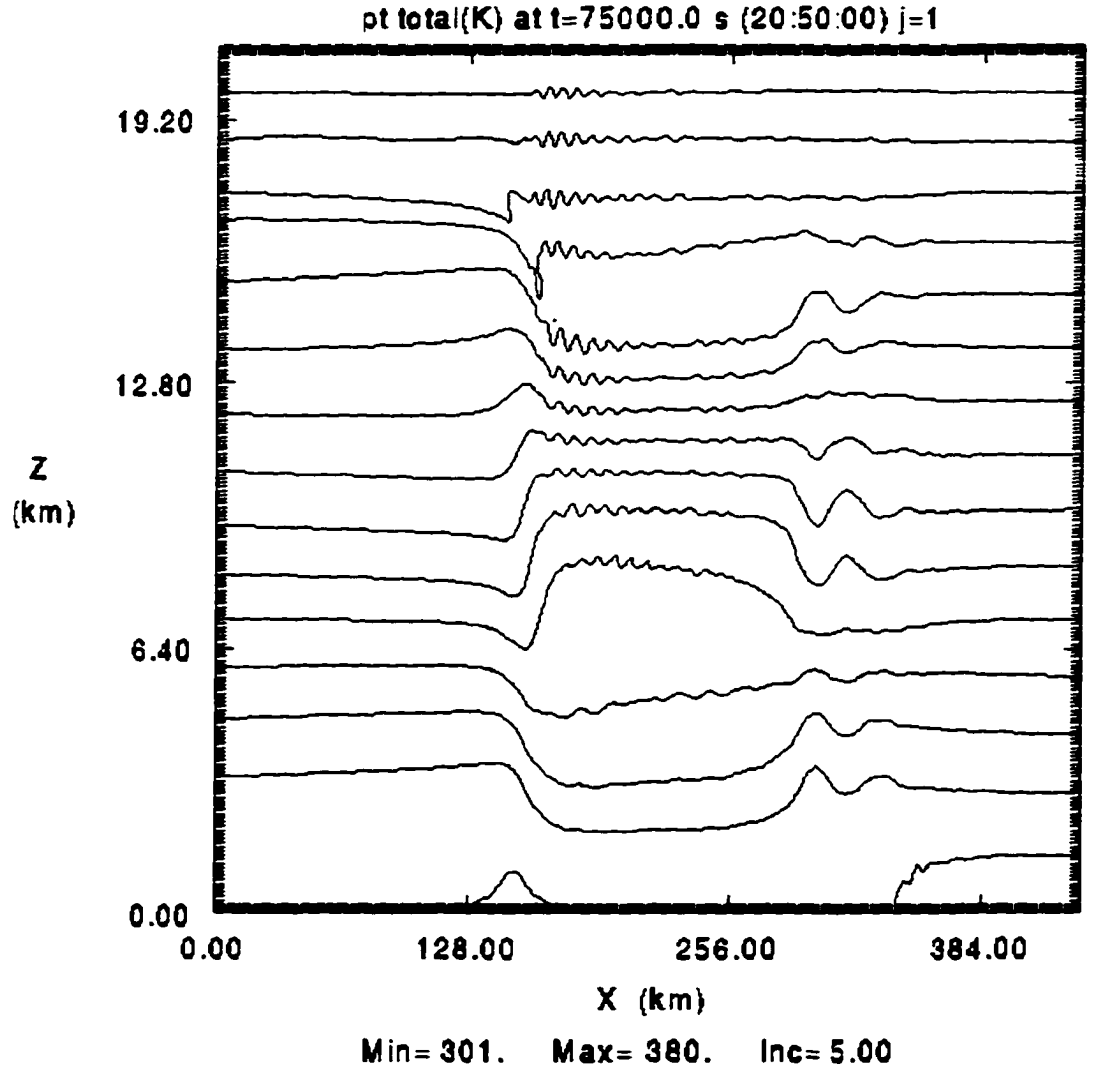

Figure 5.21. Isentropes for the heated mean state critical layer at 17 km $h = 1000$ m case at $t = 75{,}000$ seconds for the entire model domain. The contour interval is 5 ° K.

5.3.3 Discussion

In every experiment, the introduction of the diurnal heating cycle reduced the gravity wave activity in the stable layer aloft. The surface wave drag was reduced approximately 20-25% with the exception of the 7 km 600 m simulation, which realized a reduction on the order of 50%. Thus, it appears that the response is fairly predictable regardless of the placement of the critical layer. For the critical layer tests, linear theory continually overestimated the actual wave reduction by 10% to 100%. From a qualitative standpoint, the non-heated critical layer simulations compared favorably to Smith's theory and to other published numerical results. Smith's work predicts amplification for critical layer heights between $(1/4+n)\,\lambda_z$ and $(3/4+n)\,\lambda_z$ for $n \geq 0$. A notable exception is the 7 km $h = 750$ m test case. The numerical model predicted a high drag state, whereas Smith's theory does not. Other simulations with lower mountain peaks failed to generate a high drag state (see the 7 km, $h = 600$ test). Yet as heat is introduced to the $h = 750$m case, a nearly 2 km deep mixed layer develops. The mountain wave response remains in the high drag regime with a normalized flux > 2.0 (see Figure 5.13). The 7 km $h = 750$m 2 km deep neutral layer test requires nearly 20 hours to achieve a steady high drag state. The neutral layer test verifies the heated $h =$ 750 m simulation but also exposes a slow yet significant growth mode. This particular result suggests that, given sufficient time, the 2 km neutral layer test can achieve a high drag state similar to that displayed by the heated run. A mean state critical layer (with respect to terrain features) is not common in the atmosphere, while a 2 km deep mixed layer is observed frequently.

The weakly forced $h = 200$ m, 17 km critical layer test defies linear theory. This may be due to partial reflections below the critical layer, which the linear solution does not include. The reduction of the surface winds follows linear theory, as most tests produced a 10%-15% decrease in the predicted maxima at the end of the diurnal heating cycle. As shown in Chapter 2, the magnitudes of the perturbation velocity fields are functions of the mixed layer depth. Since the drag is a quadratic quantity in terms of the perturbation velocity fields, the reduction of wave drag should be more dramatic than that in each individual wind field. During the cooling period for the $h = 750$ m simulation, the wave drag rebounded, recovering only a fraction of the control runs value. This is not surprising since only a portion of the mixed layer nearest to the surface layer reestablishes stable stratification.

In the mid-latitudes, localized mean state critical layers are rarely observed. With this in mind, a numerical exercise was conducted for the $h = 1000$m 17 km critical layer test. The simulation is performed with a constant non-zero base state flow extending to the top of the domain. The results indicate a wave drag approximately 50% of the critical layer counterpart and are included in Figure 5.18 for comparison. Clearly, the presence of a critical layer enhances the response for certain atmospheric profiles.

One method used to measure the effects of surface heating is to present the results as a function of non-dimensional parameters (Figure 5.22). For this study, the relevant parameters are the static stability (N), base state wind (U), mountain height (h), heat input (Q), and the depth of the mixed layer (H). This particular

configuration was chosen because the ease of comparing it with linear theory from Chapter 2 and to radiosonde observations. Figure 5.22 displays a nearly linear decrease in wave drag as compared to the exponential decrease forecast by the linear solution of Chapter 2. Another option is to plot the normalized surface wave drag as a function of heat input (Q) to the system normalized by the perturbation kinetic energy. This approach and others were attempted but deemed unsuitable for a variety of reasons.

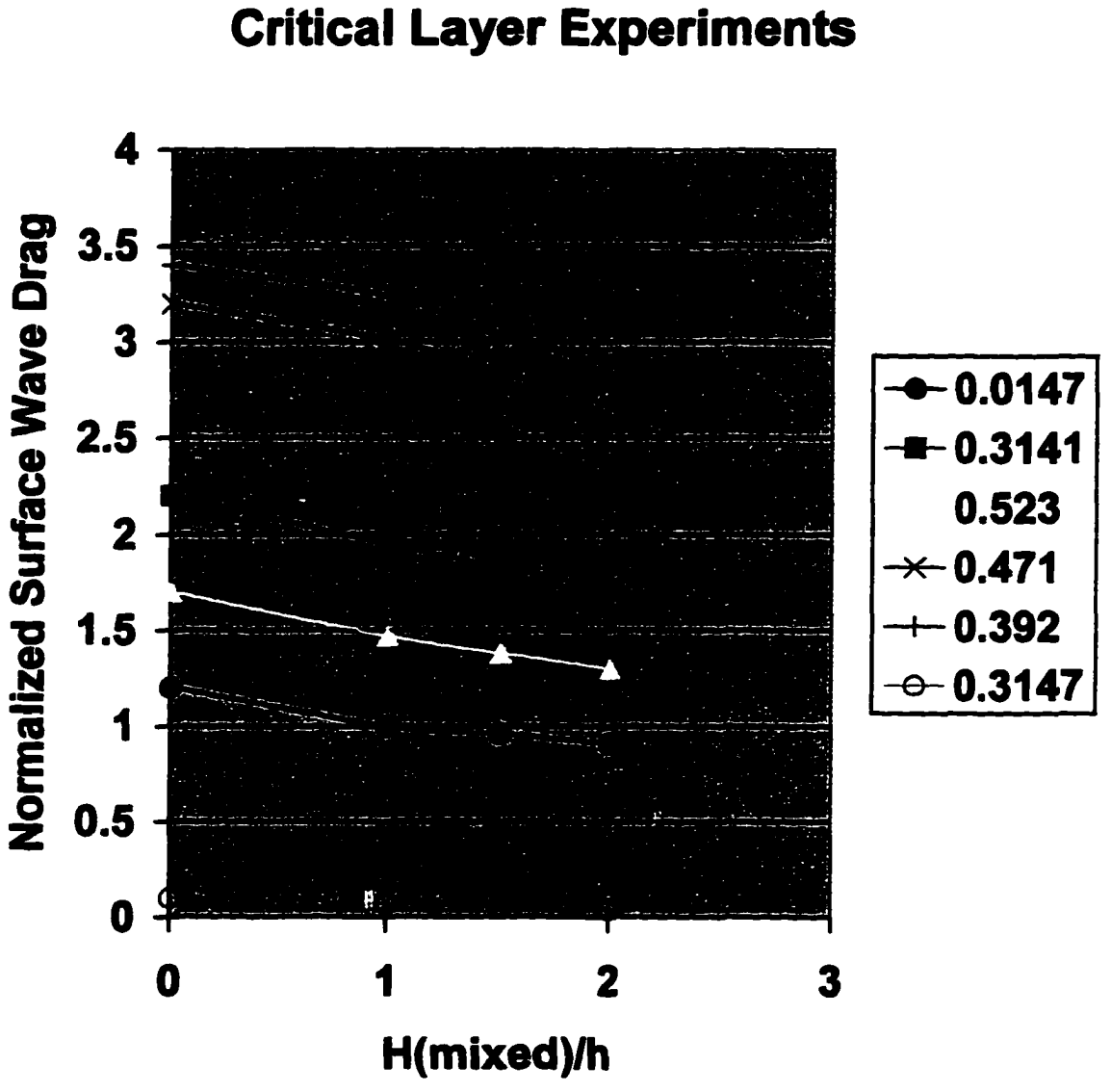

Figure 5.22. Normalized surface wave drag as a function of the ratio of the mixed layer depth to the mountain height for the critical layer experiments. The wave drag was normalized by the linear hydrostatic value.

5.4 Non-Linearity Parameter Study

In this section, a wider range of flow conditions is used to further our understanding of the effects of heating on the gravity wave environment. The work discussed earlier in this chapter involved inverse Froude number flow between 0.1 and 0.5. This section introduces results from three classes of inverse Froude number with a non-linear measure of $Nh/U = 0.2$, 1.0, and 3.0. The simulations presented here were conducted in the absence of a mean state critical layer. For $Nh/U = 1.0$, the flow is nearly blocked from the kinetic energy argument of Sheppard (1956). Smith (1988) contends that the flow unblocked remains up to $Nh/U = 1.3$. As before, each simulation is allowed to achieve a pseudo steady state and then surface heating is introduced. The magnitude of the heating is different for each case, according to the base state static stability. In these tests the only variable that is changed is the static stability. Each simulation is designed to produce a minimum 2 km deep-mixed layer. For the $Nh/U = 3.0$ test, this minimum thickness was not reached in a timely fashion (less than 1.8 days) owing to strong base state static stability. Table 5.1 contains a summary of the model parameters used here under the NLP column. In each simulation the mountain height is 1000m and the base state wind is 10m/s. The mountain quarter width $a = 15$ km is chosen to force mainly hydrostatic gravity wave modes. A horizontal Rayleigh type sponge was placed near the downstream lateral boundary to minimize the boundary effects due to sustained strong perturbation fields located near the boundary.

5.4.1 Results

Each simulation was advanced to the point where the depth of the boundary layer is equal to or greater that 2 km. For the $Nh/U = 0.2$ test, a 3 km deep mixed layer was established only after a short integration period of 10 hours or $Ut/a = 27$ using a relatively small maximum heating value of 60 w/m^2. The $Nh/U = 1.0$ and 3.0 tests required $Ut/a = 96$ and 80 and reached a depth of 2.7 km and 1.4 km, respectively. The required heating rate maxima and period lengths for the $Nh/U = 1.0$ and 3.0 tests were 300 w/m^2 and 40000 seconds, and 360 w/m^2 and 130000 seconds, respectively. Following the format given in Figure 5.22, the normalized surface wave drags are given as a function of normalized mixed layer depths in Figure 5.23 for each of the heated experiments. The control run wave drags were used to compute the H (mixed)$/h = 0$ values. The $Nh/U = 0.2$ test did not reach a high drag state or its linear equivalent. The $Nh/U = 1.0$ and 3.0 cases reached an elevated drag states and were found to be sensitive to the development of the mixed layer depth. Both tests displayed significant reductions (40% of the steady state control value) in computed surface wave drag by the end of the heating cycle.

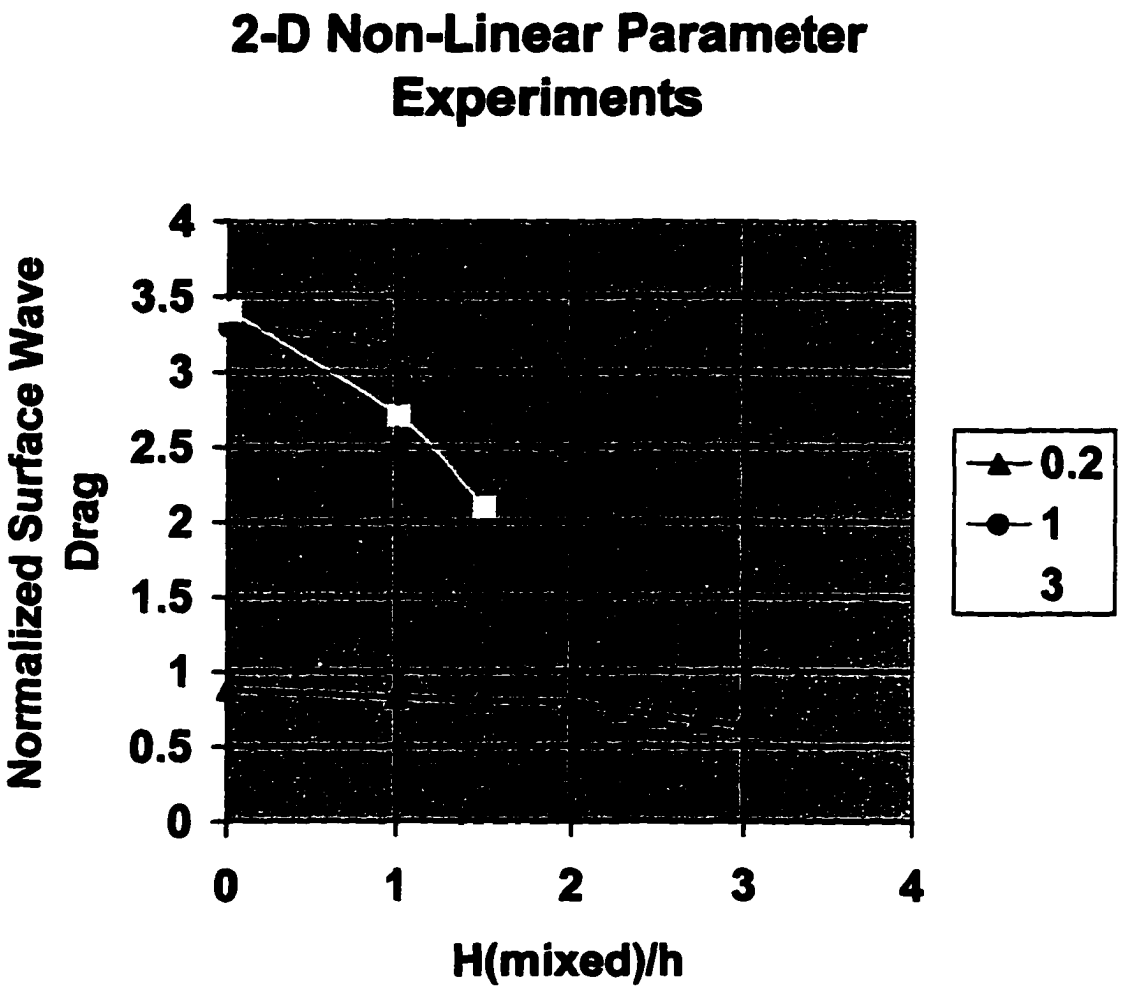

Figure 5.23. Normalized surface wave drag as a function of the ratio of the mixed layer depth to the mountain height for the two-dimensional non-linear parameter experiments.

5.4.2 Discussion

Results from this section indicate that for a meteorologically significant range of flows over a mountain, the final drag state is sensitive to the development of a well-mixed boundary layer. In each case wave activity was reduced by nearly 40% from the control case values. The slope and shape of the surface wave drag curves are more closely related to the linear theory solution than the critical layer tests. The slope of the Nh/U = 1.0 and 3.0 curves is non-linear as compared to the linear reduction trends displayed by the critical layer tests. The Nh/U = 1.0 and 3.0 tests undergo similar reductions in wave drag for differing mixed layer depths and associated energy input.

5.5 Two Layer Experiments

This section investigates the sensitivity of a strongly forced two-layer flow to surface heating. The purpose is to determine how the non-linear effects of scorer parameter layering are influenced by parameterized surface heating. Previous works assists the choice of the layering configuration. Durran (1986) performed a number of simplified multiple layer tests and found one particular case in which the expected linear response is small and the actual non-linear solution was large. This case involves a stable lower layer ½ vertical wavelength thick with an overlaying less stable upper layer with an assumed infinite depth. The expected linear response of this configuration is approximately ½ of the single lower layer analytic value. In his test, the non-linear effects created a surface wave drag nearly 6 times the expected linear value. Note that there are infinitely many multi-layer configurations to choose from and that only one of the most intriguing is investigated here.

5.5.1 Results and Discussion

The input data for these tests follow Durran's (1986) Table 1 case 2 entry and are summarized in Table 5.1 under the two-layer test group. The bottom layer stability is $N = 0.02$ and the upper layer stability is $N = 0.01$. The control and heated cases were extended to 60,000 seconds or a non-dimensional time of $Ut/a = 120$. The heating cycle was enabled at $Ut/a = 20$. As evident by a plot of the surface wave drag in Figure 5.24, an elevated drag state develops after approximately 10,000 seconds. Significant oscillations are present through the first half of the control solution, but during the last third of the simulation the wave drag is very nearly steady. The normalized surface wave drag for this test compares favorably with the results presented in Table 1 of Durran (1986).

The application of the heating cycle reduces the wave drag by almost 50% and the maximum surface wind speed by 15% (Figure 5.25). In terms of the wave response at the surface, these results compare favorably with previous non-critical layer findings. Figure 5.26 provides a comparison of the potential temperature field and indicates a 1.2km deep mixed layer (b). This equates to an expected reduction of 40% by the linear theory presented in Chapter 2. The decrease in the surface drag is approximately 20-25%. Note that the flow downstream of the mountain is weaker in the heated case. This test shows that strongly non-linear flows are just as susceptible to surface heating as their moderately non-linear and linear counterparts.

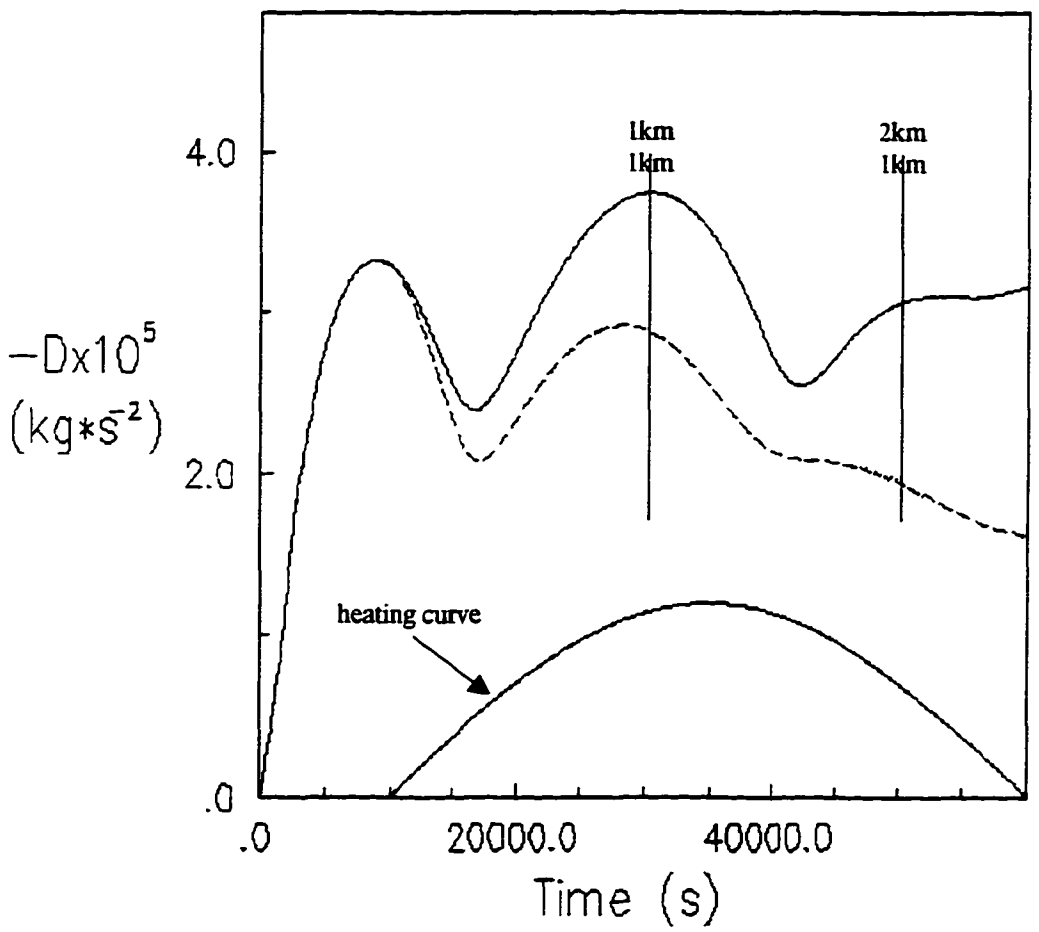

Figure 5.24. Time series of computed surface wave drag for the two-layer control (solid) and heated (dashed) simulations. The wave drag is normalized by the linear hydrostatic lower layer value. The heating cycle began at 10,000 seconds. The heating curve is provided at the bottom of the plot with a maximum heating rate of $300\, w/m^2$. Vertical lines indicate the approximate depth of the mixed layer.

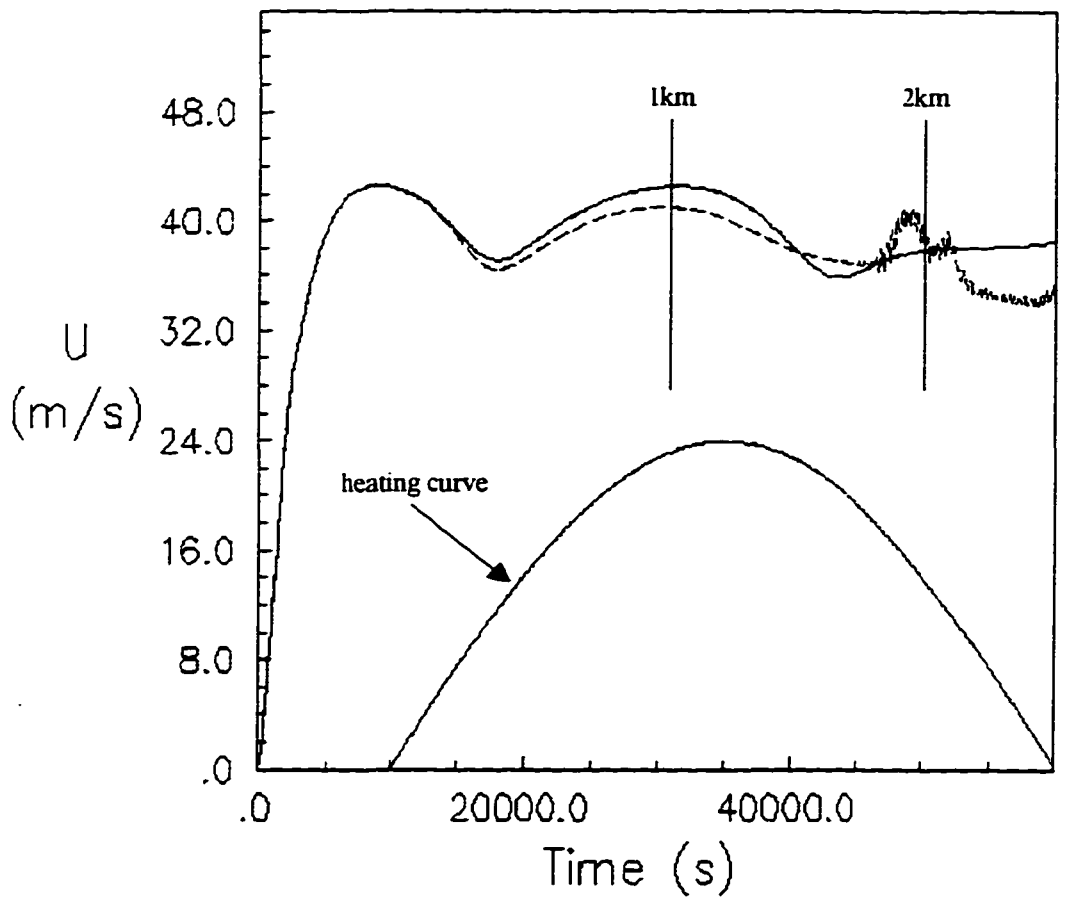

Figure 5.25. Time series of the maximum surface wind speed for the two-layer control (solid) and heated (dashed) simulations. The heating cycle was initiated at 10,000 seconds. The heating curve is provided at the bottom of the plot with a maximum heating rate of $300\,w/m^2$. Vertical lines indicate the approximate depth of the mixed layer.

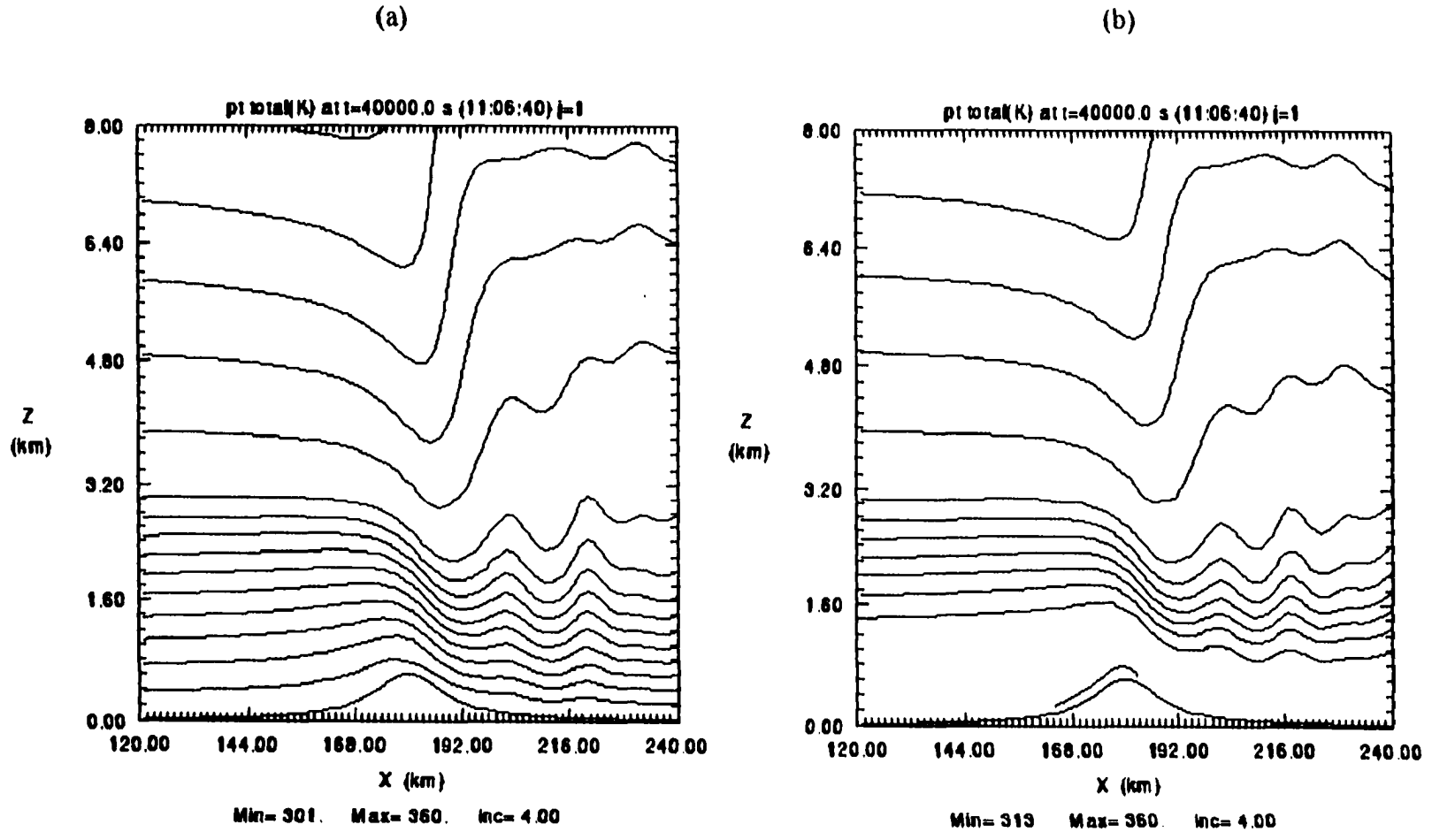

Figure 5.26. Plot of the potential temperature field for the two-layer test at 40,000 seconds for the (a) control and (b) heated runs. The contour interval is 4°K. Only a portion of the domain is shown.

5.6 January 9, 1989 Boulder, Colorado Windstorm

All previous tests involved simplified base state conditions and idealized terrain profiles. In this section, a numerical experiment is posed using the January 9, 1989 Boulder windstorm event. These simulations include observations taken upstream of the Front Range and a realistic two-dimensional mountain profile. As mentioned in Chapter 4, two-dimensional simulations of observed events have been investigated for years with the purpose of expanding our understanding of observed windstorm characteristics. The ultimate goal is to predict the timing and magnitude of windstorm features with reasonable accuracy. The intent of the simulations presented here is to classify the effects of surface heating on a more realistic atmospheric flow pattern. Comparisons are made to observations, but with the expectations that the details of the observed event are not well represented by the model. The accurate prediction of windstorm onset, magnitude, and dissipation requires a far more sophisticated numerical model and is beyond the scope of this study. Data collected during the Boulder windstorm initializes the control run. This particular event is chosen for two reasons: first, limited observational data are available for verification purposes and secondly, a comparison can be made with the published numerical results of Clark et. al. (1994).

5.6.1 Model Initialization

The model is initialized with the 2305 UTC atmospheric sounding collected from Craig, Colorado. An additional control run was performed on data collected prior to the windstorm (0505 UTC). This test (not shown) did not produce significant surface

winds or surface wave drag. Forecast Systems Lab and National Severe Storms Lab personnel collected the data and the final sounding data was provided by Clark et. al. (1994). For each experiment, the base state variables at the lateral boundaries are held fixed with respect to the horizontal advection terms for the duration of the prediction. A more complete investigation of this windstorm event, in which this scenario and others, including those with time dependent lateral boundary conditions, is found in Clark et. al. (1994). Their study contrasts the two and three-dimensional numerical model predictions to the observed surface winds, wind profiler information, and lidar data collected in the Boulder area. Their primary goal was to assess the ability of the numerical model to predict the onset and general windstorm features.

The ARPS terrain pre-processor provided a smoothed terrain profile from the raw global 5-minute resolution data set supplied by NCAR Data Services. The 5-minute data are smoothed and matched to the model grid using a multi-pass Barnes (1964) analysis technique. In this particular application, the Barnes scheme is applied twice and the resulting data field is available for direct insertion in the model. The Barnes response function for the final smoothed data field is determined from a preset first pass response and selected wavelength. Figure 5.27 displays the response function for these experiments as a function of model horizontal wavelength (in terms of Δ x). The analysis package operates from the model grid reference and not from the terrain data spacing. The response for an 8 Δx wave and 28 Δx wave is approximately 2% and 90%, respectively, of their initial values. A detailed description of the multi-pass Barnes analysis technique and response function is available in Chapter 8 of the ARPS Users Guide Version 4.0. The terrain profile is taken along the 40 ° N latitude line and passes

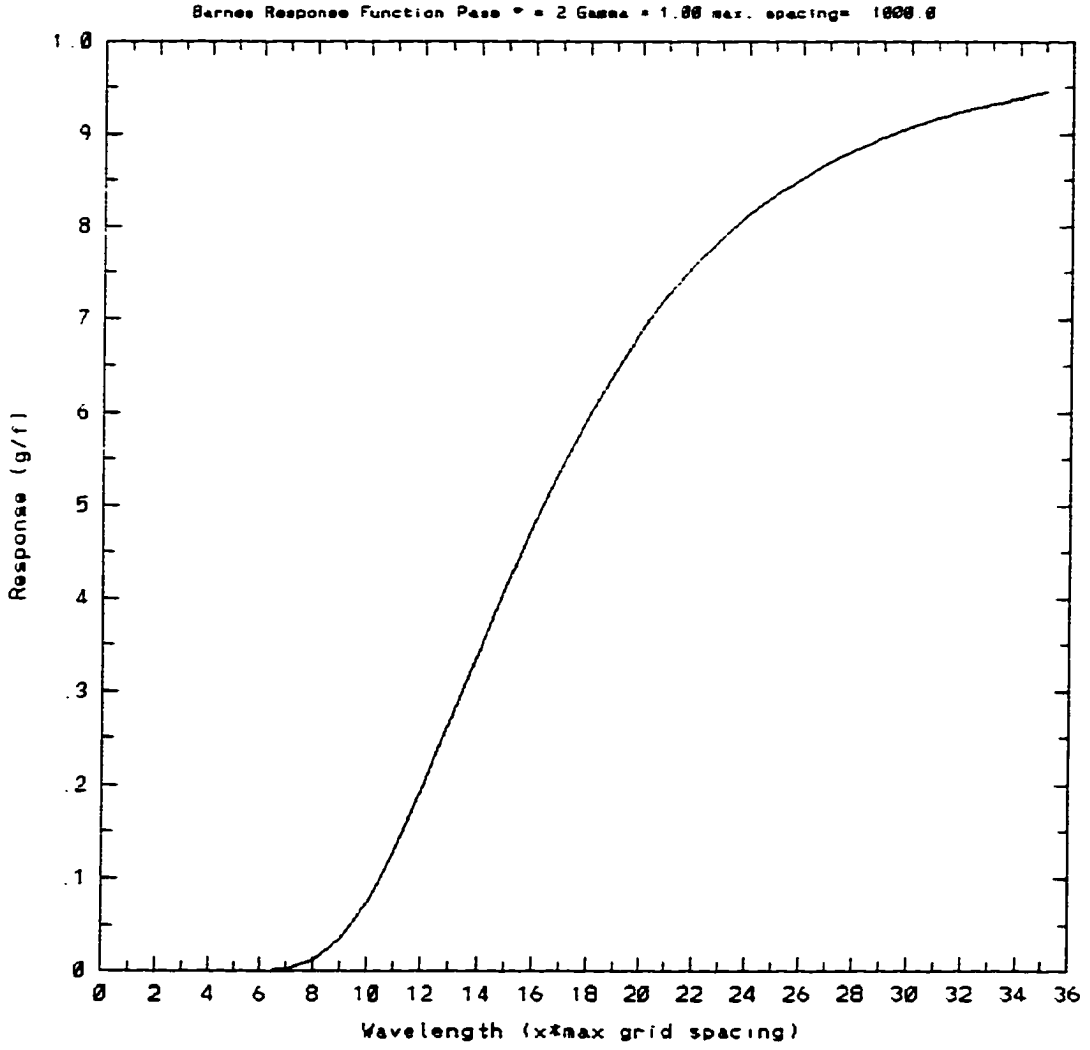

Figure 5.27. Barnes two-pass response curve as a function of model grid spacing for the terrain used in the two-dimensional January 9, 1989 Boulder windstorm experiment. The model horizontal grid spacing is 500m.

through the City of Boulder, Colorado. The model domain is 650 x 28 km and extends from Eastern Utah eastward to the western portion of the Kansas-Nebraska state line. The predictions do not include the Coriolis force but incorporate parameterized surface friction. As determined from the control run, heating begins at $t = 25{,}000$ seconds and the solution advanced to $t = 70{,}000$ seconds. The other pertinent model parameters are summarized in Table 5.1 under the Boulder test group.

One item that needs explanation is the choice of the upper boundary condition. Clark et. al. (1994) used a sponge layer in combination with a rigid lid. Bacmeister and Schoeberl (1989) presented a detailed numerical study on the impacts of breaking waves in the stratosphere on the near mountain level flow. Their results indicate that breaking waves aloft can alter the existing steady state mountain wave flow dramatically by reflecting upward propagating gravity wave energy downward. Their simulations clearly show propagation of the momentum flux reduction downward with time. For $Nh/U < 0.15$, the decrease of the vertical momentum flux computed over the mountain is found to be periodic in time. For $Nh/U = 0.8$, reductions in the computed vertical momentum flux originated in the breaking wave aloft and traveled downward, influencing the flow above the mountain, but the near surface flow is only minimally affected. Bacmeister and Schoeberl note a minimal impact of the downward moving disturbance in the momentum flux field when a breaking layer is observed near the mountain peak. For cases in which a breaking wave exists near the mountain, the importance of the upper boundary condition choice is reduced. Given their result, a linear hydrostatic radiation condition is applied in these simulations. This method allows wave breaking to occur up to the top of the model domain. Even though errors

due to the non-linear terms at the top boundary are produced, the majority of the wave energy is absorbed and/or reflected back towards the surface by breaking waves when they are present below the model top.

5.6.2 Windstorm Observations

Aside from the collection of data upstream of the Front Range (Craig, Colorado), observations were taken in the Boulder area using surface wind instruments and lidar. The observed winds at the top of the NOAA Building in Boulder are plotted in Figure 5.28. Note the abrupt increase in wind speed near 1100 UTC January 9, representing the onset of the windstorm. The winds remain above 30m/s for several hours but show a steady decrease during the afternoon. The wind speed drops below 20m/s by 0000 UTC January 10, marking the dissipation stage. Figure 5.29 displays a vertical cross section time series of Doppler Lidar observations taken in Boulder and reveal an elevated jet with maxima on the order of 30m/s. An observational study by Neiman et. al. (1988) report the existence of an elevated jet region during windstorm events. The base state wind and temperature profiles measured from the Craig, CO sounding location and used to initialize the model experiments are plotted in Figure 5.30. The data show a strong jet near a height of 10.5 km, corresponding to the level of the tropopause.

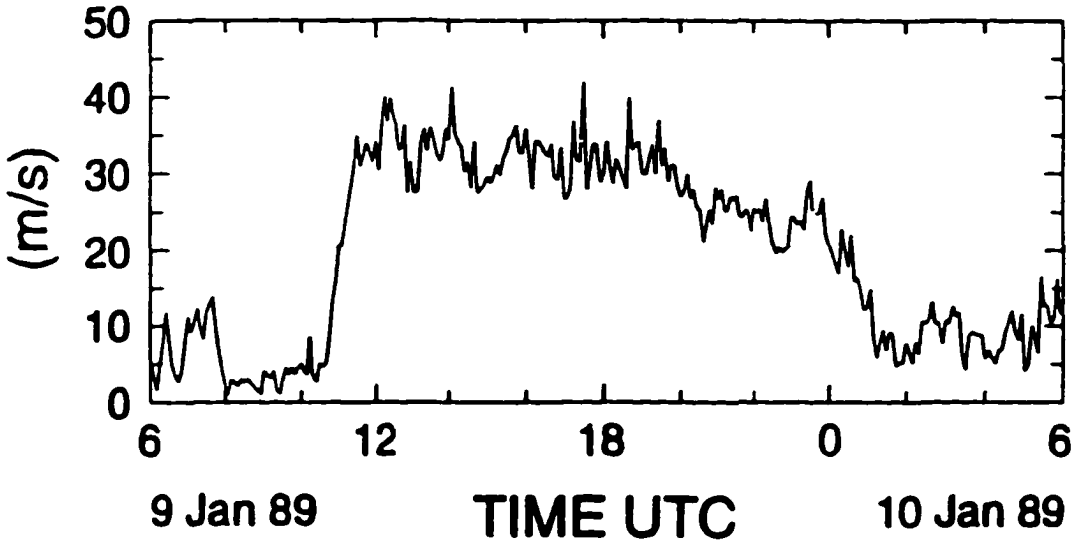

Figure 5.28. Peak 5-minute wind gusts as a function of time as measured from the roof of the NOAA Building (20m AGL). Taken from Clark et. al. (1994).

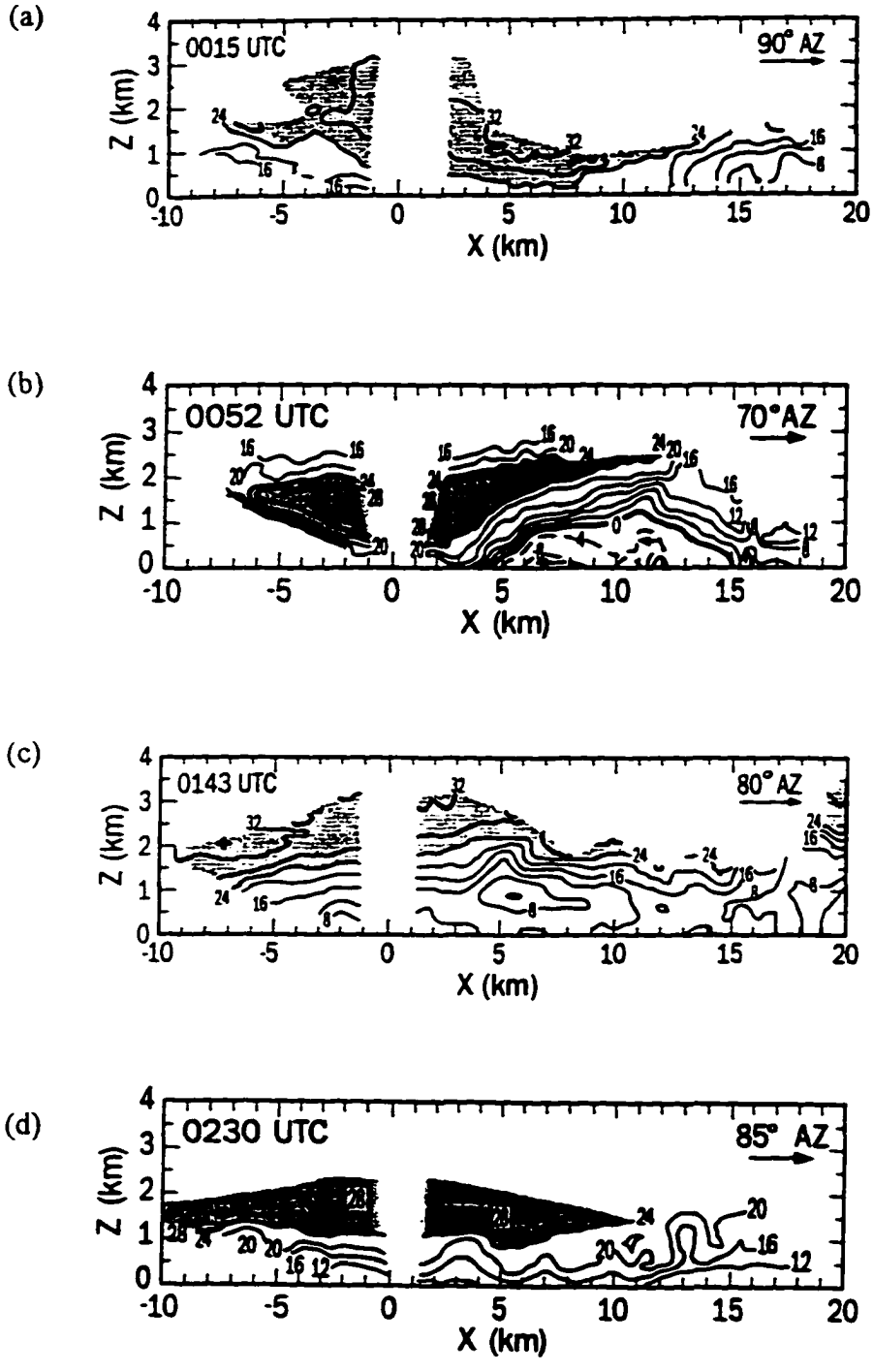

Figure 5.29. Doppler Lidar vertical cross sections from the Boulder area at (a) 0015 UTC, (b) 0052 UTC, (c) 0143 UTC, (d) 0230 UTC. Shaded regions represent velocities >24m/s. Plots taken from Clark et. al. (1994). The contour interval is 4.0 m/s.

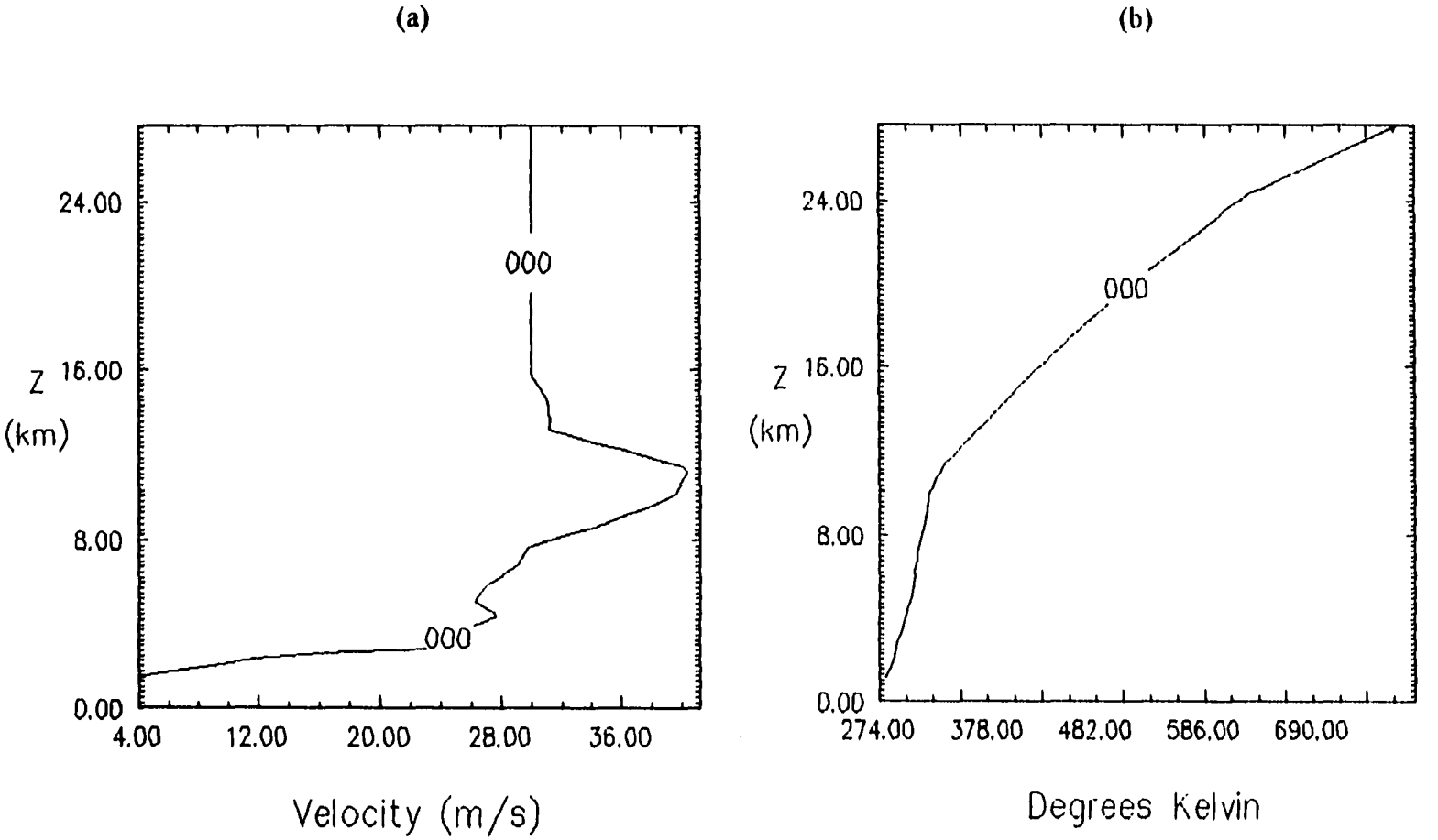

Figure 5.30. Vertical profile of base state (a) E-W wind component and (b) potential temperature measured from the Craig, Co 2305 UTC rawindsonde.

5.6.3 Results

The mountain induced surface wave drag and maximum surface wind speed as a function of time for the 2305 UTC control and heated runs are contrasted in Figures 5.31 and 5.32, respectively. The wave drag computed from the 2305 UTC heated run (dashed line) is nearly 20% lower than the control run (solid line). The maximum surface wind speed is reduced by 20% from the control run and the depth of the mixed layer reached 1.5 km. The simulated maximum surface wind speed and observed wind measurements are not directly comparable, since the model did not include the change in the upstream conditions with time. But, using data collected upstream at a 2305UTC during the downslope wind event, the simulated maximum surface wind speed is similar in magnitude to those measured near the end of the observed storm. Figure 5.33 displays cross sections of potential temperature for the control and heated tests for the region near the Front Range and the Boulder community. The heated run exhibits a relatively well-mixed boundary layer approximately 1.5 km deep near the mountain peak. The near surface total horizontal velocity is disclosed in Figure 5.34 for the 2305 UTC (a) control and (b) heated runs at t=70,000 seconds. Note in each case that the strongest winds are not at the surface but elevated a few hundred meters above the surface and are consistent with the result of Miller and Durran (1991). In the heated case, the vertical gradient of u is weakened, likely owing to the unrealistically strong parameterized vertical turbulent mixing.

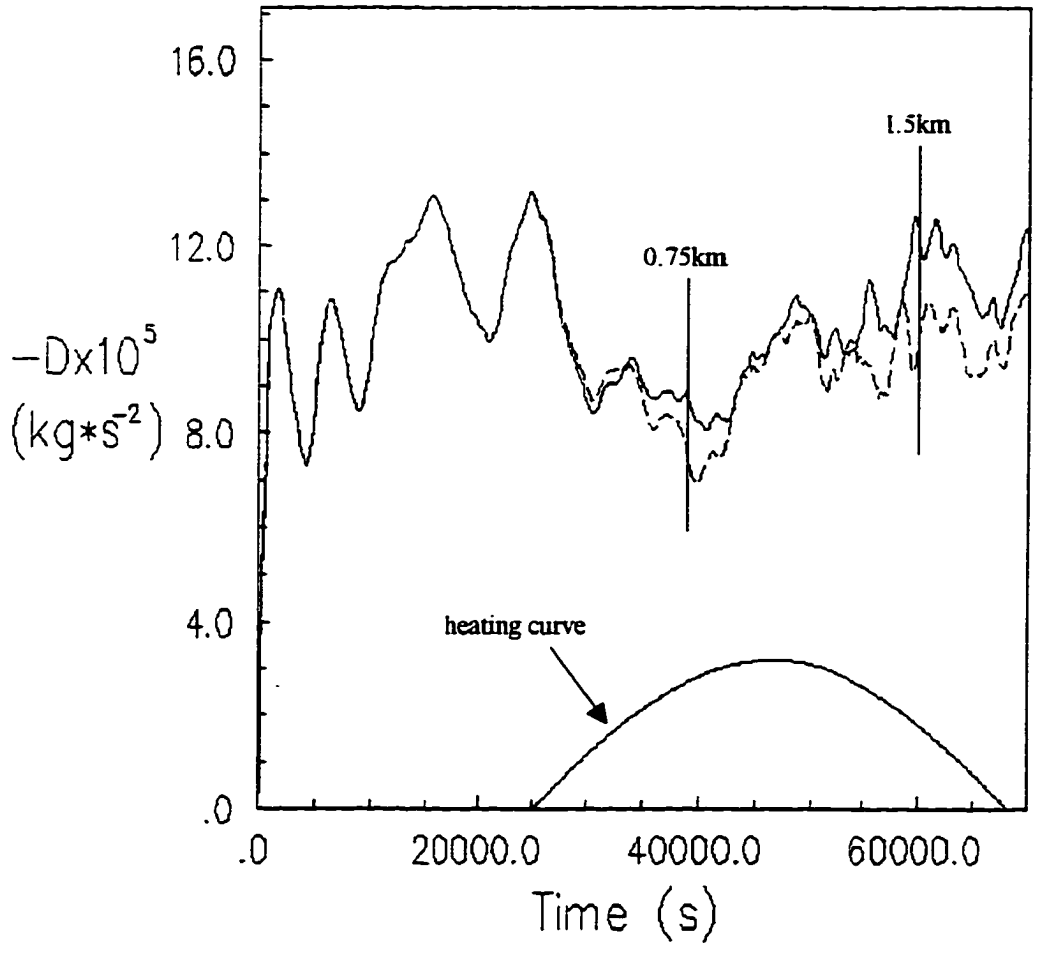

Figure 5.31. Graph of the surface wave drag for the January 9, 1989 Boulder windstorm simulation for the 2305 UTC control (solid line) and heated (dashed line) runs. The heating curve is provided at the bottom of the plot with a maximum heating rate of $200\,w/m^2$. Vertical lines indicate the approximate depth of the mixed layer.

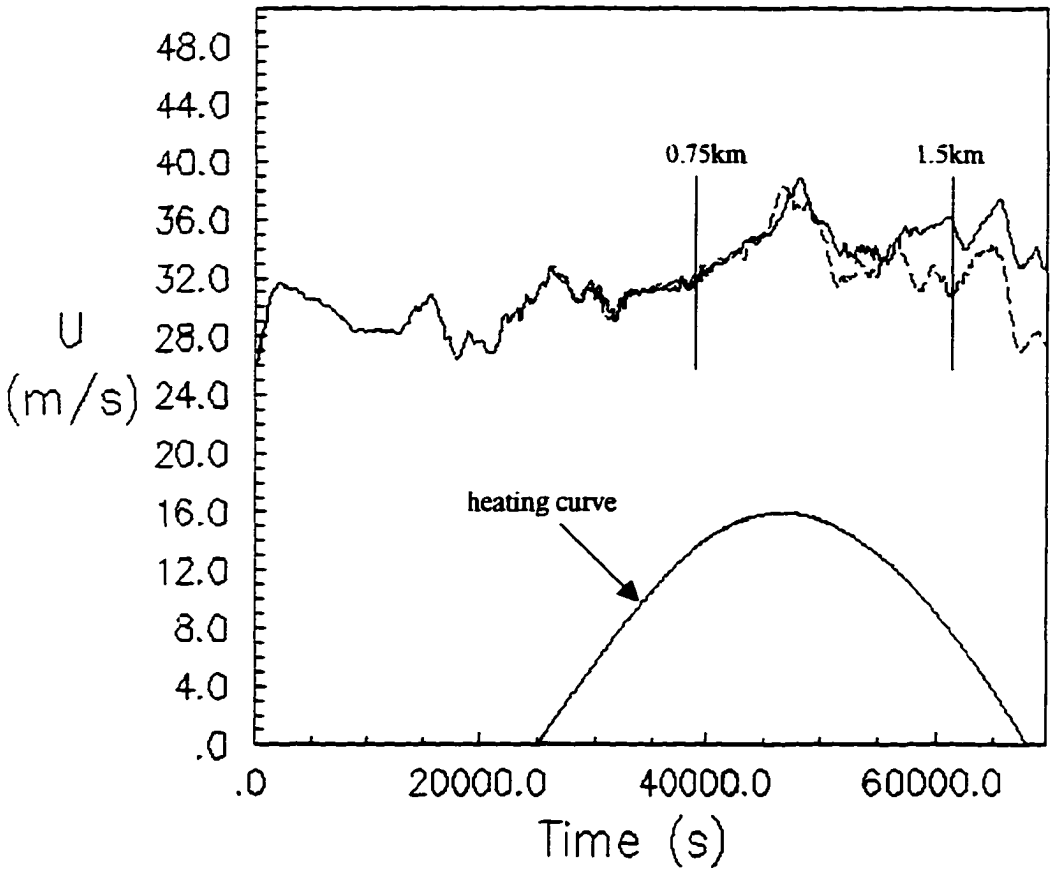

Figure 5.32. Plot of the maximum surface wind speeds for the Boulder January 9, 1989 windstorm simulation for the 2305 UTC control (solid line) and heated (dashed line) runs. The heating curve is provided at the bottom of the plot with a maximum heating rate of $200\,w/m^2$. Vertical lines indicate the approximate depth of the mixed layer.

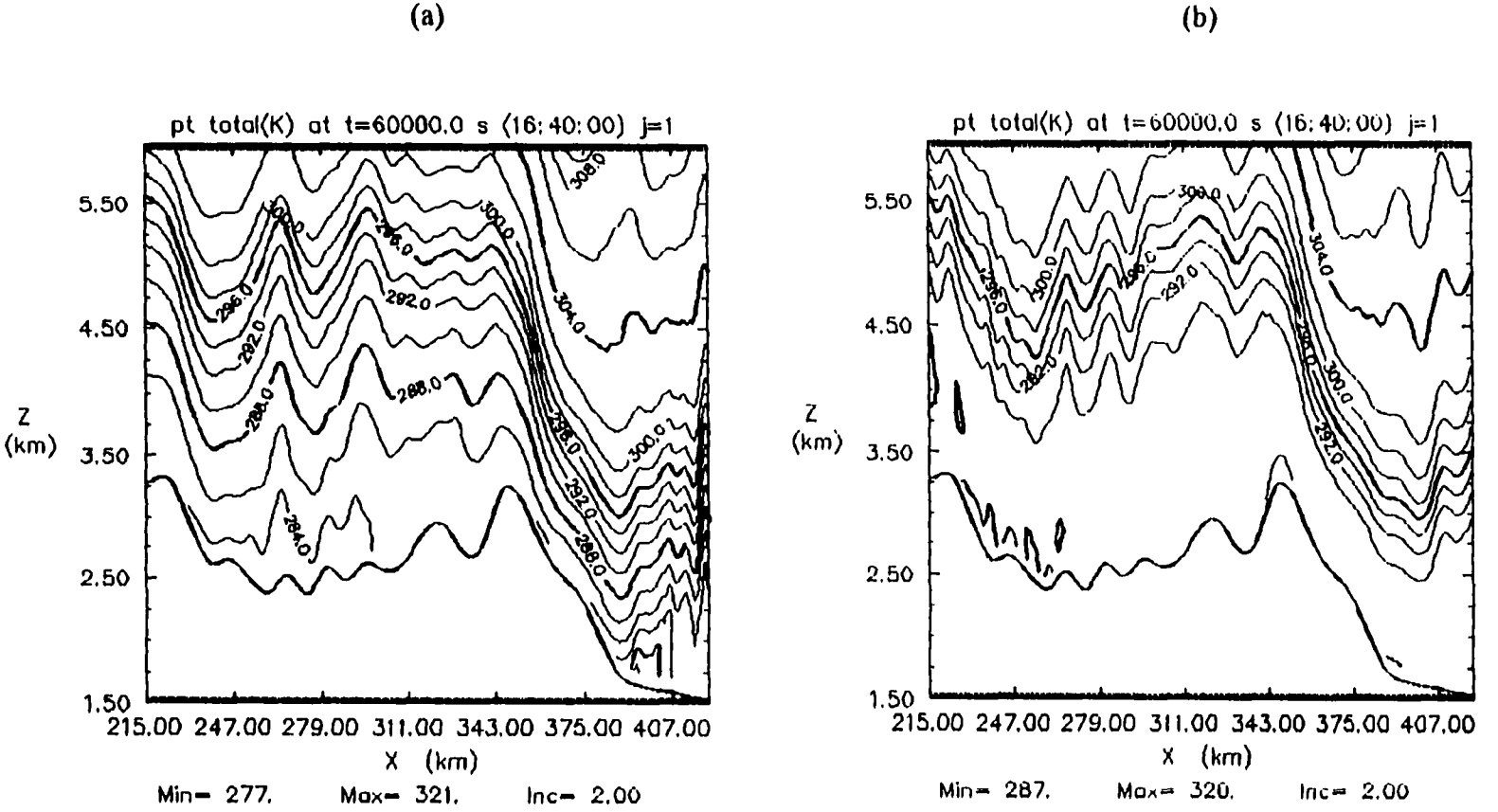

Figure 5.33. Plot of potential temperature at $t = 60{,}000$ seconds for the (a) control and (b) heated 2305 UTC Boulder windstorm simulations. The contour interval is 2.0 $^{\circ}K$.

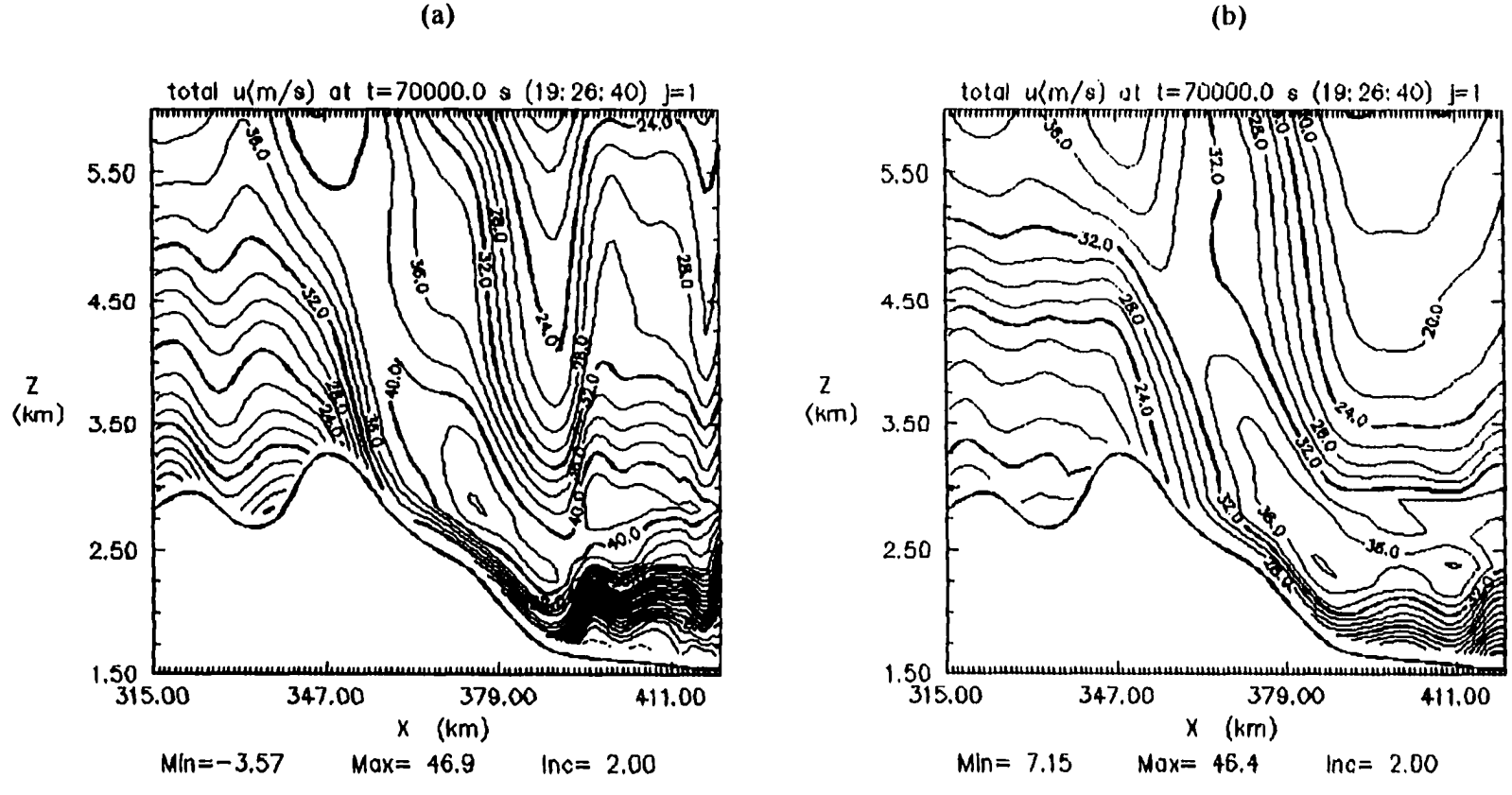

Figure 5.34. Horizontal velocity plots for the January 9, 1989 Boulder windstorm simulation at t = 70,000 seconds for the 2305 UTC (a) control and (b) heated tests. Area shown is the lower 6 km in the vicinity of the mountain peak and city of Boulder The contour interval is 5.0 m/s.

Figure 5.35 displays the perturbation u velocity at selected times for the 2305 UTC control experiment and shows that the highest winds remain near the foot of the mountain. In addition, a strong vertical gradient in wind speed is present. This is qualitatively similar to that shown by the lidar observations (Figure 5.29). Figure 5.36 presents the perturbation u field for the heated case and reveals a general decrease in the elevated jet magnitude as the mixed layer develops. Overall, surface heating acts to decrease the lee side horizontal velocity roughly 10-15%. A comparison of isentropes field for the control run (Figure 5.37a) with the January 11, 1972 simulation given in Chapter 4 reveals two distinctly different windstorm types. The deviation of the potential temperature surfaces and related wave induced critical layer directly over the mountain peak are significantly reduced in the January 9, 1989 case from those of the observations and idealized predictions of the January 11, 1972 Boulder windstorm event. This case exhibits characteristics more like the hydraulic flow analog than the critical layer amplification theory of Peltier and Clark.

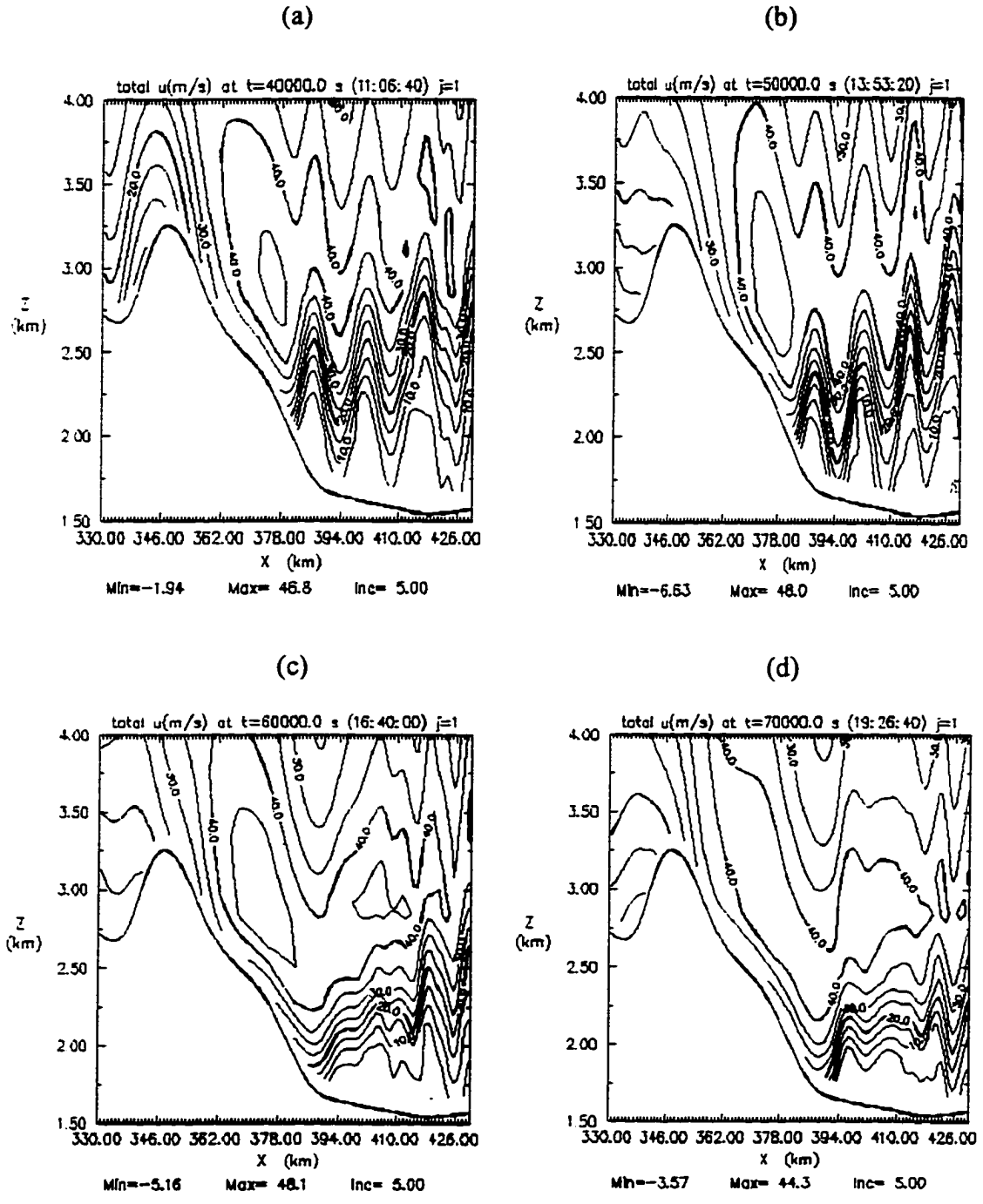

Figure 5.35. Total horizontal velocity on the lee slope for the January 9, 1989 Boulder windstorm control simulation 2305 UTC at $t =$ (a) 40,000 seconds, (b) 50,000 seconds, (c) 60,000 seconds, and (d) 70,000 seconds. The contour interval is 5.0 m/s.

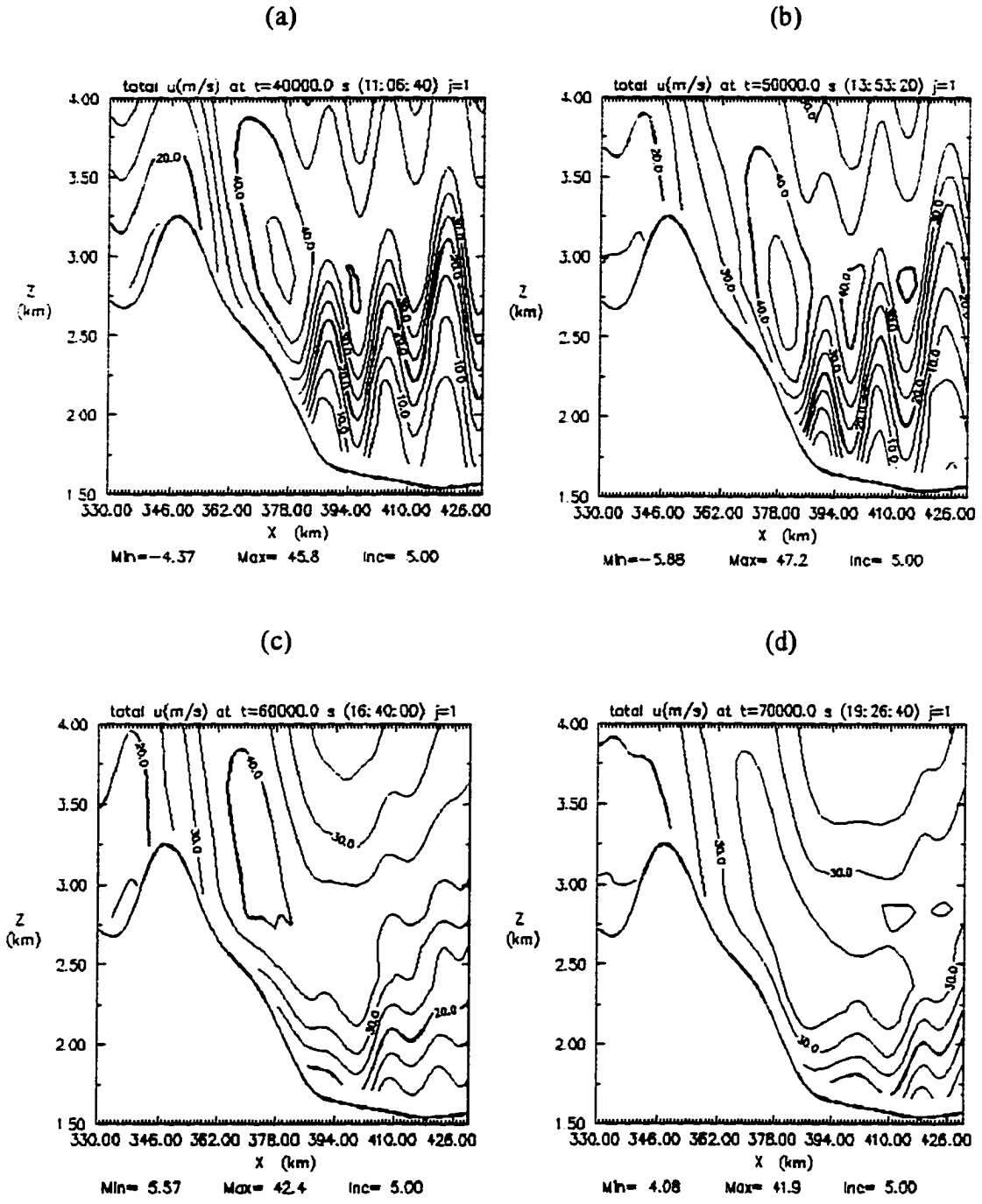

Figure 5.36. Total horizontal velocity on the lee slope for the January 9, 1989 Boulder windstorm heated simulation 2305 UTC at t = (a) 40,000 seconds, (b) 50,000 seconds, (c) 60,000 seconds, and (d) 70,000 seconds. The contour interval is 5.0 m/s.

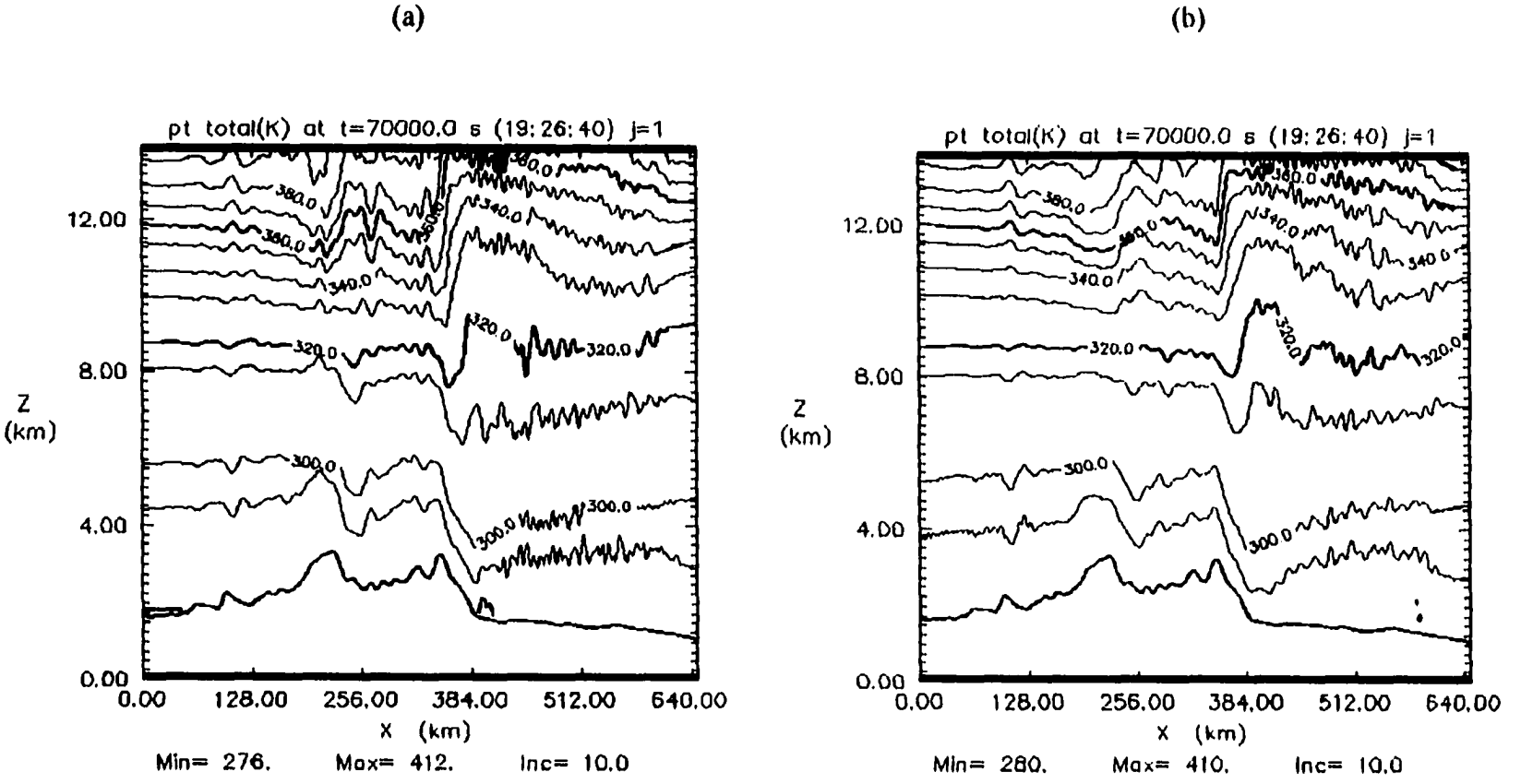

Figure 5.37. Model predicted isentropes at $t = 70{,}000$ seconds for the January 9, 1989 Boulder windstorm 2305 UTC (a) control and (b) heated simulations. The area shown is 647 x 14 km with a contour interval of 10 ° K.

5.7 Discussion

In all but one test, parameterized surface heating reduces the established mountain wave activity, as measured by surface wave drag, horizontal velocity at the surface and aloft, and by the vertical flux of horizontal momentum. Reductions on the order of 30% for the wave drag and 10-15% for the maximum surface winds were common in the heated simulations. The response to surface heating is found to be a function of the mixed layer depth, with deeper surface layers forcing larger reductions in the wave activity aloft. The decrease in the steady state flow for the critical layer experiments is approximately linear in terms of the mixed layer depth. This is contrary to the results from the non-critical layer simulations and linear theory where the impact is observed to be a non-linear function of the neutral layer depth.

In tests displaying wave-breaking characteristics, such as those from the critical layer and $Nh/U = 1.0$ and 3.0 experiments, the surface drag is weakened but a high drag state remains. The transition from the steady high drag state to a low drag state did not occur when influenced by a moderate amount of surface heating. Most of the tests performed here applied surface heating at a rate similar in magnitude to that observed in Central Canada in March. In only a few of the experiments, especially the low mountain height cases did the mixed layer motion approach that expected from potential theory. In all of the high drag simulations, the flow in the boundary layer is dominated by the upper layer wave response. This is expected since the depth of the mixed layer was rarely greater that 1/4 of a vertical wavelength. For the two-layer tests, the surface wave drag was reduced 45% by the end of the heating period. This configuration is

especially vulnerable to surface heating, since the lower layer is only 3km deep. Strong solar heating could all but wipe out the low-level stable layer. The surface wind speed did not undergo such a large decrease. It is likely due to two factors: the drag is a quadratic quantity in perturbation variables and will respond to changes in the flow more rapidly. Secondly, potential flow theory requires an increase in the flow on approach to an obstacle.

In strongly forced flows, the linear theory presented in Chapter 2 over predicts decreases in wave activity as a result of a neutral boundary layer. The largest differences with linear theory were noted in the critical layer tests. For two-dimensional flow, linear theory, as presented in Chapter 2, is quite useful in both qualitative and quantitative terms for the moderately forced heated mountain flows.

CHAPTER 6

THREE DIMENSIONAL HEATED MOUNTAIN WAVE SIMULATIONS

This chapter presents results from two groups of three-dimensional simulations. The experiments are distinguished by mountain shape. A circular mountain shape defines the first and a ridge of finite length with the long axis oriented perpendicular to the base state flow defines the second. The purpose of these experiments is to investigate the effects of surface heating on mountain wave flows in three dimensions.

6.1 Experimental Setup

These simulations can be directly compared with the numerical solutions for the similarly configured two-dimensional heated mountain wave flows. In addition, the circular and finite ridge shaped mountain flows are contrasted qualitatively with three-dimensional linear theory of Phillip's (1984), Smith (1980, 1988, 1989), and numerical results of Reisner and Smolarkiewicz (1994). A cross to parallel flow mountain axis ratio of 5:1 defines the finite ridge shape. This ratio is similar to the observed north south to east west Front Range aspect ratio near Boulder, Colorado. A modified form of (4.2) defines the circular mountain profile:

$$h_m = \frac{h_m}{1+(\frac{x}{a})^2+(\frac{y}{b})^2} \quad . \tag{6.1}$$

For a circular mountain, the parameters a and b are equivalent. For the finite ridge simulations, (6.1) is replaced by the two-dimensional equivalent (4.2) between the north and south ends of the ridge. At the ridge ends, (6.1) is applied directly where y is defined by the distance from each end of the ridge and x is the distance from the ridge line in the direction of the base state flow. For these simulations, the base state flow is directed from west to east.

In each test group, designated by the NLP groups in Table 6.1, three experiments are conducted to test the affects of surface heating over a range of inverse Froude Numbers. The static stability is varied over a range that includes the standard atmosphere. These tests follow those defined in Chapter 5 and are distinguished by their non-linear measure $Nh/U = 3.0$, 1.0, and 0.2. The domain size for all the circular mountain flow simulations was 197x117x75 and for the finite ridge $Nh/U = 3.0$ and 0.2 tests was 197x157x75 grid points in the x, y, and z directions. The $Nh/U = 1.0$ finite ridge simulation required a larger computational domain (237x193x103), owing to observed lateral and vertical boundary condition sensitivities. The initiation and duration of the heating period followed that used in the two-dimensional tests. Aside from the addition of the third dimension, all other experimental variables remained unchanged.

6.2 Results

As before, time series of surface wave drag and maximum surface wind speed and vertical cross sections of selected model fields through the mountain centerline are used to measure the wave activity. The predictions are advanced to a pseudo-steady

Table 6.1 Three Dimensional Heated Mountain Wave Parameter Summary.

Parameter	Circular Mountain	Finite Ridge
nx,ny,nz	197,157,75	197/237,157/193,75/103
Δx (m)	2000	2000
Δy (m)	2000	2000
$\Delta\zeta$ (m)	100,200,250	100,200,250
t (s)	10,20,10	5,10,20
τ (s)	2.5,4.0,4.0	2.5,4.0,4.0
U (m/s)	10	10
Nh/U	3.0,1.0,0.2	3.0,1.0,0.2
N (s^{-1})	0.03,0.01,0.002	0.03,0.01,0.002
h (m)	1000	1000
a_x (m)	15000	15000
a_y (m)	15000	75000
Q (w/m^2)	360,300,60	360,300,60
ω (hrs)	72,27.7,16.6	72,27.7,16.6
$C_h/(\Delta x^4, \Delta y^4)$	0.0005	0.0005
$C_v/\Delta\zeta^4$	0.0005	0.0005
α	0.2	0.2

state prior to the introduction of surface heating. In each test, the magnitude of the pre-heating period wave activity is smaller than the steady state infinite ridge analog and is a function of the blocking characteristics of the flow. According to Smith (1989) blocking along the y=z=0 centerline of a three-dimensional mountain with a ridge width to length ratio of 5:1 occurs at $Nh/U = 1$. When blocking commences, flow is diverted around the mountain by a north-south pressure gradient oriented along the mountain y=0 centerline. For circular terrain shapes, a larger mountain is required to produce blocked flow. This is due to the fact that gravity waves generated at the north and south ends of a finite ridge are dispersive in the y-direction. In the three-dimensional problem, the group velocity in the east-west direction is now a function of the north-south wave number and is less than the environmental flow and consequently the disturbance is swept downstream by the base state current.

6.2.1 Nh/U = 3.0

A summary of the surface wave drag computed along the mountain centerline as a function of Nh/U and H (mixed)/h for all of the three-dimensional heated mountain flow tests is presented in Figure 6.1. The three-dimensional $Nh/U = 3.0$ tests recover only 10% of the normalized surface wave drag realized by the two-dimensional counterpart (see Figure 5.23). These values are far below those expected by the linear theory of Phillips (1984) and Smith (1989). Linear theory predicts the steady state three-dimensional surface wave drag for a circular mountain to be 70% of the two-dimensional limit. For a ridge with the long axis oriented perpendicular to the flow and

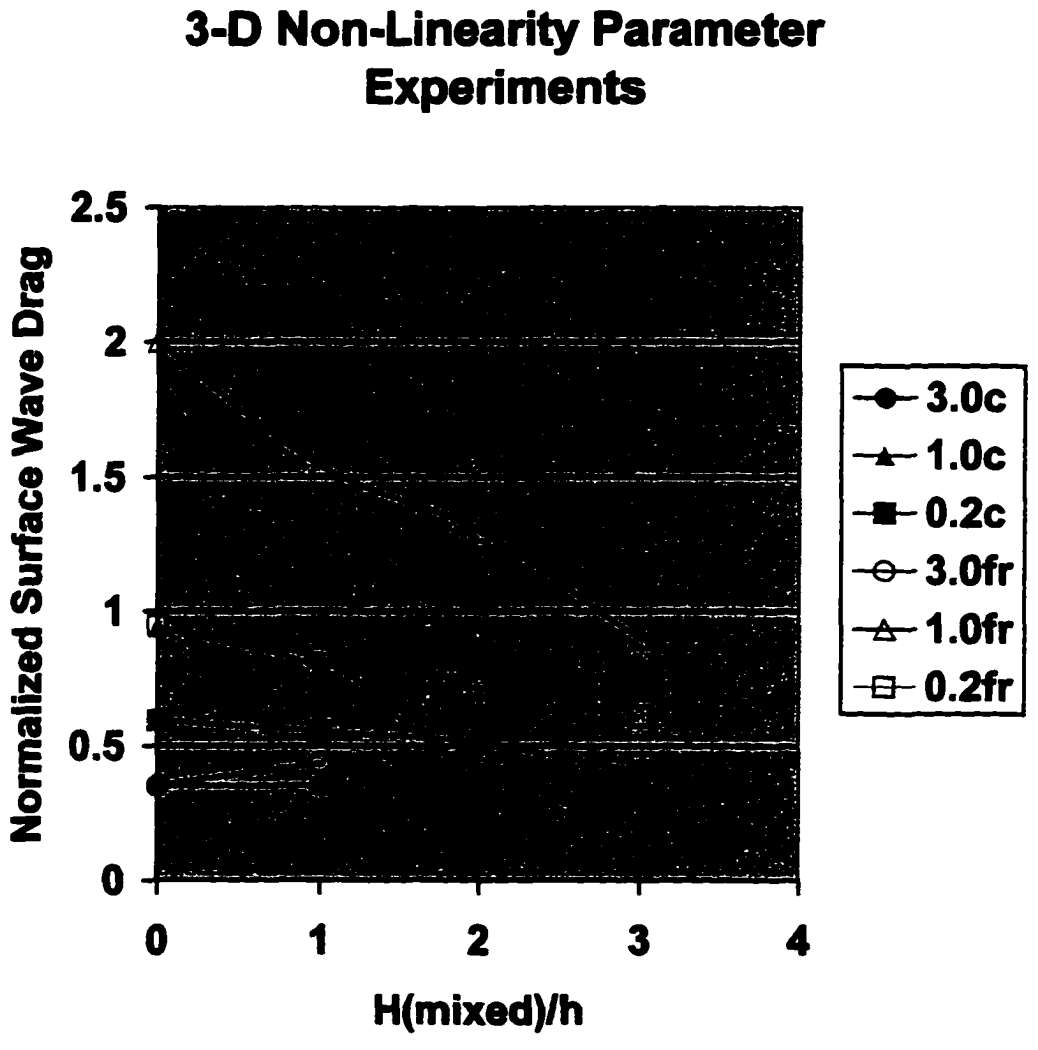

Figure 6.1. Normalized surface wave drag as a function of the ratio of the mixed layer depth H (mixed) to the mountain height h for the three-dimensional heated mountain tests. Values are normalized by linear hydrostatic two-dimensional theory.

a long to short axis ratio of > 4:1, the surface wave drag is expected to be >90% of the infinite ridge value. In this case, the mountain wave is weak, with the strongest perturbations occurring in the v field as air moves around the mountain and converges downstream. In contrast to the two-dimensional simulations, the Nh/U =3.0 circular and finite ridge experiments diverted a significant amount of flow around the mountain. Note the strong nearly horizontal flow around the peak and the lee-side convergence in the circular mountain simulation (Figure 6.2). The heating cycle had little impact on the surface wave drag and other flow characteristics above the boundary layer.

According to Smith's (1989) Figure 1, these tests lie in the region of flow splitting and wave breaking and no longer satisfy his assumptions and boundary conditions. It is apparent that flow separation has dominated the solution, with only a small portion of the flow traversing the mountain. These results are very different from the two-dimensional simulations in which wave breaking is observed above the mountain. A comparison of isentropes along the y=0 mountain centerline from the present model is made with those generated by Reisner and Smolarkiewicz (1994) (Figure 6.3). They used three-dimensional linear theory and a three-dimensional hydrostatic isentropic model to characterize and simulate heated mountain flow over isolated obstacles and the island of Hawaii. Their numerical predictions for Nh/U = 3.0 with no heating are quite similar to those predicted by the current model for a similar Froude number in their numerical simulations.

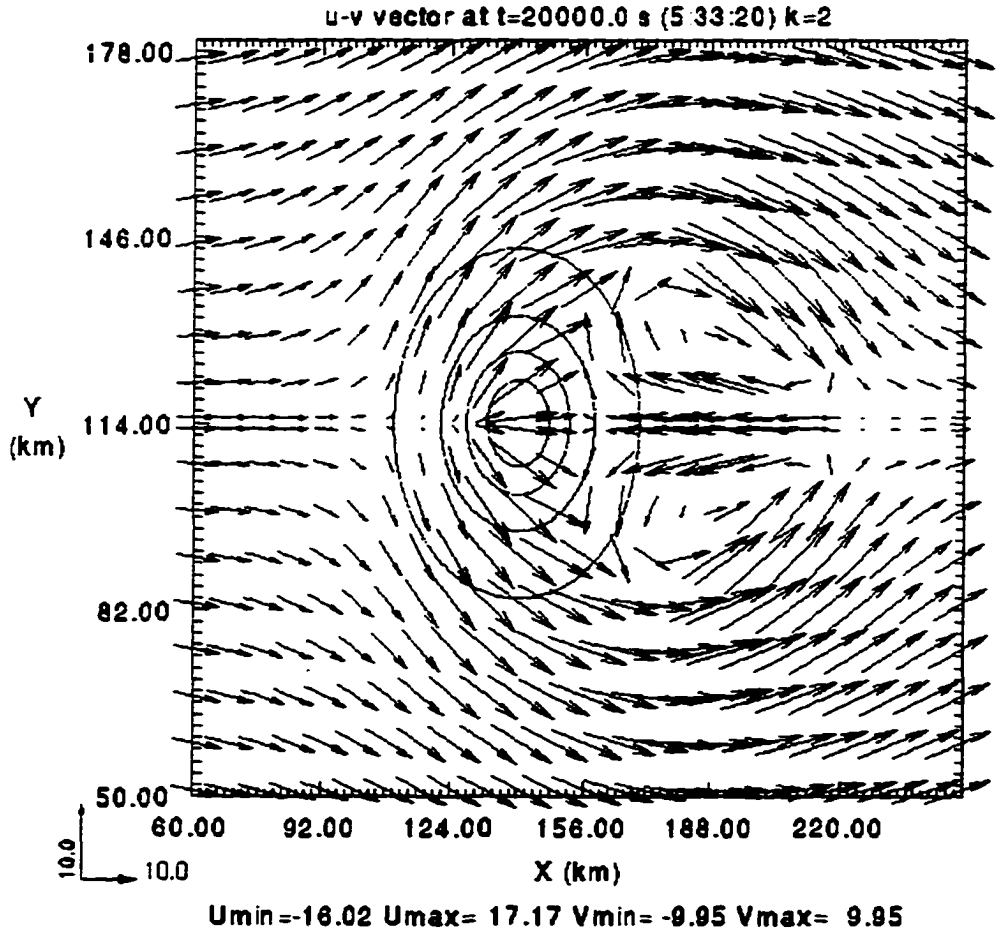

Figure 6.2. Surface horizontal velocity vector plot at $Ut/a = 13.3$ for the $Nh/U = 3.0$ circular ridge test. The terrain contour interval (dotted lines) is 200m. The area displayed is in the vicinity of the mountain peak.

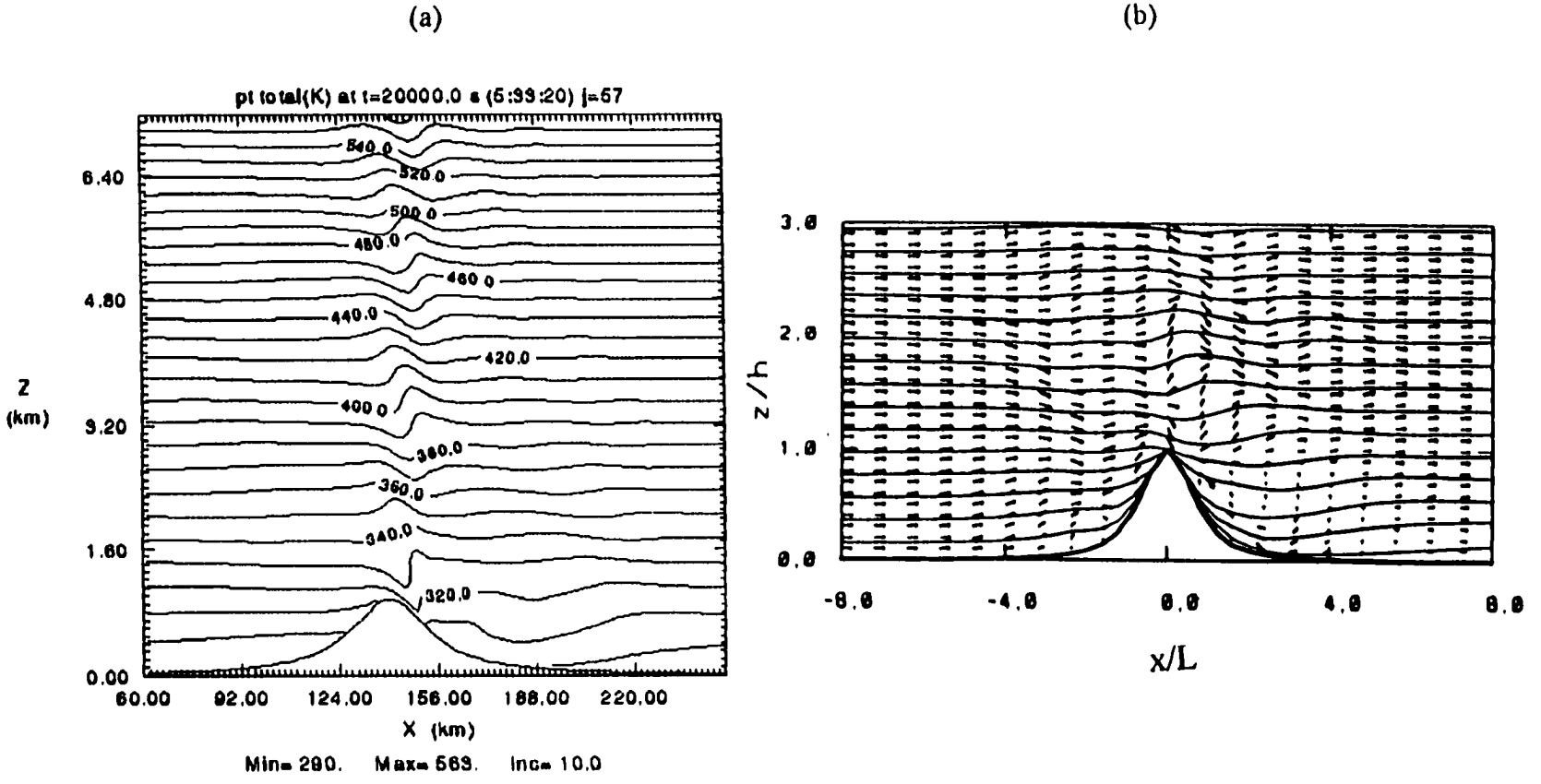

Figure 6.3. Vertical X-Z cross-section of isentropes along the mountain centerline for (a) the present model at t=20,000 seconds Nh/U=3.0 and (b) from Reisner and Smolarkiewicz (1989) (reference solution) for the U/Nh= 0.33 circular mountain flow test. The contour interval in (a) is 10° K and unknown in (b). The cross section is taken from the mountain centerline y=0.

6.2.2 Nh/U = 1.0

Both the $Nh/U = 1.0$ circular and finite ridge tests achieve steady state surface drag states equal to or greater than the two-dimensional linear normalized values. The circular mountain profile test generated a similar gravity wave response to that expected by a linear infinite ridge. During the heating period, both three-dimensional tests underwent a significant reduction in wave drag and surface wind speed (Figures 6.4 and 6.5). The reduction of surface wave drag when the mixed layer depth is approximately 2km for the three-dimensional simulations (approximately 35%) is almost 1/2 that predicted by linear theory (67%) and larger than the value in the two-dimensional $Nh/U = 1.0$ experiment (25%). The corresponding maximum surface wind for the three-dimensional tests is 10% lower than the non-heated steady state values. Near the end of the heating cycle, the maximum surface wind actually increases due to unresolved convection near the surface.

Cross sections of total horizontal velocity and potential temperature prior to heating for the two and three-dimensional ridge cases display strong near-surface flow in the lee of the mountain (Figures 6.6 and 6.7). At $t = 60{,}000$ seconds ($Ut/a = 40$), the total horizontal velocity and potential temperature variables, portrayed in Figures 6.8 and 6.9, reveal significant differences between the infinite and finite ridge experiments. The infinite ridge case exhibits a stronger mountain wave flow, with alternating levels of strong and weak flow above the mountain. The infinite ridge potential temperature and total horizontal velocity fields are similar to those shown in the 17km critical layer tests presented in Chapter 5. Well-mixed critical layers define a significant portion of

the flow above the two-dimensional mountain. The strong flow between the critical layers advects perturbations significant distances downstream. In the finite ridge case, wave breaking is only evident within a few kilometers above the mountain peak and the flow is considerably weaker. Plots of the vertical velocity at the k=2 and k=30 computational surfaces (Figure 6.10) show a spreading of the wave energy in the north-south and downstream directions with height, in accordance with three-dimensional linear theory. The spreading of the wave envelope with height plays an important role in the development of the flow above the mountain. As shown by Smith (1980), in a Boussinesq atmosphere, the wave amplitude of a three-dimensional gravity wave decreases with height above the mountain. On the other hand, the amplitude for the equivalent two-dimensional gravity wave is not a function of height. Therefore, the amplitude for a given mountain profile should be larger for the infinite ridge case. In the finite ridge tests, there is a slight increase in amplitude near the top of the model domain and is likely associated with a decrease in density with height.

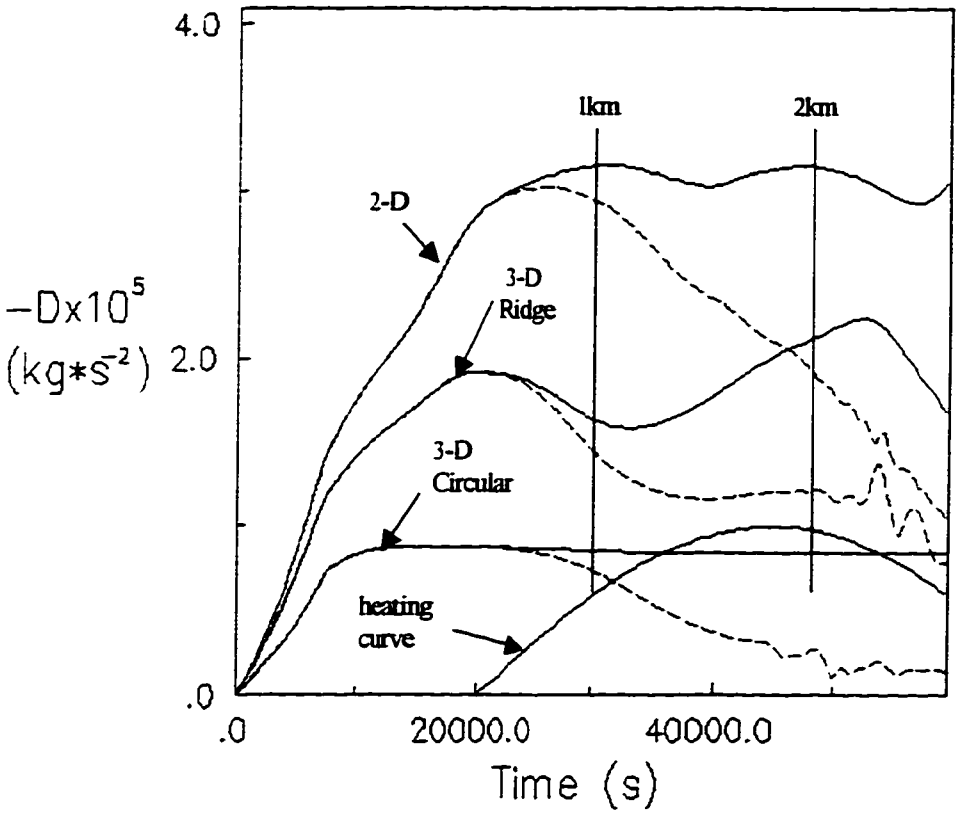

Figure 6.4. Plot of surface wave drag computed along the mountain centerline as a function of time for the Nh/U = 1.0 two and three-dimensional circular and finite ridge mountain wave simulations. The solid lines represent the control runs and dashed lines the heated experiments. The heating cycle was initiated at 20,000 seconds with a maximum of $250\,w/m^2$. The vertical lines represent the approximate mixed layer depth.

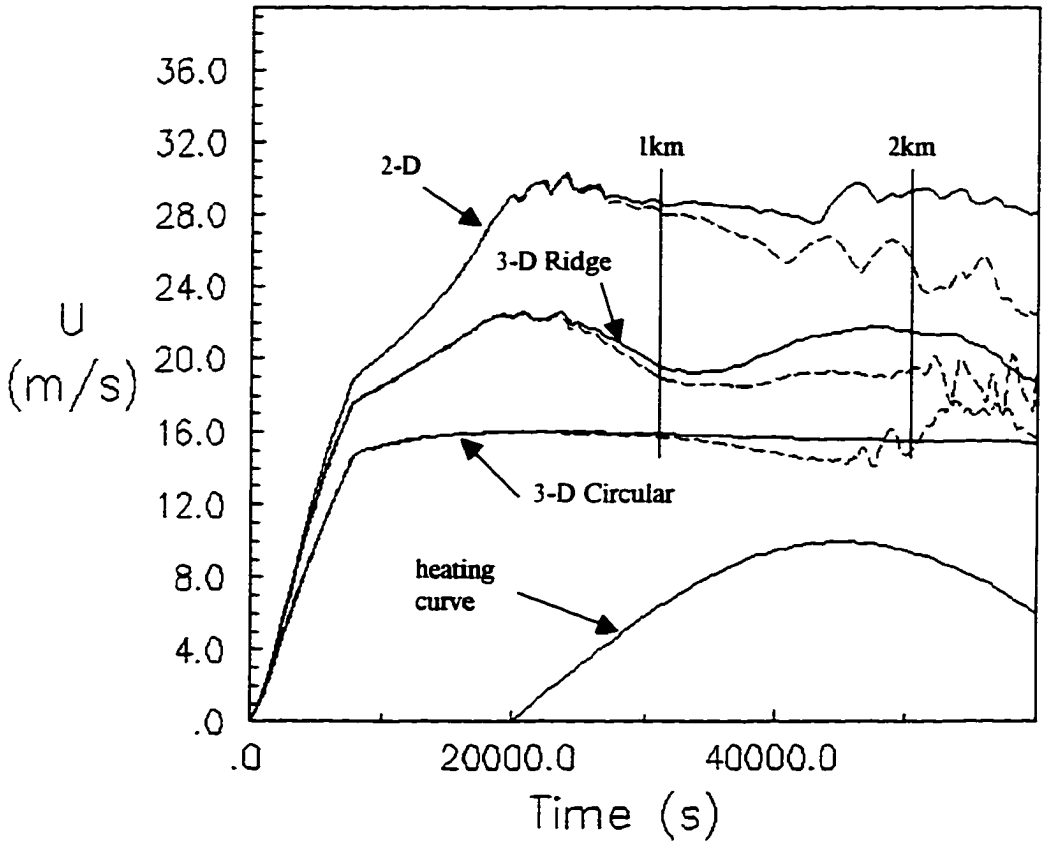

Figure 6.5. Plot of maximum u wind speed along the mountain centerline as a function of time for the $Nh/U = 1.0$ two and three-dimensional circular and finite ridge mountain wave simulations. The solid lines represent the control runs and dashed lines the heated experiments. The heating cycle was initiated at 20,000 seconds with a maximum of $250\,w/m^2$. The vertical lines represent the approximate mixed layer depth.

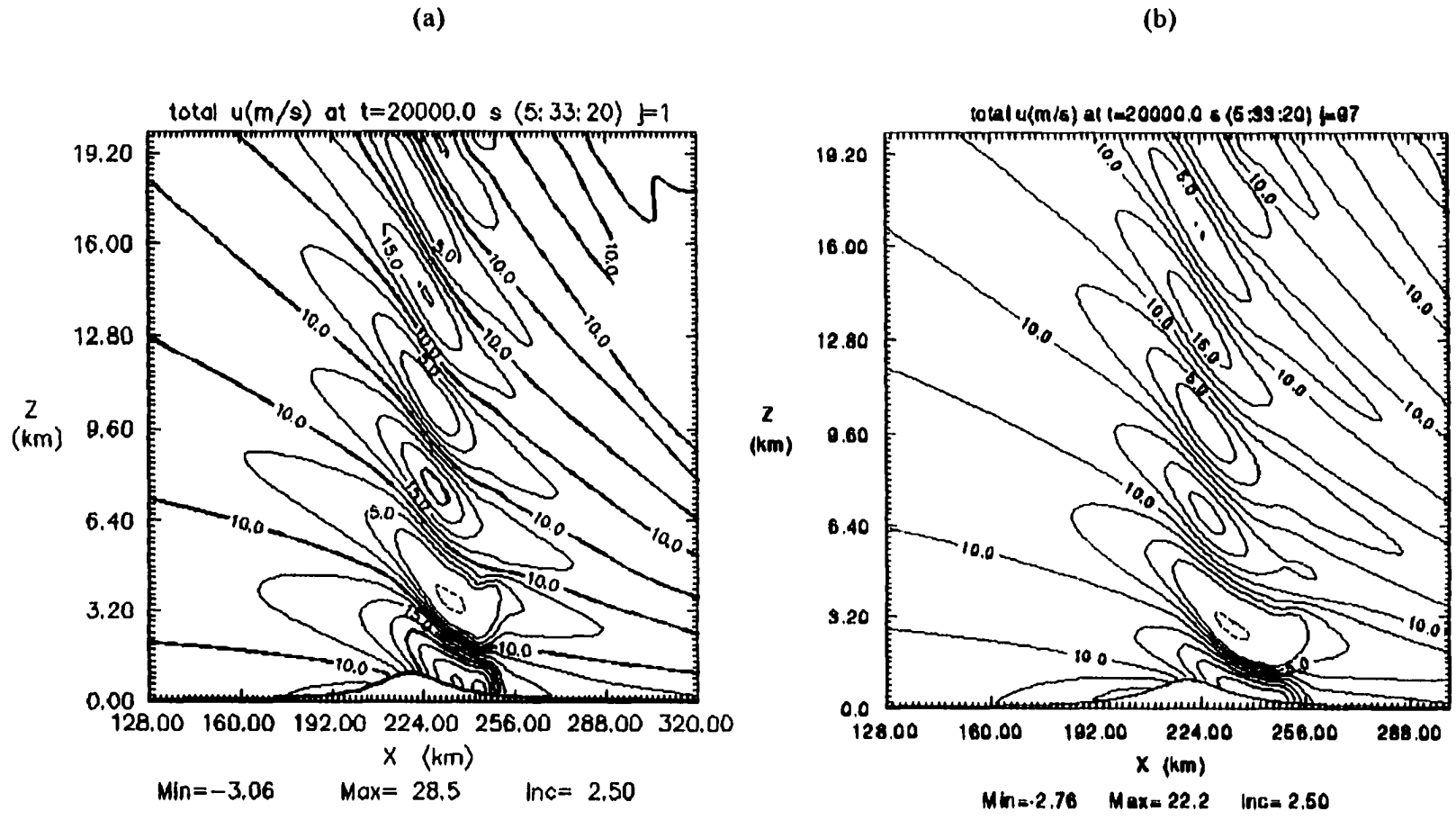

Figure 6.6. X-Z cross-section of total u velocity for (a) infinite ridge and (b) finite ridge $Nh/U=1.0$ mountain wave flows at $t=$ 20,000 seconds. The area depicted for the three dimensional test is the centerline of the ridge. The contour interval is 2.5 m/s.

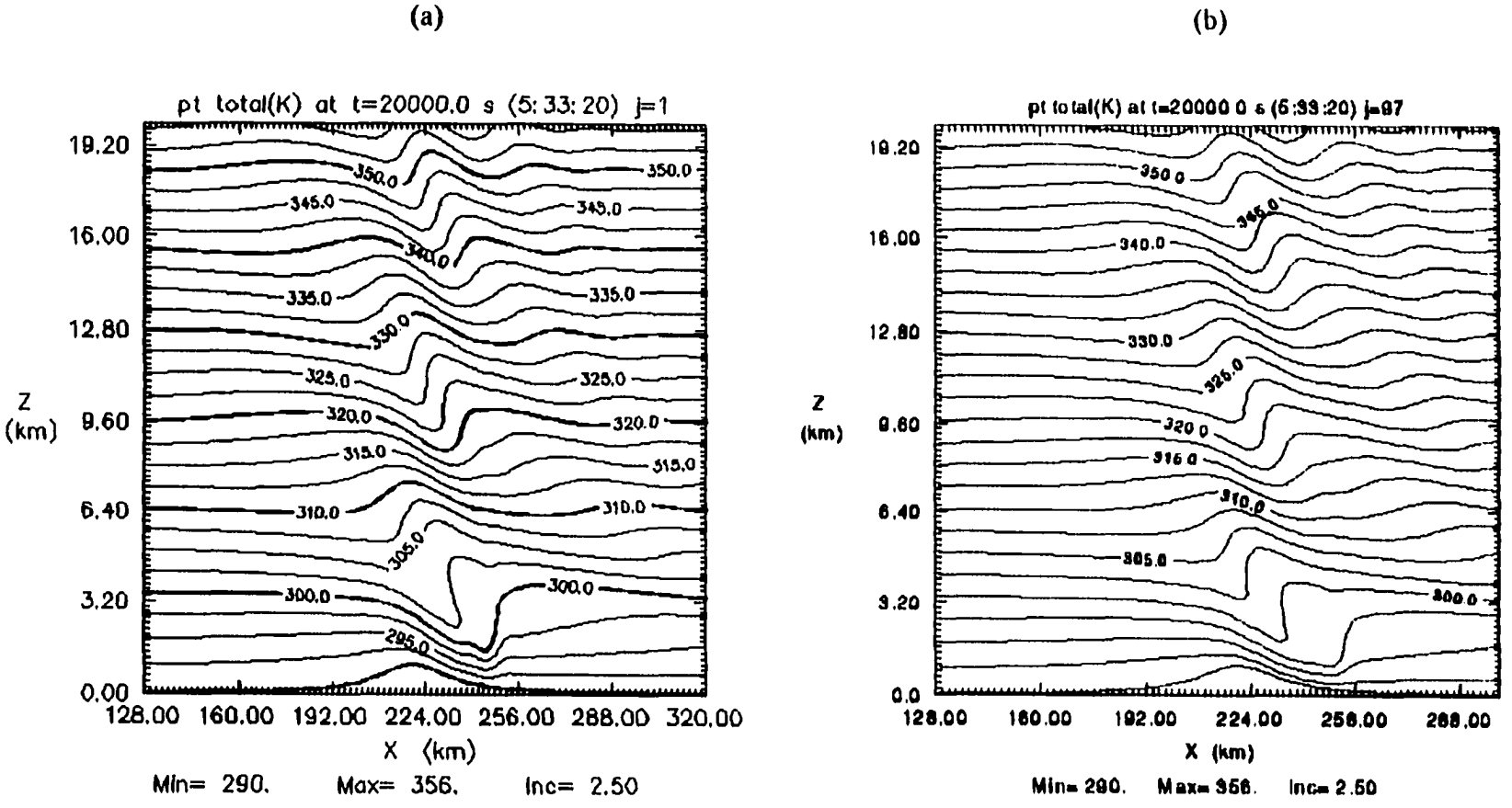

Figure 6.7. X-Z cross-section of potential temperature for (a) the infinite and (b) finite ridge $Nh/U = 1.0$ mountain wave flows at t=20,000 seconds. The area depicted for the three dimensional test is the y centerline of the ridge. The contour interval is 2.5° K.

(a)

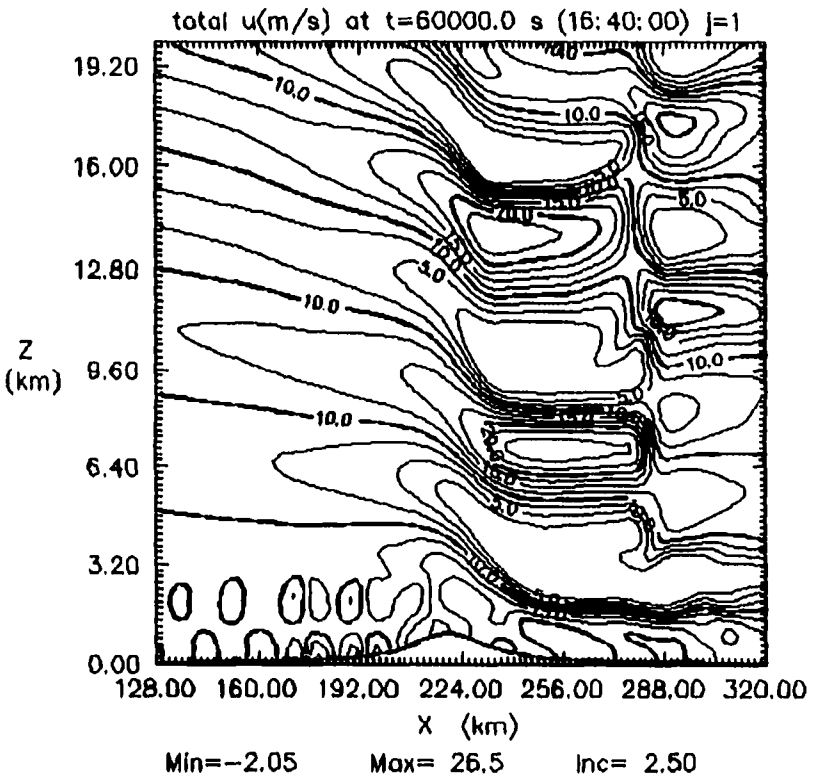

(b)

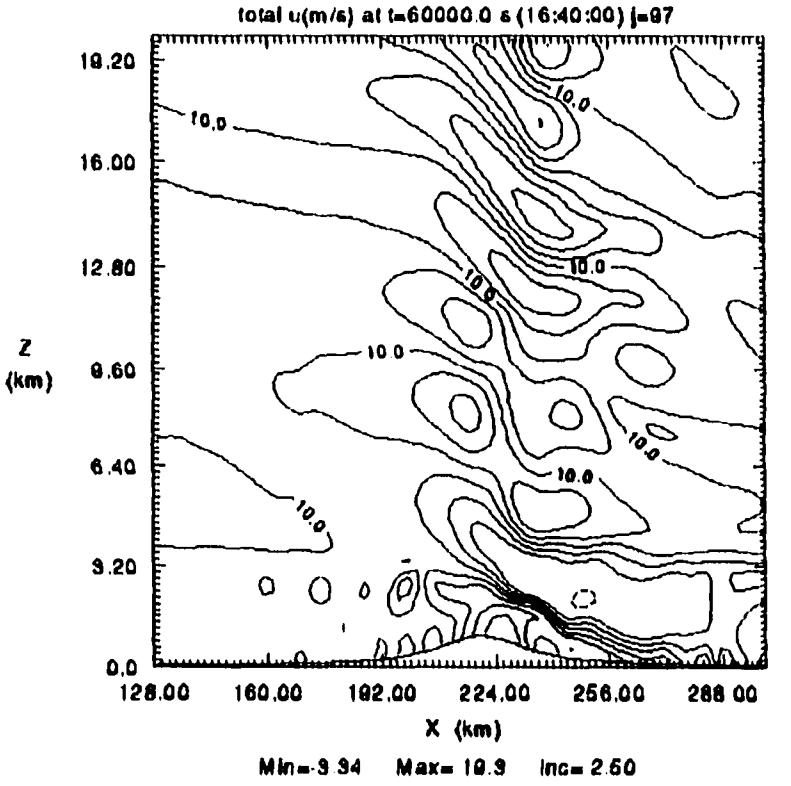

Figure 6.8. X-Z cross-section of total u velocity for the (a) infinite and (b) finite $Nh/U = 1.0$ heated mountain wave flows at $t =$ 60,000 seconds. The area depicted in the three-dimensional test is the centerline of the ridge. The contour interval is 2.5 m/s.

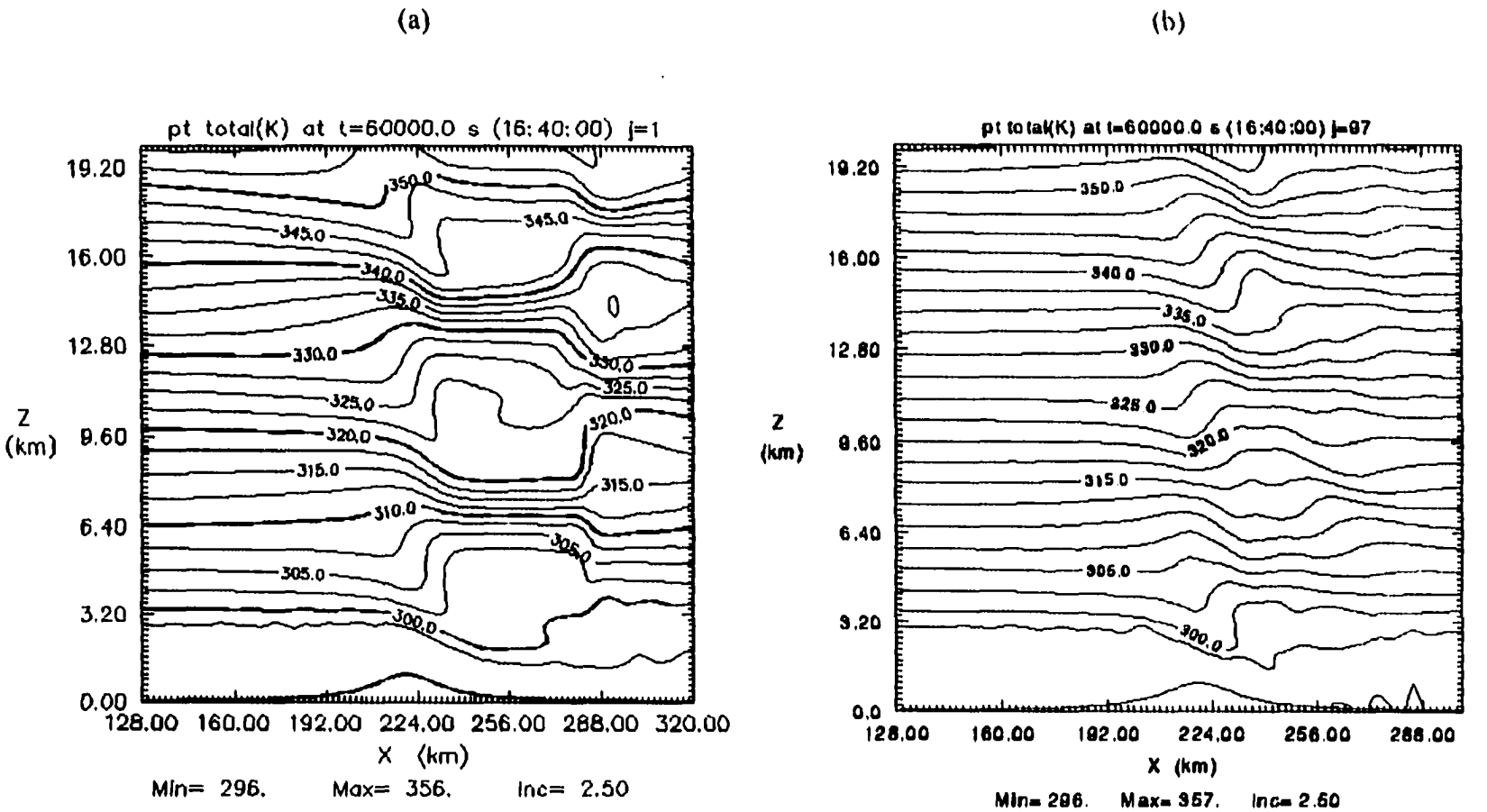

Figure 6.9. X-Z cross-section of potential temperature for the (a) infinite and (b) finite $Nh/U = 1.0$ heated mountain wave flows at $t = 60{,}000$ seconds. The area depicted in the three-dimensional plot is the centerline of the ridge. The contour interval is 2.5° K.

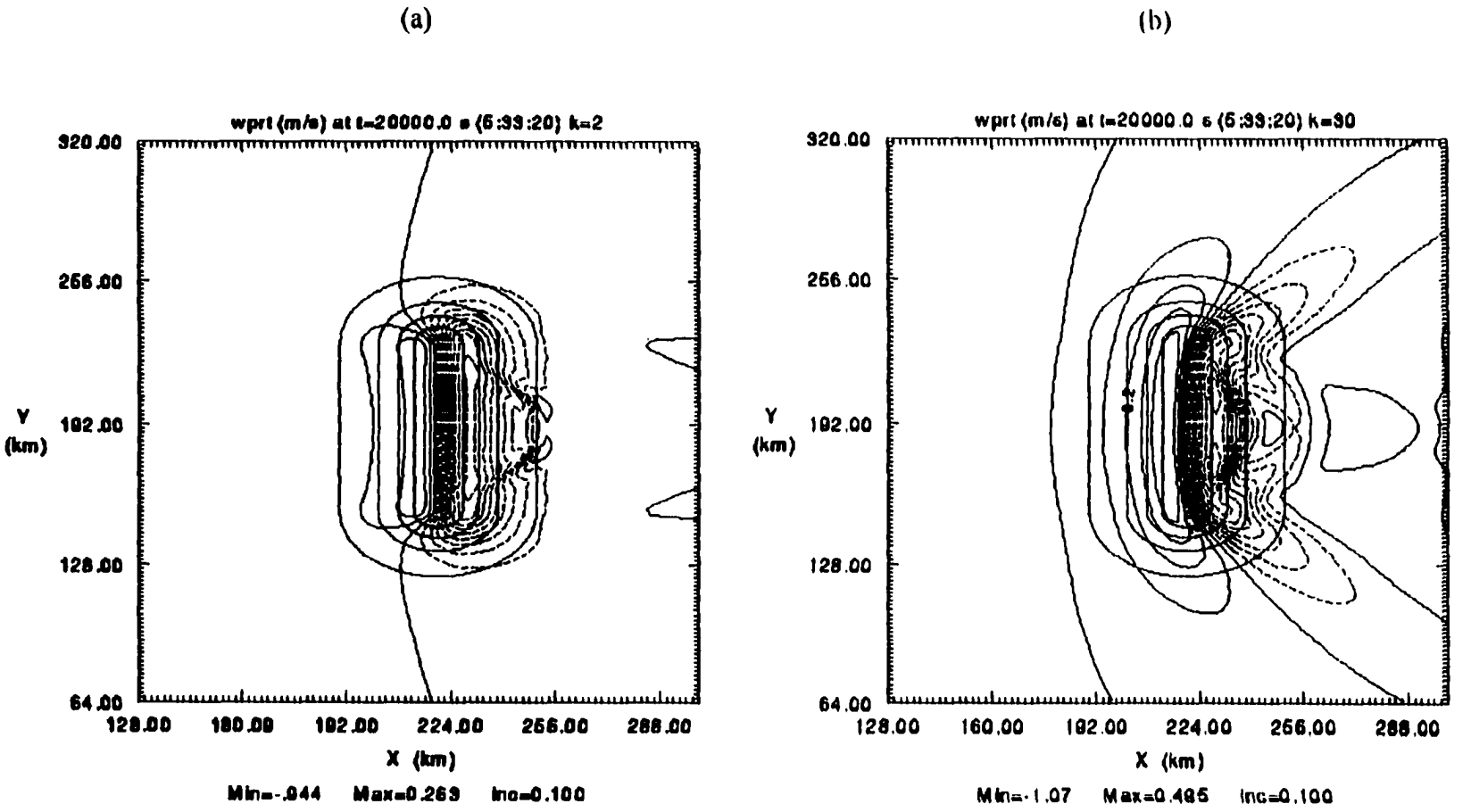

Figure 6.10. X-Y plot of vertical velocity at t = 20,000 seconds for (a) k=2 (surface) and (b) k=30 computational levels from the Nh/U = 1.0 finite ridge simulation. The w contour interval is 0.1 m/s and the terrain contour interval is 200m.

6.2.3 Nh/U = 0.2

These tests, with a nonlinear measure $Nh/U = 0.2$, are more closely related to linear theory than the two prior experiments and those presented in Chapter 5. The corresponding static stability is small and the vertical wavelength large, approximately 60km. The pre-heating steady state surface drag is nearly equivalent to the linearized analytical values for both the circular and finite ridge tests (see Figure 6.1). Both tests experience diminished surface wave drag and maximum surface wind speed (not shown). The loss in wave drag for the heated finite ridge and circular mountain profiles is 35% and 25%, respectively. The reduction in wave drag for the finite ridge is nearly identical to the two-dimensional counterpart and accounts for only 50% of that predicted by two-dimensional linear theory (Figure 6.11). The response in the surface wind field is similar between the two and three-dimensional tests (not shown). Due to the development of unresolved convection, an increase in maximum surface wind is noted near the end of the heating period. The similarity between the finite and infinite is due to the weak stratification. Smith (1988) shows that the perturbation pressure near the surface is a direct function of the stability. If the gravity wave perturbation decreases, the cross-stream velocity also decreases and more of the incident flow traverses the mountain.

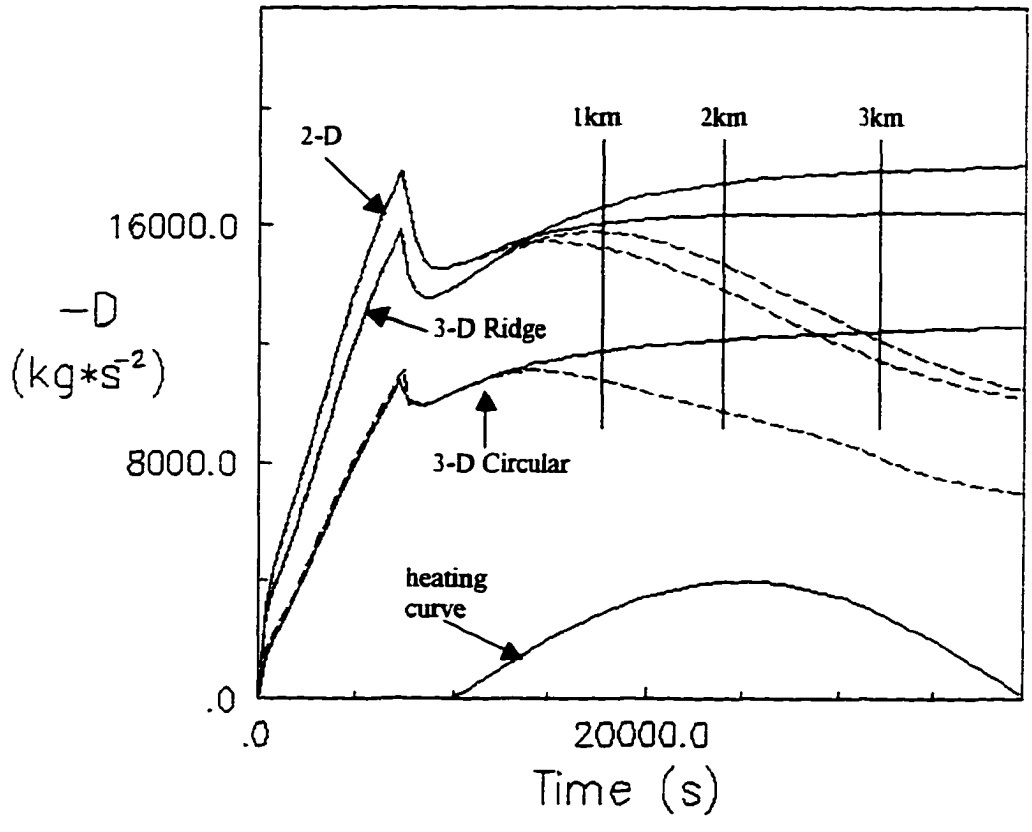

Figure 6.11. Plot of surface wave drag along the mountain centerline as a function of time for the $Nh/U = 0.2$ two and three-dimensional circular and finite ridge mountain wave simulations. The solid lines represent the control runs and dashed lines the heated experiments. The heating cycle was initiated at $t = 10{,}000$ seconds.

6.3 Discussion

The results suggest that the largest differences are associated with the development of flow around the mountain and not associated with the heating aspects of the simulation. For high Froude number tests ($Nh/U = 0.2$), the two and three-dimensional finite ridge flow characteristics are very similar in both the pre- and post heating periods. These tests were found to provide the best fit to linear theory. This is expected since the non-linear measure (Nh/U) is small.

For the low Froude number flows tests ($Nh/U = 1.0$ and 3.0), the differences in the solutions were dominated by whether the low-level flow circumvented or traversed the mountain profile. The factors that determine the near surface flow include the base state stability (N), the base state wind (U) and the mountain profile (a, b, h). The $Nh/U = 3.0$ experiments produced the largest deviations from the infinite ridge case. The three-dimensional runs produced significantly reduced perturbations aloft and surface wave drag when compared to the two-dimensional counterparts. A significant portion of the upstream flow is directed around the mountain (see Figure 6.2). Reisner and Smolarkiewicz's (1994) simulations of flow over an obstacle with $U/Nh = 0.33$ compare favorably to the present model's $Nh/U = 3.0$ results. Despite the differences in the heating function strength and spatial orientation, the model predicted lee wake regions are qualitatively similar. Only a weak gravity wave is present above the mountain, as indicated in the potential temperature field displayed in Figure 6.3.

For the marginally non-blocking flow case ($Nh/U = 1.0$), finite and infinite ridge experiments were qualitatively similar in terms of the pre-heating gravity wave

response with some notable quantitative differences. The finite ridge pre-heating wave drag is nearly 50% of the infinite ridge counterpart. At the conclusion of the heating period the potential temperature and total horizontal velocity display large differences in the flow field aloft, but the gap in surface wave drag is considerably smaller. The decrease in wave drag due to heating is qualitatively similar in terms of percentage (25% vs. 35%) from the pre-heating values in the two and three-dimensional tests, respectively. Phillips (1984) suggests that an elliptically shaped ridge with a long to short axis ratio > 4 will realize >90% of the infinite ridge surface wave drag. In the strongly non-linear tests presented here, a mountain width to length ratio of 5:1 produces a pre-heating steady state wave drag approximately 75% of the infinite ridge solution and two times the two-dimensional linear normalized estimate. Linear theory does a fair job in the marginally blocking cases.

The circular mountain shape tests failed to produce high drag states over the range of Froude numbers examined here. For the configurations that force strong mountain wave responses, the parameterized surface heating significantly impairs the mountain wave flow. The two-dimensional approximation is qualitatively similar to the finite ridge experiments but notable differences remain which are not well represented by linear theory. If blocking is an issue, the resulting three-dimensional flow pattern can be markedly different from the two-dimensional case. In this case, the introduction of surface heating has little effect on the existing weak mountain wave flow aloft.

6.4 Notes on Other Three Dimensional Simulations

Several attempts were made to simulate the January 9, 1989 windstorm in three dimensions using smoothed topography. The results within the first 10 hours are quite good, with a strong response generated in the lee of the mountain along the Front Range, but the simulation degrades during the heating cycle, preventing any useful interpretation. The problem is believed to be associated with the model mass balance. Approximately 10% of the model mass is lost during the second half of the experiment. Both the control and heated tests experienced similar losses in mass and a domain wide deceleration of the flow. The problem can be traced to significant perturbations in the normal velocity component at the upstream boundary. The decelerated flow on the windward side of the Front Range decreases the amount of mass entering the model domain. At the same time, air moves around the mountain range towards Wyoming to the north and exits the model domain. Equations (3.17) and (3.18) in combination with the other predicted variables do not conserve mass at the lateral boundaries. The vast horizontal extent of the mountains forced a compromise between computer resources and safe modeling practices. The resulting three-dimensional computational domain is not able to prevent strong perturbations at the lateral boundaries. Methods exist that can reduce boundary influences. These include nested grid techniques and specifying the lateral conditions from another larger scale model. Both are viable options but are not a part of present model's framework. The issue of strong forcing at a nested grid boundary or a pre-specified condition is only now being investigated and demands further study. The difficulty with accurately representing the flow over the Front Range stems from the vast extent of the Rocky Mountains in three of the four lateral directions.

For a high-resolution simulation (order of 400-meter horizontal grid spacing) a minimum of two nested grids is required inside a larger grid spanning hundreds of kilometers on a side. This configuration would allow strong flow in the lee of the mountain to be resolved and the important upstream conditions to remain relatively undisturbed. Other models, such as the one used by Clark et. al. (1994), incorporate multiple nested grids and update the lateral boundaries from a larger domain model. The physical domain is frequently set to 1200 by 1200 km in order to reduce the lateral boundary influences (personal communication with Bill Hall at NCAR).

CHAPTER 7

DISCUSSION

7.1 General Results

Linear theory builds a foundation for the understanding of the response of a stratified flow over a mountain (Klemp and Lilly, 1975). Gravity wave strength is a function of the static stability, with higher stabilities achieving stronger wind speeds (up to the point of upstream blocking). The initial response in a gravity wave flow is attributed to a linear term, the vertical advection of the base state density. But as Durran (1992) shows, linear theory can either under or overpredict the wave response of a two-dimensional mountain wave, depending on the upstream wind and density profiles. In a neutrally buoyant environment, gravity waves do not exist. In this situation, potential flow (if other waveforms are absent) dominates the physical processes. The perturbations associated with a neutrally stable flow decrease with increasing distance from the obstacle. The anticipated result is that deeper neutral layers correspond to smaller deflections in an overlying stable layer.

The simplified two-dimensional linear analytical solution to a two-layer atmosphere presented in Chapter 2 demonstrates that a well-mixed boundary layer reduces the existing gravity wave activity in the stable layer aloft by an appreciable amount. The neutral layer is assumed to be horizontally uniform and the result of a well-mixed convective boundary layer. This application of the upstream boundary condition is notably different from Reisner and Smolarkiewicz (1994), where the heating rate is a function of the mountain height. The present form allows for heating

far upstream of the mountain, simulating large-scale diurnal heating. For a hydrostatically forced mountain flow, linear theory predicts the decay of wave activity (Figure 2.2). For non-hydrostatic modes, the reduction of the wave activity is a function of horizontal wavelength with shorter mountains exhibiting higher reductions. The decreases in wave activity are modified significantly if a strong inversion is introduced at the top of the mixed layer. Depending on the strength of the inversion, the reduction in wave activity could be reversed, as was the case for a $10^{\circ}K$ inversion. The results from the linear analysis, related to an inversion at the top of the surface layer, compare favorably with those of Klemp and Lilly (1975).

In the numerical experiments, the amplitude of the mountain wave flow aloft is largely insensitive to the method of heat redistribution. Tests indicate that either the explicit or parameterized turbulent mixing methods are adequate for distributing the heat in the mixed layer. Both the timing and magnitude of the integrated momentum flux in the layer aloft were found to be comparable between the two mixing length methods. The explicit method generated short wave length gravity waves at the top of the mixed layer. These gravity waves did not contribute significantly to the pre-existing vertically propagating modes. An important result is that the magnitude of the mountain wave response to parameterized surface heating is a function of the mixed layer depth, with deeper mixed layer producing larger reductions from the pre-heating steady state values. This is true for both the linear and strongly non-linear flow regimes. In experiments where high drag states developed, a mixed layer of appreciable depth inhibits the wave response, but an elevated drag state remained.

The difference between the two and three-dimensional tests were most notable for small Froude number flows, or block flow. In these situations, only weak mountain waves developed and surface heating had little impact on the solution. For non-blocked flows with cross to parallel flow axis ratios >4:1, the effects of surface heating on a three-dimensional mountain wave could be approximated by the two-dimensional case. For circular mountain shapes, the control and heated mountain wave statistics are significantly lower that the two-dimensional equivalent.

7.2 Comparison with Observations

The primary objective of this work is to investigate the role of the diurnal heating cycle in downslope windstorm climatology. The tests and analyses were designed to focus on the heating portion of the diurnal cycle. Results from both the linear analysis and the numerous model simulations indicate that strong mountain waves and downslope windstorms are sensitive to parameterized surface heat fluxes. Both the analytical and numerical modeling efforts concur, surface heating decreases the strength of the windstorm. These results are in agreement with the observational studies of Whiteman and Whiteman (1974). The daily windstorm frequency distribution exhibits a distinct minimum just after the maximum solar radiation period, a time when the mixed layer is near its maximum depth. One numerical experiment included a parameterized nocturnal cooling period. The results from that test indicate a decrease in maximum surface winds during the heating period and an increase in wave activity during the cooling period, as measured by maximum surface wind speed and

integrated surface wave drag. This test, although representing a small sample size, supports the observed day and nighttime windstorm frequency climatology.

The seasonal trends shown by Julian and Julian (1969) (Figure 1.1) are more difficult to fit to the results presented here, since model heating rates were chosen to match observations from January through March, and the simulations were held to less than 1.5 days in duration. The seasonal minimum observed during the summer months may be due to weak tropospheric stability and light cross-mountain flow.

In terms of specific windstorm events, only one experiment was performed. The January 9, 1989 Boulder, CO windstorm simulation, incorporating a smoothed two-dimensional mountain profile and observed base state atmospheric data, predicted noticeably weaker wind speeds (15%) and surface wave drag (15-20%) on the lee of the mountain at the conclusion of the heating cycle. The maximum surface wind speed time series for the heated test does not register a significant deviation from the control run until seven hours into the heating cycle. This may be due to a positive velocity perturbation associated with neutral layer development near the mountain peak combined with the base state wind sheer.

The simulation was limited in many respects since is was two-dimensional, used a single sounding to initialize the domain wide model variables, and incorporated fixed inflow boundary conditions. Yet, it was able to reproduce a number of the observed windstorm characteristics, such as elevated jet region on the lee slope and strong downslope winds similar in magnitude to those observed in Boulder. The time series of the observed maximum surface wind speed peaks near noon January 9, 1989 and

steadily decreases through the afternoon hours. This observation supports the results presented here, but may be fortuitous, as the windstorm may have been adjusting to other upstream influences.

7.3 Application to Forecasting

As presented in Chapter 1, forecasting the onset, duration, and dissipation of downslope windstorms remains a challenge. With time scales on the order of a day, disturbance energy can be transported to great heights above and downstream of the terrain feature, requiring a large model domain. For numerical predictions conducted over a relatively short time period (a few hours), the onset and amplitude of the downslope windstorm remains a strong function of grid resolution and boundary conditions. Results presented in Chapter 4 stress the need for significantly enhanced vertical resolution (minimum 250m) in wave breaking regions. Tests of the lateral boundary conditions (not shown), the bulk of which were reported by Durran et. al. (1993), were found to have a profound effect on the windstorm development phase. In some instances, a specific lateral condition on the normal velocity component (Orlanski, 1976) prevented the development of a high drag state entirely.

For strong mountain wave responses, those that are most important to forecasters along susceptible mountainous regions, linear theory overpredicts the decrease of non-linear wave activity due to a developing mixed layer. This overprediction of the wave reduction varied in magnitude from 10% to 100% in the numerical simulations. Including a small inversion in the linear analysis, similar to that developed by the parameterized turbulent mixing, improves its use as a forecasting tool.

It is quite capable of predicting the trends in measurable mountain wave quantities such as wave drag, velocity perturbations, and momentum flux transfers.

Results from the analytical and numerical studies presented here provide a guide to improving windstorm forecasts. Whether it is an empirical approach or a three-dimensional time dependant numerical model, the diurnal cycle contributes to the strength of the windstorm. The numerical tests show that parameterized turbulent mixing is sufficient for capturing the time dependant mixed layer height. This is especially useful to mesoscale models, as it relaxes the horizontal resolution requirement. In terms of global climate modeling, the analytical result may be quite useful. Climate models, due to lack of computer resources, are unable to resolve gravity waves and thus, parameterize the transfer of mountain generated momentum flux. The parameterized momentum transfer formulation could be modified, following the analysis in Chapter 1, to include the contribution from a neutral surface layer.

7.4 Future Work

This study did not thoroughly investigate the cooling period of the diurnal cycle. Only one test, as an extension of a heated experiment, included parameterized nocturnal cooling. The results indicate that increases in the low-level static stability, associated with nocturnal cooling, forced amplification of the mountain wave, in support of windstorm climatology. Additional tests are needed verify this result.

The sensitivity to the vertical boundary condition was not thoroughly tested in the strong windstorm cases, although the use of the upper radiation condition and larger vertical extent of the modeling domain is supported by Bacmeister and Schoeberl

(1989). They investigated the importance of wave breaking structures in the stratosphere on the flow near the mountaintop and found a strong sensitivity of the near surface flow to breaking waves in the stratosphere. Further work is needed to validate the upper radiation boundary condition in long-term mountain wave simulations.

Satisfactory results for the three-dimensional simulations of the observed January 9, 1989 windstorm were difficult to obtain under the current model configuration. Problems with the lateral boundary conditions prevented any useful comparisons with the two-dimensional tests and the observations. A more substantial three-dimensional modeling study, using grid-nesting procedures, is posed for the future that addresses the upstream and boundary conditions in a more reliable manner.

7.5 Summary

A summary of the significant contributions is provided below.

* Analytical and numerical solutions indicate the reduction in mountain wave activity is a function of mixed layer depth, with deeper layers producing larger responses.

* The numerical simulations and analytical results support the hypothesis that the observed diurnal windstorm bias is at least partially attributed to the response from surface heating.

* Linear theory is useful in determining the reduction of wave activity due to a developing mixed layer to within a factor of two.

* Linear analysis shows that the presence of an inversion inhibits the mixed layer effect on mountain waves. The contribution from the inversion enhances the usefulness of linear theory when compared to the non-linear numerical model results. Enhanced vertical resolution is needed in the inversion.

* Parameterized turbulent mixing is sufficient for predicting the height of the mixed layer.

* Mountain wave activity decreases after the development of a surface bound mixed-layer, yet in the highly non-linear events, a high drag state remains.

* Results from experiments using real data follow the idealized counterparts.

* Onset and strength of downslope windstorms are sensitive to vertical resolution and lateral boundary conditions. Vertical resolution on the order of 250m is required to adequately resolve developing critical layers.

* For non-blocking situations, results from the two-dimensional experiments can be applied to three-dimensional mountains of sufficient cross-flow width.

* When strong upstream blocking is present (Nh/U =3.0), the three-dimensional solutions differ significantly from the two-dimensional case and surface heating has little impact on the solution.

REFERENCES

Arakawa, A., 1966: Computational design for long term integration of the equations of motion: Two-dimensional incompressible flow. Part I. J. Comput. Phys. 1, 119 -143.

Asselin, R. 1972: Frequency filter for time integrations. Mon. Wea. Rev., 100, 487 -490.

ARPS, 1995: ARPS Users Guide Version 4.0, Center for Analysis and Prediction of Storms, University of Oklahoma, 380pp.

Bacmeister, J. T., and M. R. Schoeberl, 1989: Breakdown of vertically propagating two -dimensional gravity waves forced by orography. J. Atmos. Sci., 46, 2109-2134.

Barnes, S. L., 1964: A technique for maximizing details in numerical weather map analysis. J. Appl. Meteor., 3, 396-409.

Black A., 1996: Personal communication. Department of Soil Sciences, University of British Columbia, Canada.

Blumen, W., 1965: A random model of momentum flux by mountain waves. Geofys. Publ., 20, 1-33.

Bretherton, F. P., 1966: Critical layer instability in baroclinic flows. Quart. J. Royal Meteo. Soc., 92, 325-334.

Brinkmann, W. A. R., 1974: Strc ıg downslope windstorms. Mon. Wea. Rev. ,102. 592 -602.

Brown, J. M., 1986: A decision tree for forecasting downslope winds in Colorado. Preprints 11th conference on weather forecasting and analysis, June 17-20, 1986, Kansas City, Missouri, American Meteorological Society.

Brown, J. M., A. A. Rockwood, J. F. Weaver, B. D. Jamison, and R. Holmes, 1992: An expert system for the prediction of downslope windstorms. Fourth workshop on operational meteorology, September 15-18, 1992, Whistler, B. C., Canada.

Burden, R. L., and J. D. Faires, 1989: Numerical Analysis, Fourth Edition, PWS-Kent Publishers, 70-71.

Caughey, S. J., and S. G. Palmer, 1979: Some aspects of turbulence structure through the depth of the convective layer. Quart. J. Royal Meteo. Soc., 105, 811-827.

Clark, T. L., and W. R. Peltier, 1977: On the evolution and stability of finite-amplitude mountain waves. J. Atmos. Sci., 34, 1715-1730.

Clark, T. L., and W. R. Peltier, 1984: Critical level reflection and the resonant growth of nonlinear mountain wave. J. Atmos. Sci., 41, 3122-3134.

Clark, T. L., and W. D. Hall, and R. M. Banta, 1994: Two and three-dimensional Simulations of the 9 January 1989 severe Boulder windstorm: Comparison with observations. J. Atmos. Sci., 51, 2314-2343.

Crapper, G. D., 1959: A three-dimensional solution for waves in the lee of mountains. J. Fluid Mech. 6, 51-76.

Deardorff, J. W., 1980: Stratocumulus-capped mixed layers derived from a three dimensional model. Boundary Layer Meteorology, 18, 495-527.

Durran, D. R., and J. B. Klemp, 1983: A compressible model for the simulation of moist mountain waves. Mon. Wea. Rev., 111, 2341-2361.

_____, D. R., 1986: Another look at downslope windstorms, Part I, J. Atmos. Sci., 43, 2527-2543.

_____, D. R., and J.B. Klemp, 1987: Another look at downslope windstorms, Part II, J. Atmos. Sci., 44, 3402-3412.

_____, D. R., 1990: Atmospheric processes over complex terrain, Meteorological monographs, Amer. Meteo. Soc., Chapter 4, 328pp.

_____, D. R., 1992: Two layer solutions to Long's equation for vertically propagating mountain waves: how good is linear theory? Quart. J. Royal Meteo. Soc., 118, 415-433.

_____, D. R., M. J. Yang, D. N. Slinn, and R. G. Brown, 1993: Toward more accurate wave-permeable boundary conditions. Mon. Wea. Rev., 121, 604-620.

Eliassen, A., and E. Palm, 1960: Wave energy transfer in stationary gravity waves. Geofys. Publ., Vol. 22, Number 3.

Emanuel, K. A., 1994: Atmospheric Convection. Oxford University Press, 580pp.

Fiedler, B. H., 1992: Lecture notes. University of Oklahoma, Norman Oklahoma.

Garratt, J. R., 1994: The atmospheric boundary layer. Cambridge University Press, 316pp.

Gill, A. E., 1982: Atmospheric-Ocean Dynamics. Academic Press, New York, 662pp.

Gutman, L. N., 1991: Downslope windstorms, Part I: Effect of air density decrease with height. J. Atmos. Sci., 48, 2545-2551.

Haltiner, G. J., and R. T. Williams, 1980: Numerical Prediction and Dynamic Meteorology. Second Ed., John Wiley and Sons, 447pp.

Hornbeck, R.W., 1975: Numerical Methods, Prentice-Hall, Englewood Cliff, NJ. 310pp.

Julian, L. T., and P. R. Julian, 1969: Boulders winds. Weatherwise, 22, 108-112.

Klemp, J. B., and D. R., Durran 1983: An upper radiation boundary condition Permitting internal gravity wave radiation in mesoscale models. Mon. Wea. Review, Vol. 111, 430-444.

_____, J. B., and R. B. Wilhelmson, 1978: Numerical Simulation of convective storm dynamics. J. Atmos. Sci., 35, 1070-1096.

_____, J. B., and D. K. Lilly, 1975: The dynamics of wave induced downslope winds. J. Atmos. Sci., 32, 320-339.

_____, J. B., and D. K. Lilly, 1978: Numerical simulations of hydrostatic mountain waves. J. Atmos. Sci., 35, 78-107.

_____, J. B., and D. K. Lilly, 1979: The effects of terrain shape on nonlinear hydrostatic mountain waves. J. Fluid Mech., 95, 241-261.

Kundu, P. K., 1990: Fluid Mechanics. Academic Press, New York, 638pp.

Lilly, D. K., and E. J. Zipser, 1972: The Front Range windstorm of January 11, 1972. Weatherwise, 25, 56-63.

_____, D. K., 1978: A severe downslope windstorm and aircraft turbulence event induced by a mountain wave. J. Atmos. Sci., 35, 59-77.

_____, D. K., 1983: Linear theory of internal gravity waves and mountain waves. Mesoscale Meteorology, D. Reidel Publishers, 781pp.

Lilly, D. K., 1992: Buoyant Energetics. Class treatise, University of Oklahoma.

Long, R. R, 1953: Some aspects of the flow of stratified fluids, I: A theoretical investigation. Tellus, 5, 42-58.

Malkus, J. S., and M. E. Stern, 1953: The flow of a stable atmosphere over a heat island, Part 1. J. Meteo., 10, 30-41.

Miller, P.P., and D. R. Durran, 1991: On the sensitivity of downslope windstorms to the asymmetry of the mountain profile. J. Atmos. Sci., 48, 1457-1473.

Moeng, C. H., 1984: A large eddy simulation model for the study of planetary boundary layer turbulence. J. Atmos. Sci., 41, 2052-2062.

Nance, L. B., and D. R. Durran, 1994: A comparison of the accuracy of three anelastic systems and pseudo-compressible system. J. Atmos. Sci., 51, 3549-3565.

Neiman, P. J., R. M. Hardesty, M. A. Shapiro, and R. E Cupp, 1988: Doppler lidar observations of a downslope windstorm. Mon. Wea. Review, Vol. 116, 2265 -2275.

Orlanski, I., 1976: A simple boundary condition for unbounded hyperbolic flows. J. Comput. Phys., 21 , 251-269.

Peltier, W. R. and T. L. Clark, 1979: The evolution and stability of finite amplitude mountain waves: Part 2: Surface drag and observed windstorms. J. Atmos. Sci., 36, 1498-1529.

_____, W. R., and T. L. Clark, 1983: Nonlinear mountain waves in two and three spatial dimensions. Quart. J. Royal Meteo. Soc., 109, 527-548.

Phillips, D. S., 1984: Analytical surface pressure and drag for linear hydrostatic flow over three-dimensional elliptical mountain. J. Atmos. Sci., 41, 1073-1084

Queney, P., 1948: The problem of airflow over mountains. A summary of theoretical studies. Bull. Amer. Meteo. Soc., 29, 16-26.

Raymond, D. J., 1972: Calculation of airflow over an arbitrary ridge including diabatic heating and cooling. J. Atmos. Sci., 29, 837-843.

Reisner, J. M., and P. K. Smolarkiewicz, 1994: Thermally forced low Froude number flow past three-dimensional obstacles. J. Atmos. Sci., 51, 117-133.

Scheetz, V. R., J. F. Henz, and R. A. Maddox, 1976: Colorado severe downslope windstorms: A prediction technique. Final report under contract No. 5-35431 to TDL/SDO/NWS from Geophysical Research and Development Corporation.

Scorer, R. S., 1955: Theory of airflow over mountains, Part 4: Separation of flow. Quart. J. Royal Meteo. Soc., 81, 340-350.

Sellers et.al., 1995: The boreal ecosystem atmosphere study (BOREAS): An overview and early results from the 1994 field year. Bull. Amer. Meteor. Society, Vol., 76, 1549-1578.

Sheppard, P. A., 1956: Airflow over mountains. Quart. J. Royal Meteo. Soc., 82, 528.

Skamarock, W. C., and J. B. Klemp, 1992: The stability of time-split numerical Methods for the hydrostatic and the non-hydrostatic elastic equations. Mon. Wea. Rev., 120, 2109-2127.

Smith, R. B., 1979: The influence of mountains on the atmosphere. Advances in Geophysics. Academic Press, Vol. 29, 87-230.

_____, R. B., 1980: Linear theory of stratified hydrostatic flow past an isolated mountain. Tellus, 32, 348-364.

_____, R. B., 1985: On severe downslope winds. J. Atmos. Sci., 42, 2597-2603.

_____, R. B., 1988: Linear theory of stratified flow past an isolated mountain in isosteric coordinates. J. Atmos., Sci., 45, 3889-3896.

_____, R. B., 1989: Mountain induced stagnation points in hydrostatic flow. Tellus, 41A, 270-274.

_____, R. B., and Y.L. Lin, 1982: The addition of heat to a stratified airstream with application to the dynamics of orographic rain. Quart. J. Royal Meteo. Soc., 108, 353-378.

Sullivan, P. P, J. C. McWilliams, and C. H. Moeng, 1994: A subgrid-scale model for large eddy simulations of planetary boundary layer flows. Boundary Layer Meteorology 71, 247-276.

Sun, W. Y., and C. Z. Chang, 1986: Diffusion model for a convective layer, Part 1: Numerical simulations of convective boundary layer. J. Climate and Appl. Meteo., 25, 1445-1453.

Whiteman, C. D., and J. G. Whiteman, 1974: An historical climatology of damaging downslope windstorms at Boulder, Colorado. NOAA Tech. Report ERL 336-APCL 35. [Available from the Superintendent of Documents, U.S. Government Printing Office, Washington D.C.]

Wurtele, M., 1957: The three-dimensional lee wave. Beitr. Phys. Frei. Atmos., 29, 242 -252.

Xue M. X, and S. J. Lin, 1991: On the numerical equivalence of advection terms in flux and advective form. Unpublished manuscript. Center for the Analysis and Prediction of Storms, University of Oklahoma, 10pp.

Yamada T., and G. Mellor, 1975: A simulation of the Wangara atmosphere boundary layer date. J. Atmos. Sci., 32, 2309-2329.

APPENDIX A

VERTICAL w-π IMPLICIT SOLVER

The pressure and vertical velocity are coupled in the vertical through a Crank-Nicholson scheme. This approach removes the vertical sound constraint on the small time step. The method follows that of Durran and Klemp (1983) and the ARPS (1995). The discretized equations for π and w are (from Chapter 3):

$$\frac{w^{\tau-\Delta\tau}-w^{\tau}}{\Delta\tau} = -c_p\bar{\theta}^{\zeta^t}[(1-\beta)(\overline{J_3}^{\zeta}\delta_{\zeta}\pi')^{\tau}+\beta(\overline{J_3}^{\zeta}\delta_{\zeta}\pi')^{\tau-\Delta\tau}]+g(\overline{\frac{\theta'}{\bar{\theta}}}^{\zeta^t})$$

$$-advw^t + f\bar{u}^{xz^t} + turb_w^t + D_w^t \qquad \text{(A.1)}$$

$$\frac{\pi'^{\tau-\Delta\tau}-\pi'^{\tau}}{\Delta\tau} = -advw'' - \frac{R_d}{c_v}(\overline{\Pi}+\pi^{\tau})[(\delta_x u^{\tau-\Delta\tau}++\delta_y v^{\tau-\Delta\tau}+\beta\delta_{\zeta}w^{\tau})$$

$$+\beta\frac{\overline{w}^{\zeta^t}g}{c_p\bar{\theta}}+(1-\beta)\frac{\overline{w}^{\zeta^{t-\Delta t}}g}{c_p\bar{\theta}}+\frac{R_d}{c_v}(\overline{\Pi}+\pi')\frac{1}{\theta}\delta_t\theta^t \qquad \text{(A.2)}$$

The time weighting term β is used to reduce the small to large time step instability and is applied to w in the π equation and to π in the w equation. A value of 0.6 is sufficient following the results of Durran and Klemp (1983). All the large time step forcing terms and the known small time step terms in (A.1) and (A.2) are grouped into wforce and pforce.

$$wforce = \frac{w^{\tau}}{\Delta\tau} - c_p \overline{\theta}^{\zeta^t}(1-\beta)(\overline{J_3}^{\zeta}\delta_{\zeta}\pi')^{\tau} + g\frac{\overline{\theta'}^{\zeta^t}}{\overline{\theta}} - advw^t + f\overline{u}^{\zeta^t} + turb_w^t + D_w^t \quad (A.3)$$

$$pforce = \frac{\pi'^{\tau}}{\Delta\tau} - advw^{\tau t} - \frac{R_d}{c_v}(\overline{\Pi} + \pi'^{\tau})(\delta_x u^{\tau-\Delta\tau} + +\delta_y v^{\tau-\Delta\tau} + \beta\delta_{\zeta} w^{\tau})$$

$$+\beta\frac{\overline{w}^{\zeta^t} g}{c_p\overline{\theta}} + \frac{R_d}{c_v}(\overline{\Pi} + \pi'^{\tau})\frac{1}{\theta}\delta_t\theta^t \quad (A.4)$$

In (A.4) the total non-dimensional pressure at the current small time step multiplies the divergence term and the heating term. These terms are explicit and remove some of the gain obtained from the implicit application. The effect on the time step criterion is small since perturbation pressures are rarely greater than 3kPa or 1/30th of the base state pressure. Equations (A.1) and (A.2) are rewritten as:

$$w^{\tau-\Delta\tau} = \Delta\tau(wforce - c_p\overline{\theta}^{\zeta^t}\beta\overline{J_3}^{\zeta}\delta_{\zeta}\pi'^{\tau-\Delta\tau}) \quad (A.5)$$

$$\pi'^{\tau-\Delta\tau} = \Delta\tau(pforce - \frac{r_d}{c_v}(\overline{\Pi} + \pi'^{\tau})(1-\beta)\delta_{\zeta} w^{\tau-\Delta\tau} + (1-\beta)\frac{\overline{w}^{\zeta^{\tau-\Delta\tau}} g}{c_p\overline{\theta}}) \quad (A.6)$$

Eliminating the pressure produces an equation for w at the future time step in terms of known terms.

$$A(k)w(k-1) + B(k)w(k) + C(k)w(k+1) = D(k)$$

A(k), B(k), C(k), and D(k) are given by:

$$A(k) = -a(d + e)$$

$$B(k) = 1 + a(b + c - d + e)$$

$$C(k) = a(b - c)$$

$$D(k) = wforce - a(pforce_k - pforce_{k-1})$$

where,

$$a = \frac{\Delta\tau\beta c_p(\theta_k + \theta_{k-1})(J_{3k} + J_{3k-1})}{4\Delta\varsigma}$$

$$b = \frac{\Delta\tau\beta(1 - bousopt)g}{2c_p\bar{\theta}_k}$$

$$c = \frac{\Delta\tau R_d(\bar{\Pi}_k + \pi'^{\varepsilon}_k)\beta J_{3k}}{c_v\Delta\varsigma}$$

$$d = \frac{\Delta\tau\beta(1 - bousopt)g}{2c_p\bar{\theta}_{k-1}}$$

$$e = \frac{\Delta\tau R_d(\bar{\Pi}_{k-1} + \pi'^{\varepsilon}_{k-1})\beta J_{3k-1}}{c_v\Delta\varsigma}$$

The tridiagonal system is solved with appropriate boundary conditions. The solver is applied from 3 to nz-2. The top boundary condition for the rigid lid case is w=0. For the linear radiation condition between pressure and w the formulation from Durran and Klemp (1983) is used. The details of the upper radiation condition implementation are

given in Appendix B. The performance of the implicit solver is roughly 2.0 times slower than the explicit version for a given small step. The implicit method is computationally effective when the ratio of the horizontal to vertical grid spacing is:

$$\frac{\Delta x}{\Delta \zeta} \approx 2.0$$

APPENDIX B

LINEAR HYDROSTATIC w-π TOP BOUNDARY CONDITION

Vertical energy propagation from hydrostatically forced gravity waves can be significant. A damping layer in combination with a rigid lid is commonly used in mesoscale numerical models to prevent reflection from a rigid lid. The rigid lid-sponge combination is effective (Klemp and Lilly, 1978) in preventing significant reflection. But for strong mountain waves the thickness of a properly designed damping layer can be as much as 1/2 of the model vertical domain. Another method applied by Klemp and Durran (1983) as well as others applies a linearized hydrostatic analytical relation between the vertical velocity and pressure variables at the top boundary. The advantage to this method is the number of grid points in the vertical is significantly reduced without degradation of the numerical solution. Fewer vertical grid points correspond to smaller memory and CPU cycle requirements. Since the relation between vertical velocity and pressure is linearized, the application is somewhat limited. Tests of the condition for a finite amplitude mountain wave reveals solution sensitivity to the upper radiation condition. The condition is more applicable to cases in which wave breaking takes place below the upper boundary.

The formulation implemented in ARPI3D follows Klemp and Durran (1983). For a linearized hydrostatic Boussinesq set of 3-dimensional equations, to which the derivation is not reproduced here, the Fourier transformed analytical relation between w and π' is

$$\hat{\pi}'^{\tau-\Delta\tau}_{nz-2} = \frac{\hat{N}_{nz-2}}{c_p \overline{\vartheta}_{nz-2}(k_x^2 + k_y^2)^{\frac{1}{2}}} \hat{w}^{\tau-\Delta\tau}_{nz-1} \qquad \text{(B.1)}$$

The relation (B.1) is applied at k=nz-2. The pressure and velocity points are staggered in the vertical, so (B.1) is approximate. An average of w at nz-1 and nz-2 proved to be unstable and the above relation is adopted. The outline of the solution method is:

1. Apply the reduction step of the tridiagonal solver from Appendix A to w.
2. Starting with the pressure equation, obtain a relation for w(nz-2) in terms of w(nz-1) and π(nz-2). Substitute the result into the reduced step (1). Step (1) becomes an equation relating w(nz-1) and π (nz-2).
3. Transform (2) into Fourier space.
4. Apply (B.1) to (3) obtaining an equation for w(nz-1) in Fourier space it terms of known quantities.
5. Solve (4) for w(nz-1), perform a reverse transform and apply the result to the back-substitution phase of the tridiagonal solver to recover w at all other levels.

The above method is applied to both the vertically explicit and implicit w-π solving techniques in ARPI3D. Step (2) uses the discretized pressure equation:

$$\Delta\tau\beta[\frac{g(1-bousopt)}{2c_p\bar{\theta}_{nz-2}} - \frac{R_d(\overline{\Pi}+\pi'^{\tau}_{nz-2})}{c_v J_{3nz-2}\Delta\zeta}]w^{\tau+\Delta\tau}_{nz-1} + \Delta\tau\beta[\frac{g(1-bousopt)}{2c_p\bar{\theta}_{nz-2}} + \frac{R_d(\overline{\Pi}+\pi'^{\tau}_{nz-2})}{c_v J_{3nz-2}\Delta\zeta}]w^{\tau-\Delta\tau}_{nz-2}$$

$$= \pi'^{\tau+\tau}_{nz-2} - pforce_{nz-2} \qquad \text{(B.2)}$$

The variable pforce includes all the known terms in the pressure equation including the big time step advection and heating terms and the small time step updated horizontal

velocity divergence and a weighted portion (1-β) of the vertical velocity divergence from the previous small time step. The reduction phase of the tridiagonal solver provides a relation between w(nz-2) and w(nz-1).

$$w_{nz-2}^{\tau-\Delta\tau} = d'_{nz-2} - c'_{nz-2}\, w_{nz-1}^{\tau+\Delta\tau} \qquad \text{(B.3)}$$

The coefficients c and d have been modified from the reduction steps. Substituting (B.3) into (B.2) gives:

$$(A1 - A2 \cdot c'_{nz-2})\, w_{nz-1}^{\tau-\Delta\tau} = \pi'^{\tau-\Delta\tau}_{nz-2} - pforce_{nz-2} - A2 \cdot d'_{nz-2} \qquad \text{(B.4)}$$

Where A1 and A2 are the coefficients of w(nz-1) and w(nz-2) in (B.2), respectively. The last step is the transformation of (B.4) into Fourier space and the substitution of (B.1) into (B.4) to obtain an equation for w(nz-1) in terms of known quantities. The vertical velocity at k=nz-1 is then transformed back to real space and the remaining vertical velocities at all other levels are obtained using the back substitution phase of the tridiagonal solver. Pressure is then computed using the updated three-dimensional velocity field.

APPENDIX C

STREAMLINE METHOD AND TESTS

Two-dimensional streamline-trajectory computations used in Chapter 4 to validate the numerical model formulation are described and tested here. The trajectory model applies the predictor-corrector method to the three-dimensional velocity field. No generality is lost in presenting only the x-direction, as this analysis can be equally applied in the y and z directions. In the x-direction, a parcel trajectory is defined as:

$$\frac{dx}{dt} = v \qquad (C.1)$$

where (A.1) can be integrated to obtain the new parcel location given the current parcel velocity and position. A simple approach to computing the new parcel location would be to estimate the velocity at the present location and apply a time increment obtaining the distance traveled and the new position. Assuming that the velocity field changes slowly in space the deviation from the true parcel movement would be small. However, for the case of strong spatial velocity gradients large errors are possible from simply estimating the initial velocity as the average velocity over the parcel displacement. To improve the accuracy of the scheme, the predicted parcel movement is used to obtain an updated or corrected velocity field. The initial parcel position X^o is used to obtain a linearly interpolated velocity V^o. The time step is applied to the interpolated velocity field and an updated intermediate position X^n is obtained. The relationship describing the parcel displacement is

$$X^n = X^o + \Delta t * V^{n-1} \qquad \text{(C.2)}$$

where V^{n-1} is the current interpolated velocity field. The corrected velocity field is determined using:

$$V^n = 0.5*(V^o + V^{n-1}) \qquad \text{(C.3)}$$

With the updated velocity, Equation (C.2) is reapplied n times producing a final parcel location X^n for each time step. For the n=1 case, there is no velocity correction and only Equation (C.2) is used. This process can be repeated n times but little is gained after the 2nd application. For a slowly varying velocity field, n=2 produces a convergent streamline pattern. This method is similar to the Adams-Moulton presented by Hornbeck, (1975). Tests of this trajectory method were conducted for a radially varying velocity field. The error is a function of the time step (dt) and the number of iterations (n). Figure C.1 displays the streamlines using a radially varying two-dimensional wind field for two different number of corrector steps. The radial velocity fields are defined by:

$$u = U_o \frac{(xcenter - x)}{L} \quad \text{and} \quad w = W_o \frac{(zcenter - z)}{H}$$

where L is the width and H is the height of the test domain, xcenter and zcenter are the central locations, and U_o and W_o are the velocity magnitudes.

(a)

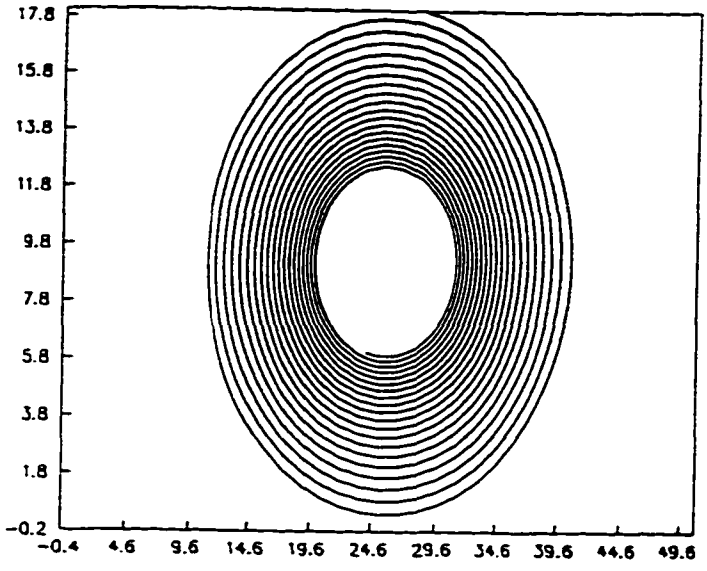

(b)

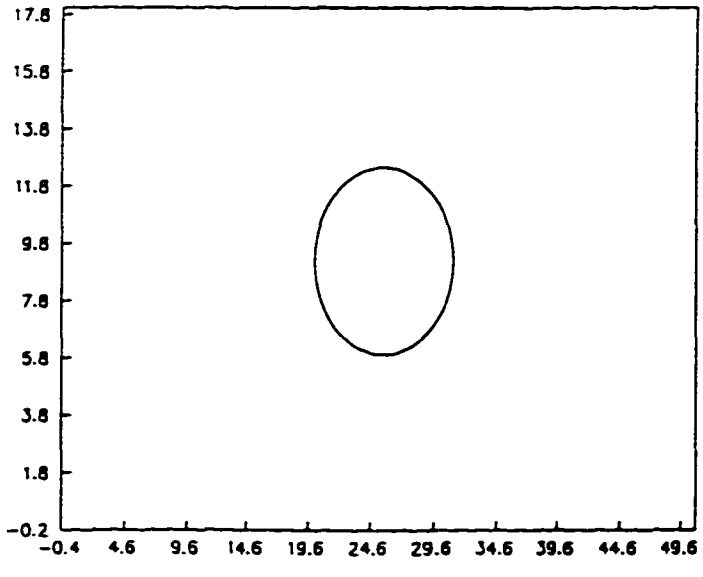

Figure C.1. Streamline test pattern for U_o=20 m/s, W_o=20m/s, dt=25 seconds, dx=400m, dz=250 m , for (a) n=1, and (b) n=2. The CFL criteria is approximately 0.2.

APPENDIX D

MODEL PERFORMANCE

The two-dimensional simulations presented in this report were run on the University of Oklahoma ECAS Cray J-90 series computer. This computer is composed of 8 processors and 256 megawords of main memory. Model performance was measured using the -perf compiler option on the Cray FORTRAN 77 compiler. The domain size is 64 x 64 x 53 grid points in the x, y, and z directions. The test was run on one processor using the –Zv compiler option. The large and small time steps were 20 and 4 seconds respectively. The grid spacing was dx = dy = 2000m and dz = 250m and the base state wind was a constant 10m/s. The vertically implicit $w-\pi$ solution technique and upper radiation were implemented. Table D-1 presents a compilation of the performance statistics by subroutine for a three-dimensional mountain wave simulation. The overall code rating for this test is 95.6 MFLOPS.

The percentage of the total time for the $w-\pi$ solver is a function of the ratio of large time steps to small time steps. For a large big to small time step ratio, the small time step solver requires a larger portion of the total CPU time. Figure D.1 presents a pie chart of the most significant contributors to the model total CPU time. Approximately 35% of the time is spent in the small time step solvers dwpim3d and tri3d. The subroutine arpi3d also contains small time step calculations for u and v.

Perftrace Statistics Report
Showing Traced Routines
(Sorted by CPU Time Used (Descending))
(CPU Times are Shown in Seconds)

Group 0 Counter Summary

Name	Called	Time	Avg Tim	EX %	ACM %	Mmems	MFlops	
DUPIM	500	6.18E+01	1.24E-01	28.5	28.5	107.3	118.1	*******
ARPI3D	1	4.63E+01	4.63E+01	21.4	49.9	109.1	85.2	*****
TUVWS	50	1.62E+01	3.24E-01	7.5	57.3	35.9	76.9	*
TRI	500	1.46E+01	2.91E-02	6.7	64.0	87.3	93.3	*
TURBS	100	1.22E+01	1.22E-01	5.6	69.6	117.9	95.6	*
THIXUVW	50	8.11E+00	1.62E-01	3.7	73.4	106.0	91.5	
STRESS	50	7.85E+00	1.57E-01	3.6	77.0	117.4	95.1	
ADVZ	300	7.81E+00	2.60E-02	3.6	80.6	113.8	98.2	
ADVX	250	6.73E+00	2.69E-02	3.1	83.7	107.5	92.9	
ADVY	250	6.33E+00	2.53E-02	2.9	86.6	114.3	98.5	
CMIXZ	200	4.29E+00	2.14E-02	2.0	88.6	102.3	83.1	
CMIXX	200	4.27E+00	2.13E-02	2.0	90.6	100.3	80.9	
CMIXY	200	4.15E+00	2.07E-02	1.9	92.5	103.2	83.2	
VRADFG	2000	3.93E+00	1.96E-03	1.8	94.3	99.8	60.4	
WCONT	100	2.83E+00	2.83E-02	1.3	95.6	127.0	119.5	
TAU3D	50	2.49E+00	4.98E-02	1.1	96.7	105.2	96.9	
MAXMIN	23	1.93E+00	8.40E-02	0.9	97.6	26.2	9.9	
TKE3D	50	1.54E+00	3.08E-02	0.7	98.3	93.6	58.9	
UPRADS	500	1.50E+00	3.00E-03	0.7	99.0	20.7	95.1	
INIT	1	7.99E-01	7.99E-01	0.4	99.4	50.0	57.2	
VCOST	2000	7.10E-01	3.55E-04	0.3	99.7	94.3	54.5	
VRFTF1	2000	2.60E-01	1.30E-04	0.1	99.8	62.6	30.6	
VRADF2	2000	2.10E-01	1.05E-04	0.1	99.9	74.8	91.4	
BCUV3D	50	6.92E-02	1.38E-03	0.0	100.0	50.0	32.0	
VRFFTF	2000	3.53E-02	1.77E-05	0.0	100.0	7.8	0.0	
PIMACH	2004	1.30E-02	6.47E-06	0.0	100.0	0.2	0.0	
VCOSTI	2	1.28E-04	6.39E-05	0.0	100.0	8.3	41.5	
VRFTI1	2	1.20E-04	5.98E-05	0.0	100.0	4.3	17.3	
VRFFTI	2	4.86E-05	2.43E-05	0.0	100.0	4.8	0.0	
ARPISHELL	1	2.47E-05	2.47E-05	0.0	100.0	14.2	0.0	
Totals	15436	2.17E+02		100.0	100.0	100.3	95.6	

Table D-1. Performance statistics for ARPI3D three-dimensional mountain wave simulation on a Cray J-90 series computer using a single processor and the vector compiler option.

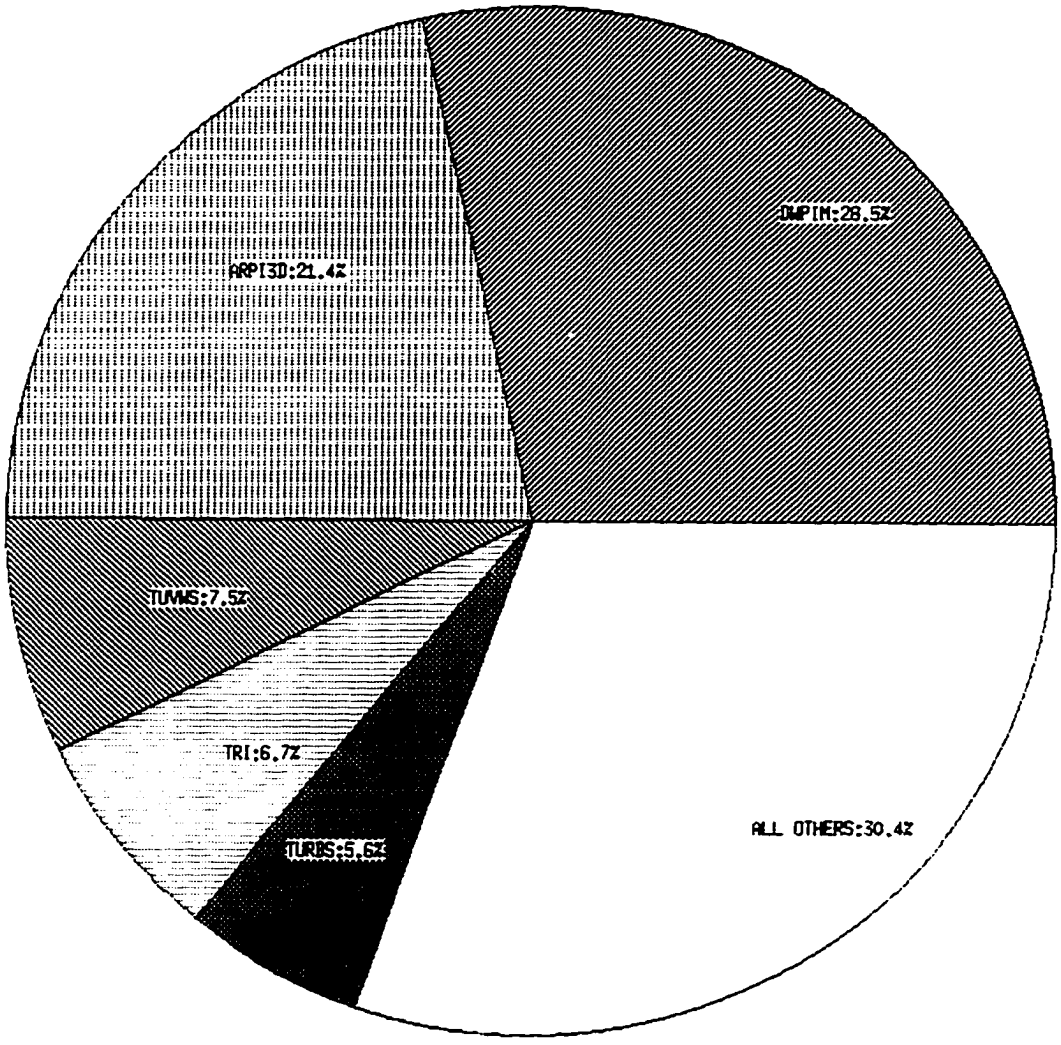

Figure D.1. Pie chart of CPU time requirements for a three-dimensional mountain wave simulation using ARPI3D and the ECAS Cray J-90 computer.

Tests were conducted during the initial model development phase which measured the efficiency of different terrain transformations and pressure equation formulations. The simple chain rule terrain formulation is found to be significantly faster (>33%, without turbulence) than the strongly conservative form used in a number of models including the ARPS. This is primarily due to the computationally intensive floating-point divisions in the strong conservation formulation. The adaptation of the system of equations from pressure to non-dimensional pressure also improves the computational efficiency of the code, as does the implementation of the advective form of the equations. In the dimensional pressure system of equations, the additional term in the buoyancy relation, due to a power series approximation, is computed on the small time step. The effect of this term was not explicitly determined but is estimated on the order of a few percent of the total solution time.

Another method of estimating computational efficiency is to test the model with other established mesoscale numerical models. A rough comparison of ARPI3D with ARPS Version 4.0 was made for a number of simple tests with the results of only two comparisons presented here. In 2-D mode, ARPI3D is on the order of 12-15 times more efficient (CPU seconds) than a similarly configured ARPS simulation. In defense of the ARPS, this is primarily due to the fact that the ARPS has a pseudo 2-dimensional option. The ARPS 2-dimensional mode computes 4 vertical slices, due to boundary condition requirements, while ARPI3D's 2-D mode computes only 1 vertical slice. A more realistic test involves a 3-dimensional cold bubble dropped over a symmetric mountain. Both models were run without moisture since ARPI3D currently uses a dry formulation. The simulation time on a Cray J-90 computer for ARPS is approximately

3 times greater than that required by ARPI3D. Such a large discrepancy is likely due to the use of a simple coordinate transformation (chain rule), equivalent advective form of the advection terms, solving non-dimensional pressure, and the absence of operator subroutines. The memory requirements between the two models are comparable with ARPI3D requiring approximately 1/2 that of the ARPS.

The three-dimensional experiments presented in this report were performed on the Pittsburgh Super Computing Center's Cray T3D and T3E massively parallel computers and the University of Oklahoma Hitachi SR2201C parallel super computer. During the winter of 1996, the source code was upgraded to include message passing interface (MPI) subroutine calls. MPI was chosen over the Parallel Virtual Machine (PVM) message passing technique because it is more efficient in passing similarly sized packets. The message passing application allows the code to be run on massively parallel computer platforms. The advantage to this method is the removal of the memory limitation existing on the Cray J90 and other symmetric multi-processor (SMP) platforms. Tests were conducted on the T3D in which the per processor model grid arrays remained constant and the number of processors increased. This experiment tests the scalability of ARPI3D on a specific machine type. As the number of processors increases the domain size also increases. A perfect code implemented on an infinitely fast computer would register the same wall clock times regardless of the number of processors. The relation for the number of grid points per processor to the global domain size is:

$$gnx = (nx - 5) * nprocx + 5 \qquad (D.1)$$

$$gny = (ny - 5) * nprocy + 5 \qquad (D.2)$$

Nx and ny are the number of grid points for each processor in the x and y-directions and gnx and gny are the number of global grid points in the x and y directions. The choice of the per processor domain in (D.1) and (D.2) is based on the desire to eliminate message passing of intermediate variables associated with fourth order spatial derivatives. In the present configuration no intermediate variable passing is required. Other models (e.g. ARPS) use a smaller more memory efficient per-processor domain (nx-3 and ny-3) but are required to pass intermediate results. Intermediate variables are present in the turbulence and fourth order advection and turbulent mixing terms. The disadvantage to the method applied to the present model is a slight increase in the number of grid points per processor. This redundancy is balanced by a more efficient message-passing configuration. Figure D.2 presents a chart of the scalability of ARPI3D through a range of processor configurations on the PSC T3D computer. The values are normalized by the 16-processor test simulation. The results indicate that as the processor domain is expanded from 16 to 512 processors the code is 80% efficient. Personnel communication with PSC consultants reveals that this efficiency rating is very good, exceeding a large fraction of the current MPP applications. The code performance was measured on the T3D using the apprentice performance monitoring software. ARPI3D is rated at approximately 10Mflops on the T3D. This is approximately 9 times slower than simulations performed on a single processor J90 and 6.5 time slower than a single Hitachi SR201C node. Attempts were made to improve

the code performance on the T3D. Optimization was minimal due to the small data cache on the DEC alpha processor. ARPS has a similar mflop rating and is equally difficult to optimize on the T3D.

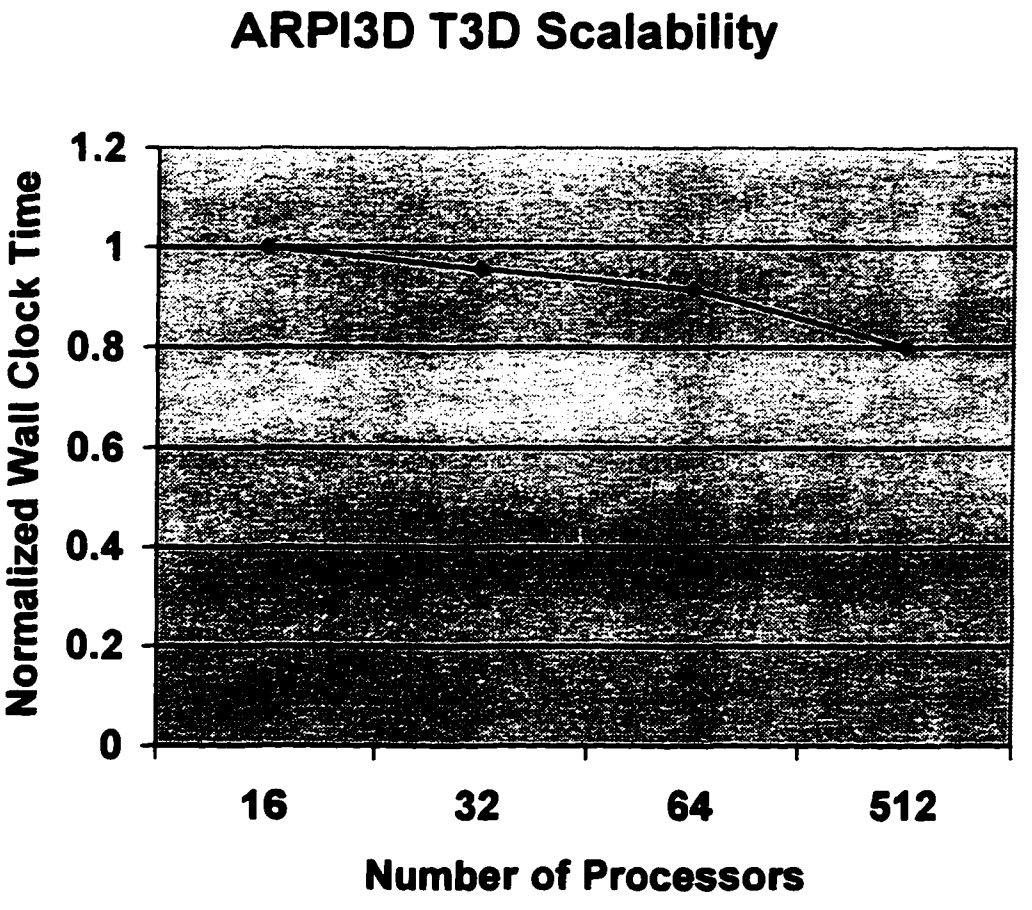

Figure D.2. Plot of the normalized wall clock time for a 20x12x115 per processor grid simulations as a function of processor configuration. Tests were conducted on the PSC Cray T3D computer.

APPENDIX E

SOUNDING PROFILES

Sounding data for Wangara Day 33 simulations.

Sounding filename = wang.snd

1-D Sounding Input for ARPI3D

Sounding Data collected at Wangara Surface Experiment,

34.5 South 144.93 East, Australia

Date: 9:00am August 16, 1967

Sounding obtained from Yamada and Mellor, 1975.

Surface Height = 0.0 m, Surface Pressure = 102,300 Pa

Number of Levels = 23

Pressure	Temp.	Qv	U	V
15000	-65.0	.00000	35.00	00.00
35000	-40.0	.00023	30.00	00.00
48000	-15.0	.00023	25.00	00.00
62300	-5.0	.00026	15.00	00.00
72300	-1.5	.00031	7.00	00.00
79900	-0.2	.00060	.50	1.10
82000	1.4	.00070	-.70	1.72
84000	1.7	.00080	-1.19	.26
86100	2.0	.00080	-1.45	.07
88300	2.3	.00150	-1.93	-.90
89000	2.6	.00180	-2.29	-1.41
90500	2.5	.00200	-2.55	-1.16
91600	2.9	.00220	-2.28	-.76
92800	3.5	.00250	-2.45	-.48
93900	3.8	.00290	-2.43	-.35
95100	4.7	.00320	-2.79	-.26
96300	5.8	.00330	-2.49	-.37
97400	6.8	.00330	-3.20	-.47
98600	7.4	.00370	-3.12	-.51
99800	7.5	.00380	-2.79	-.57
101100	5.4	.00380	-2.92	-.38
101700	5.1	.00370	-2.84	.03
102300	5.5	.00420	0.0	0.00

Sounding data for January 11, 1972 Boulder Colorado windstorm simulations.

Sounding filename = bld2.snd

1-D Sounding Input for ARPI3D

Sounding Data collected at Grand Junction, Colorado

Date: 12Z Jan. 11, 1972

Sounding estimated from Figure 10 Durran and Klemp (1983)

The top two layers were taken from Peltier and Clark (1979)

Surface Height = 0.0 m, Surface Pressure = 82000 Pa

Number of Levels = 13

Pressure	Pt	Qv	U	V
100.00000	1481.0000	0.00000	20.00	0.00
1000.00000	764.00000	0.00000	20.00	0.00
11000.00000	388.00000	0.00000	20.00	0.00
16000.00000	350.00000	0.00000	22.00	0.00
18500.00000	328.50000	0.00000	31.00	0.00
22000.00000	321.50000	0.00000	44.00	0.00
24000.00000	319.50000	0.00000	53.00	0.00
30000.00000	317.00000	0.00000	46.00	0.00
40000.00000	313.00000	0.00000	38.50	0.00
53000.00000	308.50000	0.00000	31.00	0.00
62500.00000	296.50000	0.00000	20.00	0.00
68000.00000	293.00000	0.00000	17.00	0.00
82000.00000	293.00000	0.00000	9.00	0.00

Sounding Data for the January 9, 1989 Boulder Colorado 2305UTC simulations.

Sounding filename = cl2d.snd

1-D Sounding Input for ARPI3D taken from Clark et. al. (1994)

Data collected at Craig, Colorado

Date: 15Z January 9, 1989

Surface Height 0.0 m, Surface Pressure 100000 Pa

Number of Levels = 20

Pressure	Temp.	Qv	U	V
500.00000	-55.70000	0.00000	30.00	0.00
2500.00000	-55.70000	0.00000	30.00	0.00
5000.00000	-55.70000	0.00000	30.00	0.00
9810.00000	-55.70000	0.00000	30.00	0.00
11880.00000	-55.80000	0.00000	31.09	0.00
15090.00000	-56.90000	0.00000	31.26	0.00
19980.00000	-60.90000	0.00000	40.57	0.00
24970.00000	-57.10000	0.00000	39.28	0.00
29920.00000	-47.20000	0.00000	34.74	0.00
35000.00000	-41.90000	0.00000	29.77	0.00
40030.00000	-35.00000	0.00000	29.07	0.00
45000.00000	-28.80000	0.00000	27.14	0.00
50170.00000	-22.60000	0.00000	26.11	0.00
55210.00000	-20.30000	0.00000	27.99	0.00
60290.00000	-15.30000	0.00000	25.50	0.00
69460.00000	-11.90000	0.00000	23.26	0.00
70220.00000	-11.00000	0.00000	13.34	0.00
75420.00000	-6.80000	0.00000	9.96	0.00
81160.00000	-6.00000	0.00000	3.75	0.00
100000.0000	-6.00000	0.00000	3.75	0.00